Deeply Virtual Compton Scattering off Unpolarised Deuterium at HERMES

Gordon D. Hill

A thesis presented for the degree of
Doctor of Philosophy

Nuclear Physics Experimental Research Group
Department of Physics and Astronomy
University of Glasgow
Scotland

August 2008

Deeply Virtual Compton Scattering off Unpolarised Deuterium at HERMES

Gordon D. Hill

Submitted for the degree of Doctor of Philosophy
August 2008

Abstract

The HERMES experiment was a forward angle spectrometer on the HERA storage ring at DESY, Hamburg, Germany. HERMES successfully increased understanding of the "spin puzzle", the spin structure of the nucleon, by providing high precision measurements of $\Delta\Sigma$ in the Quark Parton Model, the fraction of the spin carried by the current quarks.

Following the link of another piece of the puzzle, the orbital angular momentum of quarks and gluons, to the Generalised Parton Distribution (GPD) theoretical framework, HERMES focused on measurements of the Deeply Virtual Compton Scattering (DVCS) process. These measurements are sensitive to GPDs, allowing further experimental constraints to be made on the components of nucleon spin.

In the Winter shutdown period 2005-2006 HERMES was upgraded with a Recoil Detector in the target region. This allowed the experiment to make exclusive measurements of the DVCS process for the first time, reducing background and increasing the resolution of various kinematic variables. The method for reconstructing particle tracks in the inhomogeneous magnetic field is investigated here.

DVCS off a deuterium target is measured with all available data prior to the installation of the Recoil Detector. A comparison is made to currently available models of spin-$\frac{1}{2}$ GPDs. This analysis has been approved for publication by the HERMES collaboration. The data is further employed in an investigation of a model dependent constraint of the total angular momentum of up and down quarks in the nucleon.

Declaration

The work in this thesis is based on research carried out at the Nuclear Physics Experimental Research Group, Department of Physics and Astronomy, University of Glasgow, Scotland. No part of this thesis has been submitted elsewhere for any other degree or qualification and is all my own work unless referenced to the contrary in the text.

Acknowledgements

This thesis represents four years of work, which would not have been completed without the help and support of many people. Whilst there are too many to list here in full, I'd particularly like to thank the following people for their efforts.

Firstly, thanks to my supervisors, Prof. Guenther Rosner and Prof. Ralf Kaiser for giving me the opportunity to obtain my Ph.D. within the Nuclear Physics group at the University of Glasgow. I have travelled far and wide and have learnt many skills which I expect will be of great benefit to me in the future. They have been generous in providing me with the support I needed throughout my studies.

During my track reconstruction studies I worked with many members of the HERMES collaboration. In particular I'd like to thank Andrew Osborne for starting my training in programming and passing on his knowledge of the tracking method. Bjoern Seitz, Sergey Yaschenko, Andreas Mussgiller, Craig Shearer, Inti Lehmann and Larry Felawka all provided help with various parts of the code and deserve my thanks.

My data analysis work was greatly assisted by Morgan Murray, who provided help in all aspects. His experience was an invaluable resource, I hope to pass on what I have learned in turn. Thanks to Hrachya Marukyan for working with me to finalise these results and for always being willing to help. Thanks also to Hongxue Ye and Dietmar Zeiler for their assistance with the model calculations and to Markus Diehl and Dieter Mueller for theoretical insights.

The Glasgow HERMES students, Craig, Andrew, Morgan, Jonathan Burns and David Mahon, provided support in every way and have been a pleasure to work with. Working at DESY was made bearable by their efforts.

The daily coffee trips in Glasgow provided the right mix of procrastination and caffeine. Thanks to the many students over the years who participated, too many to list here. Thanks particularly to those who put up with me in Room 407 over the years: Craig, Kris Monstad, Evie Downie, Morgan, Eilidh McNicoll, Jonathan, David Howdle and Seian Al Jebali. Thanks also to my proof readers: Morgan, Inti and David Hamilton.

Pub Wednesday was the perfect way to relax in the middle of the week, thanks to all my friends who provided beer and alternative Ph.D. and legal horror stories.

Finally, thanks to all my family for their support over the years.

Contents

List of Figures

List of Tables

Chapter 1

Introduction

Protons and neutrons, known as nucleons, form the atomic nucleus [GM64] and are two of the fundamental building blocks of matter in nature. Though originally postulated as fundamental particles, experiments such as those carried out at the Stanford Linear Accelerator Center (SLAC) [A$^+$76] have shown that nucleons have internal structure. Nucleons are now thought to consist of partons [Fey69]: quarks and gluons.

One of the fundamental properties of elementary particles is spin, the intrinsic angular momentum of the particle, expressed in units of $\hbar$. Both nucleons and quarks are spin-$\frac{1}{2}$ particles, with gluons spin-1. The spin of a nucleon can be expressed as [Ji97b]:

$$\begin{aligned} \frac{1}{2} &= J_Q + J_G & (1.1) \\ &= \frac{1}{2}\Delta\Sigma + L_Q + \Delta G + L_G & (1.2) \end{aligned}$$

where $J_Q\,(J_G)$ are the total angular momenta of quarks (gluons) in the nucleon, $\Delta\Sigma$ (ΔG) is the fraction of the spin carried by the constituent quarks (gluons) and $L_Q\,(L_G)$ is the orbital angular momenta of the quarks (gluons).

The HERMES experiment [Col93] was designed to help solve the “spin puzzle” [LA88], a problem arising from the differences between model predictions and measurements made by the EMC experiment at CERN [A$^+$88, A$^+$89].

The EMC result showed that $\Delta\Sigma$ was small, compatible with zero. These results

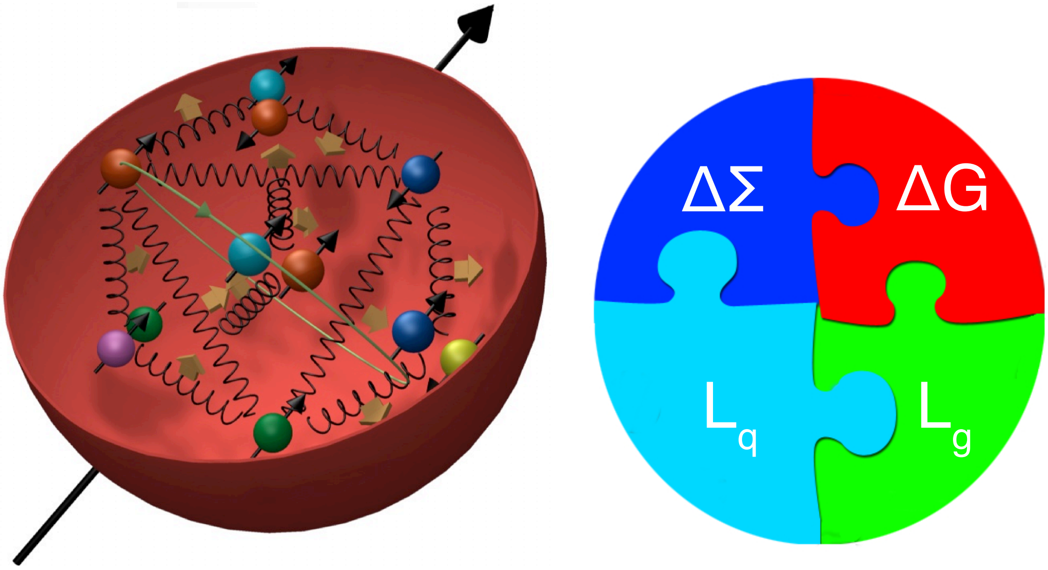

Figure 1.1: Left: illustration of the structure of the nucleon, showing quarks held together by gluons, each with intrinsic spin. Right: the spin puzzle, illustrating the respective contributions of spin and orbital angular momenta of quarks and gluons to the overall spin of a nucleon.

contain gluonic contributions due to the axial anomaly [Bas08], a fundamental property of quantum field theory, where the quark spin contribution cannot be treated independently from the gluon fields pertaining to the quarks. Later measurements showed the quark contribution to be approximately 30% of the total spin, such as recently reported from HERMES [A^{+}07a]. However, the "spin puzzle" is far from solved, with the remaining contributions to the overall nucleon spin still under investigation. HERMES continues to be at the forefront of this field, along with experiments at other laboratories such as CERN, Jefferson Lab and the Brookhaven National Laboratory.

In 1997 Ji published a relation of J_Q to the spin-$\frac{1}{2}$ Generalised Parton Distributions (GPDs) H and E [Ji97b], allowing experimentalists to access this part of the nucleon spin puzzle for the first time. The Deeply Virtual Compton Scattering process was found to be the simplest and most direct way to access these GPDs [DMR^{+}88, MRG^{+}94, Ji97a, Ji97b, Rad97]. Efforts were made to upgrade the existing HERMES apparatus to measure this process exclusively at the event level [K^{+}01] by installing a Recoil Detector to directly measure kinematics of the scattered target nucleon.

Measurements of DVCS azimuthal asymmetries in electro-photoproduction have been published by HERMES, e.g. [A^+01, A^+07b, A^+08], where the asymmetries depend on the azimuthal angle ϕ, defined as the angle between the scattering plane, between the lepton and the virtual photon, and the production plane, the real photon and the recoiling nucleon. Using information from models of GPDs, a constraint has been made of J_u and J_d using transversely polarised hydrogen DVCS data [A^+08], where u (d) refers to up (down) quarks in the nucleon. This result could be interpreted with other experimental spin physics results to give a better picture of the spin structure of the nucleon [Mur07].

This thesis will describe the DVCS process and its relationship to GPDs in chapter 2. The HERMES apparatus will be discussed in chapter 3, with the Recoil Detector detailed in section 3.4. The software solution for track reconstruction in the inhomogeneous magnetic field of the Recoil Detector is discussed in chapter 4. This solution is currently employed in productions of Recoil Detector data and used to complete the commissioning of the detector.

Chapter 5 contains the analysis of all data taken at HERMES with a deuterium target, prior to the installation of the Recoil Detector. Measurements of Beam Charge and Beam Spin Asymmetries are presented, with a discussion of systematic uncertainties also given. This analysis has been approved for future publication by the HERMES collaboration.

Finally, an investigation into providing a complementary result to those given in [A^+08] and [M^+07] is shown in chapter 6. Constraints of the total angular momentum of up and down quarks in the neutron, based on models of proton and neutron GPDs and using results given in chapter 5, are shown.

Chapter 2

Generalised Parton Distributions and Deeply Virtual Compton Scattering

In 1997 Xiangdong Ji related the total angular momentum of quarks (gluons), J_Q (J_G), to the theoretical framework to describe nucleon structure known as Generalised Parton Distributions (GPDs) [Ji97b]. Constraints on J_Q combined with measurements of $\Delta\Sigma$, the fraction of the spin carried by the constituent quarks, will allow access to the orbital angular momentum L_Q, one of the remaining pieces of the "spin puzzle", as discussed in chapter 1. Interest in GPDs greatly increased amongst theorists and experimentalists as a result, with over 400 papers published in the field since 1997 [SPI08].

This chapter will introduce the concepts of Generalised Parton Distributions and Deeply Virtual Compton Scattering (DVCS), a process which can be used to access GPDs experimentally. The DVCS observables measured at HERMES are detailed, with their relation to GPDs shown. Models of GPDs, based on parameterisations where J_Q enter as free parameters, are also discussed.

2.1 Generalised Parton Distributions (GPDs)

Development of Generalised Parton Distributions [DMR+88, MRG+94] arose from extending the Parton Distribution Function (PDF) framework. PDFs are well known and have been confirmed experimentally, but are valid only in the forward limit, i.e. where the transverse momentum transfer $t \to 0$ and the scaling parameter $\xi \to 0$. GPDs are commonly described in terms of four kinematic variables: x, the longitudinal momentum fraction of the struck quark in the nucleon, ξ, t and μ^2, the measurement scale. In order to define these variables it is necessary to first discuss the Deep Inelastic Scattering (DIS) process.

2.1.1 Variables to Describe GPDs

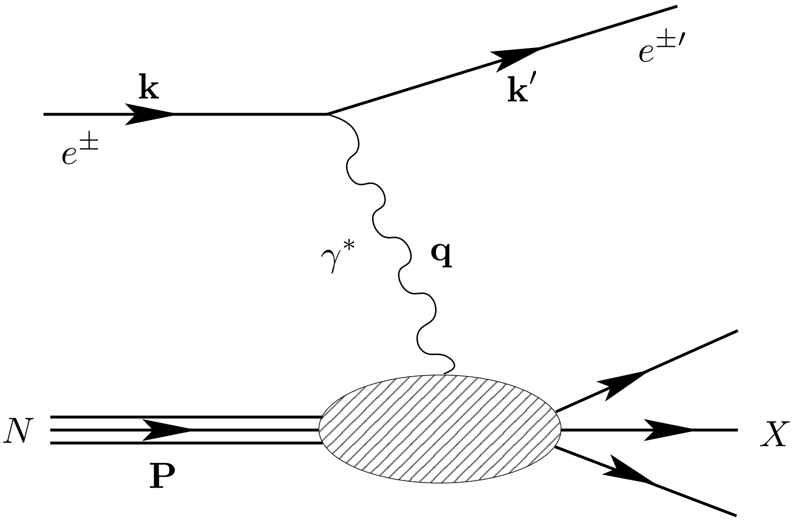

Figure 2.1: Illustration of the Deep Inelastic Scattering process. An incoming lepton with four-momentum $\mathbf{k}$ scatters off a nucleon N with four-momentum $\mathbf{P}$ and leaves with four-momentum $\mathbf{k}'$. The four-momentum of the emitted virtual photon is $\mathbf{q}$. In DIS the final state of the nucleon, X, is undefined.

In DIS a high energy lepton (electron or positron at the HERMES experiment) with four-momentum $\mathbf{k}$ emits a virtual photon with four-momentum $\mathbf{q}$ which is absorbed by a nucleon N with four-momentum $\mathbf{P}$. The lepton is scattered and leaves with four-momentum $\mathbf{k}'$ whilst the nucleon fragments into a final state X. This process is shown in figure 2.1. In the elastic scattering case the nucleon remains intact. It is this case that is considered in this thesis.

The following four-vector convention is adopted here: the metric tensor $g_{\mu\nu}$ is given by

$$g_{\mu\nu} = \begin{pmatrix} 1 & 0 & 0 & 0 \\ 0 & -1 & 0 & 0 \\ 0 & 0 & -1 & 0 \\ 0 & 0 & 0 & -1 \end{pmatrix}, \tag{2.1}$$

where μ and ν run from 0 to 3. The scalar product of two four-vectors $x = (x^0, x^1, x^2, x^3)$ and $y = (y^0, y^1, y^2, y^3)$ is written

$$x \cdot y = g_{\mu\nu} x^\mu y^\nu \tag{2.2}$$

where the Einstein summation convention is applied. Hereafter the scalar product shall be written $\mathbf{x} \cdot \mathbf{y}$.

This process can be described in terms of the following quantities:

$$q^2 \equiv -Q^2 = (\mathbf{k} - \mathbf{k}')^2 < 0 \tag{2.3}$$

$$s \equiv (\mathbf{k} + \mathbf{P})^2 \tag{2.4}$$

$$W^2 \equiv (\mathbf{P} + \mathbf{q})^2 \tag{2.5}$$

$$\nu \equiv \frac{\mathbf{P} \cdot \mathbf{q}}{M} \tag{2.6}$$

where q^2 is the squared four-momentum transfer of the virtual photon, s is the total available centre of mass energy squared, W^2 is the square of the invariant mass of the final hadronic state X and M is the rest mass of the nucleon. The variables s, q^2 and W^2 are Lorentz-invariant; ν is not. A formulation of ν can be obtained more easily in the lab frame, a reference frame where the nucleon is initially at rest, as in the case of fixed target experiments such as HERMES. In the lab frame, denoted by $\overset{\text{lab}}{=}$, the following relations are obtained:

$$Q^2 \overset{\text{lab}}{=} 4EE' \sin^2 \frac{\theta}{2} \tag{2.7}$$

$$s \overset{\text{lab}}{=} 2ME + M^2 \tag{2.8}$$

$$W^2 \overset{\text{lab}}{=} M^2 + 2M\nu - Q^2 \tag{2.9}$$

$$\nu \overset{\text{lab}}{=} E - E', \tag{2.10}$$

where E (E') is the initial (final) energy of the incoming (scattered) lepton and θ is its scattering angle with respect to the initial lepton direction. In this frame ν is defined as the energy loss of the scattered lepton. Here the DIS process is considered in the Bjorken limit, where $Q^2, \nu \rightarrow \infty$, with Q^2 spacelike.

Further dimensionless quantities, useful for interpretation of the process, can also be defined in the infinite momentum frame (IMF):

$$x_B = \frac{Q^2}{2\mathbf{P}\cdot\mathbf{q}} \tag{2.11}$$

$$y = \frac{\mathbf{P}\cdot\mathbf{q}}{\mathbf{P}\cdot\mathbf{k}}. \tag{2.12}$$

The IMF is the frame in which the nucleon is moving with momentum approaching ∞, chosen in this case along the z direction [TW01]. Now one considers an incarnation of the infinite momentum formalism known as light-front dynamics [LB80]. A particle with four momentum $p^\mu = (p^0, p^1, p^2, p^3)$ can be represented in the infinite momentum frame as $p^3 \rightarrow \infty$, giving:

$$p^{\pm} = p^0 \pm p^3 = constant. \tag{2.13}$$

In this system, the four momentum is given by $p^\mu = (p^+, p^-, \mathbf{p}_\perp)$, with momenta on the light-front surface of $p^{\pm}$ and transverse momenta $\mathbf{p}_\perp = (p^1, p^2)$.

In the nucleon rest frame these become:

$$x_B \overset{\text{lab}}{=} \frac{Q^2}{M\nu} \tag{2.14}$$

$$y \overset{\text{lab}}{=} \frac{\nu}{E}. \tag{2.15}$$

In the regular DIS process in the IMF, the Bjorken variable x_B is the fraction of the longitudinal momentum of the nucleon caried by the struck quark. In the case of DVCS the definition is more complicated; x_B can be interpreted as the momentum fraction lost by the nucleon [Die07a]. As such x_B is the equivalent of x for the DIS process at HERMES kinematics, and can therefore be used to describe GPDs. y is the fraction of the beam energy carried by the virtual photon in the nucleon rest frame. These variables will be used throughout this work, with further variables used in the analysis of the DVCS process defined in chapter 5.

The Mandelstam variable t is the transverse momentum transfer to the nucleon during the process. This is given by

$$t = (\mathbf{P} - \mathbf{P}')^2 \tag{2.16}$$

where $\mathbf{P}$ ($\mathbf{P}'$) is the four-momentum of the nucleon in the initial (final) state.

The scaling parameter ξ is the light-cone momentum fraction transferred to the target nucleon, defined as:

$$\xi = \frac{-t^+}{2p^+} \tag{2.17}$$

in the light-cone formalism described previously. The parameter ξ is related to η by [BMK02]

$$\eta = -\xi \left(1 + \frac{t}{2Q^2} \right)^{-1}, \tag{2.18}$$

where η the "skewedness" parameter, which describes the deviation of the x dependence of GPDs from that of PDFs. In the Bjorken limit where $Q^2 \to \infty$, $\xi \approx -\eta$. Furthermore, at HERMES kinematics ξ is approximately related to x_B: $\xi \approx \frac{x_B}{2-x_B}$.

GPDs are also dependent on the measurement scale, μ^2, which defines the coupling constant $\alpha_s(\mu^2)$ in QCD. By selecting the $\overline{MS}$ renormalisation scheme $\mu^2 \approx Q^2$ in DIS. Model predictions in this thesis are calculated at HERMES kinematics, therefore the measurement scale dependence is not explicitly stated.

When discussing GPDs a term commonly referred to is *twist*. Twist is a pseudo-quantum number derived from operator product expansions that arises whilst manipulating the hadronic tensor, defined as the dimension minus the spin of the operator [Jaf96]. For this thesis it is sufficient to note that the twist of a term usually refers to its suppression by factors of $\mathcal{O}(\frac{1}{Q})$. The smallest possible twist is two, where twist-2 objects have no suppression by $(\frac{1}{Q})$, twist-3 objects have suppression of $(\frac{1}{Q})$, twist-4 objects have suppression of $(\frac{1}{Q^2})$ and so on. Twist-2 is said to be "at leading twist", and unless otherwise stated this thesis deals with twist-2 objects only.

2.1.2 GPDs of Interest

GPDs were formulated from two independent approaches, known as Off-Forward Parton Distributions (OFPDs) as described by Ji [Ji97a, Ji97b], and Non-Forward Parton Distributions (NFPDs) as described by Radyushkin [Rad97]. OFPDs describe the longitudinal momentum fraction of the struck quark in the nucleon x in terms of $x+\xi$ and $x-\xi$. NFPDs, on the other hand, describe the momentum fraction of the quark as X with a loss of momentum fraction ζ. Following the 2002 Trento Convention [BDDM04] HERMES has chosen to use the OFPD description [Ell04], which has since become the standard description of GPDs.

The analysis of this work as detailed in chapter 5 considers the $e'\gamma X$ final state from scattering off a deuterium target, which can occur through coherent, incoherent, resonant or semi-inclusive processes. Of particular interest are the Bethe-Heitler and DVCS processes. In the case of coherent scattering the deuteron is preserved in the final state. In incoherent or quasi-elastic scattering the deuteron breaks up into a proton or neutron final state. It is these two cases which are dominant at HERMES kinematics. The deuteron is a spin-1 particle, while the proton and neutron are spin-$\frac{1}{2}$ particles. Different GPDs are required to describe the process depending on the scattering process in question, shown in table 2.1. GPDs H ($\tilde{H}$) and E ($\tilde{E}$) are helicity conserving and helicity flip spin-$\frac{1}{2}$ GPDs respectively, where $\tilde{}$ denotes polarised GPDs. The deuteron is a more complex system, described with unpolarised GPDs H_1, H_2, H_3, H_4, H_5 and polarised GPDs $\tilde{H}_1$, $\tilde{H}_2$, $\tilde{H}_3$, $\tilde{H}_4$.

Spin	Target	Unpolarised GPDs	Polarised GPDs
$\frac{1}{2}$	p, n	H, E	$\tilde{H}$, $\tilde{E}$
1	^{2}D	H_1, H_2, H_3, H_4, H_5	$\tilde{H}_1$, $\tilde{H}_2$, $\tilde{H}_3$, $\tilde{H}_4$

Table 2.1: Table of GPDs at leading twist of interest in this work. Due to different scattering processes both spin-$\frac{1}{2}$ and spin-1 GPDs must be considered. Here $\tilde{}$ denotes polarised GPDs.

Table 2.1 shows GPDs of interest in this work, at leading twist in the HERMES measurement range. Each GPD exists for each quark flavour q and also an equivalent for gluons. Gluon GPDs dominate at very small x, where $x \leq 10^{-2}$, thus do not contribute significantly at HERMES kinematics, therefore these will not be discussed here further. The case where excited states of the proton or neutron appear in the final state is not considered here, where transition GPDs would also be required [BMK02].

Modern models of spin-1 GPDs for the deuteron are not currently available, with published theoretical predictions [KM03] considered to be out of date [Mue08]. In this thesis the deuteron final state will be considered in the impulse approximation as incoherent scattering on either the proton or neutron, with the remaining nucleon treated as a spectator in the process, neglecting Fermi momentum. As such, only spin-$\frac{1}{2}$ nucleon GPDs will be considered hereafter.

2.1.3 Relating GPDs to Currently Known Distributions

Parton Distribution Functions (PDFs) describe the longitudinal momentum distribution of partons in the nucleon, and provide no information on the transverse plane. Electromagnetic form factors F_1 and F_2 provide information on the electromagnetic distribution of partons in a nucleon. Ji showed [Ji97a] that GPDs provide the opportunity to link PDFs with form factors and hence provide a more complete description of the nucleon. The relation between GPDs, form factors and PDFs will now be discussed.

Parton Distribution Functions and GPDs

At the forward limit where $t \longrightarrow 0$ and $\xi \longrightarrow 0$, GPDs recover the regular PDFs. For spin-$\frac{1}{2}$ GPDs:

$$H^q(x,0,0) = \begin{cases} q(|x|) & \text{for } x > 0 \\ -\bar{q}(|x|) & \text{for } x < 0 \end{cases} \tag{2.19}$$

and

$$\tilde{H}^q(x,0,0) = \begin{cases} \Delta q(|x|) & \text{for } x > 0 \\ \Delta \bar{q}(|x|) & \text{for } x < 0 \end{cases}, \tag{2.20}$$

where $q(x)$ is the longitudinal momentum distribution of quarks of flavour q in the nucleon and Δq is the helicity distribution inside the longitudinally polarised nucleon. Negative x values refer to antiquarks, $\bar{q}$.

As noted in the introduction, measurements of $\Delta\Sigma = \sum_q (\Delta q + \Delta\bar{q})$ were made by EMC [A$^+$88, A$^+$89], where $\Delta\Sigma$ was found to be smaller than expected. The total spin of the nucleon could not be accounted for at that time in the Quark Parton Model, leading to the “spin puzzle”.

Electromagnetic Form Factors and GPDs

GPDs can also be related to the well known electromagnetic form factors, as shown in [Ji97b]. For spin-$\frac{1}{2}$ GPDs:

$$\int_{-1}^{1} dx H^q(x,\xi,t,Q^2) = F_1^q(t) \tag{2.21}$$

$$\int_{-1}^{1} dx \tilde{H}(x,\xi,t,Q^2) = G_A^q(t) \tag{2.22}$$

$$\int_{-1}^{1} dx E^q(x,\xi,t,Q^2) = F_2^q(t) \tag{2.23}$$

$$\int_{-1}^{1} dx \tilde{E}(x,\xi,t,Q^2) = G_P^q(t) \tag{2.24}$$

where F_1^q, F_2^q are the elastic Dirac and Pauli form factors, and G_A^q, G_P^q are the axial and pseudo-scalar form factors for each quark flavour q. The variable ξ is related to x, therefore by integrating over all x the resulting electromagnetic form factors depend only on t.

2.1.4 GPDs and the Spin Structure of the Nucleon

As noted in the introduction, the primary goal of the HERMES experiment is to improve knowledge of the spin structure of the nucleon. One of the unknowns of the nucleon spin structure equation, shown in equation (1.1), is the total angular momentum of quarks J_q. In 1997 Xiangdong Ji published [Ji97b] the relation between

J_q and GPDs, thus allowing experimentalists for the first time to relate experimental measurements to J_q in a model dependent fashion [GPV01], thus helping to increase understanding of the nucleon spin structure.

Ji's relation, known as "Ji's Sum Rule", is given by:

$$J_q\left(\mu^2\right) = \frac{1}{2}\lim_{t\to 0}\int\limits_{-1}^{1} dx\ x\left[H_q(x,\xi,t,\mu^2) + E_q\left(x,\xi,t,\mu^2\right)\right] \tag{2.25}$$

and relates the second moment of spin-$\frac{1}{2}$ GPDs H and E to J_q, valid in the limit $t \to 0$. Measurements of H and E would therefore be an important step to understanding the spin structure of the nucleon. This led to experimentalists seeking ways to measure GPDs at small t.

2.1.5 Models and Parameterisations of GPDs

This work compares the results of the data analysis described in chapter 5 with results of two models of spin-$\frac{1}{2}$ GPDs, based on either Double Distributions or a Dual Parameterisation of these GPDs. A brief discussion of these models with the parameterisations of GPDs used will be given here. Both models describe proton and neutron spin-$\frac{1}{2}$ GPDs, with modeled results from each target nucleon combined to approximate the deuterium data analysed in this thesis, in the impulse approximation and neglecting Fermi motion. As previously stated, mature models of spin-1 GPDs which describe the deuteron are not currently available.

Double Distribution Model ("VGG")

The Double Distribution model is described fully in [VGG99, GPV01], based on the Double Distribution formalism described in [Rad99]. Double Distributions specify the fractions of the initial momentum and the momentum transfer carried by the active parton of the parent hadron in a given scattering process [Rad00]. In practice the computational code of Vanderhaeghen, Guidal and Guichon [VGG03] is used in this work to calculate experimental observables for comparison with experimental results and is denoted "VGG" in these result comparisons.

Ji's Sum Rule, equation (2.25), is used by [GPV01] as one of many phenomenological and physical constraints that provide limiting cases for the modeling of GPDs. By choosing an appropriate parameterisation of GPDs H and E, detailed in the following, the total angular momentum of up and down quarks J_u and J_d, enter into the model as free parameters. Thus a model dependent constraint on J_u and J_d can be made using experimental results, constraining these pieces of the spin puzzle and increasing knowledge of the spin structure of the nucleon from experiment.

Parameterisation of Nucleon GPD H

Equation (2.21) shows the relation between GPD $H^q(x,\xi,t)$ and the Dirac form factor $F_1^q(t)$ for quark flavour q. Using this relation the t-dependence of the GPD can be factorised, an ansatz which gives the relation

$$H^q\left(x,\xi,t\right) = H^q\left(x,\xi\right)\cdot F_1^q\left(t\right). \tag{2.26}$$

The t-independent GPD can be written as [GPV01]

$$H^q\left(x,\xi\right) = H^q_{DD}\left(x,\xi\right) + \theta\left(\xi - |x|\right) D^q\left(\frac{x}{\xi}\right), \tag{2.27}$$

with the second term known as the "D-term". The validity of the use of this ansatz is currently under debate, for further discussion see [Wak07]. The H^q_{DD} term can be obtained from the double distribution $F^q(\beta,\alpha)$ [MR00, Rad99, PW99]:

$$H^q_{DD} = \int\limits_{-1}^{1} d\beta \int\limits_{-1+|\beta|}^{1-|\beta|} d\alpha\delta\left(x-\beta-\alpha\xi\right) F^q\left(\beta,\alpha\right), \tag{2.28}$$

where β and α are x and ξ respectively in the Double Distribution notation of e.g. [Rad99, Rad00].

The assumption of a factorised t-dependence made above is not supported by experimental evidence from study of elastic processes, with Lattice QCD [GHH$^+$07] and phenomenological [Bur04] calculations also disfavouring this approach. Results from this thesis also disfavour this ansatz, such as figure 5.15 where the VGG model factorised t-dependence is disfavoured. As such an alternative approach can be applied to the GPD, where the t-dependence is factorised out with an exponential dependence. This approach is known as "Regge-type" t-dependence, based on

Regge phenomenology, where structure functions are expected to behave as $\frac{1}{x^{\alpha'}}$ with $\alpha' = 0.8\,\mathrm{GeV}^2$ the leading Regge intercept. Using this approach the $F^q(\beta, \alpha)$ term is written as

$$F^q(\beta, \alpha, t) = F^q(\beta, \alpha) \frac{1}{|\beta|^{\alpha' t}}. \tag{2.29}$$

Using either the Regge or factorised t-dependence ansatz, the double distribution $F^q(\beta, \alpha)$ can be written such that it depends on the ordinary quark PDF, with an additional dependence on a profile function, $h(\beta, \alpha)$:

$$F^q(\beta, \alpha) = h(\beta, \alpha)\, q(\beta). \tag{2.30}$$

For positive values of β, $q(\beta)$ represents the ordinary quark PDF, with negative β values giving the antiquark PDF. The profile function is written

$$h(\beta, \alpha) = \frac{\Gamma(2b+2)}{2^{2b+1}\Gamma^2(b+1)} \frac{[(1-|\beta|)^2 - \alpha^2]^b}{(1-|\beta|)^{2b+1}} \tag{2.31}$$

and contains a free parameter b that controls the "skewedness" of the GPD, i.e. its dependence on ξ. The b parameter sets the contribution of valence (b_{val}) and sea (b_{sea}) quarks to the GPD, where valence quarks carry the quantum numbers of the hadron and sea quarks are quark-antiquark pairs arising from gluon decays.

Parameterisation of Nucleon GPD E

Following a similar procedure as for GPD H, one can now parameterise the GPD E, where the total angular momentum of quarks enters as a free parameter. This parameterisation of E is more difficult than that of H due to the lack of x-dependence in the forward limit, where $\xi = t = 0$. Under the assumption of a factorised t-dependence, an analogous equation to (2.27) for E can be written as

$$E^q(x, \xi, t) = E^q_{DD}(x, \xi, t) - \theta(\xi - |x|) \frac{1}{N_f} D\Big(\frac{x}{\xi}, t\Big) \tag{2.32}$$

which reduces to $E(x)$ in the forward limit, currently an unknown function. By considering that the Pauli form factor F_2^h at the forward limit reduces to the anomalous magnetic moment of the hadron h and considering equation (2.23) at the forward limit, one obtains:

$$\int_{-1}^{1} dx E^q_{DD}(x) = \kappa^q. \tag{2.33}$$

Since $\kappa^u = 2\kappa^p + \kappa^n = 1.673$ and $\kappa^d = 2\kappa^n + \kappa^u = -2.033$ under the assumption of isospin symmetry, a real-valued normalisation constraint can be determined for the function $E^q_{DD}(x)$. In order to satisfy this normalisation condition the function can be assumed to have the same x-dependence as the valence quark distribution, giving:

$$\begin{aligned} E^u_{DD} &= \frac{1}{2} u_{val}(x)\kappa^u \qquad (2.34) \\ E^d_{DD} &= d_{val}(x)\kappa^d \\ E^s_{DD} &= 0. \end{aligned}$$

Equation group (2.34) gives the valence quark parameterisation of E. The sea quark contribution must now be determined. Chiral quark soliton model calculation results [DPP89] show that the sea quark component of $E^q_{DD}(x)$ is narrowly peaked around $x = 0$ and symmetric. Thus a δ function is assumed for the parameterisation, giving

$$\begin{aligned} E^u_{DD} &= A^u u_{val}(x) + B^u \delta(x) \\ E^d_{DD} &= A^d d_{val}(x) + B^d \delta(x) \\ E^s_{DD} &= 0. \qquad (2.35) \end{aligned}$$

Here A_q and B_q are coefficients with dependences given below:

$$A_q = \frac{2J_q - M_q}{M_{q_{val}}}, \qquad (2.36)$$

$$B_u = 2\left[\frac{1}{2}\kappa_u - \frac{2J_u - M_u}{M_{u_{val}}}\right] \qquad (2.37)$$

$$B_d = \kappa_d - \frac{2J_d - M_d}{M_{d_{val}}} \qquad (2.38)$$

where J_q is the total angular momentum of both valence and sea quarks of flavour q, $M_{q_{val}}$ is the fraction of the valence quark contribution of quark flavour q to the nucleon angular momentum and M_q is the fraction of the total quark contribution of quark flavour q to the same,

$$M_{q_{val}} = \int_0^1 x q_{val}(x) dx, \tag{2.39}$$

$$M_q = \int_0^1 x[q_{val}(x) + 2\bar{q}(x)]dx, \tag{2.40}$$

where the parton distribution functions $q_{val}(x), \bar{q}(x)$ are based on experimental data, treated as input to the model.

Thus J_u and J_d enter into the parameterisation of GPD E as free parameters, allowing a model dependent constraint of these parameters to be made using experimental data. An investigation into this constraint for the neutron from deuterium data at HERMES is detailed in chapter 6.

Dual Parameterisation Model ("Dual")

The Dual Parameterisation model is described fully in [GT06], based on the initial work of [PS02]. Computational code was provided by Guzey [Guz08b] in order to calculate experimental observables for comparison with results from data analysis and is denoted "Dual" in this report. Initially the model provided results for the proton only [GT06], with extension to the neutron given in [Guz08a]. For the proton both factorised and Regge-type t-dependence models are available, but for the neutron only Regge-type t is provided, thus for the data analysis only Regge-type is compared from the "Dual" model.

The Dual Parameterisation model is based on an infinite sum of t-channel resonances [GT06], initially derived for pion GPDs [Pol99] but later postulated for proton GPDs [PS02]. Compton Form Factors, convolutions of GPDs with hard scattering kernels, defined in 2.2, are obtained from this model and are combined with expressions for experimental observables given in [BMK02] for comparison with experimental results, see section 2.2 for further details.

Parameterisation of Nucleon GPD H

GPD H is paramerised by the following [GT06]:

$$H^q(x,\xi,t,\mu^2) = \sum_{\substack{n=1\\ \text{odd}}}^{\infty}\sum_{\substack{l=0\\ \text{even}}}^{n+1} B^q_{nl}(t,\mu^2)\theta(\xi-|x|)\Big(1-\frac{x^2}{\xi^2}\Big)C_n^{3/2}\Big(\frac{x}{\xi}\Big)P_l\Big(\frac{1}{\xi}\Big) \tag{2.41}$$

where B^q_{nl} are the unknown form factors, $C_n^{3/2}$ are Gegenbauer polynomials and P_l are Legendre polynomials. Further details are available in [GT06].

Parameterisation of Nucleon GPD E

GPD E is parameterised as the following [GT06]:

$$E^q(x,\xi,t,\mu^2) = \sum_{\substack{n=1\\ \text{odd}}}^{\infty}\sum_{\substack{l=0\\ \text{even}}}^{n+1} C^q_{nl}(t,\mu^2)\theta(\xi-|x|)\Big(1-\frac{x^2}{\xi^2}\Big)C_n^{3/2}\Big(\frac{x}{\xi}\Big)P_l\Big(\frac{1}{\xi}\Big) \tag{2.42}$$

where C^q_{nl} are unknown Compton Form Factors for GPD E and all other terms are described previously. This can be written, following the procedure in [PS02], as

$$\begin{aligned} E^q(x,\xi,t,\mu^2) = \sum_{\substack{k=0\\ \text{even}}}^{\infty} \Big[& \frac{\xi^k}{2}(E^{q(k)}(x,\xi,t,\mu^2) - E^{q(k)}(-x,\xi,t,\mu^2)) \\ & + \Big(1-\frac{x^2}{\xi^2}\Big)\theta(\xi-|x|)\sum_{\substack{l=1\\ \text{odd}}}^{k-3} C^{3/2}_{k-l-2}\Big(\frac{x}{\xi}\Big)P_l\Big(\frac{1}{\xi}\Big)\int_0^1 dy\ y^{k-l-2}R^q_k \end{aligned} \tag{2.43}$$

where R^q_k are generating functions. In the forward limit, R^q_0 are completely determined,

$$R^q_0(x,t,\mu^2) = e^q(x,t,\mu^2)+e^{-q}(x,t,\mu^2)-\frac{x}{2}\int_x^1 \frac{dz}{z^2}\Big(e^q(z,t,\mu^2)+e^{-q}(z,t,\mu^2)\Big), \tag{2.44}$$

constrained by the forward limit of GPD E^q. However, in the forward limit GPD E^q is currently unknown, therefore the functions $e^q(x,t,\mu^2)+e^{-q}(x,t,\mu^2)$ are unconstrained. By following the same approach as applied for the Double Distribution model, given in [GPV01] and detailed previously in this work, the functions e^q+e^{-q} can be written

$$e^q(x,\mu^2) = A_i(\mu^2)q^q_{val}(x,\mu^2)+\frac{B_i(\mu^2)}{2}\delta(x) \tag{2.45}$$

$$e^{-q}(x,\mu^2) = \frac{B_i(\mu^2)}{2}\delta(x) \tag{2.46}$$

where $q^q_{val}(x, \mu^2)$ is the valence quark distribution, taken in this thesis from the MRST02 parameterisation [MRS+03] from experimental data. As for the Double Distribution model, the total angular momentum of quarks of flavour q enters into the Dual Parameterisation model here:

$$A_q(\mu^2) = \frac{2J_q(\mu^2) - M_q(\mu^2)}{M_{q_{val}}}, \tag{2.47}$$

$$B_u(\mu^2) = \kappa_u - 2A_u(\mu^2),\ B_d(\mu^2) = \kappa_d - A_d(\mu^2) \tag{2.48}$$

Thus the Dual Parameterisation model can be used to constrain the total angular momentum of up and down quarks in the nucleon.

2.2 Accessing GPDs via DVCS at HERMES

As noted in the previous section, by measuring GPDs experimentally a piece of the spin puzzle could be solved. The simplest process with which to measure GPDs is Deeply Virtual Compton Scattering (DVCS). From the experimental point of view DVCS is simpler than other processes such as Deep Virtual Meson Production (DVMP), requiring lower centre of mass energies and fewer final state products to be detected. From the theoretical point of view DVCS is preferred due to theoretical prediction accuracy at next to next to leading order (NNLO), and due to its closeness to inclusive DIS [Die07a].

DVCS is similar to the single photon exchange DIS process. A quark in the target nucleon is struck by a virtual photon and is interpreted as leaving the nucleon with longitudinal momentum fraction $x + \xi$. The quark emits a real photon and returns to the nucleon with momentum fraction $x - \xi$, leading to an overall momentum transfer of 2ξ.

At the HERMES experiment DVCS is not the only process which satisfies the equation $eN \to e'N'\gamma$. The most significant background process is the Bethe-Heitler (BH) process [KN02], a QED process where the photon is emitted from the incoming or scattered lepton. These processes are illustrated in figure 2.2. The fourfold differential cross section is given by [BMK02]:

$$\frac{d\sigma}{dx_B dy dt d\phi} = \frac{\alpha_{em}^3 x_B y}{8\pi Q^2 \sqrt{1+\epsilon^2}} |\frac{\tau}{e^3}|^2 \tag{2.49}$$

where α_{em} is the fine structure constant, e is the lepton charge and ϵ given by:

$$\epsilon \equiv 2x_B \frac{M_N}{Q}, \tag{2.50}$$

a factor included for brevity here.

BH interferes with DVCS at the amplitude level, leading to a cross section σ proportional to the total scattering amplitude $|\tau|^2$, given by:

$$\sigma \sim |\tau|^2 = |\tau_{\mathrm{BH}}^2| + |\tau_{\mathrm{DVCS}}^2| + \tau_{\mathcal{I}} \tag{2.51}$$

where τ_{BH} and τ_{DVCS} are the pure BH and DVCS amplitudes and $\tau_{\mathcal{I}} = \tau_{BH}\tau_{DVCS}^* + \tau_{DVCS}\tau_{BH}^*$ is the interference term. Studies [KN02] have shown that the BH term dominates at HERMES kinematics. BH is exactly calculable in QED, but subtracting the BH contribution from the total real photon cross section would introduce large uncertainties which prohibits the measurement of the DVCS cross section. This leaves the interference term as that of most interest.

Reference [BMK02] gives a mathematical description of the terms in equation (2.51), showing a rich and complex angular dependence, as:

$$|\tau_{BH}|^2 = \frac{e^6}{x_B^2 y^2 (1+\epsilon^2)^2 t P_1(\phi) P_2(\phi) t} \left(c_0^{BH} + \sum_{n=1}^{2} c_n^{BH} \cos(n\phi) \right), \tag{2.52}$$

$$|\tau_{DVCS}|^2 = \frac{e^6}{y^2 Q^2} \left(c_0^{DVCS} \sum_{n=1}^{2} c_n^{DVCS} \cos(n\phi) + \lambda s_1^{DVCS} \sin(\phi) \right), \tag{2.53}$$

$$\tau_{\mathcal{I}} = -\frac{\eta e^6}{x_B y^3 P_1(\phi) P_2(\phi) t} \left(c_o^{\mathcal{I}} + \sum_{n=1}^{3} c_n^{\mathcal{I}} \cos(n\phi) + \lambda \sum_{n=1}^{2} s_n^{\mathcal{I}} \sin(n\phi) \right) \tag{2.54}$$

where η refers to the beam charge, λ the beam helicity and $P_{1,2}(\phi)$ are the lepton propagators:

$$Q^2 P_1(\phi) \equiv (k-q')^2, \tag{2.55}$$

$$Q^2 P_2(\phi) \equiv (k-q+q')^2. \tag{2.56}$$

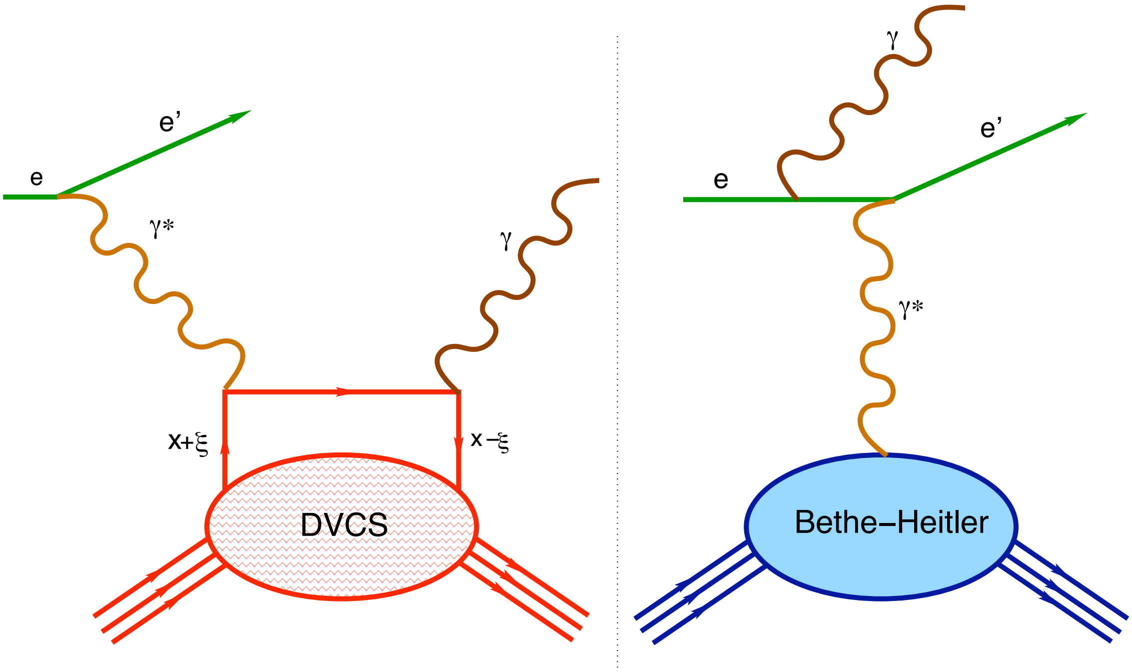

Figure 2.2: The DVCS (left) and Bethe-Heitler (BH, right) processes. In both processes the incoming lepton scatters off the target nucleon through the exchange of a virtual photon, γ^*. In the DVCS process the virtual photon scatters off a parton with longitudinal momentum fraction $x+\xi$. This parton emits a real photon, returning to the target nucleon with longitudinal momentum fraction $x-\xi$. This real photon contains information on the nucleon, allowing experimental access to GPDs. The BH process produces a real photon either before (shown) or after scattering off the nucleon as a whole. The real photon contains no information on the nucleon, thus cannot be used to access GPDs. Image taken from [Mur07].

The angle ϕ is the azimuthal angle around the direction of the exchanged virtual photon in the DVCS process, illustrated in figure 2.3, defined in accordance with the Trento convention of 2002 [BDDM04].

The Fourier coefficients depend linearly on Compton Form Factors (CFFs), which are convolutions of GPDs with “hard scattering kernels”, $C^{\pm}$:

$$\begin{pmatrix} \mathcal{H} \\ \mathcal{E} \end{pmatrix} (\xi, t) = \int_{-1}^{1} C^{-}(x, \xi)\, dx \begin{pmatrix} H \\ E \end{pmatrix} (x, \xi, t) \tag{2.57}$$

$$\begin{pmatrix} \tilde{\mathcal{H}} \\ \tilde{\mathcal{E}} \end{pmatrix} (\xi, t) = \int_{-1}^{1} C^{+}(x, \xi)\, dx \begin{pmatrix} \tilde{H} \\ \tilde{E} \end{pmatrix} (x, \xi, t) \tag{2.58}$$

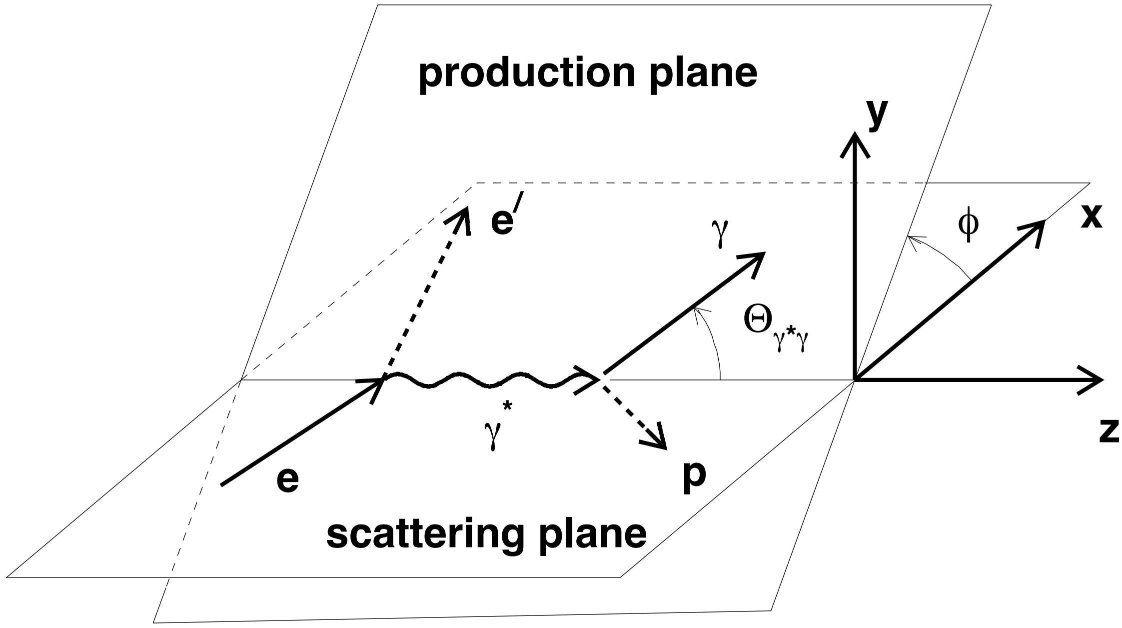

Figure 2.3: Production plane azimuthal angle ϕ of the DVCS process [Col02], defined in accordance with the Trento convention of 2002 [BDDM04].

where the right hand side of each equation above expands to

$$C^{\pm}F = \sum_{q=u,d,s} C^{\pm} e_q^2 F_q \tag{2.59}$$

for each GPD F and quark flavour q. The scattering kernels $C^{\pm}$ expand to:

$$C^{\pm} = \frac{1}{x-\xi-i\epsilon} \pm \frac{1}{x+\xi-i\epsilon} + \mathcal{O}(\alpha) \tag{2.60}$$

where ϵ is a small, non-zero term which allows $C^{\pm}$ to exist in the case of $x = \xi = 0$. The terms involving i lead to real and imaginary parts of the CFFs:

$$\Re(\mathcal{F}) = \mathcal{P}\int_{-1}^{1} dx \left(\frac{F}{x-\xi} \pm \frac{F}{x+\xi}\right) \tag{2.61}$$

$$\Im(\mathcal{F}) = F(x,\xi) \pm F(x,-\xi) \tag{2.62}$$

where $\mathcal{P}$ denotes Cauchy's principle value and terms of $\mathcal{O}(\alpha)$ are ignored.

The real and imaginary parts of these CFFs can be written in terms of DVCS observables, detailed in the following section, allowing experimental access to GPDs. As shown in equation (2.61) an observable relating to the real part of a CFF can access only the integral value of the GPD at a given ξ. Observables relating to the imaginary part of a CFF can access the GPD along the line $x = \pm\xi$, e.g. as shown in figure 2.4 for GPD H. Furthermore, observables arising from the squared DVCS term of the cross section have a bilinear dependence on GPDs, while observables from the interference term depend linearly on GPDs.

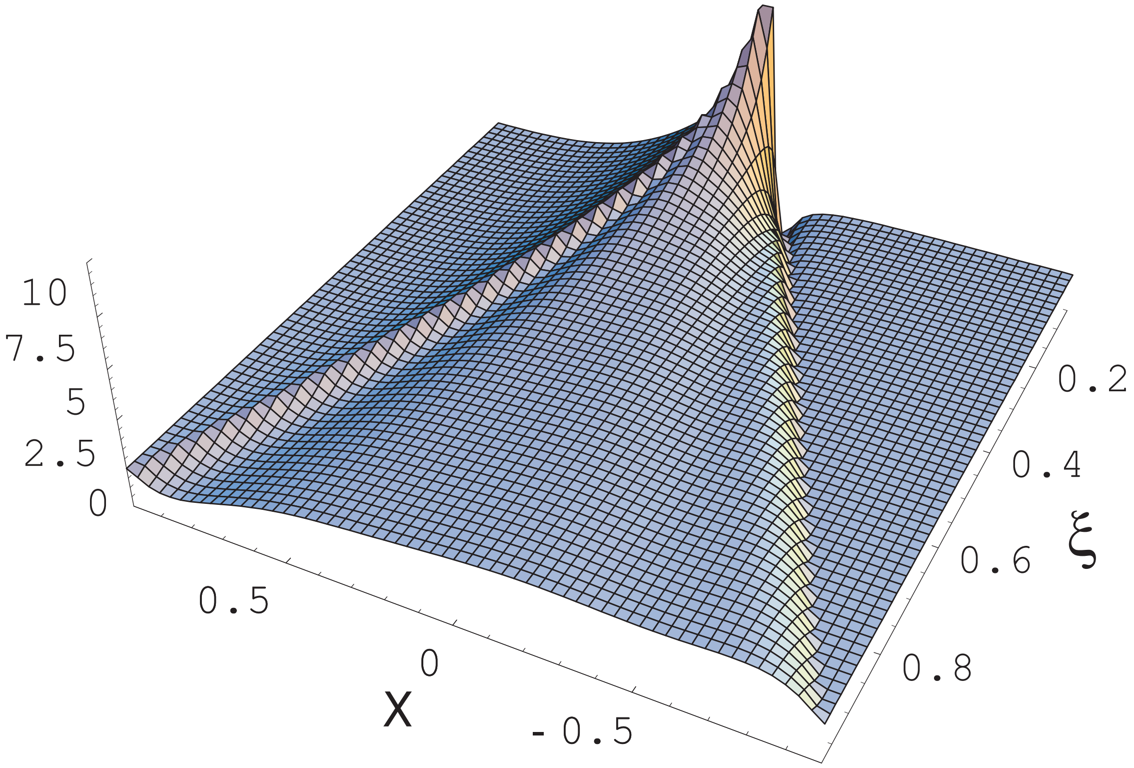

Figure 2.4: The x and ξ dependence of GPD H [GPV01]. DVCS observables relating to the imaginary part of the CFF $\mathcal{H}$ can access H along the line $x = \pm\xi$.

2.3 Beam Dependent DVCS Asymmetries at HERMES

HERMES has the capability to measure asymmetries in the electroproduction of a real photon of the DVCS/BH processes for observables with both polarised beam dependence and/or polarised target dependence. The analysis detailed in chapter 5 concerns an unpolarised target only; the polarised target asymmetries will not be detailed here, see e.g. [Kop06, Ye06, Mur07] for more details on measurements of these asymmetries at HERMES.

Section 5.1.1 describes the DVCS process and its kinematics in more detail. In the following beam dependent DVCS asymmetries and their observables are detailed, with their dependence on spin-$\frac{1}{2}$ GPDs also shown.

2.3.1 Beam Spin Asymmetry Arising from the Interference Term of the eγX Cross Section

The Beam Spin Asymmetry (BSA) is the best measured DVCS-related asymmetry, with results available from more than one experiment [S$^+$01]. BSA measurements require only a polarised beam and are therefore the simplest asymmetry to measure. It is usually denoted $A_{LU}^{\mathcal{I}}$ where A stands for asymmetry, $\mathcal{I}$ refers to its appearance due to the interference term given in equation (2.54), L refers to a longitudinally polarised beam and U refers to an unpolarised target. $A_{LU}^{\mathcal{I}}$ is defined as:

$$A_{LU}^{\mathcal{I}}(\phi) = \frac{d\sigma\left(\overrightarrow{e}^{+},\phi\right) - d\sigma\left(\overleftarrow{e}^{+},\phi\right) - d\sigma\left(\overrightarrow{e}^{-},\phi\right) + d\sigma\left(\overleftarrow{e}^{-},\phi\right)}{d\sigma\left(\overrightarrow{e}^{+},\phi\right) + d\sigma\left(\overleftarrow{e}^{+},\phi\right) + d\sigma\left(\overrightarrow{e}^{-},\phi\right) + d\sigma\left(\overleftarrow{e}^{-},\phi\right)} \tag{2.63}$$

where $\overrightarrow{e}$ ($\overleftarrow{e}$) refer to positive (negative) beam helicity states and ± refers to the beam charge η, combining all data taken with both electrons and positrons at HERMES for maximal statistical precision.

Relation to Cross Section

The cross section shown in equation (2.49) can be defined independent of the beam charge and helicity as [LY07]:

$$\sigma_{UU}^{0}(\phi) = \frac{\alpha_{em}^{3} x_B}{8\pi y Q^2\sqrt{1+\epsilon^2}}\left[\frac{c_0^{BH} + \sum_{n=1}^{2} c_n^{BH}\cos(n\phi)}{x_B^2(1+\epsilon^2)^2 t P_1(\phi)P_2(\phi)} + \frac{c_0^{DVCS}\sum_{n=1}^{2} c_n^{DVCS}\cos(n\phi)}{Q^2}\right], \tag{2.64}$$

where UU refers to unpolarised beam and unpolarised target. The cross section for longitudinally polarised beam, unpolarised target, dependent on beam charge, η, and helicity, λ, can be expressed as:

$$\begin{aligned}\sigma_{LU}(\phi,\lambda,\eta) = \sigma^0_{UU}(\phi)\Bigg(& 1 + \lambda K_1 \frac{s_1^{DVCS}\sin(\phi)}{\sigma^0_{UU}(\phi)} - \eta K_2 \frac{c_0^{\mathcal{I}} + \sum\limits_{n=1}^{3} c_n^{\mathcal{I}}\cos(n\phi)}{\sigma^0_{UU}(\phi)} \\ & - \eta\lambda K_2 \frac{s_1^{\mathcal{I}}\sin(\phi) + s_2^{\mathcal{I}}\sin(2\phi)}{\sigma^0_{UU}(\phi)}\Bigg) \\ = & \, \sigma^0_{UU}(\phi)\big[1 + \lambda A_{LU}^{DVCS}(\phi) + \eta A_C(\phi) + \eta\lambda A_{LU}^{\mathcal{I}}(\phi)\big] \quad (2.65)\end{aligned}$$

where $K_{1,2}$ are kinematic factors, independent of ϕ. The A_{LU}^{DVCS} and A_C terms will be described in sections 2.3.2 and 2.3.3 respectively. From equations (2.63), (2.64) and(2.65) the BSA term $A_{LU}^{\mathcal{I}}$ can defined as

$$A_{LU}^{\mathcal{I}} = -\frac{\frac{x_B}{y}\sum\limits_{n=1}^{2} s_n^{\mathcal{I}}\sin(n\phi)}{\frac{\sum_{n=0}^{2} c_n^{BH}\cos(n\phi)}{(1+\epsilon^2)^2} + Z\sum\limits_{n=0}^{2} c_n^{DVCS}\cos(n\phi)}. \quad (2.66)$$

where Z is a factor defined by

$$Z = \frac{x_B^2 t P_1(\phi) P_2(\phi)}{Q^2}, \quad (2.67)$$

included for brevity of equations in this work.

The BH cross section is dominant, as shown in [KN02]. The BH factors are dominant in the denominator of equation (2.66) with c_0^{BH} dominant over $c_{1,2}^{BH}$. In the numerator the $s_1^{\mathcal{I}}$ term, at leading twist, is expected to dominate the $s_2^{\mathcal{I}}$ term, a twist-3 term and therefore suppressed by a factor $\sim \frac{1}{Q}$. As such the $A_{LU}^{\mathcal{I}}$ can be approximated by

$$A_{LU}^{\mathcal{I}} \approx -\frac{x_B}{y}\frac{s_1^{\mathcal{I}}}{c_0^{BH}}\sin(\phi). \quad (2.68)$$

Thus measurements of the asymmetry are expected to show a $\sin(\phi)$ dependence, with a suppressed $\sin(2\phi)$ dependence.

Relation to GPDs

The interference of the Bethe-Heitler and DVCS amplitudes for an unpolarised nucleon target (proton or neutron) can be written as [BMK02]

$$\mathcal{C}^{\mathcal{I}}_{unp} = F_1\mathcal{H} + \frac{x_B}{2-x_B}(F_1+F_2)\tilde{\mathcal{H}} - \frac{t}{4M^2}F_2\mathcal{E}, \quad (2.69)$$

where the Compton Form Factors $\mathcal{H}, \tilde{\mathcal{H}}, \mathcal{E}$ are related to the spin-$\frac{1}{2}$ GPDs $H, \tilde{H}, E$ as shown in section 2.2. The Fourier coefficients of the BSA from the Interference term are related to the Interference amplitude as shown [BMK02]:

$$\begin{aligned} s_1^{\mathcal{I}} &= 8K\lambda y(2-y)\ \Im\mathcal{C}_{unp}^{\mathcal{I}}(\mathcal{F}), && (2.70) \\ s_2^{\mathcal{I}} &= \frac{16K^2}{2-x_B}\lambda y\ \Im\mathcal{C}_{unp}^{\mathcal{I}}(\mathcal{F}) && (2.71) \end{aligned}$$

for CFF $\mathcal{F}$, where K is a kinematic prefactor defined in [BMK02]. Thus the experimentally measured asymmetry amplitudes for the BSA arising from the Interference term are related to the imaginary part of GPDs $H, \tilde{H}$ and E. In the case of a neutron, the GPD E is dominant, while for the proton GPD H is dominant due to the relative magnitudes of the electromagnetic form factors F_1 and F_2. When combined with models of GPD E with J_u and J_d as free parameters, a model-dependent constraint of these parameters can be made. An investigation into this constraint is detailed in chapter 6.

Experimental Results at HERMES

HERMES has recently approved new preliminary results of the BSA arising from the Interference term for publication [ZL08]. These include all data taken with an unpolarised hydrogen target prior to the installation of the Recoil Detector, as described in section 3.4. Figure 2.5 shows results of the $\cos(0\phi)$ constant term and the $\sin(\phi)$ and $\sin(2\phi)$ amplitudes, as shown in equation (2.66). Results are shown integrated over HERMES kinematics and their dependence on Q^2, x_B and $-t$. The results show an improvement over those previously published by HERMES [A$^+$01] due to the much larger data set analysed. This thesis will provide new results for an unpolarised deuterium target over the same data taking period and following a similar extraction method.

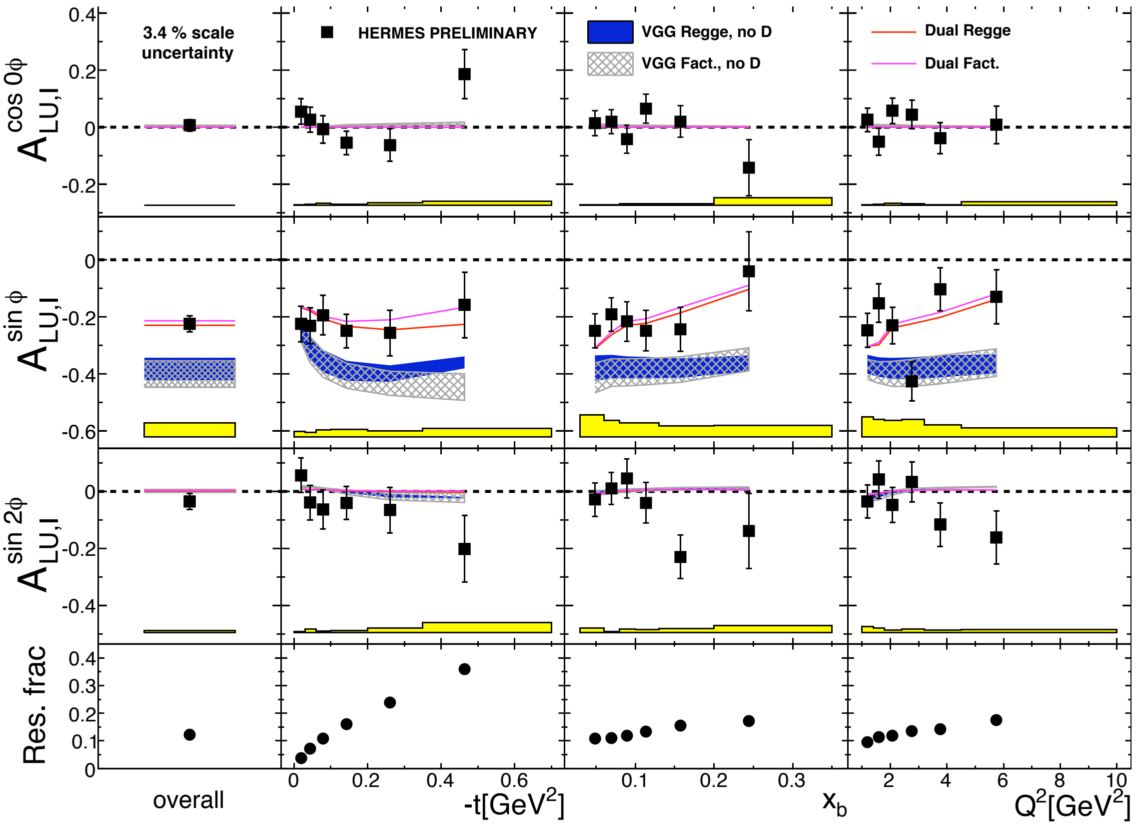

Figure 2.5: Preliminary results for the BSA from the Interference term at HERMES for an unpolarised hydrogen target. Results of the $\cos(0\phi)$ constant term and the $\sin(\phi)$ and $\sin(2\phi)$ amplitudes, see equation (2.66), are shown integrated over HERMES kinematics, with the dependences on $-t, x_B$ and Q^2 also shown. Theoretical predictions from models of GPDs, described in section 2.1.5, are also shown. The expected fraction of events from background processes is noted in the "Res. frac" row, estimated from Monte Carlo studies. Plot taken from [ZL08].

2.3.2 Beam Spin Asymmetry Arising from the Squared DVCS Term of the eγX Cross Section

As noted in section 2.2, the DVCS cross section is suppressed with respect to the Bethe-Heitler component. This makes measurements of asymmetries in the DVCS cross section difficult, as the squared DVCS component cannot be easily isolated. However by removing the charge dependence of the BSA, one can access the squared

DVCS asymmetries, with A_{LU}^{DVCS} is defined as:

$$A_{LU}^{DVCS}(\phi) = \frac{d\sigma\left(\overrightarrow{e^+},\phi\right) - d\sigma\left(\overleftarrow{e^+},\phi\right) + d\sigma\left(\overrightarrow{e^-},\phi\right) - d\sigma\left(\overleftarrow{e^-},\phi\right)}{d\sigma\left(\overrightarrow{e^+},\phi\right) + d\sigma\left(\overleftarrow{e^+},\phi\right) + d\sigma\left(\overrightarrow{e^-},\phi\right) + d\sigma\left(\overleftarrow{e^-},\phi\right)}. \tag{2.72}$$

Asymmetry amplitudes proportional to $\cos(2\phi)$ and $\sin(2\phi)$ in the squared DVCS term arise from twist-two double helicity-flip gluonic GPDs [BMK02]. However, these contributions are highly suppressed at HERMES kinematics. Results for asymmetries from the squared DVCS term for an unpolarised hydrogen target have recently been approved for publication [ZL08].

Relation to Cross Section

Equation (2.65) shows the relation of the A_{LU}^{DVCS} term to the overall cross section. As in section 2.3.1, from this equation the asymmetry can be defined as [LY07]

$$A_{LU}^{DVCS} = \frac{Z s_1^{DVCS}\sin(\phi)}{\frac{\sum_{n=0}^{2} c_n^{BH}\cos(n\phi)}{(1+\epsilon^2)^2} + Z\sum_{n=0}^{2} c_n^{DVCS}\cos(n\phi)}, \tag{2.73}$$

with Z as defined in equation (2.67). Similarly to equation (2.68), this can be simplified to

$$A_{LU}^{DVCS} \approx \frac{x_B^2 t P_1(\phi)P_2(\phi)}{Q^2}\frac{s_1^{DVCS}}{c_0^{BH}}\sin(\phi). \tag{2.74}$$

Thus measurements of this asymmetry are expected to show a $\sin(\phi)$ dependence. However, the dominance of BH over DVCS in the cross section should lead to suppression of this asymmetry. Furthermore, the s_1^{DVCS} term is twist-3, thus is further suppressed by a factor $\sim \frac{1}{Q}$.

Relation to GPDs

The squared DVCS amplitude can be written in terms of CFFs as the following [BMK02]:

$$\mathcal{C}_{unp}^{DVCS}(\mathcal{F},\mathcal{F}^*) = \frac{1}{(2-x_B)^2}\Bigg\{4(1-x_B)(\mathcal{H}\mathcal{H}^*) - x_B^2(\mathcal{H}\mathcal{E}^* + \mathcal{E}\mathcal{H}^* + \tilde{\mathcal{H}}\tilde{\mathcal{E}}^* + \tilde{\mathcal{E}}\tilde{\mathcal{H}}^*) \\ - \left(x_B^2 + (2-x_B)^2\frac{t}{4M^2}\right)\mathcal{E}\mathcal{E}^* - x_B^2\frac{t}{4M^2}\tilde{\mathcal{E}}\tilde{\mathcal{E}}^*\Bigg\}. \tag{2.75}$$

Similarly as in section 2.3.1, the asymmetry amplitudes for the BSA from the squared DVCS term can be written:

$$c_0^{DVCS} = 2(2-2y+y^2)\mathcal{C}_{unp}^{DVCS}(\mathcal{F},\mathcal{F}^*), \tag{2.76}$$

$$s_1^{DVCS} = \frac{8K}{2-x_B} - \lambda y \, \Im\mathcal{C}_{unp}^{DVCS}(\mathcal{F},\mathcal{F}^*). \tag{2.77}$$

These asymmetry amplitudes give information on the imaginary part of CFF $\mathcal{F}$ and its complex conjugate $\mathcal{F}^*$. However, these terms are expected to be highly suppressed with respect to those of the Interference term at HERMES kinematics. Furthermore, these terms exhibit a bilinear dependence on CFFs, whereas asymmetries from the interference term depend linearly on CFFs.

Experimental Results at HERMES

Similarly as shown in section 2.3.1, figure 2.6 presents results for the BSA arising from the squared DVCS term of the cross section for the $\cos(0\phi)$ constant term and the $\sin(\phi)$ and $\sin(2\phi)$ amplitudes, as shown in equation (2.73). Results are shown integrated over HERMES kinematics and with their dependence on Q^2, x_B and $-t$ for an unpolarised hydrogen target. This thesis will provide new results for these asymmetries for an unpolarised deuterium target over the same data taking period, following a similar extraction procedure.

2.3.3 Beam Charge Asymmetry

The Beam Charge Asymmetry (BCA) A_C is defined as:

$$A_C\left(\phi\right) = \frac{d\sigma\left(\overset{\rightarrow}{e^+},\phi\right) + d\sigma\left(\overset{\leftarrow}{e^+},\phi\right) - d\sigma\left(\overset{\rightarrow}{e^-},\phi\right) - d\sigma\left(\overset{\leftarrow}{e^-},\phi\right)}{d\sigma\left(\overset{\rightarrow}{e^+},\phi\right) + d\sigma\left(\overset{\leftarrow}{e^+},\phi\right) + d\sigma\left(\overset{\rightarrow}{e^-},\phi\right) + d\sigma\left(\overset{\leftarrow}{e^-},\phi\right)}. \tag{2.78}$$

HERMES was the first experiment to publish results of the BCA [A$^+$07b], as it was the only experiment at a medium x value with the capability to take data with an electron and positron beam at that time. Measurements of BCA have been made at low x by H1 and ZEUS [Sch07]. Recent results from HERMES with improved statistics were published in [A$^+$08].

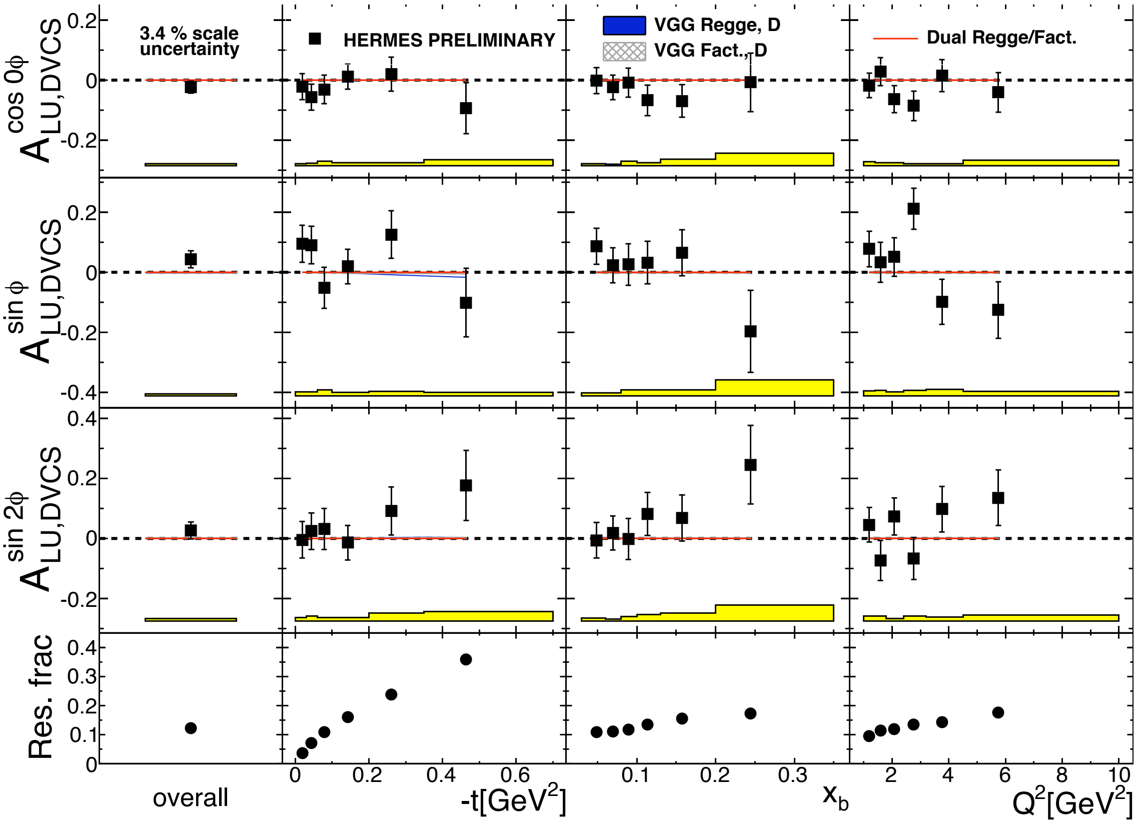

Figure 2.6: Preliminary results for the BSA from the DVCS term at HERMES for an unpolarised hydrogen target. Results of the $\cos(0\phi)$ constant term and the $\sin(\phi)$ and $\sin(2\phi)$ amplitudes, see equation (2.73), are presented integrated over HERMES kinematics, with the dependences on $-t, x_B$ and Q^2 also shown. Theoretical predictions from models of GPDs, described in section 2.1.5 are also shown. Plot taken from [ZL08].

Relation to Cross Section

Equation (2.65) shows the relation of the A_C term to the eγN cross section. As in section 2.3.1 and 2.3.2, from this equation the asymmetry can be defined as [LY07]

$$A_C = -\frac{\frac{x_B}{y}\sum\limits_{n=0}^{3} c_n^{\mathcal{I}}\cos(n\phi)}{\frac{\sum\limits_{n=0}^{2} c_n^{BH}\cos(n\phi)}{(1+\epsilon^2)^2} + Z\sum\limits_{n=0}^{2} c_n^{DVCS}\cos(n\phi)}, \tag{2.79}$$

with Z as defined in equation (2.67). Similarly to equation (2.68), this can be simplified to

$$A_C \approx -\frac{x_B}{y}\frac{c_1^{\mathcal{I}}}{c_0^{BH}}\cos(\phi). \tag{2.80}$$

Thus measurements of this asymmetry are expected to show a $\cos(\phi)$ dependence. The $c^{\mathcal{I}}_{2,3}$ terms should be suppressed with respect to the $c^{\mathcal{I}}_{1}$ term as they are of higher twist. The $c^{\mathcal{I}}_{0}$ term is expected to be of opposite sign to the $c^{\mathcal{I}}_{1}$ term.

Relation to GPDs

As in section 2.3.1, the BCA asymmetry amplitudes can be related to GPDs through the Interference amplitude defined in equation (2.69). The $c^{\mathcal{I}}_{1}$ amplitude of the BCA is related thus [BMK02]:

$$c^{\mathcal{I}}_{1} = 8K - (2 - 2y + y^2)\ \Re\mathcal{C}^{\mathcal{I}}_{unp}(\mathcal{F}). \tag{2.81}$$

Measurements of the BCA $c^{\mathcal{I}}_{1}$ amplitude can therefore access information on the real part of GPDs $H, \tilde{H}$ and E. As noted in section 2.3.1, GPD H is dominant for a proton target, while GPD E is dominant for a neutron target.

Experimental Results at HERMES

Similarly as shown in section 2.3.1, figure 2.7 presents results for the BCA $\cos(0\phi)$ constant term and the $\cos(\phi)$, $\cos(2\phi)$ and $\cos(3\phi)$ amplitudes, as shown in equation (2.79), over all kinematics and their dependence on Q^2, x_B and $-t$. These results are shown for an unpolarised hydrogen target, with an improvement over those previously published by HERMES [A$^+$07b] due to the much larger data set analysed. This thesis will provide similar results for an unpolarised deuterium target over the same data taking period, following a similar extraction procedure.

The HERMES collaboration has approved for publication measurements of the asymmetries detailed previously using an unpolarised deuterium target. This thesis will present these results. In chapter 3 the experimental apparatus used to make these measurements will be detailed.

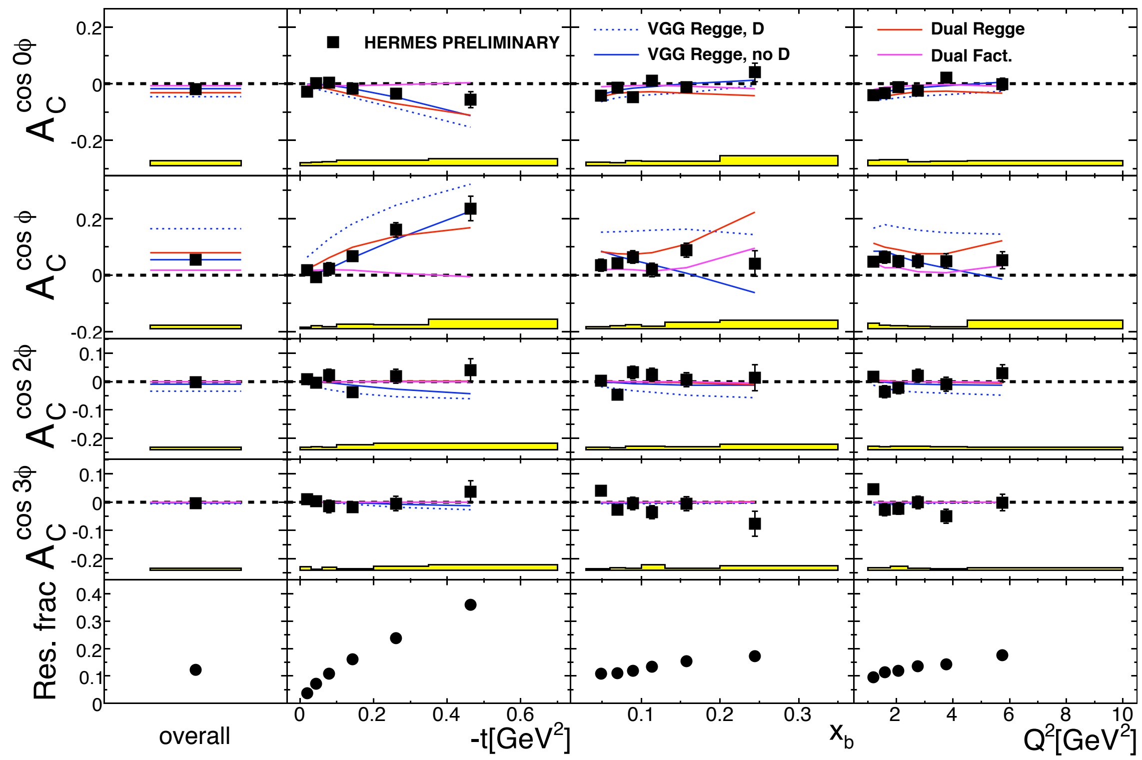

Figure 2.7: Preliminary results for the BCA at HERMES for an unpolarised hydrogen target. Results of the cos(0ϕ) constant term and the cos(ϕ), cos(2ϕ) and cos(3ϕ) amplitudes, see equation (2.79), are presented integrated over HERMES kinematics and with dependences on $-t, x_B$ and Q^2 shown. Theoretical predictions from models of GPDs, described in section 2.1.5, are also shown. Plot taken from [ZL08].

Chapter 3

The HERMES Experiment

The HERMES experiment was proposed to increase understanding of the spin structure of the nucleon. Construction of HERMES began in 1993 and data was first taken in 1995 [Due95]. Over the course of the experiment the physics program was expanded to investigate many aspects of hadronic physics.

HERMES was located at the Deutches Elektronen SYnchrotron (DESY) facility in Hamburg, Germany, one of four experiments situated on the Hadron-Elektron Ring Anlage (HERA) storage ring. H1 and ZEUS were collider experiments using both of HERA's proton and electron/positron beams. HERMES and HERA-B were fixed target experiments using the electron/positron and proton beams respectively. The H1, ZEUS and HERMES experiments accumulated data until the final shutdown of HERA in 2007.

The HERA storage ring and the HERMES apparatus used in the data analysis of this work, including the target and spectrometer, will be detailed herein.

HERMES Coordinate System

Throughout this work reference will be made to the HERMES coordinate system. A right handed coordinate system is used, with positive z direction from the target cell and passing along the direction of the beam through the forward spectrometer. Azimuthal angles (ϕ) are defined as customary in the x-y plane, with x increasing to the left looking downstream, and polar angles (θ) in the y-z plane. This system is illustrated in figure 3.1.

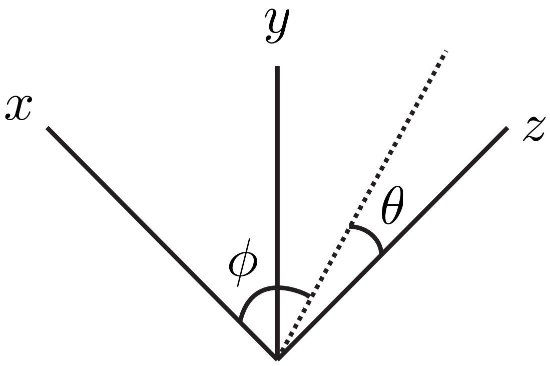

Figure 3.1: Illustration of the HERMES coordinate system. The positive z direction is taken along the beam line. Azimuthal angles ϕ are defined in the x-y plane and polar angles θ in the y-z plane.

3.1 The HERA Storage Ring

The Hadron-Elektron Ring Anlage (HERA) accelerated and stored a 920 GeV proton beam and a 27.56 GeV positron or electron beam, which orbited in opposite directions. HERMES measured interactions of the electron/positron beam and a gaseous target internal to that beam, detailed later. A schematic diagram of HERA is shown in figure 3.2.

The Polarised Electron/Positron Beam

The electron/positron beam is first accelerated at the DESY facility by the Linac II linear accelerator to 450 MeV. The beam is then further accelerated to 7.5 GeV in the DESY-II storage ring. The final pre-acceleration stage occurs in the PETRA storage ring, to 12 GeV, after which the beam is provided unpolarised to HERA and accelerated to the final operation energy of 27.56 GeV.

The experiments required a longitudinally polarised beam. HERA's beams were polarised through bending around the beam path by the Sokolov-Ternov effect [ST64], using correctly tuned beam optics. The circular motion of the electron/positron

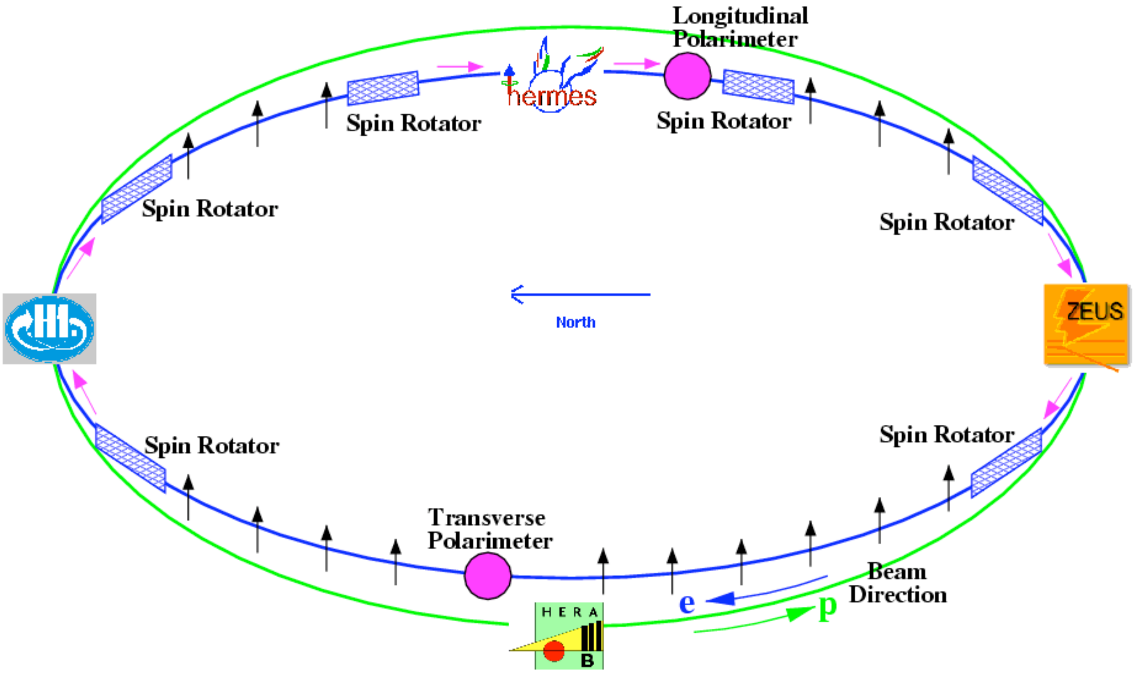

Figure 3.2: Schematic overview of the HERA storage ring at DESY, showing the positions of the experiments, spin rotators and polarimeters.

beam accelerated in a synchrotron caused the emission of synchrotron radiation, which could cause the electrons/positrons to flip their spins. This resulted in a transverse beam polarisation parallel (↑) / antiparallel (↓) for positrons/electrons with respect to the direction of the magnetic fields of the HERA bending magnets. The beam polarisation is defined as:

$$P = \frac{N^{\uparrow} - N^{\downarrow}}{N^{\uparrow} + N^{\downarrow}} \tag{3.1}$$

where $N^{\uparrow}$ ($N^{\downarrow}$) denotes the number of electrons/positrons with polarisation ↑ (↓). Under normal operating conditions the polarisation rose exponentially with time following the relation:

$$P = P_{ST} \cdot \left(1 - \exp\left\{-\frac{t}{\tau_{ST}}\right\}\right) \tag{3.2}$$

where P_{ST} is the theoretical maximum possible polarisation, $\sim 90\,\%$, P is the achieved polarisation in practice and τ_{ST} is the characteristic rise time, $\sim$40 minutes at HERA, depending on P_{ST}, the beam energy and the bending radius in the magnetic field.

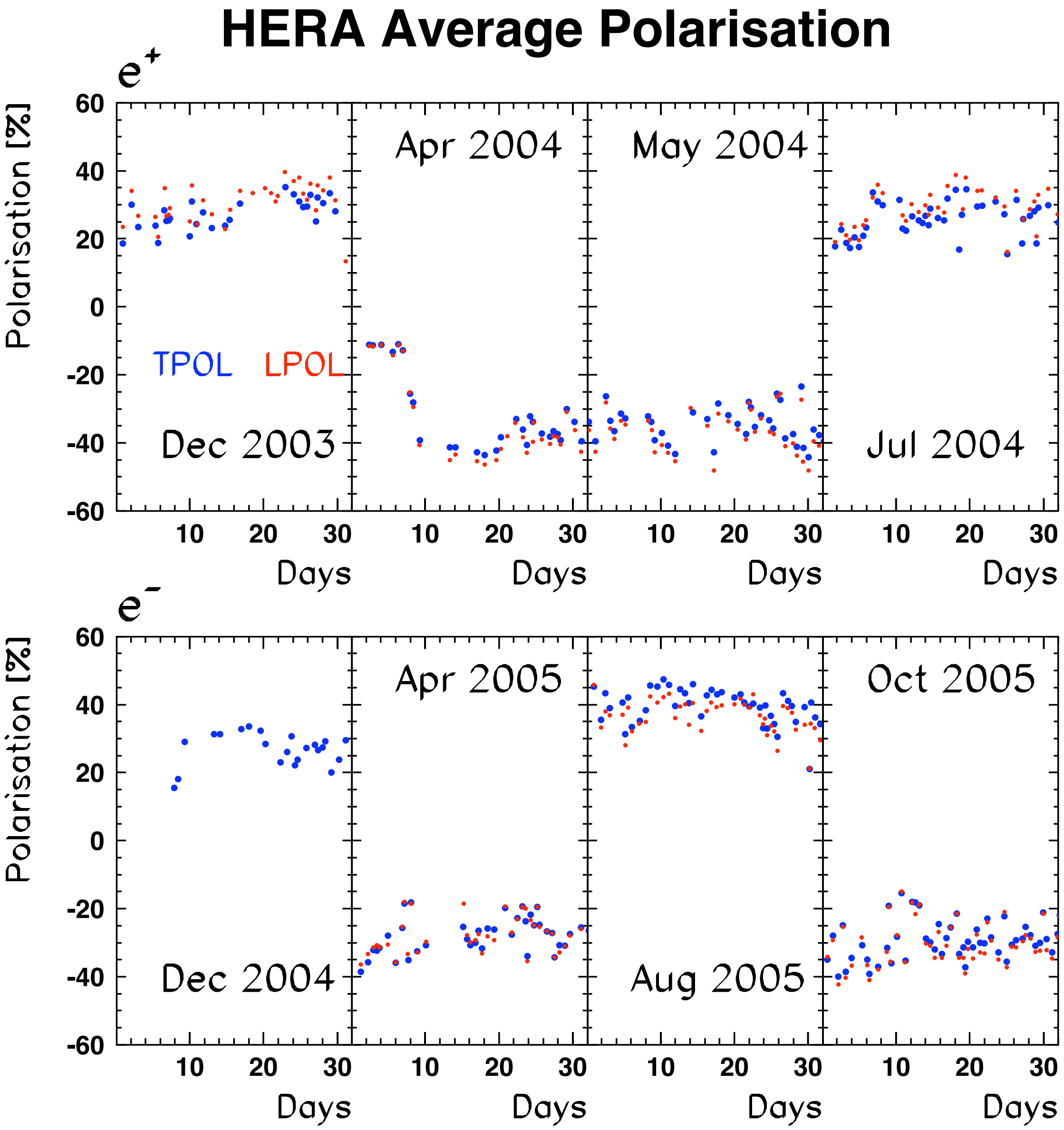

Figure 3.3: The polarisation of HERA electron/positron beams over selected months as measured by both polarimeters. The polarimeters showed good agreement, save for December 2004, when the LPOL was not operational.

Many factors influenced the actual value of the polarisation during HERA operational running. These included non-perfect alignment of the magnetic fields which bent the beam around the beam path; interactions of the proton and electron or positron beams at the ZEUS and H1 interaction points; interactions of the electron or positron beam with the HERMES target gas; energy loss from electrons/positrons due to the emission of synchrotron radiation, which gave rise to non-aligned magnetic fields within the beam [Due95]. These factors resulted in polarisation values lower than the theoretical maximum defined in equation (3.2). In the first period of HERA operation, HERA-I (1995 - 2000), polarisation values were of the order of 50 % to 60 %, with values as high as 70 % observed. During HERA-II, the second running period following upgrades to the accelerator, the polarisation values observed were lower due to changes in the beam optics, between 30 % and 40 %. Polarisation variations over time are shown in figure 3.3.

The lepto-hadronic cross section for transversely polarised electrons/positrons is highly supressed compared to the longitudinally polarised cross section, hence longitudinally polarised beams were preferred by the experiments at HERA. Arrangements of magnets known as spin rotators [BS86] were installed along the beam path before and after the experimental halls. Transverse polarisation was preferred for optimal transmission around the beam path, with the spin rotators employed to provide longitudinal beam polarisation to the experiments.

Beam Polarimetry

Many experimental measurements at HERMES required a longitudinally polarised beam. In analyses where an unpolarised beam was preferred the polarisation of the data set is balanced such that the net polarisation is 0 %. Accurate measurements of the polarisation were required for these analyses in either case. HERA provided measurements from two polarimeters - known as the Transverse Polarimeter (TPOL) and the Longitudinal Polarimeter (LPOL). Both were Compton polarimeters, with the TPOL situated near the West Hall and the LPOL near the East Hall, see figure 3.2. The spin rotators mentioned previously could not change the magnitude of the polarisation, only the direction, thus the LPOL and TPOL measurements should have been of the same absolute magnitude and therefore provided a crosscheck of the polarisation measurement.

The Transverse Polarimeter

The Transverse Polarimeter (TPOL) [B$^+$94] used the interaction of circularly polarised photons on the y-polarised electron/positron beam, where y is defined in the HERMES coordinate system (see the beginning of chapter 3), the transverse direction of the polarised beam. Backscattered photons were detected in a calorimeter. The polarisation of the incident photons was flipped at ~83 Hz, creating an asymmetry in the y-distribution of the detected photons. This asymmetrical distribution is given by

$$\Delta y(E_\gamma) = \frac{1}{2}(\langle y(E_\gamma)\rangle^+) = \Delta S_3 \cdot P_y \cdot \Pi_y(E_y) \tag{3.3}$$

and is dependent upon the energy of the photons E_γ , the y polarisation (P_y) of the electron/positron beam and the mean magnitude of the circular polarisation, ΔS_3. The relationship to E_γ is given by a second function Π_y, the analysing power of the polarimeter. Typically one minute of data taking was required to obtain a polarisation measurement with a statistical accuracy of less than 1 %, with the TPOL measurement having a systematic uncertainty of 3.4 % [B$^+$02].

The Longitudinal Polarimeter

The Longitudinal Polarimeter (LPOL) [B$^+$02] also used circularly-polarised photons, but rather than a spatial asymmetry as in the case of the TPOL, the LPOL measured an energy asymmetry incident on a longitudinally polarised beam. A laser was used to produce photons which were then circularly polarised. Following interaction with the beam, the LPOL detected around 1000 backscattered photons per laser pulse. An asymmetry was measured given by

$$A(\Delta S_3, P_z) = \Delta S_3 \cdot P_z \cdot \Pi_z \tag{3.4}$$

where the analysing power Π_z relates the longitudinal polarisation P_z to the polar scattering angle of the detected photon. ΔS_3 is defined above as in equation (3.3). The LPOL provided measurements with a systematic uncertainty of 1.6 % [B$^+$02].

3.2 The HERMES Target

The HERMES experiment had the ability to measure interactions of the electron/ positron beam with many types of gaseous hadronic targets, including unpolarised, longitudinally polarised and transversely polarised nucleons, or unpolarised nuclei, depending on the target apparatus installed, changing over the experiment lifetime. The data analysis detailed in chapter 5 involves only an unpolarised deuterium target, thus only the unpolarised target system will be discussed here.

Unlike other experiments measuring similar physical processes, such as COMPASS at CERN, HERMES was situated on a storage ring shared with other experiments. Solid or liquid targets would have prevented the beam passing to the other experiments, obviously unacceptable for the collider experiments ZEUS and H1, and impeded the operation of HERA. Hence a gaseous target was preferred at HERMES. Target density and reaction rate were lower than for solid or liquid targets, but target materials and density could be altered easily with no access to the experimental hardware required, even during operation of the storage ring.

The Unpolarised Gas Feed System

The Unpolarised Gas Feed System (UGFS) was the simplest of the systems used at HERMES to fill the target cell. The alternative system was the Atomic Beam Source (ABS), which had been used to provide longitudinally or transversely polarised hydrogen, deuterium or helium-3 targets depending on the type of target magnet installed. This system is detailed elsewhere, e.g. [N$^+$03]. By contrast the UGFS required only that the experimenter selected the correct target gas and density. This gas was then pumped into the target cell, detailed below. During the lifetime of HERMES unpolarised hydrogen, deuterium, helium, nitrogen, neon, krypton and xenon target gases were used.

The UGFS had no technical limitations on the target density, itself limited by the lifetime of the electron/positron beam, which under normal HERA running conditions was to be more than 10 hours. The total lifetime τ can be expressed as

$$\frac{1}{\tau} = \frac{1}{\tau_{\text{HERMES}}} + \frac{1}{\tau_{\text{HERA}}}. \tag{3.5}$$

During normal running the contribution τ_{HERMES} had to be greater than 45 hours, with a corresponding areal target density of 0.162×10^{15} nucleons / cm^2. The electron/positron beam current was typically around 35 mA after injection, and degraded exponentially over the course of one period of data taking, known as a fill. Once the beam current dropped below ∼15 mA (depending on the arrangement between HERA and the experiments at the time) HERMES was permitted to increase the target density to 0.313×10^{16} nucleons / cm^2, leading to $\tau_{\text{HERMES}} = 2$ hours [Col07]. The background rates were typically low during this period, allowing HERMES to take high quality data at comparatively high luminosities. The majority of the data analysed in this work were taken under these conditions.

Another limit on the target density was the HERMES Data Acquisition System (DAQ). The DAQ had a maximum trigger rate of 500 Hz. Excessively high target densities would not only have reduced the beam lifetime, but also increased the background of Møller electrons in the HERMES front region, increasing the DAQ deadtime.

The Target Cell

HERMES used an internal gas target [B$^+$03] to the HERA-e storage ring, designed to provide the maximum data taking rate for HERMES whilst minimising any negative effects on the other experiments on HERA. The cell was a 400 mm long aluminium tube of elliptical cross section, 21 mm by 8.9 mm, with 75 μm thick walls. The target gas was injected into the centre of the cell and, after diffusion of the gas to the ends of the cell, was pumped away to ensure the high vacuum of the beam pipe was maintained. A set of collimators at the front of the target protected the cell and the spectrometer from synchrotron radiation and secondary particle showers. The cell was connected to the beampipe by wake-field suppressors which minimised radio frequency excitations induced by the bunch structure of the beam at these discontinuities of the beampipe. A schematic diagram is shown in figure 3.4.

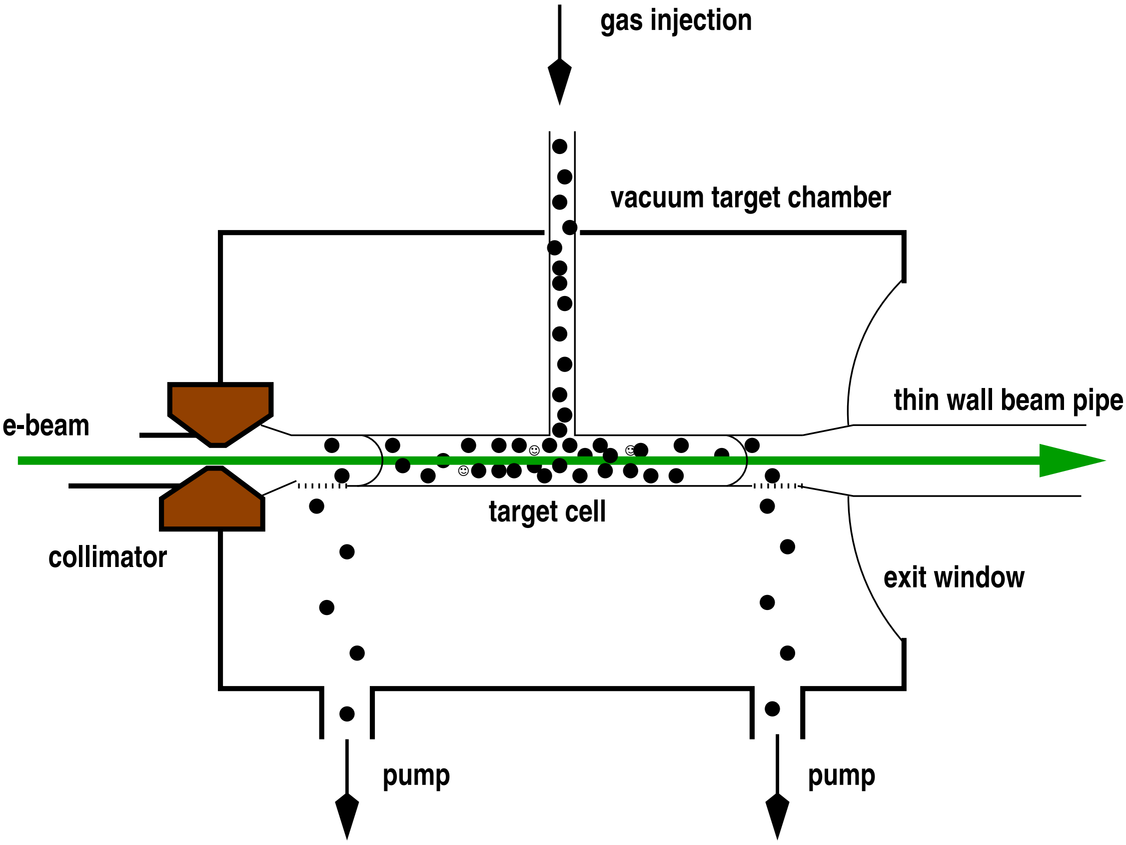

Figure 3.4: Schematic y-z view of the HERMES target region. The target gas was injected into the centre of the cell and after diffusion to the ends was pumped away. This ensured a high beam vacuum. Taken from [She05].

3.3 The HERMES Spectrometer

The HERMES experiment made use of a forward angle spectrometer [A^{+}98a] symmetric above and below the HERA beam lines, shown in figure 3.5. A large iron plate shielded the beam lines from the spectrometer magnet, restricting the acceptance at low scattering angles to $40 < |\theta_y| < 140\,\mathrm{mrad}$ and $|\theta_x| < 170\,\mathrm{mrad}$ in the vertical and horizontal planes respectively. The spectrometer provided Particle Identification (PID) and track reconstruction capability for particles from interactions of the HERA electron/positron beam and the target.

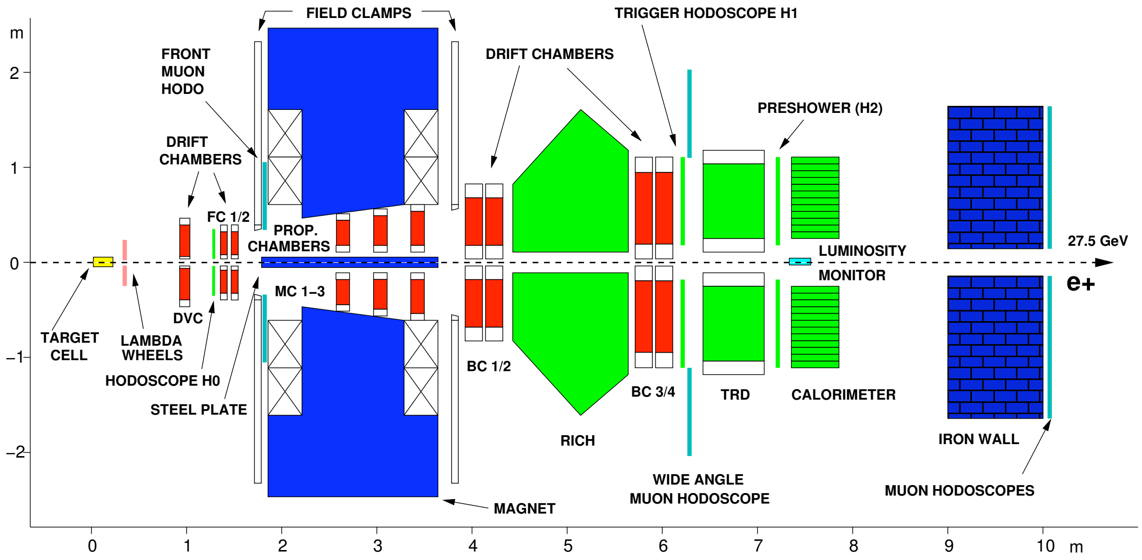

Figure 3.5: Schematic view in the y-z plane of the HERMES spectrometer. All detectors are shown but only those used in the data analysis are detailed in the text. PID detectors are shown in green (light shading) and tracking detectors in red (intermediate shading). The spectrometer magnet is shown in blue (dark shading). The beam enters the experiment from the left. The Recoil Detector will be installed around the target cell.

3.3.1 Tracking Detectors

The HERMES tracking detectors could be regarded as split into three regions along the beam line: front, magnet and rear, defined with respect to the spectrometer magnet. The scattered lepton of the physics processes of interest must be detected in both the front and rear regions of the spectrometer if it is to be used in the data analysis detailed later. The front region contained the Drift-Vertex Chamber (DVC) and the Front Chambers (FCs), the magnet region contained the Magnet Chambers (MCs) and the rear region contained the Back Chambers (BCs), shown in figure 3.5. Each detector used in the data analysis was a wire chamber of one of two types: Multi-Wire Proportional Chambers (MWPCs) or Drift Chambers. Both of these relied on the principle of charge amplification in a gas [Cha93].

Multi-Wire Proportional Chambers

Detectors of this type consist of a three dimensional grid of anode (cathode) wires surrounded by a gas, contained between cathode (anode) plates. As charged particles pass through the detector the gas is ionised, with the produced electrons (positrons) accelerating through the internal electric field to the anode (cathode) wires. During this acceleration the electrons (positrons) cause more ionisation, a cascade effect known as the Townsend Avalanche. This cascade current is directly proportional to the energy of the incident charged particle. The signal from the avalanche was read out from the anode (cathode) wires using the LeCroy PCOS IV system. The aforementioned MCs were of this type.

Drift Chambers

Detectors of this type are of similar design to MWPCs, with a smaller internal electric field. Due to this the Townsend Avalanche does not take place, the drift time is used instead to calculate the intersection of the detector and the track. Signals were read out using amplifier-shaper-discriminator cards mounted on-board the chambers, connected to FastBus Multihit Time-to-Digital Converters (TDCs) with a time resolution of 0.5 ns. The DVCs, FCs and BCs were of this type.

Track Reconstruction

The software package HERMES Reconstruction Code (HRC) was developed to calculate the momentum of charged particle tracks in the spectrometer. The package uses the Treesearch algorithm [Wan97] which searches for space points in the tracking detectors and compares these with a database of child patterns both in front of and behind the magnet. This continues until a unique track is found that bridges the magnet gap. The DVCS analysis detailed later relies on tracks found in this manner, although HRC can provide measurements of partial tracks in the spectrometer. A look-up table is used to calculate the particle momentum, which is combined with information from the PID detectors detailed below to provide position, momentum and particle type to data analysers.

HRC has been expanded as new detectors have been added to the spectrometer over the lifetime of the experiment. Extensions to the reconstruction software are found in the software package eXternal Tracking Code (XTC). A reconstruction algorithm for a recoil detector, included in XTC, is investigated in chapter 4.

Photon Reconstruction

The method detailed above is only suitable for charged particles - photon trajectories are not bent by the spectrometer magnet. Photons were detected only by the calorimeter, which provided poorer energy resolution than for charged particles. The analysis detailed in chapter 5 uses a missing mass assumption to minimise the reliance on information from the calorimeter on photons. By assuming the missing mass of the interaction to be the rest mass of the target nucleon, a new method can be used to calculate the energy of the photon, and subsequently used in the calculation of the Mandelstam variable t. See section 5.1.1 for further details.

3.3.2 Particle Identification Detectors

Particle Identification (PID) at HERMES was provided by 4 detectors: the Transition Radiation Detector (TRD), a pre-shower detector in front of the calorimeter, the calorimeter itself and a Čerenkov detector; between 1995 and 1997 a Threshold Čerenkov detector was installed, replaced from 1998 onwards by a Dual Ring Imaging Čerenkov (RICH) detector. PID at HERMES provided excellent separation of hadrons and electrons, with $< 1\,\%$ hadron contamination in the electron/positron sample. In the DVCS analysis of chapter 5 the Čerenkov detectors are not used, thus they will not be discussed here. PID was performed using a likelihood technique [Kai97], based on empirical knowledge of the detectors.

The Pre-shower Detector

The pre-shower detector [A$^+$98a] converted incident leptons into electromagnetic showers using two radiation lengths of lead, 11 mm thick. These showers were detected with an array of 84 scintillator bars, divided equally above and below the beam line. The scintillator array was also known as the H2 hodoscope.

The detector provided an important contribution to hadron-electron/positron PID. Hadrons did not produce an electromagnetic shower when passing through the lead layer, thus they produced an amount of light in the H2 hodoscope different to that of an incident lepton. Part of the light production distribution of the hadrons and leptons overlaps, shown in figure 3.6, however the calorimeter worked by a similar principle and had better separation in this area.

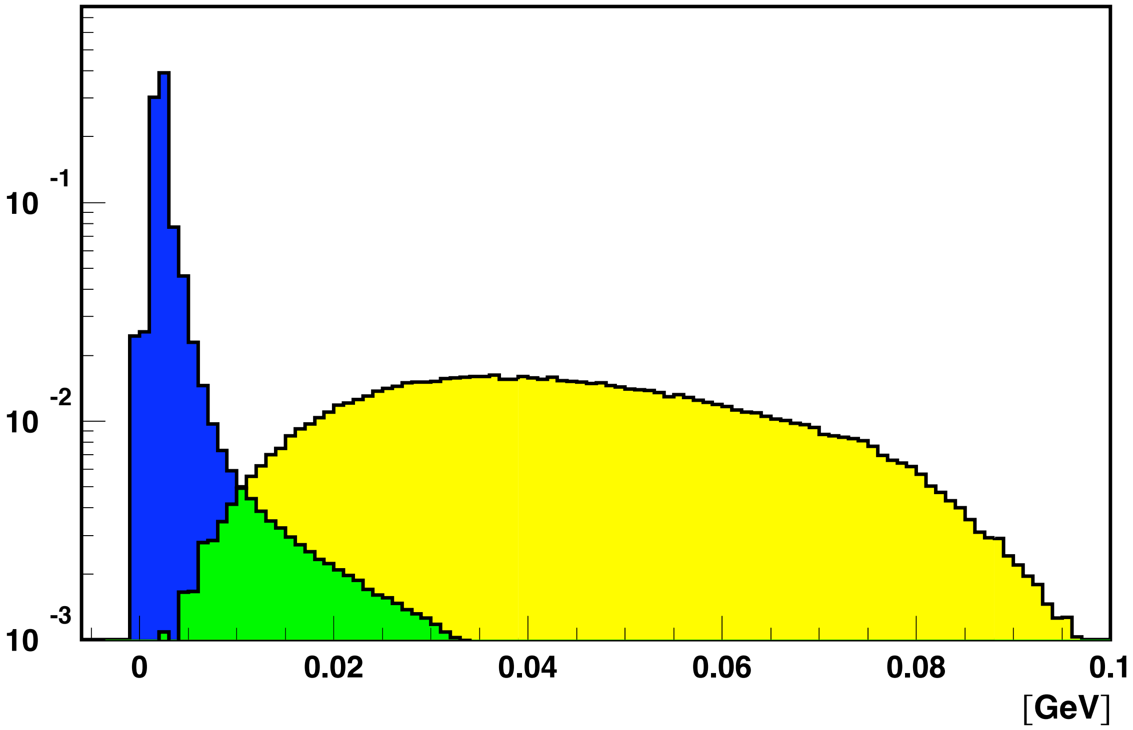

Figure 3.6: The distribution of energy deposited in the preshower detector. The yellow region is electron/positron energy deposition, the blue shows hadron energy deposition. Separation in the overlap area can be made using information from the Electromagnetic Calorimeter. Taken from [Kai97].

The Transition Radiation Detector

The TRD [A+98a] had six modules, each consisted of a radiator with $20\,\mu$m thick plastic fibres and a gas (90 % Xe_3, 10 % CH_4) filled proportional chamber with 12.7 mm separated vertical wires. Hadrons and electrons/positrons deposited energy in the TRD, but only the leptons produced transition radiation at HERMES energies. Combining the responses of all six modules and using a probability-based analysis gave a pion rejection factor better than 1400, for a lepton efficiency of about 90 %.

The Electromagnetic Calorimeter

The electromagnetic calorimeter [A$^+$98b] fulfilled many roles in the HERMES experiment. As well as providing PID for hadrons and electron/positrons, it provided energy measurements of photons for processes such as DVCS/BH, energy measurements of electro-produced π^0, η and other radiative decays and was used as part of the DIS event trigger, see section 3.3.3. The calorimeter did not provide high resolution energy measurements for photons, so for DVCS analysis steps are taken to avoid reliance on these measurements, see chapter 5 for details. The calorimeter also provided the only position measurement of the photon, which otherwise passed through the spectrometer untracked.

The calorimeter consisted of 840 radiation-hard lead glass blocks, arranged in two 42×10 arrays, either above or below the beam line. Blocks measured $9 \times 9 \times 50$ cm, with that length approximately 18 radiation lengths. A schematic diagram is shown in figure 3.7.

The length of these blocks was significant. As electromagnetic showers of electrons or positrons passed through the detector they radiated Čerenkov light. An incident particle will cease to radiate due to energy loss while passing through the calorimeter block, with atom ionisation causing the particle to stop. By selecting calorimeter blocks of the correct length an electromagnetic shower could be contained within the block. At HERMES energies this lead to a ratio of $E_{\text{calo}}/p \simeq 1$, where E_{calo} is the energy deposition in the calorimeter and p is the momentum of the electron/positron measured by the tracking detectors, see figure 3.8. The HERMES calorimeter was designed to contain a full electromagnetic shower, with photomultiplier tubes (PMTs) used to detect the Čerenkov light.

Hadrons in the calorimeter behaved differently: energy was lost through ionising

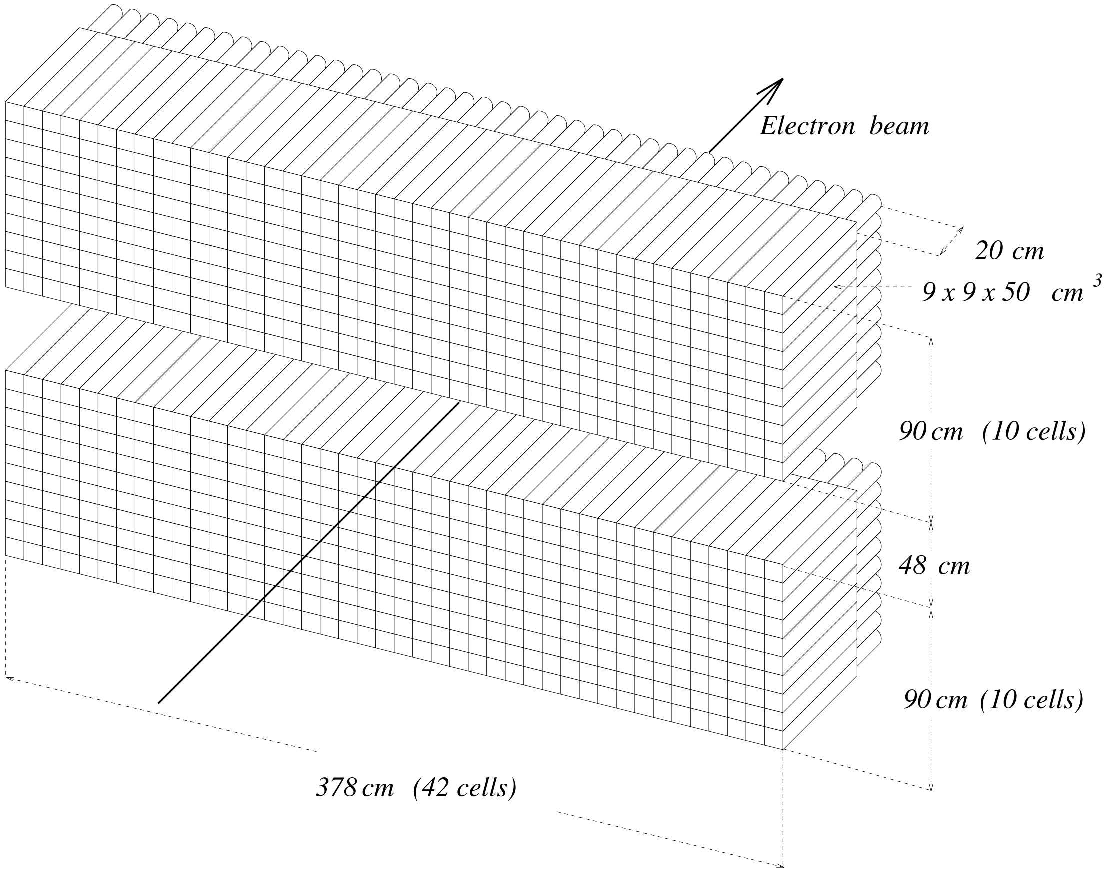

Figure 3.7: Schematic diagram of the electromagnetic calorimeter [A+98b], which contained 840 lead glass blocks divided equally above and below the beam line. The length of each block was approximately 18 radiation lengths.

atomic collisions and nuclear interactions only. However, particles could still be produced through these collisions, including photons and neutral pions. These could create e^+e^- pairs, leading to a electromagnetic shower. The process of particle production from hadrons, known as a hadronic shower, did not begin immediately in the calorimeter, nor was it fully contained within it. These properties, combined with the loss of neutrons and nuclear binding energy, lead to a ratio of $E_{\text{calo}}/p < 1$ for hadrons, allowing the separation of hadrons for PID.

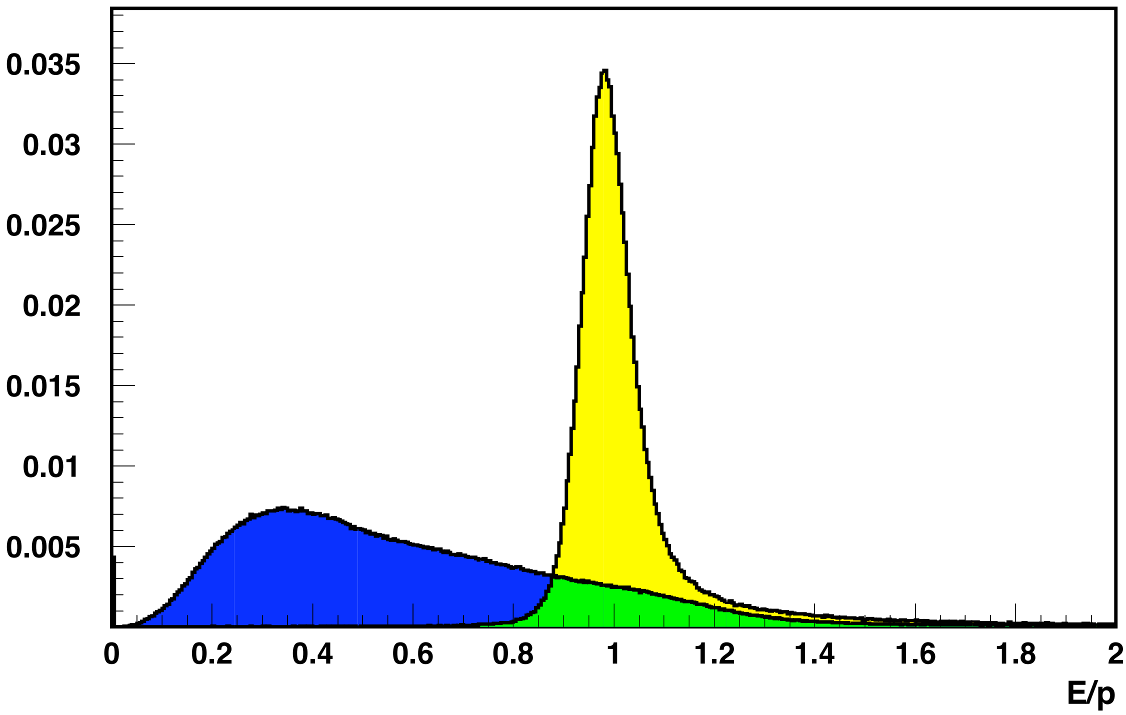

Figure 3.8: Energy response of the calorimeter, normalised to the incident particle momentum. The blue (dark) shading represents hadrons, yellow (light) electrons/positrons and green (intermediate) the overlap region [Kai97].

3.3.3 Event Trigger

The event trigger began the readout of all detectors for an event considered to be of interest. At HERMES there were many triggers relating to different physics processes. This thesis will concentrate on trigger-21, the main physics trigger for a candidate DIS event, employed in the track reconstruction studies of chapter 4 and physics analysis of chapter 5.

An event was marked as a DIS candidate event when the scattered electron/positron passed through the full length of the spectrometer, in either the top or bottom half, with an energy deposition above a preset threshold in the calorimeter also required. In order to quickly identify such a candidate, coincidences were sought in the H0 and H1 hodoscopes, the pre-shower detector and the electromagnetic calorimeter. The pre-shower detector and the electromagnetic calorimeter have been described in the previous section. The H0 hodoscope was located in the front half of the spectrometer, see figure 3.5, and consisted of a single scintillator paddle in each half of the spectrometer, read out by two PMTs. The H1 hodoscope was located in front of the TRD in the rear half of the spectrometer, constructed as per the preshower detector described previously.

Trigger-21 was fired following the satisfaction of the following conditions:

- A signal in the H0 hodoscope.
- A signal in the H1 hodoscope.
- A signal in the pre-shower detector above the minimum ionisation level to indicate the passage of an electron/positron.
- The signals in two neighbouring calorimeter blocks must be above the desired threshold. For normal data taking conditions this threshold was 1.4 GeV, while for high density running at the end of a fill the threshold was raised to 3.5 GeV. This allowed good hadron-electron/positron separation as very few hadrons deposited sufficient energy in the calorimeter to pass the threshold.
- All signals must have coincided with the HERA bunch crossing signal.

3.3.4 Luminosity Monitor

The HERMES luminosity measurement was based on Bhabba scattering, elastic scattering of beam positrons off target gas electrons which annihilate into pairs of photons, or Møller scattering, elastic scattering of beam electrons off target gas electrons. The luminosity monitor [B^+01] consisted of two small calorimeters mounted symmetrically to the left and right of the beam pipe, 7.2 m downstream from the target cell, see figure 3.5. Due to the proximity of the detector to the beam pipe it experienced a high radiation background. To suppress the detection of background events, coincident signals above a threshold of 4.5 GeV were required from both calorimeters.

The absolute luminosity was calculated from the measured coincidence rate multiplied by the luminosity constant. This constant was obtained from the precisely known Bhabba or Møller cross sections combined with knowledge of the detector acceptance and efficiency. The systematic uncertainty of the luminosity constant was 7-8% [Els02] for Bhabba scattering data. For data taken with the electron beam an additional systematic uncertainty of 10% was introduced [Els03], due to the imperfectly simulated cross section ratio between the electron and positron beam.

The HERMES spectrometer was a forward spectrometer, designed to measure reaction products with large longitudinal momenta, in the same direction as the beam line direction. The scattered target nucleon from processes such as DVCS may have scattered in a transverse direction to the beam line, thus emitted outside the acceptance of the spectrometer. In order to improve analysis of these processes the HERMES experiment was upgraded with the Recoil Detector, designed to detect these particles and so reduce systematic uncertainties in measurements. The detector hardware is detailed in the following section.

3.4 The Recoil Detector

The final upgrade to the HERMES spectrometer was the Recoil Detector, installed in the HERA winter shutdown period of 2005 / 2006. With growing interest amongst theorists and experimentalists in GPDs and DVCS, the HERMES collaboration built a detector designed primarily to measure DVCS with greater accuracy [K$^+$01,Col02]. For the first time HERMES was then able to make exclusive measurements at the event level by detecting the recoiling target nucleon - analyses of data prior to the Recoil Detector installation required the use of missing mass cuts to establish exclusivity, with the recoiling nucleon scattered out of the acceptance of the spectrometer. This approach inevitably included background events in the data sample. By detecting the recoiling nucleon this source of background can be reduced.

The design of the detector allowed measurements of exclusive processes at low t, down to $t \approx 0.01\,\mathrm{GeV}^2/\mathrm{c}^2$, where t is the Mandelstam variable detailed in chapter 2, increasing the resolution of the experiment and allowing measurements of the t dependence of these processes. Finally the detector provided background rejection for processes where alongside the outgoing photon a Δ^+ resonance was produced

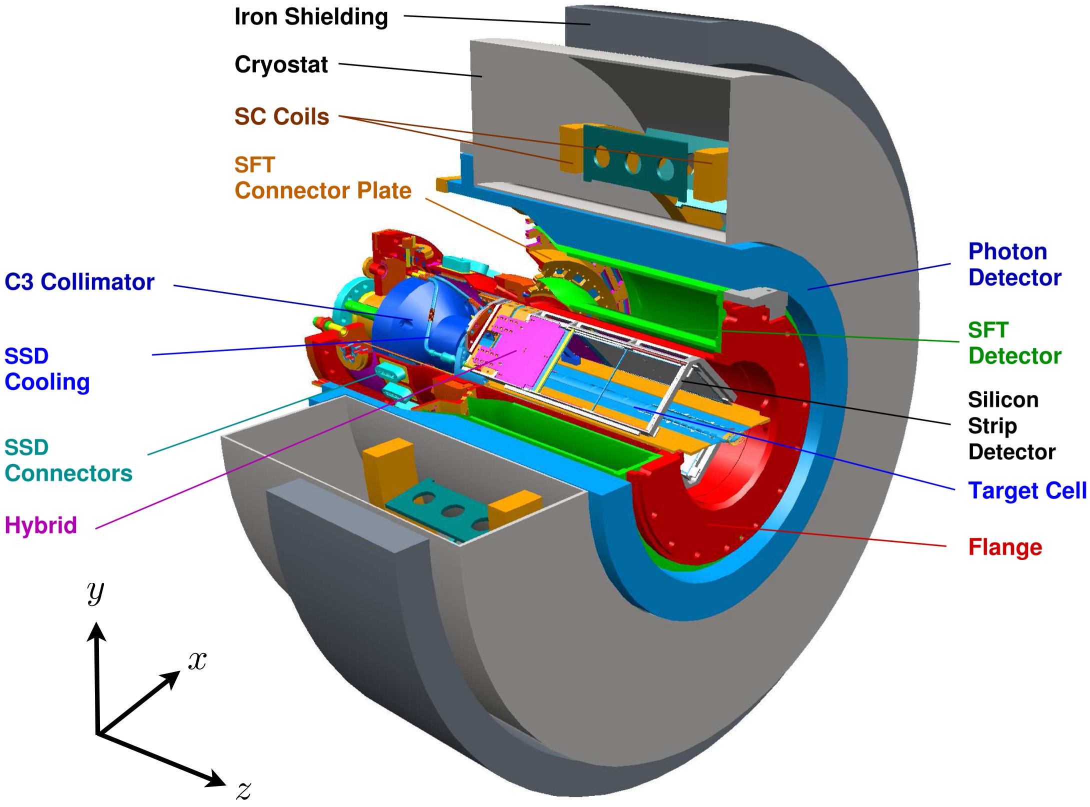

Figure 3.9: CAD schematic diagram of the Recoil Detector, showing the sensitive components, the Silicon Strip Detector, Scintillating Fibre Tracker and Photon Detector, surrounded by the superconducting magnet [Col02]. The HERMES coordinate system is also shown for clarity.

in place of a proton. The Δ^+ decayed into either a proton and π^0, which further decayed into two photons emitted back-to-back in the π^0 rest frame, or a neutron and a π^+, with only the π^+ detected in this case. The Recoil Detector could detect these decay particles sufficiently well to allow these events to be rejected from the exclusive sample.

3.4.1 Detector Overview

The Recoil Detector consisted of three active subdetectors providing both track reconstruction and PID capabilities. From the inside outwards, the structure consisted of a new target cell and a Silicon Strip Detector (SSD) inside the HERA beamline vacuum, a Scintillating Fibre Tracker (SFT) and a Photon Detector, all surrounded by a 1 Tesla superconducting magnet. A schematic diagram is shown in figure 3.9. The detector components and their roles are detailed further here.

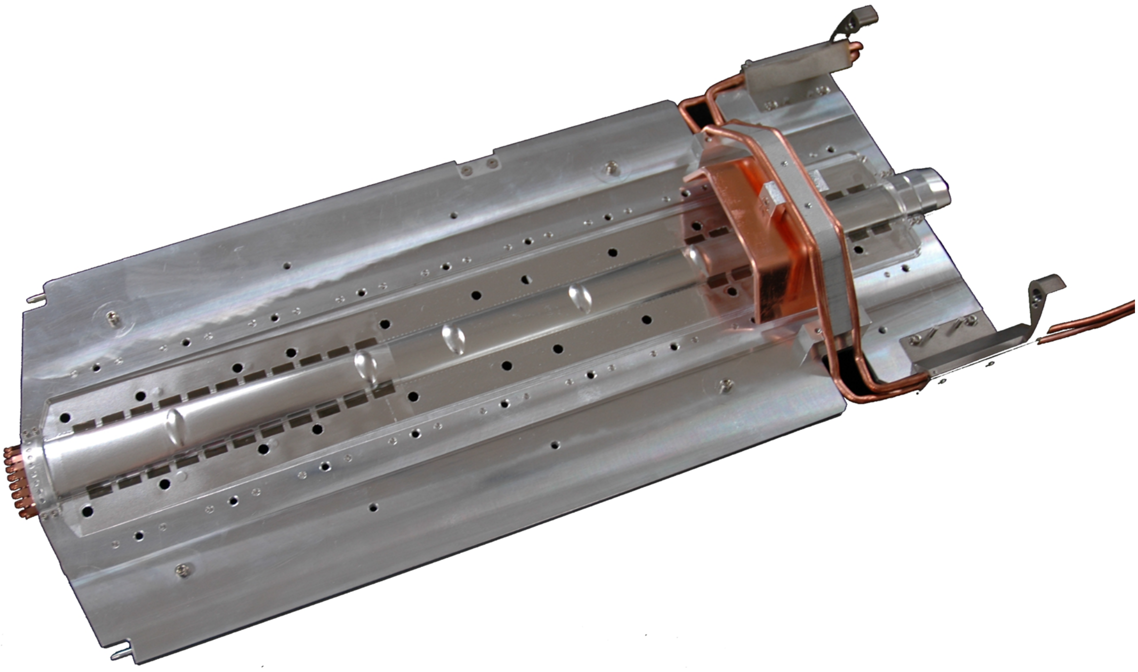

Figure 3.10: A photograph of the Recoil Detector target cell, with 75 μm thick cell walls. The cell contained either unpolarised hydrogen or deuterium gases. The copper connections on the left ensured an adequate electrical connection with the beam pipe, whilst those on the right connected to the copper heat sink for cooling. Image from [Mur07].

3.4.2 The Storage Cell

The Storage Cell, shown in figure 3.10, was very similar to the target cell detailed in chapter 3, with a shorter active length of 150 mm. The target cell was centred at +125 mm in the Z direction of the HERMES coordinate system, whilst the previous cell was centred at the 0 mm position in Z. The cell was of elliptical cross section, with a major (minor) axis of 21 (9) mm [Col02].

Originally the cell was designed with a wall thickness of 50 μm, but was replaced with a 75 μm wall thickness model in the spring of 2006 during a HERA maintenance period. An accident during injection of the beam caused damage to the original, 50 μm walled cell, thus a larger cell was chosen as the replacement to help prevent further damage in case of future recurrences of the problem. The cooling of the cell was also improved at this time [LPR$^+$06]. The thickness of the cell wall determined the minimum cut-off of momentum measurements of recoiling protons, and so the minimum resolution in t. Unpolarised gas was injected into the centre of the cell and dissipated to the outer edges before being pumped away.

3.4.3 Silicon Strip Detector

The Silicon Strip Detector (SSD) provided both track reconstruction and charged particle identification capabilities. At the lower range of particle momenta expected to be detected, energy deposition (dE/dx) in the detector allowed momentum to be reconstructed for particles between 135 and 500 MeV/c. At the higher momentum range, 300 - 1400 MeV/c, the detector provided two spacepoints which, combined with spacepoints from the SFT detector, could be used to reconstruct particle momentum by deflection in the magnetic field. Overall this momentum range corresponded to a kinetic energy range of 9 - 750 MeV. The detector was used to detect and identify recoiling particles from events of interest, especially exclusive events, whilst also rejecting background events with intermediate Δ resonances which decayed to charged pions [Col02].

Monte Carlo simulations of the DVCS process at HERMES [Kra05], using a single simulated electron/positron track in the forward spectrometer as a trigger (see section 3.3.3), have shown that the recoiling proton was expected in the polar angle region $10° < \theta < 80°$, see figure 3.11. The Recoil Detector was designed to provide acceptance in this region and cover as much of the $2\,\pi$ azimuthal angle range as made possible by construction constraints such as the support structures of the detectors. When using dE/dx to determine PID, the SSD angular resolution was not crucial, allowing the use of a relatively large strip pitch of 758 μm in the detector design. The decision to use the SSD to provide spacepoints for use in momentum reconstruction by magnetic field deflection was made later, where a better angular

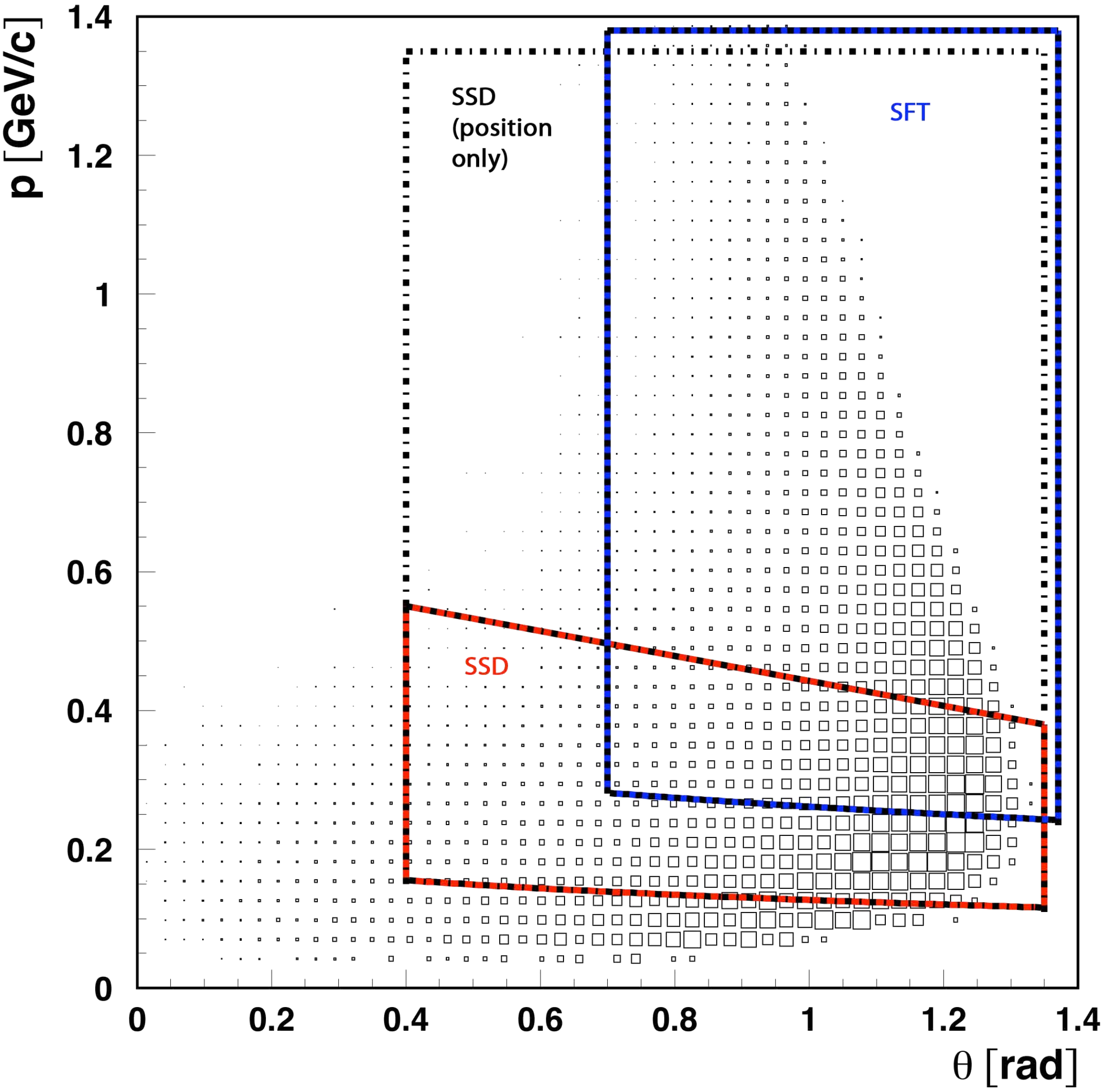

Figure 3.11: Acceptance of the Recoil Detector in the polar angle θ for a given particle momentum, based on Monte Carlo simulations of the detector. Here θ is the angle in the y-z plane of the scattered nucleon of the exclusive process. The SSD provided momentum measurements at low momentum alone, marked in red, with acceptance over a larger momentum range given by position measurements only, marked by the black dashed region. These were used in conjunction with position measurements from the SFT, marked in blue.

resolution would have been preferred.

The low energy measurement capability of the SSD required that a minimal amount of material was placed between the silicon sensors and the interaction point, in order to reduce sources of secondary scattering. The SSD was installed within the HERA beam vacuum to remove relatively thick vacuum walls from the particle trajectories, hence the detector was vacuum compatible.

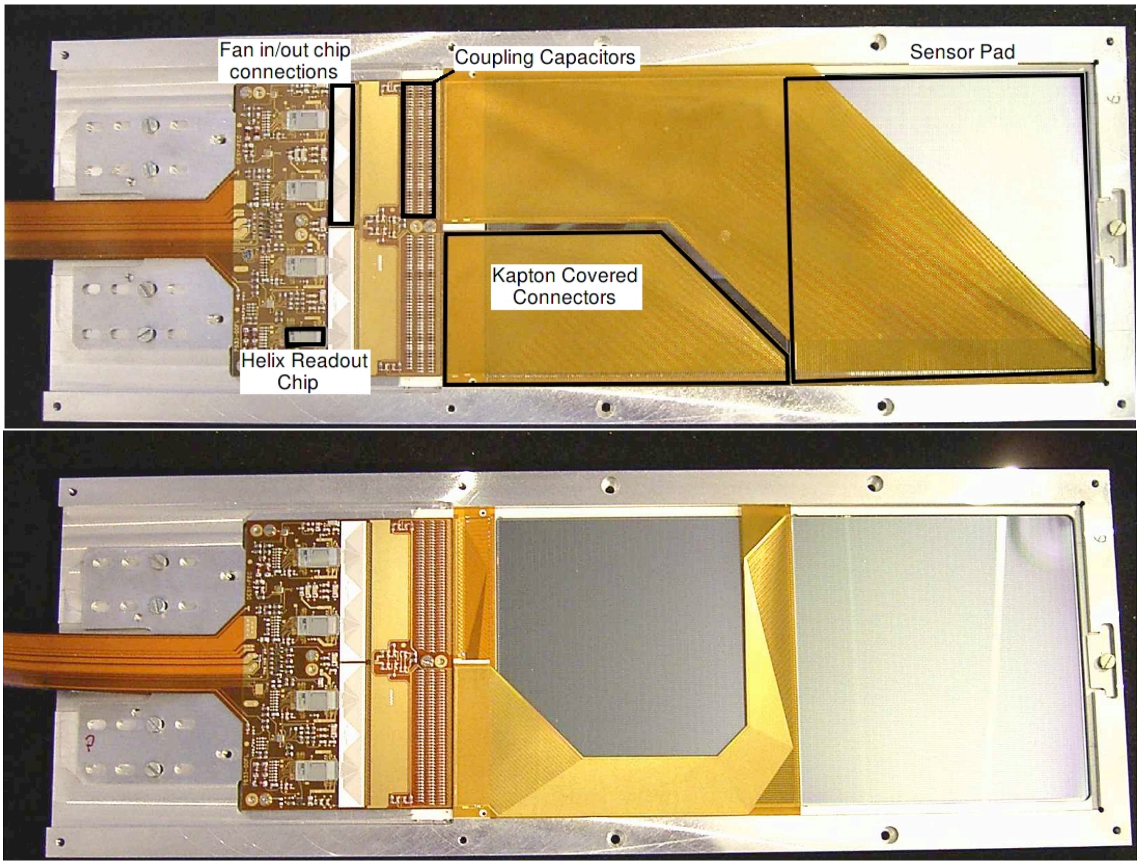

Figure 3.12: Photographs of a Silicon Strip Detector module, n-side shown above, p-side shown below. The n-side picture labels the most important parts of the silicon detector, highlighting one of the 4 readout chips on each side and the connections between the chip and the sensor. The kapton foils that surround the connections are also labelled.

In order to reduce development time the silicon sensors and readout chips were chosen from suitable existing designs. TIGRE silicon microstrip detectors obtained from Micron Semiconductor Ltd. were used, measuring 99 mm × 99 mm, with a thickness of 300 μm [Col02]. The sensors were double sided, with 128 strips per side arranged such that one side lies orthogonal to the other. This allowed a spacepoint to be reconstructed from the crossing of these strips, with n-doped silicon strips parallel to the beam line providing a position measurement in the (x, y) plane and p-doped silicon strips orthogonal to the n-doped side providing the z position component.

The SSD was arranged into 4 modules in a "diamond" configuration centred around the target cell. Each module contained 4 silicon sensors in 2 layers, separated by 15 mm and staggered such that the outer layer is shifted downstream with respect to the inner layer. Each layer also contained readout chips and electronics for each sensor. These modules are shown in Figure 3.12.

3.4.4 Scintillating Fibre Tracker

The SSD detailed above provided PID for charged particles from dE/dx measurements and track reconstruction from deflection in the magnetic field. The Scintillating Fibre Tracker (SFT), shown in figure 3.13, primarily provided momentum reconstruction information through the detection of the magnetic field deflection of particle tracks. Measurements of the produced scintillating light from incident particles were also used as secondary PID information, with the amount of light produced dependent on the incident particle type for a given incident particle momentum.

The SFT was designed to operate over the particle momentum range 0.3 to 1.4 GeV/c, which the SSD momentum reconstruction range partly overlapped [Hoe06]. The SSD dE/dx momentum resolution was expected to be optimum at lower momenta, where particles deposited most of their energy in the SSD. At higher momenta particles passed through the SSD and reached the SFT, where reconstruction provided better momentum resolution in this range. Due to the relatively poor angular resolution and the small separation of the SSD layers, reconstruction using deflection in the magnetic field relied on information from the SFT. Details of this reconstruction method are given in chapter 4.

The SFT was located outside the beam vacuum, held between the scattering chamber and the Photon Detector. Due to the lack of space and inaccessibility after installation, the detector was designed to be self supporting, also minimising foreign material in and around the interaction point. It consisted of two concentric rings of scintillating fibres, known as the inner and outer barrels, containing over 7000 fibres in total. The inner barrel radius measured 109 mm, the outer barrel 183 mm, with each fibre 1 mm in diameter and 280 mm in length. Each barrel contained 4 layers

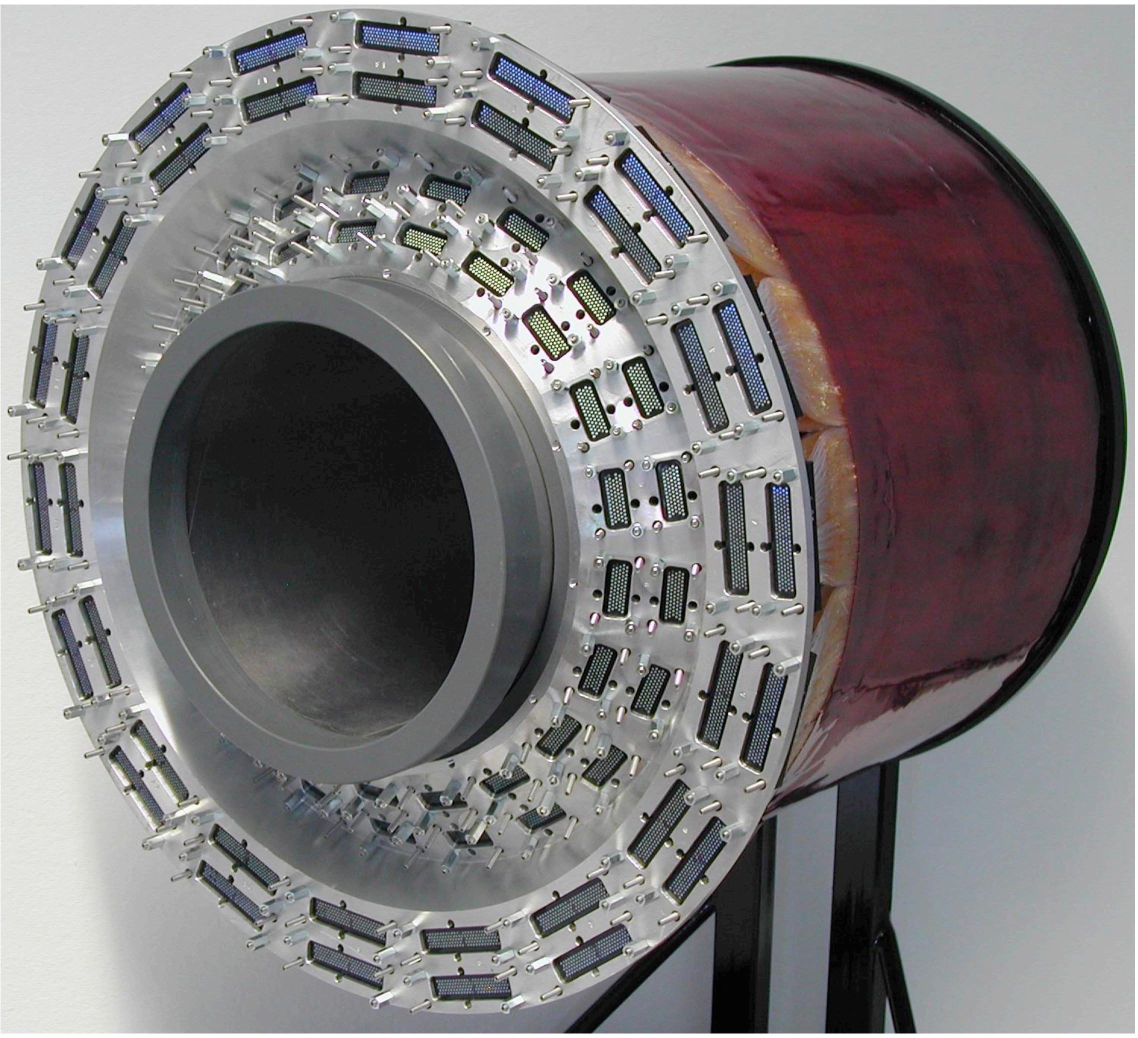

Figure 3.13: Photograph of the SFT prior to installation in the Recoil Detector showing the connecters to the light guides and the two barrel structure of the detector.

of fibres, with the inner 2 layers lying parallel to the beam line (the “parallel layer”) and the outer 2 layers at a stereo angle of 10 ° with respect to the parallel layers (the “stereo layer”). To maximise the detector acceptance the fibres were staggered such that they filled the gaps in the layer below, as shown in figure 3.14. These barrels provide two “space points” used in the reconstruction of particle tracks. A method for reconstructing these tracks in the inhomogeneous magnetic field is given in chapter 4.

The parallel layer allowed the reconstruction of the track transverse momentum component and azimuthal angle ϕ, the angle of the track in the x-y plane. The detector

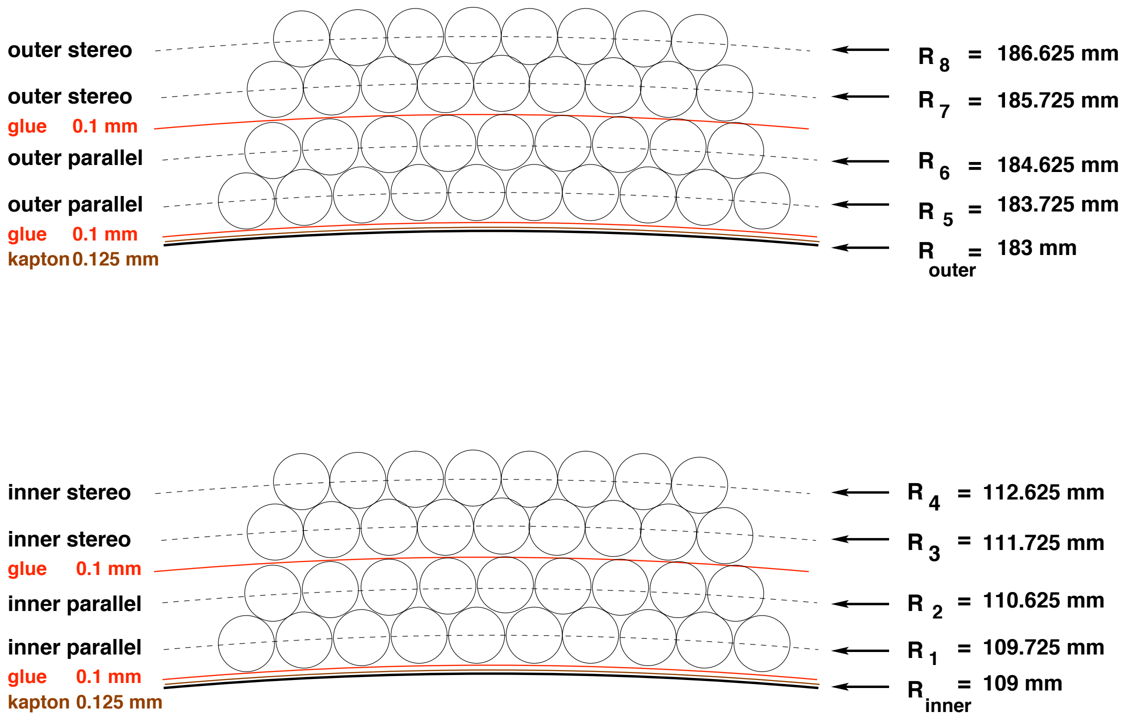

Figure 3.14: Diagram showing the structure of SFT barrels. The stereo layer lay at an angle of 10 ° with respect to the parallel layer. Each fibre had a radius of 1 mm and a length of 280 mm.

had full 2π azimuthal acceptance. The stereo layer allowed the reconstruction of the vertex position in the z-direction, i.e. along the beam line, the track longitudinal momentum component and the polar angle θ, the angle between the track and the z-axis. The acceptance in θ ranged from $\frac{\pi}{2}$ rad down to the acceptance region of the Lambda Wheels installed behind the Recoil Detector, 0.4 rad [Col02]. The primary vertex in the x-y plane, i.e. tracks originating in the target region, was provided by beam position monitors. Secondary vertices, such as those from tracks originating from secondary decays, could not be reconstructed by the SFT alone, this must be done in combination with the SSD.

The amount of scintillation light produced by incident particles was used in PID, in addition to momentum measurements, to separate positive pions and protons, with negative pions identified as having opposite curvature in the magnetic field. However, this required a good calibration of the energy response of each fibre. It is currently unknown if the required sample of events is available for this task for each fibre.

At the downstream end the fibres were mirrored and polished to prevent light losses. At the upstream end the scintillating fibres connected with clear light guides, fibres fabricated from similar material to the scintillating fibres but not doped with organic compounds which produce scintillation light. These light guides are connected to 64 channel PMTs. 78 PMTs were used to read out the 4992 channels of the SFT.

3.4.5 Photon Detector

The final sensitive component of the Recoil Detector was the Photon Detector. The SSD and SFT were designed to detect and measure the scattered target nucleon from exclusive processes, whilst the Photon Detector was designed to suppress background from associated production. Associated production involves the decay of a Δ^+ resonance producing either a proton or a neutron, which could be mistaken for a DVCS/BH event as a real photon and a scattered lepton are detected in the forward spectrometer in each of these processes. The decay channel $\Delta^+ \to n\pi^+$ could be easily rejected as a DVCS/BH event candidate by the detection of the π^+ by the SSD and SFT. However, the channel $\Delta^+ \to p\pi^0$ could not be rejected by the SSD and SFT alone. The neutral pion further decays to two photons, emitted back to back in the π^0 rest frame, with at least one of these photons detected by the Photon Detector. An event with both a proton and one or two photons detected in the target region could subsequently be rejected as a candidate for a DVCS event [Col02]. The photon detector is not designed to detect the produced photon of the DVCS or BH processes, which are produced in the acceptance of the forward spectrometer and are therefore detected by the calorimeter.

The Photon Detector was installed between the SFT and the superconducting magnet and consisted of 6 layers, alternating between Tungsten preshower material and scintillator bars. The innermost Tungsten layer was 6 mm thick with the remaining layers each 3 mm thick. Each scintillator bar was 11 mm thick, with the innermost layer containing 60 trapezoidal bars parallel to the beam line and the remaining

Figure 3.15: Photograph of the Photon Detector prior to installation in the Recoil Detector showing the outer scintillator layer at a 45 ° angle and the connecting fibres which lead to the PMTs. The detector is designed to detect photons from decays of the π^0, a reaction product of associated production and a source of background of exclusive processes. The produced photon of DVCS and BH processes is not detected.

layers containing 44 bars aligned at $+45^\circ$ and -45° with respect to the beam. Scintillation light was collected by two light guide fibres in grooves in the sides of the scintillator blocks, with the fibres connected to 64 channel PMTs similar to those used in the SFT and read out by ADCs. These signals could be used in PID between $\pi^\pm$ which reach the Photon Detector and electromagnetic showers. A photograph of the Photon Detector prior to installation can be seen in Figure 3.15.

The efficiency of the Photon Detector was highly constrained by the detector geometry. Decay photons are often emitted at low polar angles, with those emitted at 220 mrad entering the forward spectrometer acceptance and those emitted up to 400 mrad not being detected. The barrel design of the detector provided 2π azimuthal acceptance, but its dimensions in z matched that of the Recoil Detector as a whole, constraining the polar acceptance. Simulations gave detection probabilities of between 77 and 80 % for a single photon, but for a pair of photons from a single interaction vertex the probability reduced to between 18 and 20 % [Kra05].

3.4.6 Superconducting Magnet

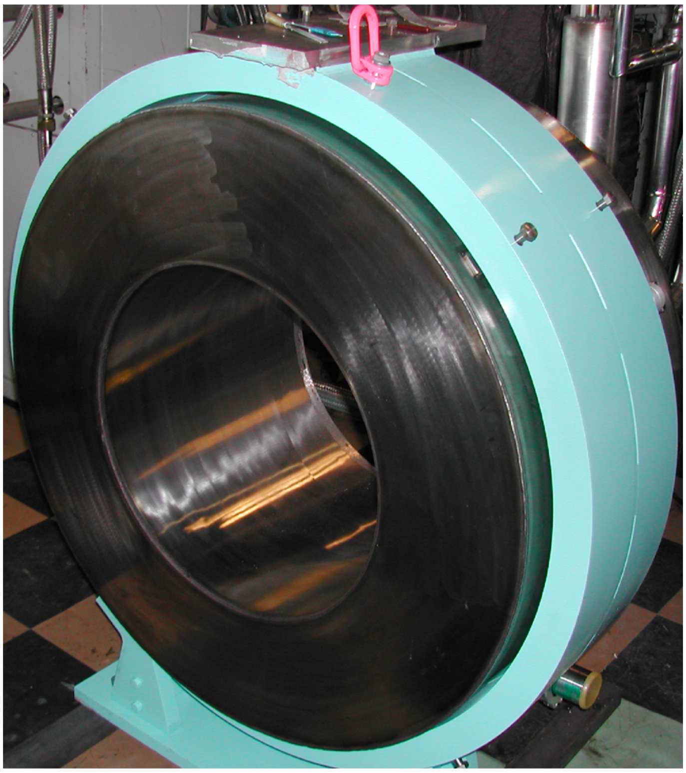

Figure 3.16: Photograph of the Superconducting Magnet prior to installation in the Recoil Detector. The magnet surrounded the sensitive detectors and provided both protection from background electrons and the magnetic field for track momentum reconstruction.

The Recoil Detector was surrounded by a superconducting magnet which had two important roles. Firstly the magnetic field was necessary for track momentum reconstruction in the SSD and SFT. In order to provide sufficient overlap between the momentum resolutions of the SSD and SFT the field homogeneity had to exceed 20 % and a sufficient field strength had to be used, in this case 1 Tesla. Field inhomogeneity had to be well understood for accurate momentum reconstruction, a discussion of which can be found in section 4.3.2.

Secondly the magnet provided protection for the sensitive SSD from background electrons from Møller scattering events, where electrons originating from the beam scatter on electrons belonging to the target atom. This process produces energetic background electrons which would damage the SSD. The equivalent process for a positron beam is known as Bhabba scattering. The magnetic field removed these electrons from the SSD acceptance. The magnet consisted of two Helmholtz coils immersed in liquid Helium and is shown in Figure 3.16.

The Recoil Detector required software to reconstruct measurements of particle momentum. The next chapter details a method to reconstruct momentum from particles passing through both the SSD and SFT and deflected by the magnetic field. The performance of this track reconstruction method is investigated, with first data taken with the Recoil Detector during operation in the experiment compared to Monte Carlo simulations of the detector.

Chapter 4

Track Reconstruction Using the Recoil Detector

In order to identify particles in the Recoil Detector a measurement must be made of both the energy deposited in the detector and of the particle momentum. Low momentum particles, particularly nucleons, can be stopped in the Silicon Strip Detector, whereby the energy deposited is directly proportional to the particle momentum. However, most particles in the Recoil Detector pass through the SSD and reach the Scintillating Fibre Tracker. These are deflected by the magnetic field, allowing a measurement of the particle momentum. This chapter will detail a method for reconstructing particle tracks through deflection in the magnetic field. Studies of the method performance with Monte Carlo simulated data will be presented, with first results from experimental data also shown. Momentum measurements from this method will be combined with energy deposition measurements to identify particles in the Recoil Detector. The detector is currently in commissioning; the software for particle identification is the subject of another thesis, therefore not detailed here.

Throughout this chapter two terms will be used which may require some clarification. "Hit" refers to an impact of a particle on a particular detector surface with sufficient energy deposited for a measurement. Depending on the detector geometry this hit may give only limited position information. "Space point" or "point" refers to a combination of hits from the same incoming particle to produce a point with full position information and an energy deposition measurement constructed from a combination of the individual hit energy measurements at individual hit positions.

For further clarity, ϕ_t hereafter refers to the azimuthal angle in the x-y plane of the reconstructed track in the Recoil Detector. The polar angle between the track and the z axis is denoted θ_t.

4.1 Introduction to Track Reconstruction

Track reconstruction in a particle physics experiment is the process of separating a data sample of energy and position measurements per triggered event from various particle detectors into tracks, containing measurements belonging to a single incident particle and thus allowing the identification of the particle and measurement of its kinematical properties, for use in later data analysis. Generally this task can be split into two processes: track finding, the separation into candidate subsets, and track fitting, the calculation of kinematical properties from these candidates. This method is used for the Recoil Detector track reconstruction algorithm described here. Global methods such as Kalman Filtering [Fru87] also exist where both tasks are carried out simultaneously.

Track Finding

The process of track finding produces subsets of space points from the data sample per event, with each subset candidates to be a particle track [F$^+$00]. These track candidates contain measurements which should belong to a single incident particle. The track candidate should be similar to the expected track model, based on the equation of motion of the particle. Any hits or space points not matching these conditions belong to the remaining subset. These space points may arise from detector noise, multiple scattering or other such factors.

The track finding procedure is based on pattern recognition. This task is trivially completed by eye for low track multiplicities, even in the presence of noise signals, overlapping tracks, track shape discontinuities and multiple vertices. However, the volume of data produced by particle physics experiments clearly requires an automated process. The aim of track reconstruction software is to perform this task as accurately as possible with high speed and processing capacity.

Track Fitting

Following the finding of track candidates, the track fitting procedure estimates parameters of the track such as angles, curvature and intersection points with the coordinate system axes. Many of these parameters can be directly related to kinematical properties of the particle, see equations (4.1) – (4.3). The procedure also allows the measurement of the quality of the fit to the expected track model, in this case via the standard χ^2 parameter. This can be used in an iterative procedure to reject track candidates which have a poor quality of fit. Track fitting requires knowledge of the geometry and material budget of the detector, the detector resolutions, any relevant technical details such as magnetic fields and an accurate model of the particle trajectories [F$^+$00].

Requirements for Track Reconstruction in the Recoil Detector

Due to time constraints, the track reconstruction software was developed concurrently with Monte Carlo simulation software and the detector hardware [Osb06]. By doing so the requirements of the track reconstruction software were unknown at the beginning of development. Modifications to the detector software continued to be made throughout the data taking of the detector.

The track reconstruction software was to be capable of:

- finding tracks in the presence of noise from background and multiple scattering;
- performing track fitting in an inhomogeneous magnetic field;
- finding tracks in an environment with a maximum of 5 space points per track available. This included the primary interaction vertex, initially calculated from the Recoil Detector space points and later refined during track fitting;

- the capability to run online and offline as part of the HERMES reconstruction software chain;
- execute as quickly as possible to reduce data production time for analysers.

4.2 HERMES Reconstruction Software

The HERMES collaboration has developed various software packages and data structures to process the raw experimental data. These software packages and structures have evolved over the experiment lifetime to include information from new detectors. The Recoil Detector software had also to be included in this software chain, placing some restrictions on the nature of this software, such as the input and output structures and the language in which it was written. The HERMES software chain will be described in the following section.

HERMES Reconstruction Software

The HERMES data taking begins with the HERMES DAQ (Data AcQuisition), software which builds events in response to detector trigger signals. The DAQ also responds to “scaler” events, occurring every 10 seconds and containing information such as trigger dead time, see section 3.3.3, and luminosity, see section 3.3.4. These change at the same rate as the event trigger. It would be unnecessary to be read out these events as frequently as trigger events, doing so would greatly increase data file size and hence data processing time. The DAQ outputs EPIO (Experimental Physics Input-Output) files containing the trigger and scaler events [Mak02].

Information such as vacuum pressures, high voltage readings and phototube gains are recorded every few minutes by the HERMES Slow Control package. These change at a slower rate than the scaler events and hence are read out separately. The DAQ and Slow Control form the online processing section of the HERMES production chain, the main production chain is carried out offline.

A flowchart showing the structure of the HERMES offline software chain is shown in figure 4.1. The HERMES Decoder (HDC) package reads in EPIO files containing readout information from each detector. HDC combines this information with information from calibration, geometry and mapping servers to produce calibrated quantities such as wire hit positions and energy deposition. The HDC package produces output in the ADAMO format [PTG93], a structured data format developed at CERN for high energy physics experiments. HERMES uses DAD (Distributed ADAMO Database) [Wan95] files as output which allow processes to share output over a network in a client-server model. The Slow Control package also provides output in ADAMO format.

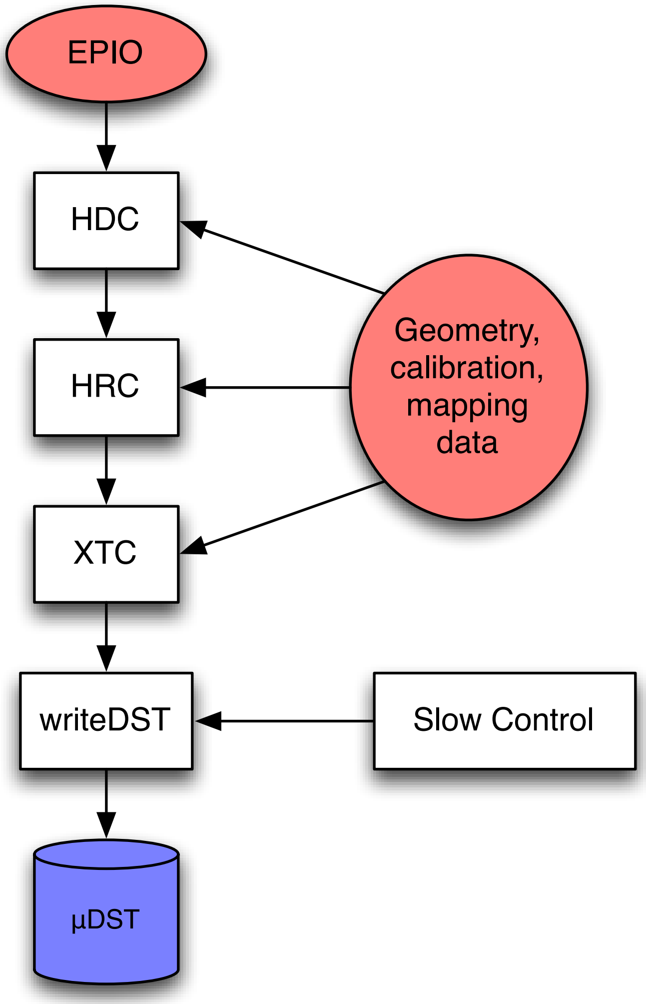

Figure 4.1: Simplified flowchart showing the structure of the HERMES offline software chain. The Recoil Detector track reconstruction software is integrated into the XTC (eXternal Tracking Code) Package.

Following decoding the data are processed by the HERMES Reconstruction (HRC) package which provides track reconstruction and PID for all detectors in the main spectrometer downstream from the Lambda Wheels, see figure 3.5. Track reconstruction for the remaining detectors is then carried out in XTC (eXternal Tracking Code). The reconstruction for the Recoil Detector is integrated into XTC, and hence must use ADAMO tables as input and output. The writeDST package synchronises the ADAMO tables from the XTC and Slow Control packages to produce μDST files, the final data production files used in physics analysis.

The track reconstruction routines for the Recoil Detector were integrated into the full software chain in the XTC package. This allows the reconstruction to use information from HRC ADAMO tables, such as the beam position and primary interaction vertex from the main spectrometer reconstruction and to ensure each triggered event in the Recoil Detector is synchronised to the correct spectrometer event. In order to integrate easily with the existing XTC code, the Recoil Detector routines were written in C.

HERMES Monte Carlo Productions

Monte Carlo simulated data is produced by two software packages at HERMES. GMC (Generator Monte Carlo) simulates a variety of physics processes using custom written generators, including DVCS / BH processes of particular relevance to the Recoil Detector physics program. These generated events are then propagated through a simulation of the detector hardware in the HMC (HERMES Monte Carlo) package. The HMC package outputs in ADAMO format which can be directly read by HRC, and hence XTC, for track reconstruction. Thus GMC and HMC in the Monte Carlo production chain substitute for the DAQ and HDC in the experimental data chain. A flowchart for the Monte Carlo production chain is shown in figure 4.2.

HMC uses the GEANT Monte Carlo package developed at CERN to simulate the propagation of particles through a simulation of the detector hardware and readout. The HERMES Database (HDB) package provides this simulation by processing a geometry file containing the position, composition and dimensions of each compo-

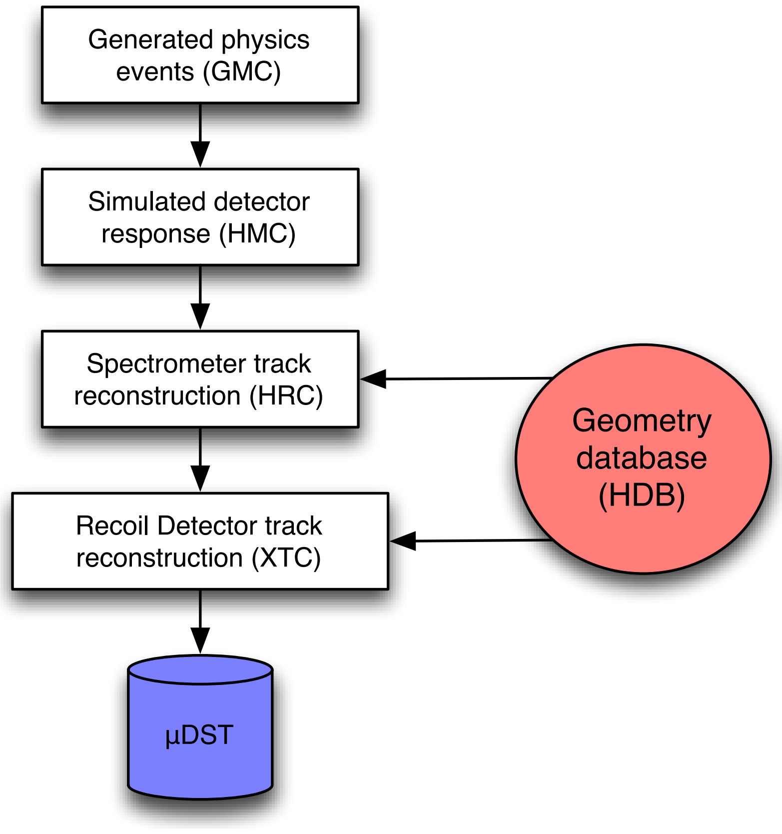

Figure 4.2: Simplified flowchart showing the structure of the HERMES Monte Carlo Production chain.

nent of the detector hardware. This geometry file is also used by HDC, HRC and XTC in track reconstruction via the geometry, mapping and calibration servers.

Monte Carlo data allows calculation of track reconstruction resolutions and efficiencies by comparing the output of the track reconstruction routines with the known input track parameters. Monte Carlo is also essential in physics analyses for a variety of purposes, including understanding background contributions, detector acceptance and systematic uncertainties.

XTC: eXternal Tracking Code

The software package XTC contains subroutines relevant to many detectors in the HERMES spectrometer, including detectors installed over the course of the experiment's data taking period such as the Lambda Wheels. The software for reconstructing tracks for the Recoil Detector is also included in this package. In addition to track reconstruction routines, the package also includes clustering and space point reconstruction routines, interfaces to the ADAMO tables and libraries for compatibility with the HERMES production chain. Figure 4.3 shows the structure of the XTC package relevant to the Recoil Detector. Development of the track reconstruction routines for the Recoil Detector is detailed in the remainder of this chapter.

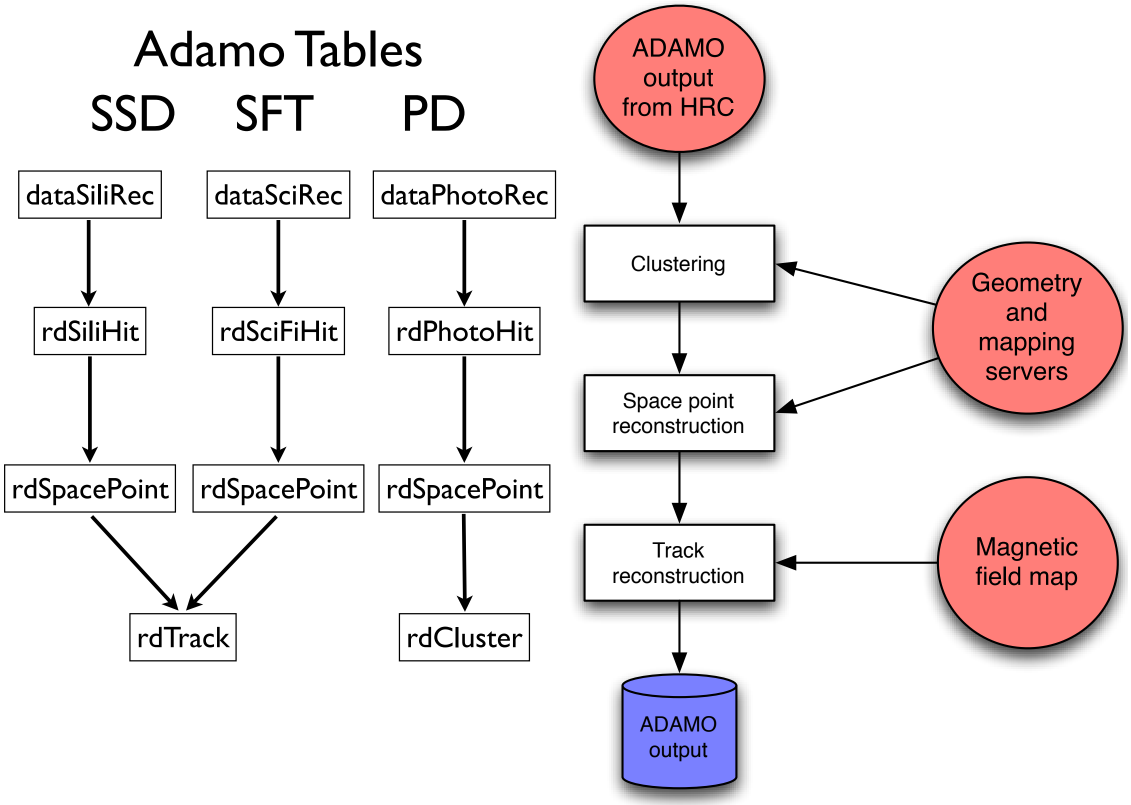

Figure 4.3: Simplified flowchart showing the structure of the XTC software package relevant for the Recoil Detector. Subroutines relating to other parts of the HERMES spectrometer are not shown.

4.3 Development of a Track Reconstruction Routine for the Recoil Detector

The main purposes of the Recoil Detector are to provide exclusivity by detecting the recoiling target nucleon from exclusive processes such as DVCS and to improve the resolution in t of the HERMES experiment by detecting low momentum recoiling nucleons. The detector also provides vital background suppression by detecting pions from decays of associated production of the Δ. These particles are emitted close to the beam position and pass through the SSD, with most reaching the SFT. Tracks that reach the SFT are known as “long tracks”, with “short tracks” being those that are stopped in the SSD.

A method has been implemented to reconstruct tracks from the beam line position through both the SSD and SFT, here labelled as “SSD + SFT reconstruction”, in order to identify these particles in later data analyses [Osb06]. This section will describe this method, with performance tests using Monte Carlo simulated data shown and first results with data taken during running of the experiment also shown. The author was responsible for integrating these routines into the full XTC software package to be run in the offline data production chain, making improvements based on tests with both MC and experimental data.

4.3.1 Recoil Detector Monte Carlo

The Recoil Detector hardware and software packages were developed in parallel to increase development efficiency with the available manpower. The track reconstruction routines were to be tested with Monte Carlo (MC) simulated tracks, however the MC simulations were also being developed at this time. This lead to many evolutions in the development of both packages, as both the track reconstruction and detector simulations improved over time.

Initial tests of the reconstruction code relied on space point information taken directly from the GMC package output ADAMO tables. The MC sample used in tests detailed here uses a more advanced Recoil Detector MC package which allows

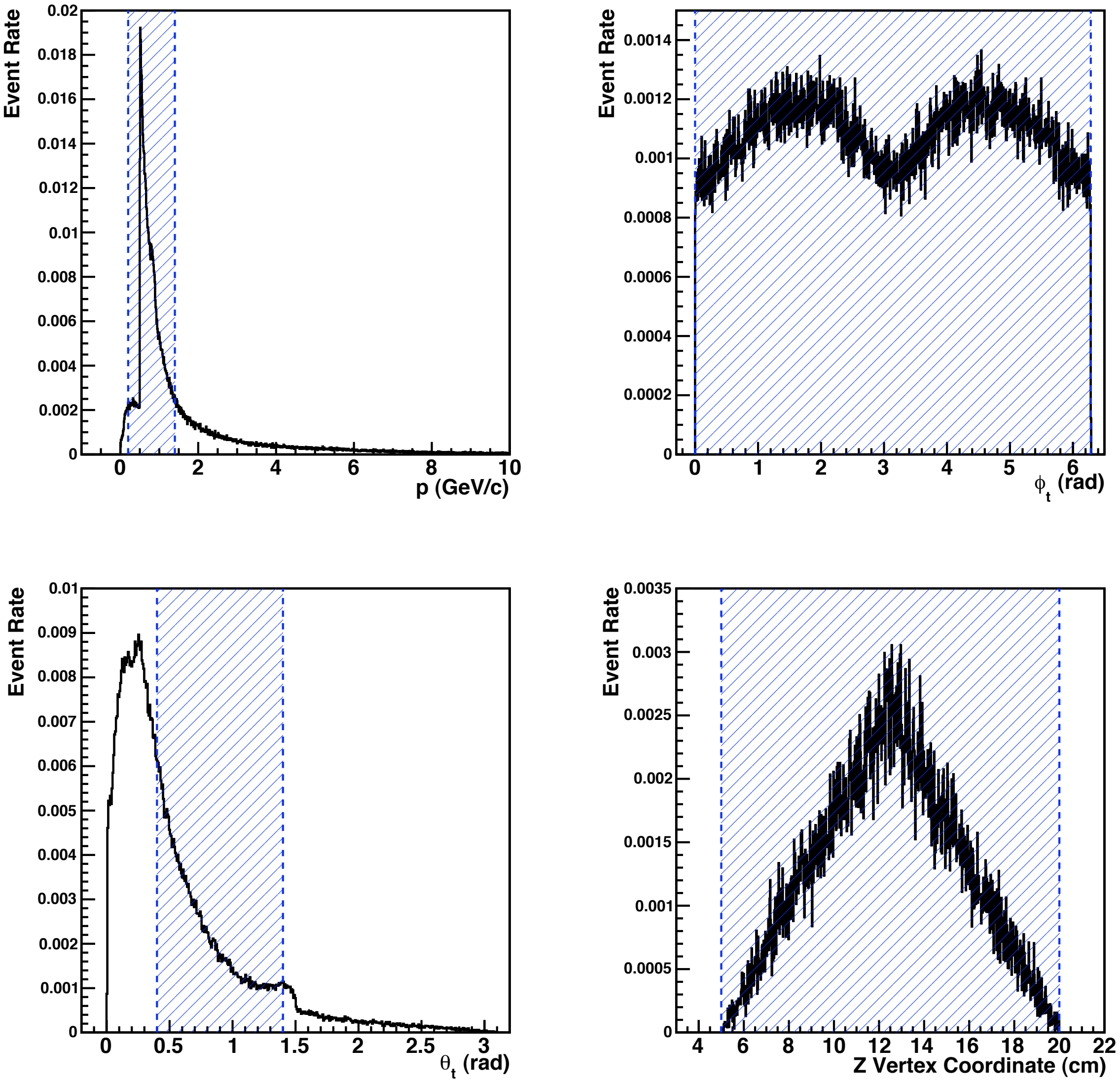

Figure 4.4: Distributions of kinematics and track parameters from a MC sample of recoiled proton and produced pion tracks only, generated by gmc_disNG and normalised to the total number of events. Here θ_t and ϕ_t refer to the azimuthal and polar angles of the proton or pion track, as defined at the beginning of chapter 3. This sample includes both DIS and DVCS events, with the acceptance of the Recoil Detector shown in the blue shaded regions. The peak of the momentum distribution is covered by the detector, with particles at small θ_t entering the forward spectrometer.

the full Recoil Detector XTC routines (see figure 4.3) to be tested with more realistically simulated MC data. At the time of writing background simulations have been included in the simulations of the SFT, with background simulations under development for the SSD.

The Recoil Detector MC routines have now been integrated into the full HMC software package, allowing the Recoil Detector and the forward spectrometer to be simulated simultaneously. The standard HERMES DIS generator, known as gmc_disNG, is now used as the main MC production generator, containing both DIS and DVCS events in the sample. Sample distributions of track parameters for proton and pion tracks generated by gmc_disNG are shown in figure 4.4. This allows the track reconstruction routines to be tested on a realistic sample of events as expected in the experimental data. However, not all of the tracks generated by gmc_disNG are found in the acceptance region of the Recoil Detector.

4.3.2 Magnetic Field Inhomogeneity

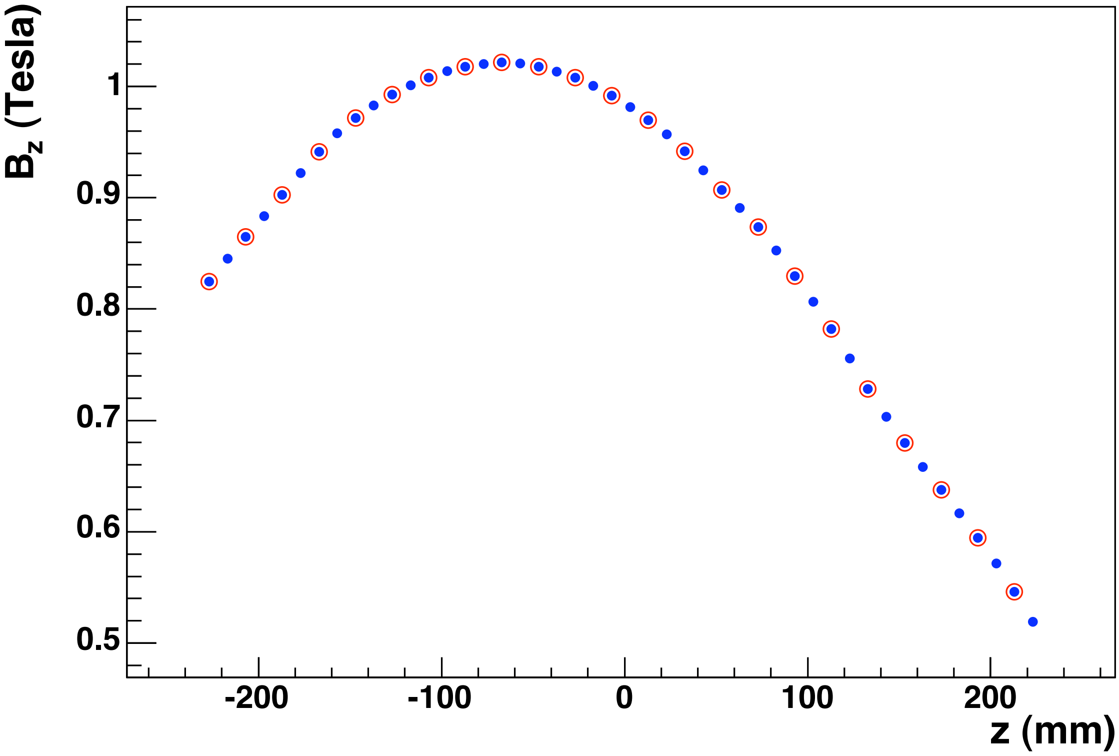

Figure 4.5: Calculated magnetic field component B_z (red circles) and interpolated points (blue dots). The magnetic field is depicted at $r = 0$ mm, the centre of the detector in the x-y plane, and covers the length of the Recoil Detector in the z direction.

The Recoil Detector contains a superconducting magnet generating a ~ 1 Tesla magnetic field, used to deflect charged particles for both protection from background and for momentum reconstruction. The momentum of a charged particle in motion in a homogeneous, longitudinal magnetic field is proportional to the radius of curvature of the particle track. However, the Recoil Detector magnetic field is inhomogeneous, which must be considered by the track reconstruction routines. The track reconstruction routines detailed later uses a magnetic field map to account for this inhomogeneity.

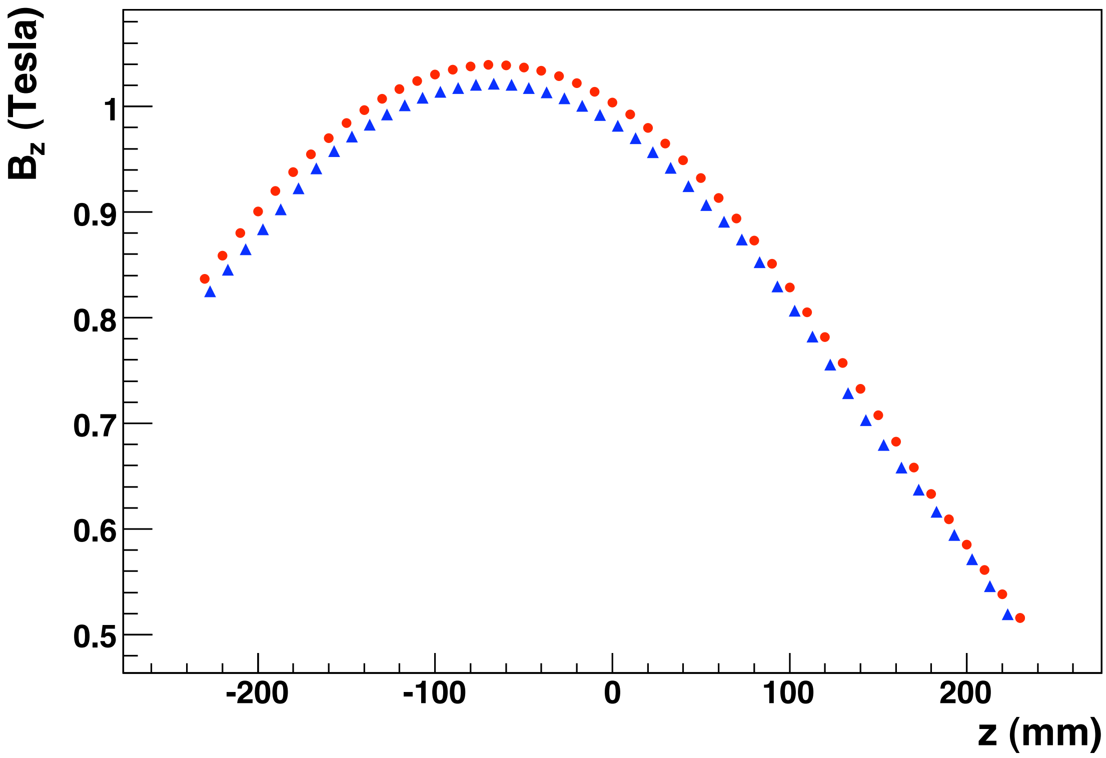

Figure 4.6: Measured magnetic field component B_z (red circles) and interpolated points (blue triangles), depicted at $r = 0$ mm, the centre of the detector in the x-y plane, and covering the length of the Recoil Detector in the z direction [Zih04].

Prior to the construction of the magnet the Efremov institute calculated a magnetic field map, from which a field map for XTC was created. The calculated field map describes a rotationally symmetric solenoidal magnetic field with a resolution of 20 mm in both r and z, spanning the range of the HERMES spectrometer in order to ensure the field had no influence on the forward spectrometer. This was deemed insufficient for track reconstruction in the Recoil Detector, as the magnetic field only affects particles in the region of the Recoil Detector up to the radius of the outer

SFT barrel, 183 mm. The field was interpolated with a 2-D cubic spline function to provide a map with 10 mm resolution, shown in figure 4.5.

In October 2004 a measurement was made of the magnetic field in order to check the accuracy of the interpolated field map. Figure 4.6 shows the comparison of this measurement and the interpolated field of figure 4.5. The field was measured with the required resolution of 10 mm. The interpolated map compares well with the measured values, within 2%, and is compatible with the Monte Carlo simulation routines. Monte Carlo studies are used to investigate the performance of the track reconstruction software, therefore the interpolated field map is employed. For reconstruction of experimental data the measured field map is used by the track reconstruction routines.

4.3.3 Track Finding

As noted in section 4.1, it is advantageous to perform track reconstruction in two steps, track finding and track fitting. For the Recoil Detector long tracks, track finding is carried out by pattern matching the Recoil Detector long tracks to an expected track model, in this case a parameterised helix equation in three dimensions [Osb06]. The track finding routines takes all reconstructed space points in both the SSD and SFT and finds three points within certain restrictions to define a track seed, the basis of the track helix. One of these points may be the primary interaction vertex, as reconstructed by HRC from forward spectrometer tracks, though if that is not available the seed must be formed from space points in different layers of the Recoil Detector.

Once a suitable seed has been found the maximum bending angle, the azimuthal angle ϕ_t, is used to reject unreasonable track candidates. For a proton of momentum 50 MeV/c the maximum bending angle is 0.25 radians, with a 250 MeV/c proton having a maximum bend of only 0.06 radians. The minimum of the expected momentum range of the SFT is 0.3 GeV/c, thus a cut on the maximum bending angle of 0.25 radians will not remove any tracks from useful physics events but will help reduce background from “ghost” tracks, e.g. those formed from noise hits or combinatorics in the SFT. Execution speed is also improved as track candidates that fail this cut are not processed further.

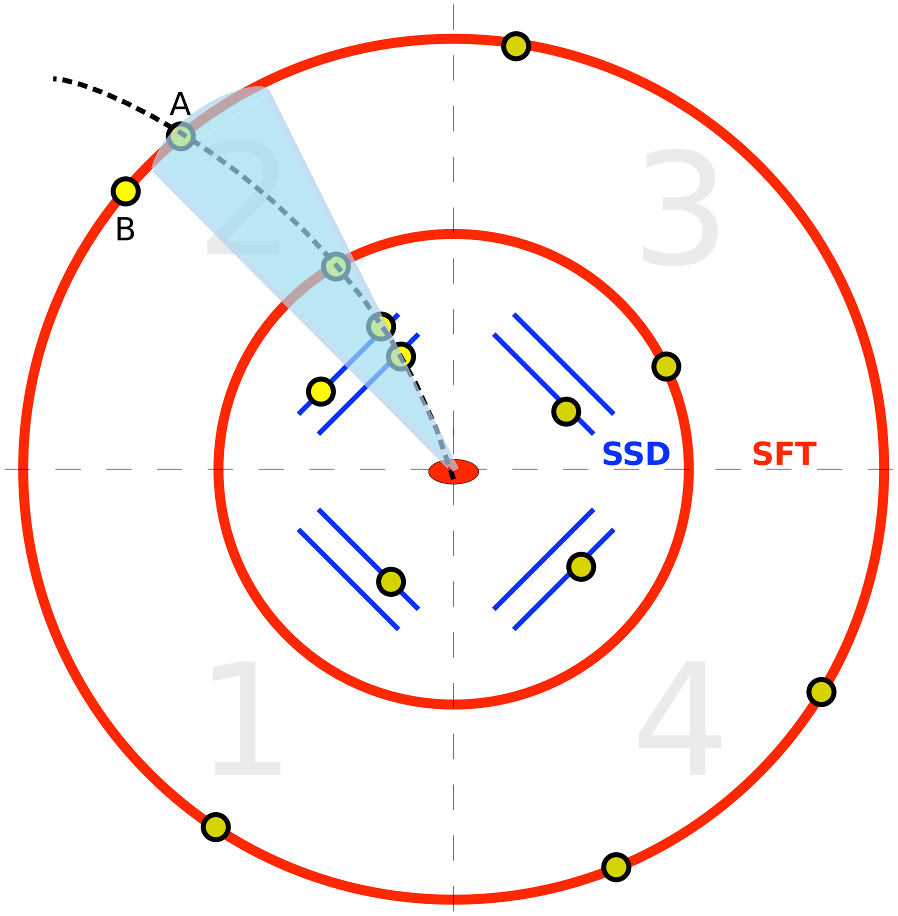

Figure 4.7: Illustration of the use of the maximum bending angle cut to reject track candidates. A seed is formed from two space points in the SSD and the target cell vertex position. Space point A lies within the maximum bending angle cut, as shown by the shaded area, while point B does not and is therefore not used to define a track candidate.

By taking a larger bending angle cut than necessary multiple scattering could also be taken into account, where particles scatter off the individual layers of the detector. However this has not been accurately simulated in MC and cannot be fully tested at this time. The deflection in the magnetic field is expected to be the dominant factor in any case. An illustration of the use of the cut to reject track candidates is shown in figure 4.7.

A point lying on a helix will satisfy the following:

$$x = r\cos(\phi_t) + x_0 \tag{4.1}$$

$$y = r\sin(\phi_t) + y_0 \tag{4.2}$$

$$z = c\phi_t + z_0 \tag{4.3}$$

where r is the helix radius, c is a constant related to the loop separation (the gradient of z with respect to ϕ_t) and $x_0,\ y_0$ and z_0 are the coordinates of the origin of the helix, the primary interaction vertex.

For each of the remaining space points i in the Recoil Detector sample the vector $\vec{a}_i = \begin{bmatrix} x_i \\ y_i \\ z_i \end{bmatrix}$ is calculated according to the helix equations:

$$x = r\cos(\phi_{t,i}) + x_0 \tag{4.4}$$

$$y = r\sin(\phi_{t,i}) + y_0 \tag{4.5}$$

$$z = c\phi_{t,i} + z_0. \tag{4.6}$$

The difference $\delta a = |\vec{a} - \vec{a}_i|$ is the distance from the space point to the helix, defined as the track road width, R. A maximum road width is established such that any space point inside this road width, with $\delta a < R$, is marked as belonging to that track, with the further restriction that the space point must be from a different layer than those already marked as belonging to the track.

4.3.4 Track Fitting

Once a set of track candidates has been found, a fit must be carried out to reconstruct track momentum, angles and vertex coordinates. Momenta of particle tracks passing through the SSD and SFT are reconstructed from the track curvature in the magnetic field. However, the magnetic field in the case of the Recoil Detector exhibits some inhomogeneity which must be accounted for, leading to a more complex method than might be used conventionally.

The track fitting algorithm proceeds by minimising the χ^2 difference between an approximation of the track shape, given by the equation of motion of the particle, with the space points found belonging to the track candidate [Osb06]. The inhomogeneity of the magnetic field leads to a departure from the usual track shape, a helix of constant radius, leading to modifications to the original approximation.

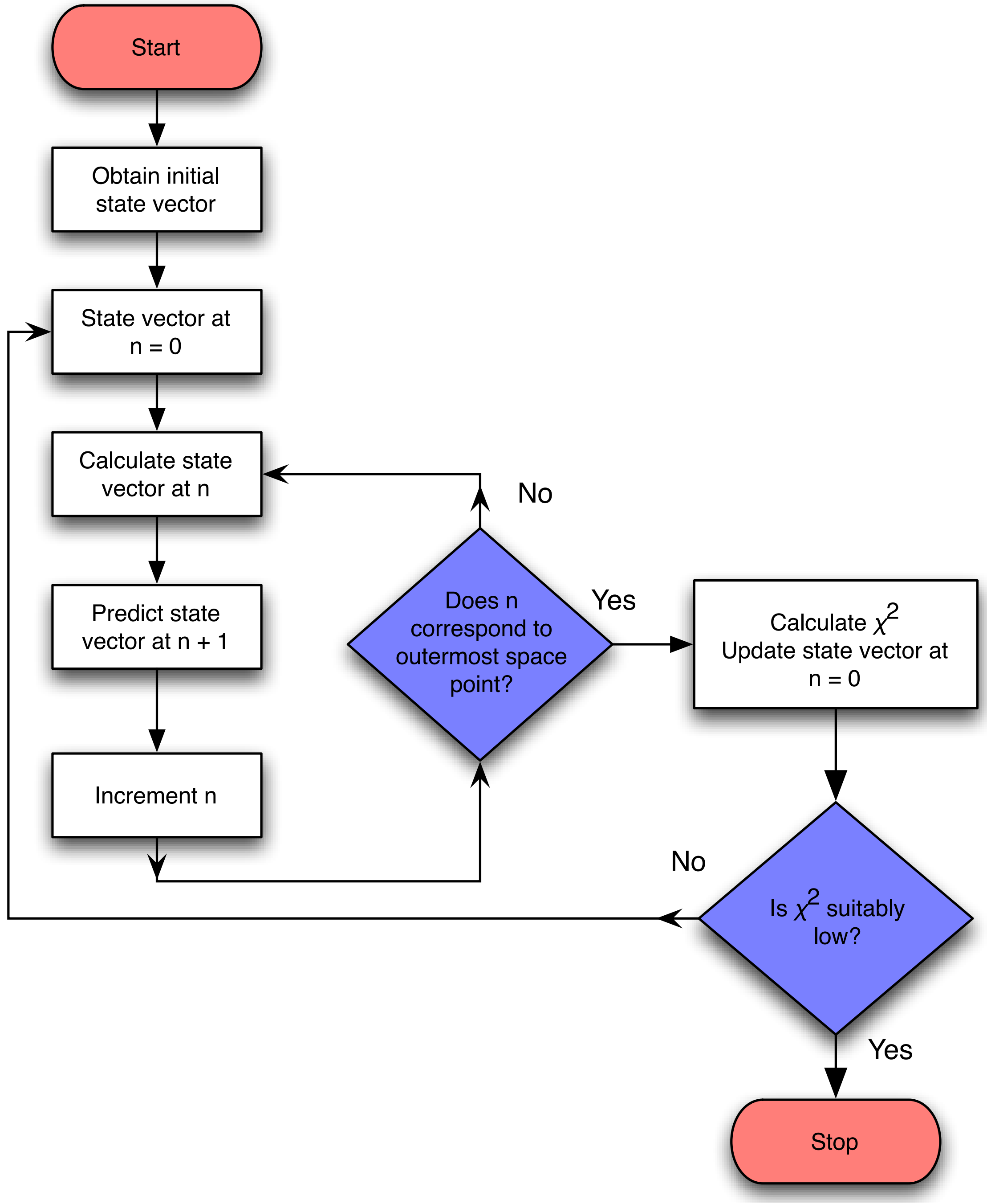

Figure 4.8: Flowchart showing fitting procedure for Recoil Detector long tracks. At the end of this procedure the track parameters are written out to ADAMO tables for use in the next part of the HERMES offline software production chain.

The track shape model used instead is a smooth spiral of varying radius. This is described by propagating by numerical integration a set of parameters, known as the "state vector", through a map of the magnetic field [HS84], from the centre of the detector in the x-y plane outwards in increasing radial steps until the outermost point, the radius of the outer SFT layer. Following this propagation a set of track parameters is obtained. The χ^2 difference between the measured space points and the fitted track coordinates at the radius of that space point is minimised according to a Newton-Raphson iteration method, with further iterations made if the χ^2 difference is above a certain threshold. The Newton-Raphson method is a well-known mathematical formalism used to find the roots of a real-valued function.

When the χ^2 difference is sufficiently low, the procedure is completed and the track parameters are written to the output ADAMO tables to be used in the next part of the HERMES offline software production chain. This procedure is outlined in figure 4.8.

The formalism given in [HS84] is given in Cartesian coordinates. For the geometry of the Recoil Detector it is preferable to use cylindrical polar coordinates, with a formalism derived from [BM81]. The following is a summary of the track reconstruction method, full details can be found in [Osb06].

The state vector of a particle at step n, corresponding to a step of 1 mm in the radial direction r, is given by:

$$\vec{v}_n = \begin{bmatrix} \phi_{t,n} \\ \phi'_{t,n} \\ z_n \\ z'_n \\ \lambda \end{bmatrix} \tag{4.7}$$

where primed coordinates denote first derivatives with respect to r and $\lambda = \frac{1}{|p|}$ is the inverse momentum of the particle track, constant for each propagation made.

Following successful propagations with sufficiently low difference in χ^2 the final state vector at $n = 0$ gives the required track parameters ϕ_t and the z vertex coordinate, with the track momentum p calculated from

$$p = \frac{q}{\lambda} \tag{4.8}$$

where q is the charge, ±1. The remaining track angle θ_t can be trivially calculated from the fitted z coordinates of the propagation.

The state vector $\vec{v}_n$ is propagated as n increases in steps of $1\,\mathrm{mm}$ from the beam axis at the centre of the detector, $r = 0\,\mathrm{mm}$, to the maximum radial point, the outermost radius of the SFT, $r \approx 183\,\mathrm{mm}$. There are 190 steps in r made to ensure that the propagation includes the outermost space point. As the particle momentum is fixed for each propagation, i.e. $\lambda_n = \lambda_0$, the track direction is altered by adjusting the parameters $\phi_{t,n}$ and z_n according to the particle momentum and the magnetic field strength at the points given by ϕ_t and $r = n$.

The equation of motion for the particle is derived from the equation of motion in a magnetic field, neglecting energy loss:

$$\frac{d\vec{p}}{dt} = q\vec{v} \times \vec{B}(\vec{r}) \tag{4.9}$$

In cylindrical polar coordinates

$$\frac{d^2\phi_t}{dr^2} = \phi_t'' = -\frac{2\phi_t'}{r} - r\phi_t'^3 + \frac{qQ}{pr}(z'B_r + r\phi_t'z'B_{\phi_t} - [1 + r^2\phi_t'^2]B_z) \tag{4.10}$$

and

$$\frac{d^2 z}{dr^2} = z'' = -r\phi_t'^2 z' + \frac{qQ}{p}(-r\phi_t' B_r + [1 + z'^2]B_{\phi_t} - r\phi_t' z' B_z) \tag{4.11}$$

where terms involving B_{ϕ_t} cancel due to the magnetic field being solenoidal, i.e. $B_{\phi_t} = 0$, double primes denote second derivatives with respect to r, with Q given by

$$Q = \sqrt{[1 + r^2\phi_t'^2 + z'^2]} \tag{4.12}$$

and λ as defined in equation (4.8) [BM81].

The state vector is propagated in steps of n by estimating the vector $\vec{v}_{n+1}$ when $\vec{v}_n$ is given. Estimates are calculated from equations (4.10) and (4.11), with improvements made by expanding them in leading terms of a Taylor series.

The initial state vector $\vec{v}_0$ is given, including the initial ϕ_t' and z'. The second derivatives ϕ_t'' and z'' are calculated from equations (4.10) and (4.11). For each step $n \geq 1$ the estimates are calculated from

$$h = r_{n+1} - r_n \tag{4.13}$$

$$\phi_{t,n+1} = \phi_{t,n} + h\phi_{t,n}' + \frac{1}{2}h^2\phi_{t,n}'' \tag{4.14}$$

$$\phi_{t,n+1}' = \phi_{t,n}' + h\phi_{t,n}'' \tag{4.15}$$

$$z_{n+1} = z_n + hz_n' + \frac{1}{2}h^2 z_n'' \tag{4.16}$$

$$z_{n+1}' = z_n' + hz_n'', \tag{4.17}$$

with new values of $\phi_{t,n+1}''$ and z_{n+1}'' calculated from substitutions into equations (4.10) and (4.11).

These estimates of ϕ_t and z and their first derivatives can be improved by instead using the first two terms of a Taylor series:

$$\begin{aligned}
\phi_{t,n+1} &= \phi_{t,n} + h\phi_{t,n}' + h^2(2\phi_{t,n}'' + \phi_{t,n+1}'')/6 \\
\phi_{t,n+1}' &= \phi_{t,n}' + h(\phi_{t,n}'' + \phi_{t,n+1}'')/2 \\
z_{n+1} &= z_n + hz_n' + h^2(2z_n'' + z_{n+1}'')/6 \\
z_{n+1}' &= z_n' + h(z_n'' + z_{n+1}'')/2,
\end{aligned}$$

with again the new values of $\phi_{t,n+1}''$ and z_{n+1}'' calculated from substitutions into equations (4.10) and (4.11).

Following these propagation steps the χ^2 difference must now be checked to establish if further propagations are required. As stated earlier, this χ^2 difference is minimised according to a Newton-Raphson iteration method. This method requires knowledge of the partial derivatives of $\vec{v}_{n+1}$ with respect to $\vec{v}_n$, as given in the matrix $\mathbf{M}^{n+1,n}$:

$$\mathbf{M}^{n+1,n} = \frac{\partial \vec{v}_{n+1}}{\partial \vec{v}_n} = \begin{bmatrix}
\frac{\partial \phi_{t,n+1}}{\partial \phi_{t,n}} & \frac{\partial \phi_{t,n+1}}{\partial \phi_{t,n}'} & \frac{\partial \phi_{t,n+1}}{\partial z_n} & \frac{\partial \phi_{t,n+1}}{\partial z_n'} & \frac{\partial \phi_{t,n+1}}{\partial \lambda} \\
\frac{\partial \phi_{t,n+1}'}{\partial \phi_{t,n}} & \frac{\partial \phi_{t,n+1}'}{\partial \phi_{t,n}'} & \frac{\partial \phi_{t,n+1}'}{\partial z_n} & \frac{\partial \phi_{t,n+1}'}{\partial z_n'} & \frac{\partial \phi_{t,n+1}'}{\partial \lambda} \\
\frac{\partial z_{n+1}}{\partial \phi_{t,n}} & \frac{\partial z_{n+1}}{\partial \phi_{t,n}'} & \frac{\partial z_{n+1}}{\partial z_n} & \frac{\partial z_{n+1}}{\partial z_n'} & \frac{\partial z_{n+1}}{\partial \lambda} \\
\frac{\partial z_{n+1}'}{\partial \phi_{t,n}} & \frac{\partial z_{n+1}'}{\partial \phi_{t,n}'} & \frac{\partial z_{n+1}'}{\partial z_n} & \frac{\partial z_{n+1}'}{\partial z_n'} & \frac{\partial z_{n+1}'}{\partial \lambda} \\
\frac{\partial \lambda}{\partial \phi_{t,n}} & \frac{\partial \lambda}{\partial \phi_{t,n}'} & \frac{\partial \lambda}{\partial z_n} & \frac{\partial \lambda}{\partial z_n'} & \frac{\partial \lambda}{\partial \lambda}
\end{bmatrix} \tag{4.18}$$

with explicit calculations for the matrix entries given in [Osb06]. Particularly important for use in the Newton Raphson iteration method is the matrix $\mathbf{M}^{n,0}$ where

$$\mathbf{M}^{n,0} = \mathbf{M}^{n,n-1}\mathbf{M}^{n-1,n-2}...\mathbf{M}^{1,0}. \tag{4.19}$$

For each successful iteration the initial state vector $\vec{v}_0$ is updated to calculate the new track momentum, ϕ_t angle and Z vertex coordinate. This is calculated according to Newton's method:

$$\vec{v}_0^{N+1} = \vec{v}_0^{N} - \mathbf{G}^{-1}g \tag{4.20}$$

where the superscript N now refers to the iteration and the subscript n refers to the state of propagation as before. $\mathbf{G}$ is another 5 × 5 matrix given by

$$\mathbf{G}_{\alpha\beta} = 2\sum_{j}^{N_{\text{spacepoints}}} \frac{\mathbf{M}^{j,0}_{0\alpha}\mathbf{M}^{j,0}_{0\beta}}{\sigma^2_{\phi_t}} + \frac{\mathbf{M}^{j,0}_{2\alpha}\mathbf{M}^{j,0}_{2\beta}}{\sigma^2_{z}} \tag{4.21}$$

where σ_{ϕ_t} and σ_z are the uncertainties associated with the measurements of the space point positions, different for the SSD and SFT.

g is a 5 component vector given by

$$g_{\alpha} = -2\sum_{j}^{N_{\text{spacepoints}}} A_j\mathbf{M}^{j,0}_{0\alpha} + B_j\mathbf{M}^{j,0}_{2\alpha} \tag{4.22}$$

where

$$A_j = \frac{\phi^m_{t,j} - \phi^e_{t,j}}{\sigma^2_{\phi_t}} \tag{4.23}$$

and

$$B_j = \frac{z^m_j - z^e_j}{\sigma^2_z} \tag{4.24}$$

where the superscript m refers to the measured space point value, the superscript e refers to the estimate taken from the calculated values of the propagation at the step value $n = j$, where the subscript j is the radius of the measured space point.

The iteration proceeds until $\frac{\chi^2_N - \chi^2_{N-1}}{\chi^2_{N-1}}$ is sufficiently low, ≤ 0.06 chosen for this method, or a maximum of 6 iterations is reached, with convergence typically achieved in 3 iterations.

4.3.5 Performance Tests with Monte Carlo Data

In order to test the performance of the track reconstruction routines the XTC software package was executed using Monte Carlo event files as input, as described in section 4.3.1. Performance of the reconstruction of the main track parameters, momentum p, transverse momentum transfer t, track azimuthal angle ϕ_t, polar angle θ_t and the Z vertex coordinate, is shown here. Performance is quantified by measuring the resolution of the reconstructed variable, where the resolution σ_x of a track parameter x is given by the standard deviation of a Gaussian fit to the distribution of $x_{\mathrm{rec}} - x_{\mathrm{MC}}$, where x_{rec} is the reconstructed value taken from XTC output track tables and x_{MC} is the expected value taken from the Monte Carlo track tables. σ_x is expressed in the units of x.

Momentum Resolution

The momentum resolution σ_p is expected to have some dependence on the expected momentum, hence the resolution is defined as the standard deviation of a Gaussian fit to the distribution of $\frac{p_{\mathrm{rec}}-p_{\mathrm{MC}}}{p_{\mathrm{MC}}}$. In this case σ_p gives a fractional value for the resolution.

Figure 4.9 (4.10) shows the resolution σ_p for 9 momentum bins in the acceptance region of the Recoil Detector for protons (pions), with a Gaussian fit made to each bin distribution shown in blue (red). The mean of the fit for each momentum distribution for both protons and pions is shown in figure 4.11. Lower momentum protons lose a larger fraction of their momentum in progressive interactions with the detector layers than higher momentum protons. This leads to an increase in the bending radius of the particle path through the magnetic field for lower momentum protons. Reconstructed momentum is inversely proportional to the bending radius, therefore the reconstructed momentum from this path with increased bending radius is therefore lower than the generated momentum, which assumes an unaltered particle path with no losses from particle scattering in the detector layers. This effect leads to a negative shift in the mean of the $\frac{p_{\mathrm{rec}}-p_{\mathrm{MC}}}{p_{\mathrm{MC}}}$ distribution for lower momentum bins.

The change in bending radius for pions is much less pronounced due to the lower

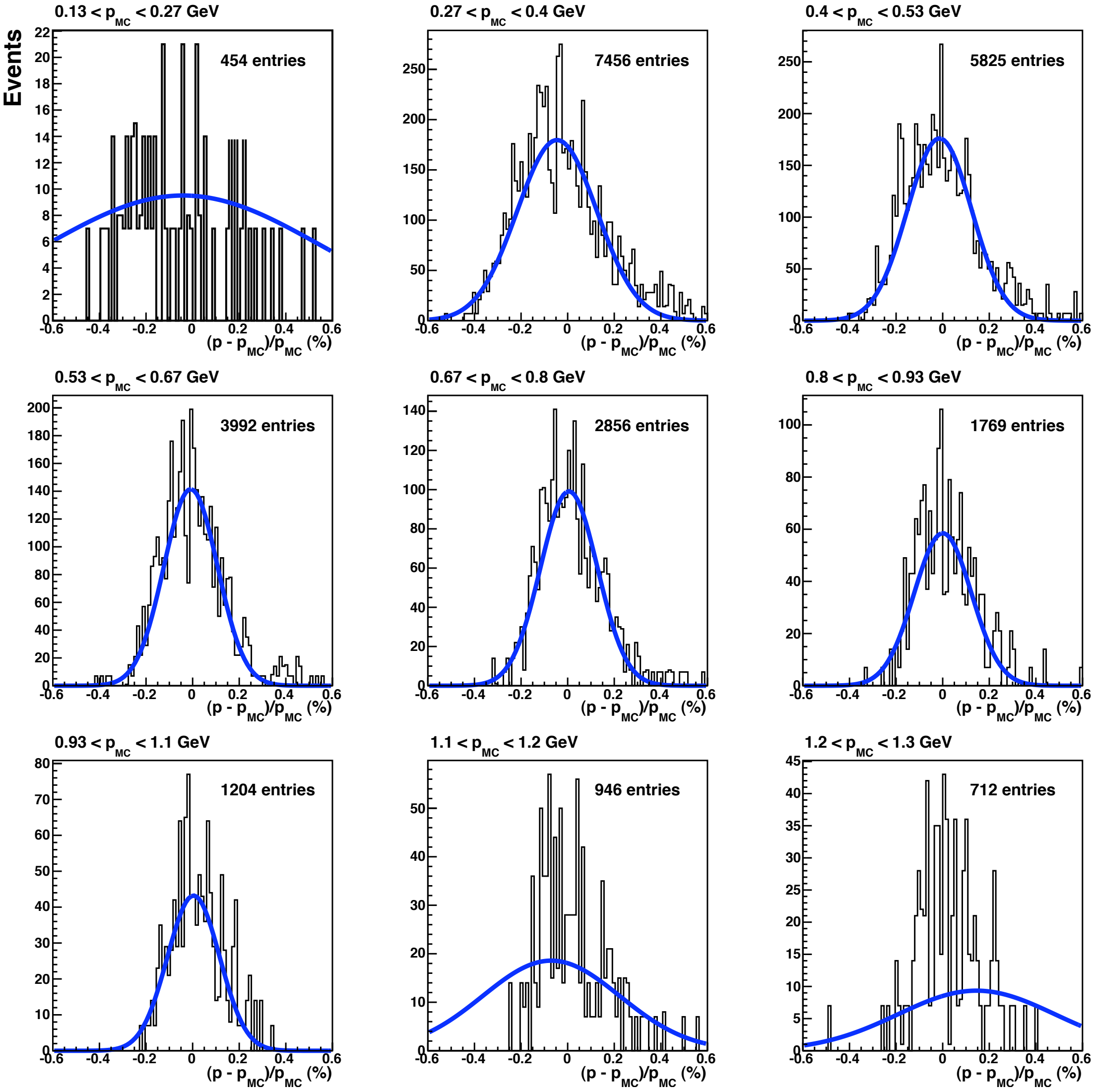

Figure 4.9: Momentum resolution for proton tracks in 9 momentum bins in the acceptance of the Recoil Detector. A systematic shift in the mean of the fit to negative values for low momentum bins is observed due to energy losses in the detector layers.

mass of these particles leading to lower energy loss in collisions. These effects can be accounted for by a function to correct the momentum value for protons at lower momentum, however this requires PID as figure 4.11 shows that the shift depends on the incident particle. PID is not available at this time as the detector is currently in commissioning.

The standard deviation σ of the Gaussian fit and its uncertainty for each momentum bin is plotted against the mean MC momentum of that bin for both protons and

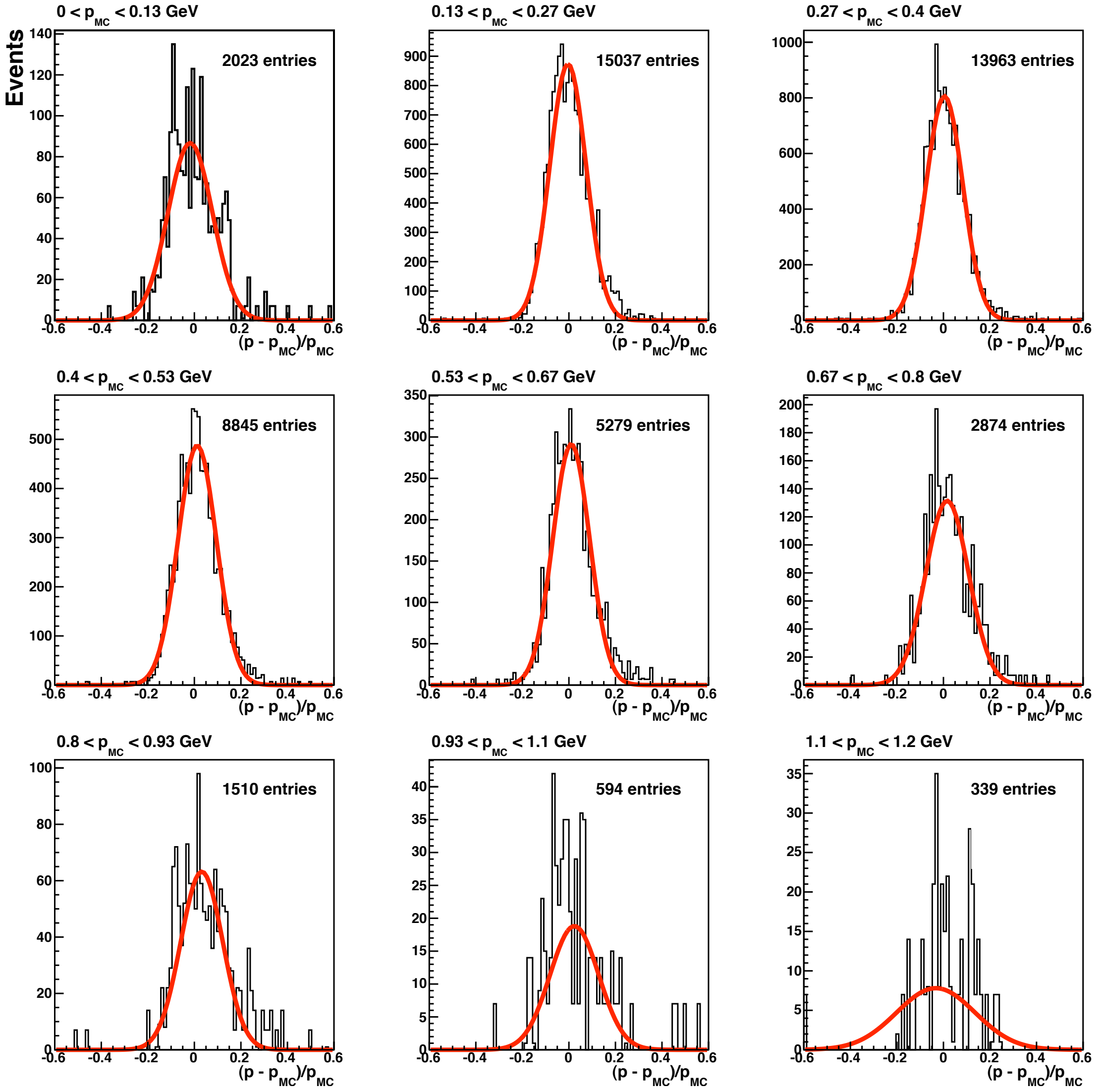

Figure 4.10: Momentum resolution for pion tracks in 9 momentum bins. Systematic shifts in the mean due to energy losses are less pronounced due to the lower mass of pions.

pions in figure 4.12. Also shown are resolution values for protons and pions taken from the Technical Design Report (TDR) [Col02]. These values were estimated with an early Monte Carlo simulation of the Recoil Detector using a homogeneous magnetic field and a simple circle fit to particle tracks, with the fitted momentum directly proportional to the radius of the fitted circle.

The results from the inhomogeneous fit are an improvement over the TDR values, with improvements of between 1 % and 2 % shown over most momentum bins for both protons and pions. In the momentum range below 0.6 GeV/c the reconstruc-

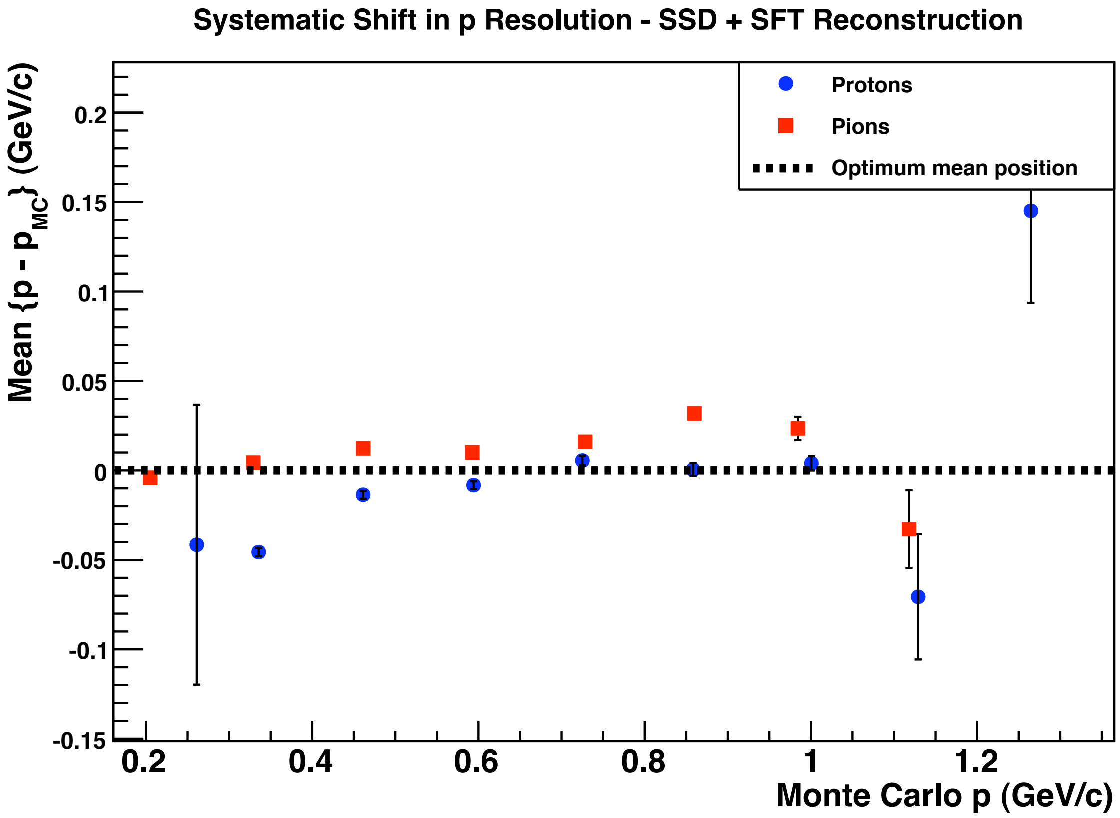

Figure 4.11: Systematic shift in momentum resolution for proton (blue) and pion (red) tracks as a function of the mean momentum of each bin. Low momentum protons are systematically shifted due to energy losses, with the shifts different for protons and pions. Error bars are statistical errors in the fit mean calculation.

tion from dE/dx using the SSD is expected to provide optimum proton momentum resolution, while above 0.6 GeV/c figure 4.12 shows a ∼ 1 % improvement over the TDR values, where the long track reconstruction method is expected to provide optimum proton reconstruction. The pion reconstruction is less critical for DVCS event analysis, however more accurate reconstruction of pions allows for improved PID separation.

Total Energy Deposition Versus Momentum

The momentum reconstructed by the SSD + SFT method is plotted against the energy deposited in the SSD and SFT detectors in figure 4.13. The particle type for each track is known for MC data. Negative pions can be identified from the negative

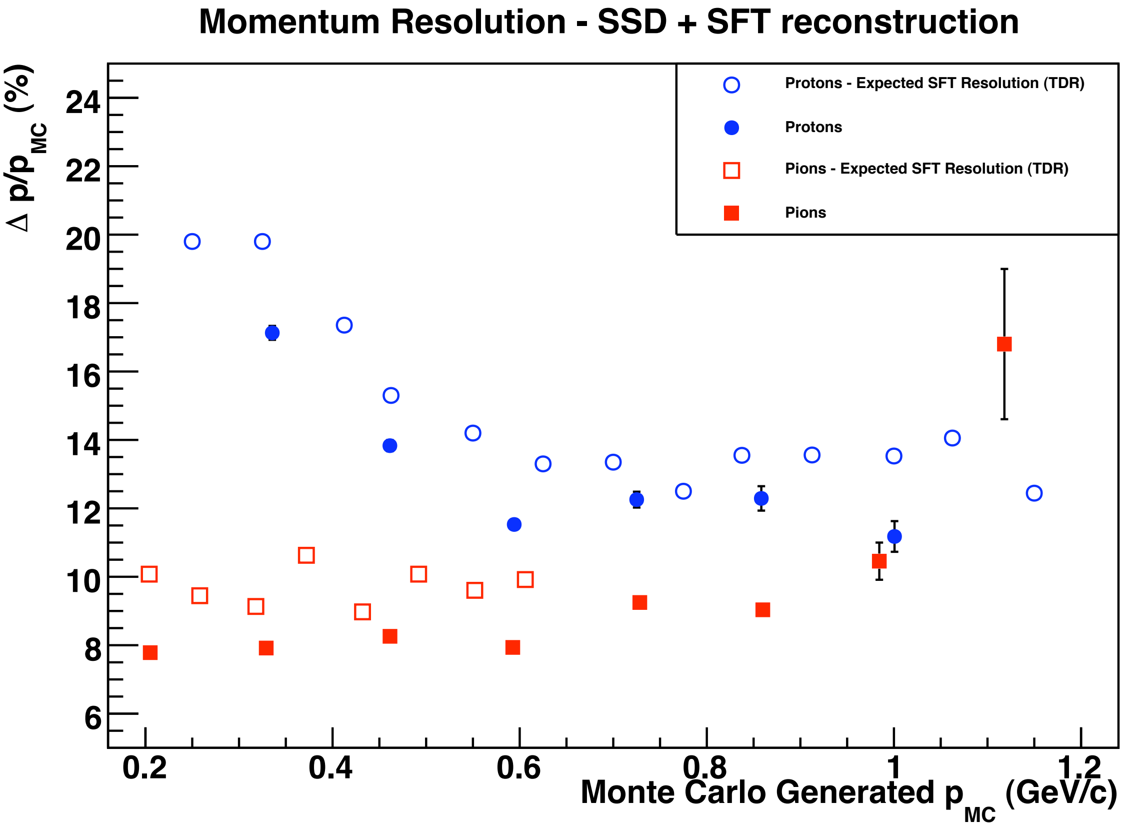

Figure 4.12: Momentum resolution for proton (solid blue) and pion (solid red) tracks as a function of the mean momentum of each bin. Also shown are values for proton (open blue) and pion (open red) tracks in the SFT taken from the Technical Design Report (open circles) [Col02].

curvature of the particle track and are assigned negative momentum values, plotted in black. Two bands can be seen for positive momentum values. A mirror image of the negatively charged pion band can be seen around the $p = 0$ axis, identified as positively charged pions and plotted in blue. Protons deposit more energy for a given momentum due to their larger mass. A second band, shown in red, demonstrates this property and is thus identified as arising from protons. Seperation of protons and pions is best defined at low momentum values. This property can be used to reduce background events in DVCS data analysis and hence ensure exclusivity, one of the primary goals of the Recoil Detector.

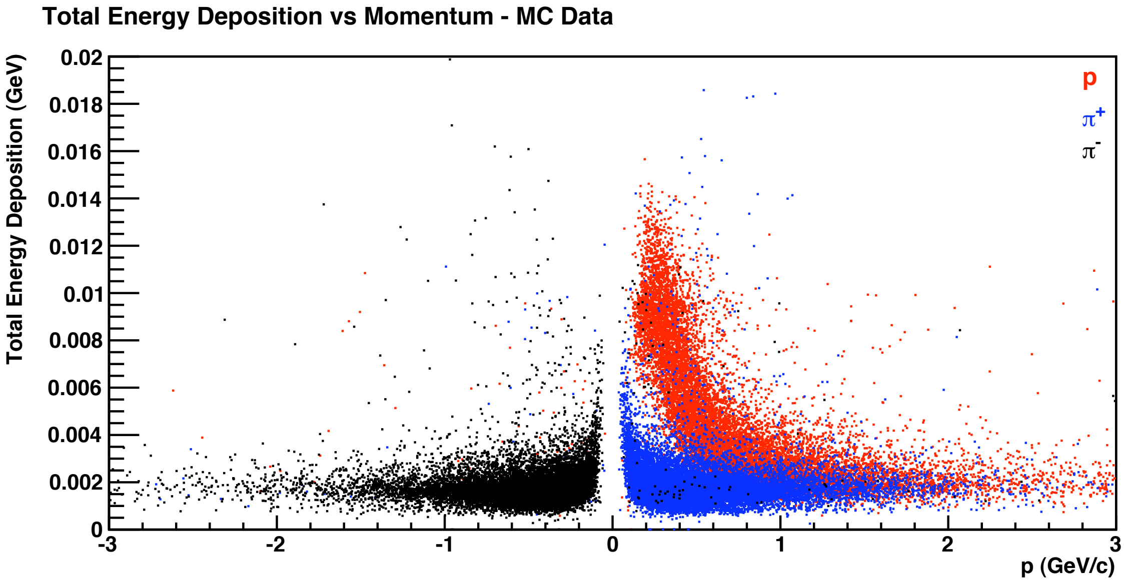

Figure 4.13: Total energy deposited in SSD and SFT detectors versus the reconstructed momentum from MC data. The incident particle is known, allowing the separation of protons (blue), π^+ (blue) and π^- (black). The separation of the bands at low positive momentum values allows particle identification of protons and positively charged pions.

t Resolution

The second primary goal of the Recoil Detector is the improvement of the t reconstruction and resolution of the HERMES experiment, particularly at low t, where t is the momentum transfer to the nucleon. Ji's Sum Rule, defined in equation (2.25), is valid at low t and thus improvements to measurements in this kinematic range are sought for future HERMES DVCS analyses. Analyses of data taken prior to the installation of the Recoil Detector require t to be reconstructed from measurements of the produced photon and scattered electron/positron, see section 5.1.1. The calorimeter does not provide accurate measurements of this photon, leading to sub-optimum t resolution of the experiment, between 15 % and 20 %.

In a similar manner to momentum resolutions shown previously, a Gaussian fit is made to the difference between the generated MC t and the reconstructed t in equidistant t bins. The standard deviation σ of this fit is the resolution in t and shown in figure 4.14. Also shown are the expected Recoil Detector t resolution from the TDR and the forward spectrometer resolution in t [Col02].

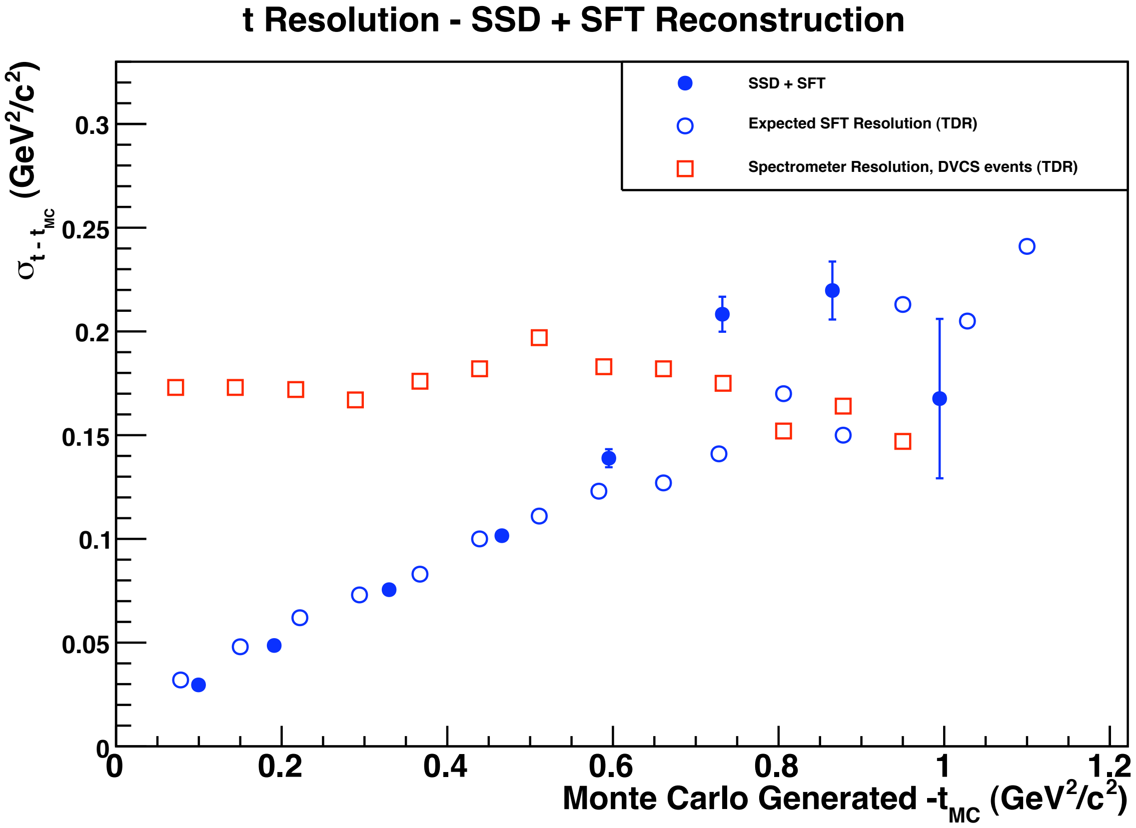

Figure 4.14: t resolution for proton tracks as a function of the mean t of each bin. The SSD + SFT reconstruction (filled circles) is comparable to the expected performance of the detector (open circles, [Col02]) and shows a large improvement over the forward spectrometer resolution (open squares, [Col02]), particularly at low t.

At low t the SSD + SFT reconstruction method resolution matches the expected resolution from the TDR, and shows a large improvement of between 4 % and 14 % over the forward spectrometer resolution, fulfilling the second important goal of the detector.

Track ϕ_t Resolution

The angle of the production plane of the produced photon and the scattered nucleon, ϕ, in the DVCS process is illustrated in figure 2.3. A measurement of the azimuthal angle of the scattered nucleon can therefore be used to reject background events if the detected particle does not lie in the production plane defined by the produced photon.

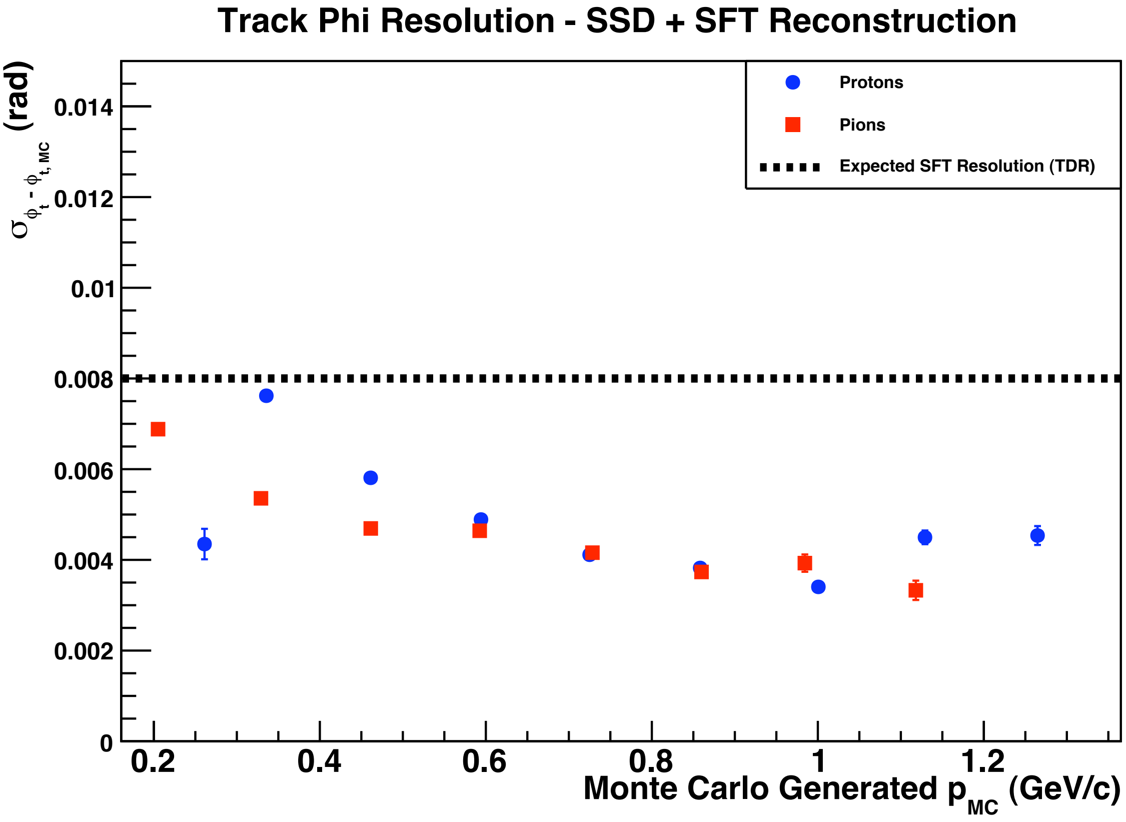

Figure 4.15: ϕ_t resolution for proton and pion tracks as a function of the mean momentum of each bin. The expected resolution of the SFT is also shown [Col02]. The reconstruction performs better than expected for most bins, with the optimal momentum range of the reconstruction being > 0.3 GeV/c.

As for the momentum resolutions presented previously, the resolution in ϕ_t, $\sigma_{\phi_t - \phi_{t,MC}}$, and its uncertainty for 9 equidistant momentum bins is plotted against the mean MC momentum of each bin for both protons and pions in figure 4.15. Above 0.3 GeV/c, the optimum proton momentum range for the SSD + SFT reconstruction, the resolution in ϕ_t for both protons and pions is between 4 mrad and 6 mrad, with no significant momentum dependence observed.

The SSD is close to the primary interaction vertex and has an expected resolution in ϕ_t of 30 mrad [Kra05]. The SFT is further from the beam line and provides the best measure of the track curvature in the magnetic field. The SSD + SFT reconstruction is therefore heavily influenced by the resolutions of the SFT. The SFT provides 2π acceptance in ϕ_t with an expected resolution of 8 mrad [Col02].

Figure 4.15 clearly illustrates that the SSD + SFT reconstruction provides better than expected resolution in ϕ_t over the full momentum range.

Track θ_t Resolution

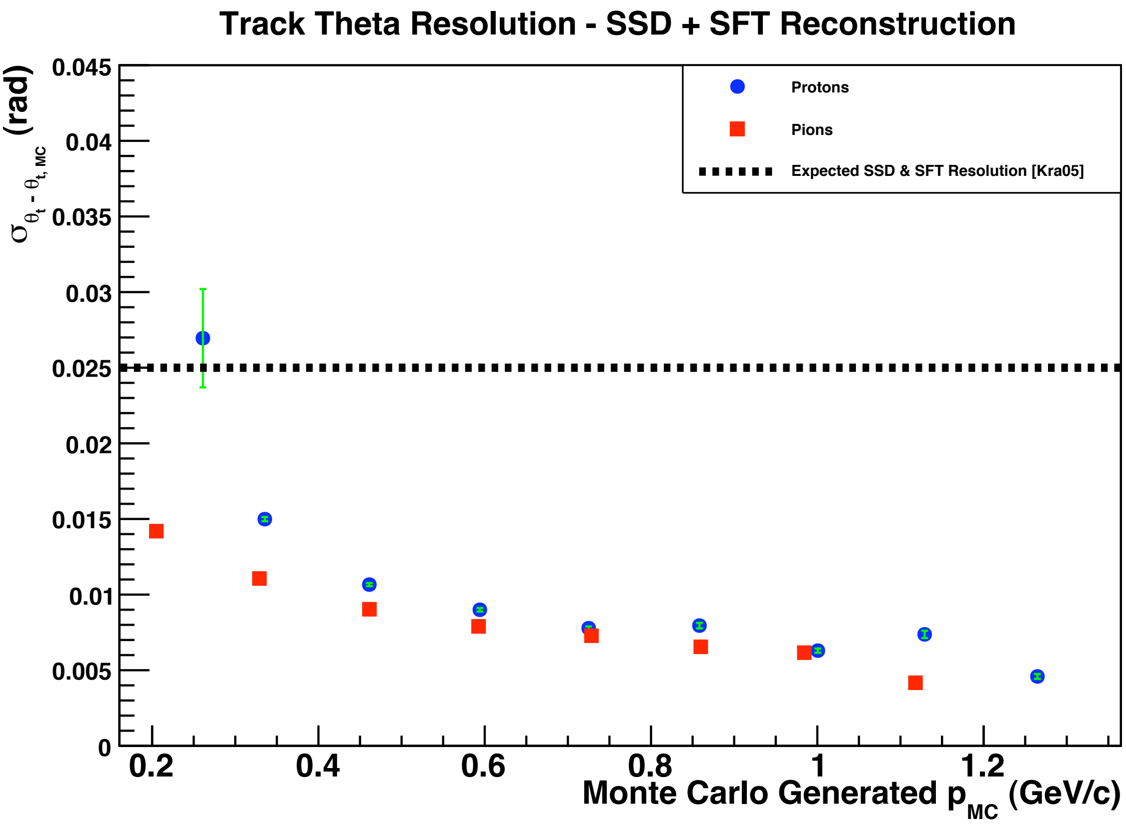

Figure 4.16: θ_t resolution for proton and pion tracks as a function of the mean momentum of each bin. The expected resolution of the SSD and SFT is also shown [Kra05]. The reconstruction performs better than expected for most bins, with the optimal momentum range of the reconstruction being $> 0.3\,\text{GeV/c}$.

In a similar manner to the previously shown resolutions, the resolution in θ_t, $\sigma_{\theta_t - \theta_{t,MC}}$, and its uncertainty for 9 equidistant momentum bins is plotted against the mean MC momentum of each bin for both protons and pions in figure 4.16. Above 0.3 GeV/c, the optimum momentum range for the SSD + SFT reconstruction, the resolution in θ_t for both protons and pions is approximately 7 mrad, with no significant momentum dependence observed. Both the SSD and SFT have an expected resolution of 25 mrad [Kra05], an upper estimate based on early simulations of the detector, thus the reconstruction method performs better than anticipated.

Interaction Vertex Z Coordinate Resolution

The forward spectrometer provides resolution in the interaction vertex Z coordinate position of approximately 1.5 cm [Ye06]. Due to its position around the target cell, the Recoil Detector is expected to provide a large improvement, approximately a factor of 10, in the resolution of this track parameter.

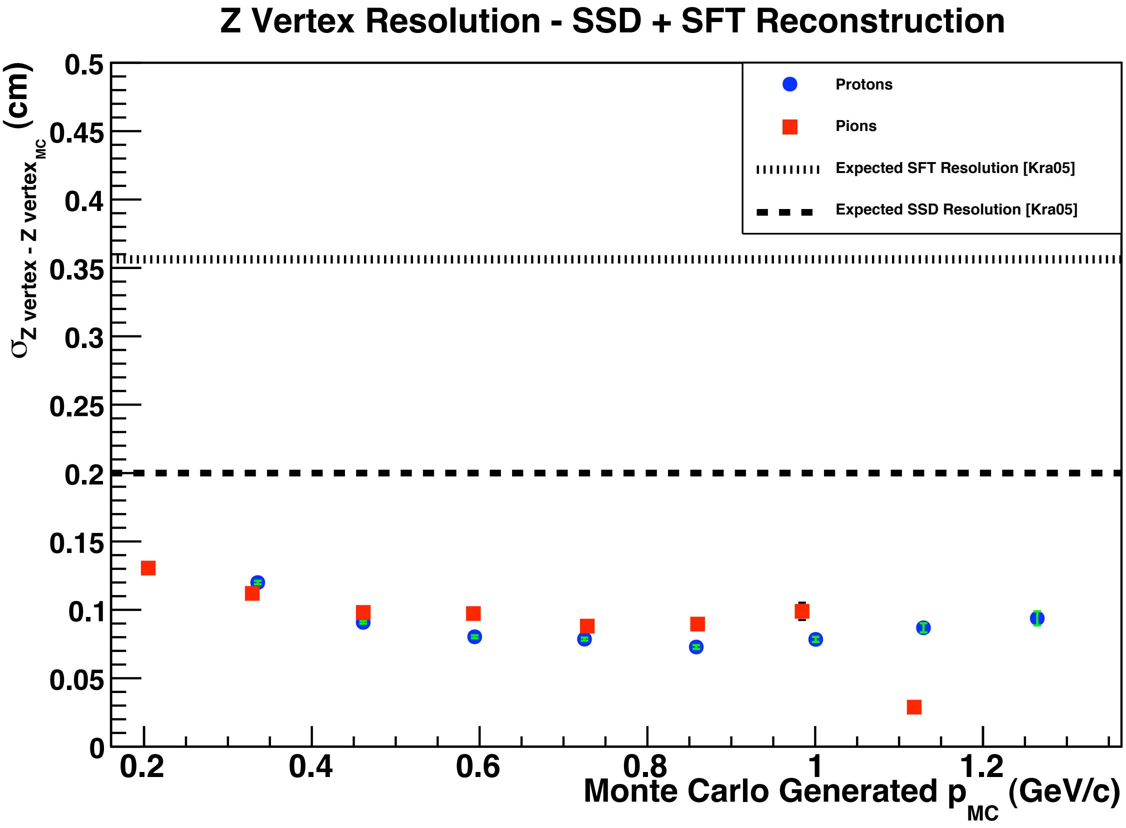

Figure 4.17: Z Vertex Coordinate resolution for proton and pion tracks as a function of the mean momentum of each bin. The expected resolution of the SSD and SFT is also shown [Kra05]. The reconstruction performs better than expected for most bins, with the optimal momentum range of the reconstruction being > 0.3 GeV/c.

In a similar manner to the previously shown resolutions, the resolution in the interaction vertex Z cordinate, $\sigma_{\mathrm{Z\ Vertex-Z\ Vertex}_{MC}}$, and its uncertainty for 9 equidistant momentum bins is plotted against the mean MC momentum of each bin for both protons and pions in figure 4.17. Above 0.3 GeV/c, the optimum momentum range for the SSD + SFT reconstruction, the resolution in Z for both protons and pions is approximately 1 mm with no significant momentum dependence observed. The SSD provides the most accurate Z position resolution, 2 mm [Kra05], with the SSD + SFT reconstruction performing better than expected.

4.3.6 Results with Experimental Data

Reconstructed Momentum Distribution

Figure 4.18 shows the expected momentum distribution from Monte Carlo simulations of the Recoil Detector with a reconstructed momentum distribution from experimental data, taken in 2006. The distributions are close to identical, allowing for noise in the experimental data sample.

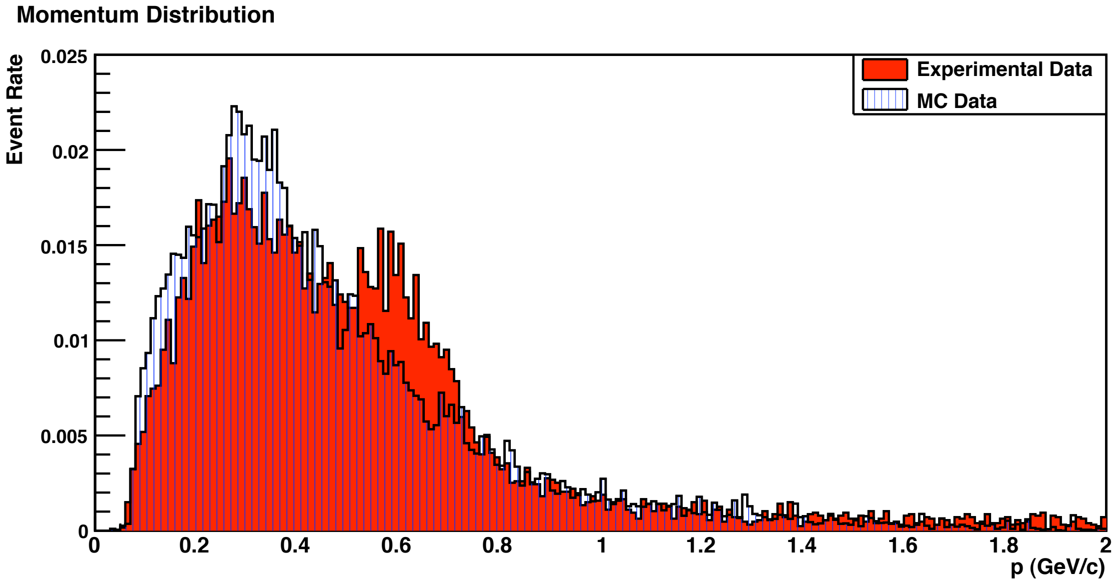

Figure 4.18: Expected momentum distribution from Monte Carlo simulation and reconstructed momentum distribution for experimental data, normalised to the total number of events. The distributions are similar when accounting for noise in the experimental data sample.

Track ϕ_t Distribution

Figure 4.19 shows the expected ϕ_t distribution from MC simulations with a reconstructed ϕ_t distribution from experimental data, taken in 2006. Both distributions share the same 4 peak structure, arising from the acceptance of the SSD. The MC sample has approximately uniform peaks in each quadrant of the acceptance, while the experimental data peaks vary in magnitude. A hardware fault in a SSD sensor in the region $0 \leq \phi_t \leq \frac{\pi}{2}$ radians leads to a loss of experimental data in that quadrant. The MC data does not simulate this fault, leading to a difference in the distributions in this region.

Peaks in the experimental data distribution are observed around $\phi_t \approx \frac{\pi}{2}$ radians and around $\phi_t \approx \frac{3\pi}{2}$ radians, corresponding to the vertical plane of the detector. These peaks arise from scattering on the collimators installed in the region in front of the Recoil Detector, leading to increased noise in this plane.

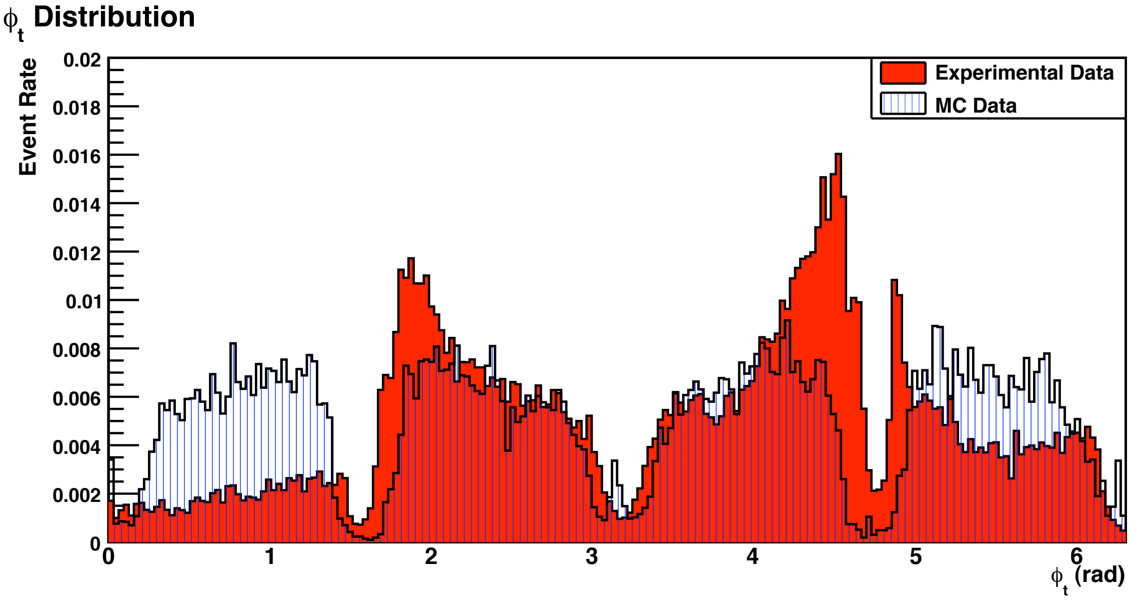

Figure 4.19: Expected ϕ_t distribution from Monte Carlo simulation (left) and reconstructed ϕ_t distribution for experimental data (right), normalised to the total number of events. A fault in the SSD sensor in the region $0 \leq \phi_t \leq \frac{\pi}{2}$ radians leads to a loss of data in that region. Peaks in the experimental data around $\phi_t \approx \frac{\pi}{2}$ radians and around $\phi_t \approx \frac{3\pi}{2}$ radians arise from collimator scattering, leading to increased noise.

Track θ_t Distribution

Figure 4.20 shows the expected θ_t distribution from MC simulations with a reconstructed θ_t distribution from experimental data, taken in 2006. The MC data sample shows that a peak in the distribution is expected around $\theta_t \approx \frac{\pi}{2}$ radians. This peak is not replicated in the experimental data, the cause of this discrepancy is currently under investigation by the collaboration during the commissioning phase of the detector.

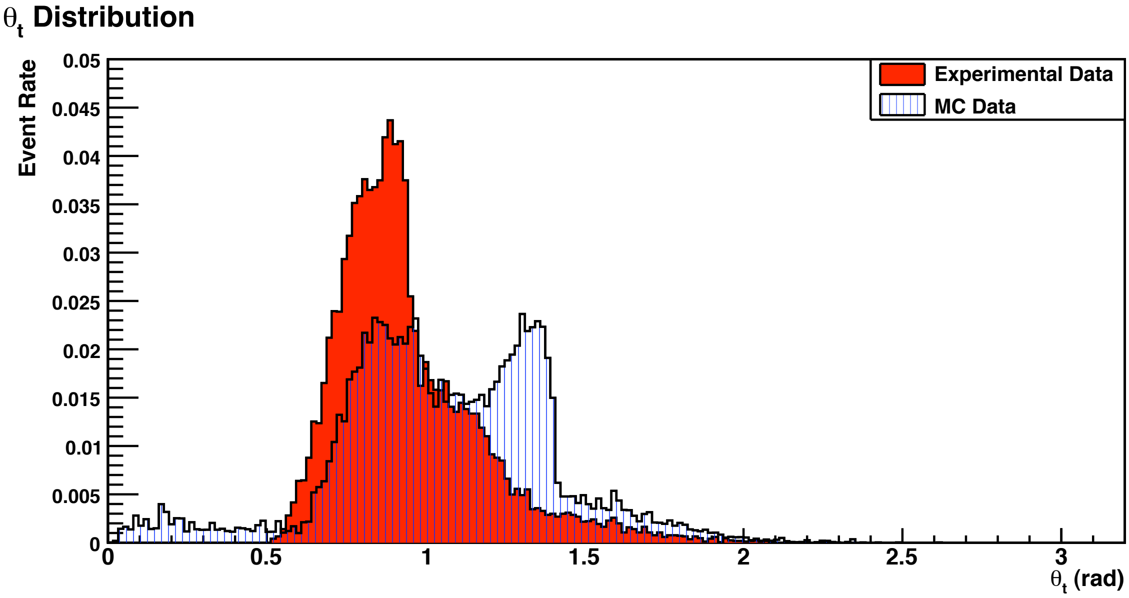

Figure 4.20: Expected θ_t distribution from Monte Carlo simulation and reconstructed θ_t distribution for experimental data, normalised to the total number of events. A peak is observed in the Monte Carlo distribution around $\theta_t \approx \frac{\pi}{2}$ radians, not replicated in the experimental data distribution.

Track Z Vertex Position Distribution

Figure 4.21 shows the expected Z vertex position distribution from MC simulations with a reconstructed Z vertex position distribution from experimental data, taken in 2006. All simulated tracks in the MC data sample arise from scattering in the target cell region, $5 \leq Z_{\mathrm{Vertex}} \leq 20\,\mathrm{cm}$, due to conditions selected in the event generator. No noise tracks are simulated as originating from outside the target cell. In order to remove tracks reconstructed from outside the target cell, such as noise arising from Møller or Bhabba scattering events, a cut is placed on the experimental data distribution at 5 cm and 20 cm.

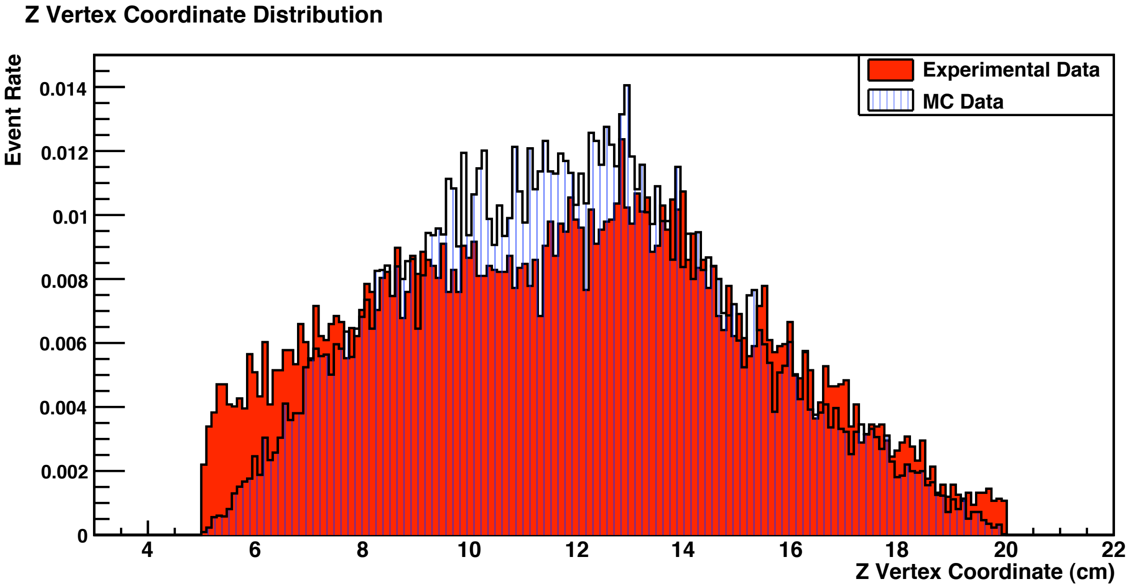

Figure 4.21: Expected Z vertex position distribution from Monte Carlo simulation and reconstructed Z vertex position distribution for experimental data, normalised to the total number of events. Both distributions peak at $Z_{\text{Vertex}} \approx 12.5$ cm, the centre of the target cell.

Both MC and experimental data distributions display a peak at $Z_{\text{Vertex}} \approx 12.5$ cm, the centre of the target cell. The target gas is injected at the centre of the cell and dissipates to either end, therefore the majority of interactions should take place at the centre of the cell. Both MC and experimental results demonstrate this feature.

Figure 4.22 compares the reconstructed vertex position in Z from the Recoil Detector and the forward spectrometer. The Recoil Detector reconstruction has superior resolution, allowing for a narrower distribution in the Recoil Detector data, in the region from 12.5 cm to 20 cm, than from the spectrometer. This corresponds to the second half of the cell. Background from collimator scattering in the Recoil Detector distorts the distribution from 5 cm to 12.5 cm, the first half of the cell.

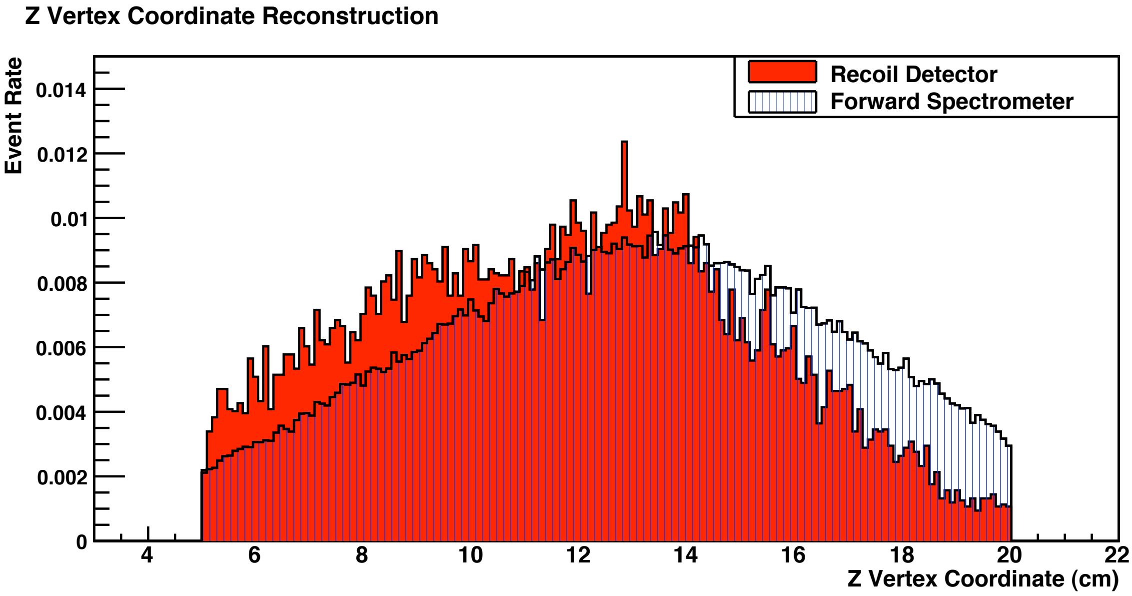

Figure 4.22: Comparison of reconstructed Z Vertex position from the Recoil Detector and from the forward spectrometer, both from experimental data, normalised to the total number of events. The Recoil Detector reconstruction has superior resolution, allowing for a narrower distribution from 12.5 cm to 20 cm, the second half of the cell. Background from collimator scattering distorts the distribution from 5 cm to 12.5 cm, the first half of the cell.

Total Energy Deposition Versus Momentum

Figure 4.13 shows the expected distribution of energy deposited in the SSD and SFT plotted against the reconstructed momentum from the SSD + SFT reconstruction for MC data. The energy values are obtained by summing the individual energy measurements for each space point belonging to the track. These measurements are calibrated from test experiments of the SSD and SFT using Minimum Ionising Particles (MIPs), see e.g. [Mur07, Hoe06] for further details.

Bands can clearly be seen to arise from different particle types, thus facilitating PID separation. Figure 4.23 shows this distribution for experimental data. A similar band structure is observed in the experiment, allowing protons and positively charged pions to be separated in the event sample. This demonstrates that protons have been detected by the Recoil Detector, the major goal of the detector.

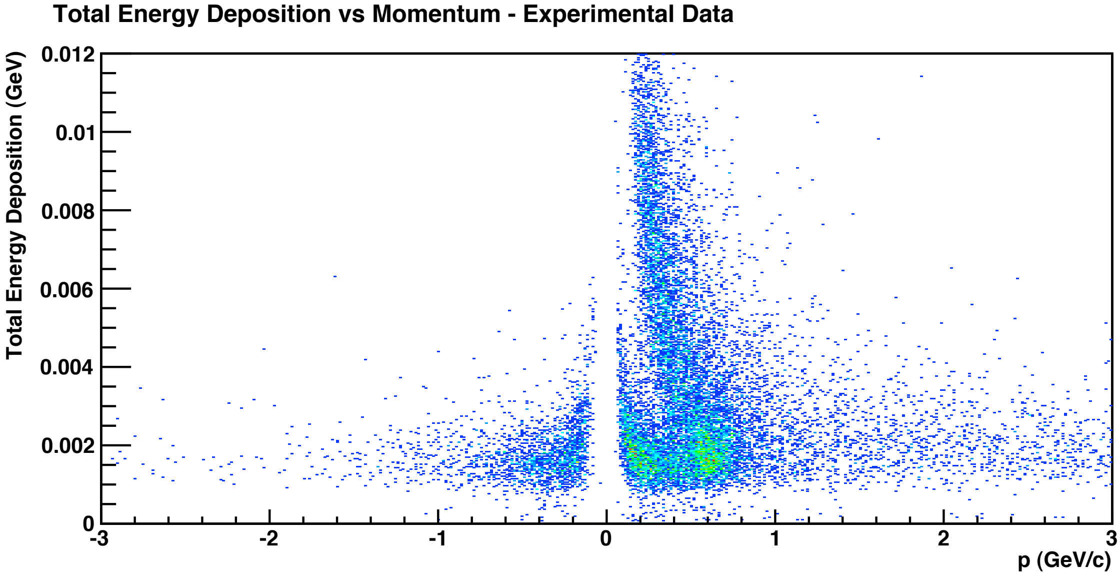

Figure 4.23: Total energy deposited in SSD and SFT detectors versus the reconstructed momentum from experimental data. As shown in figure 4.13, the separation of the bands at low momentum values allows PID separation of protons and positive charge pions. The same band structure can be seen in experimental data.

Visualisation with the Event Display

The author was involved in the development of an event display for the Recoil Detector, allowing the visualisation of experimental data taken with the detector. The author provided the underlying track reconstruction routines for the visualisation and the geometrical model to be used. The author participated in the development of interfaces to the track reconstruction data and of the human-computer interface. Figure 4.24 shows a reconstructed track from experimental data.

The left-hand side of the figure shows an end-on view of the detector, with crossed circles representing space points and the dashed line showing the ϕ_t angle of the track. The curvature of the particle in the magnetic field can be seen from the deviation of the space points from the straight line. The right-hand side of the figure shows a side-on view of the detector. The particle track is shown to emanate from the target cell and pass through both layers of the SSD and SFT.

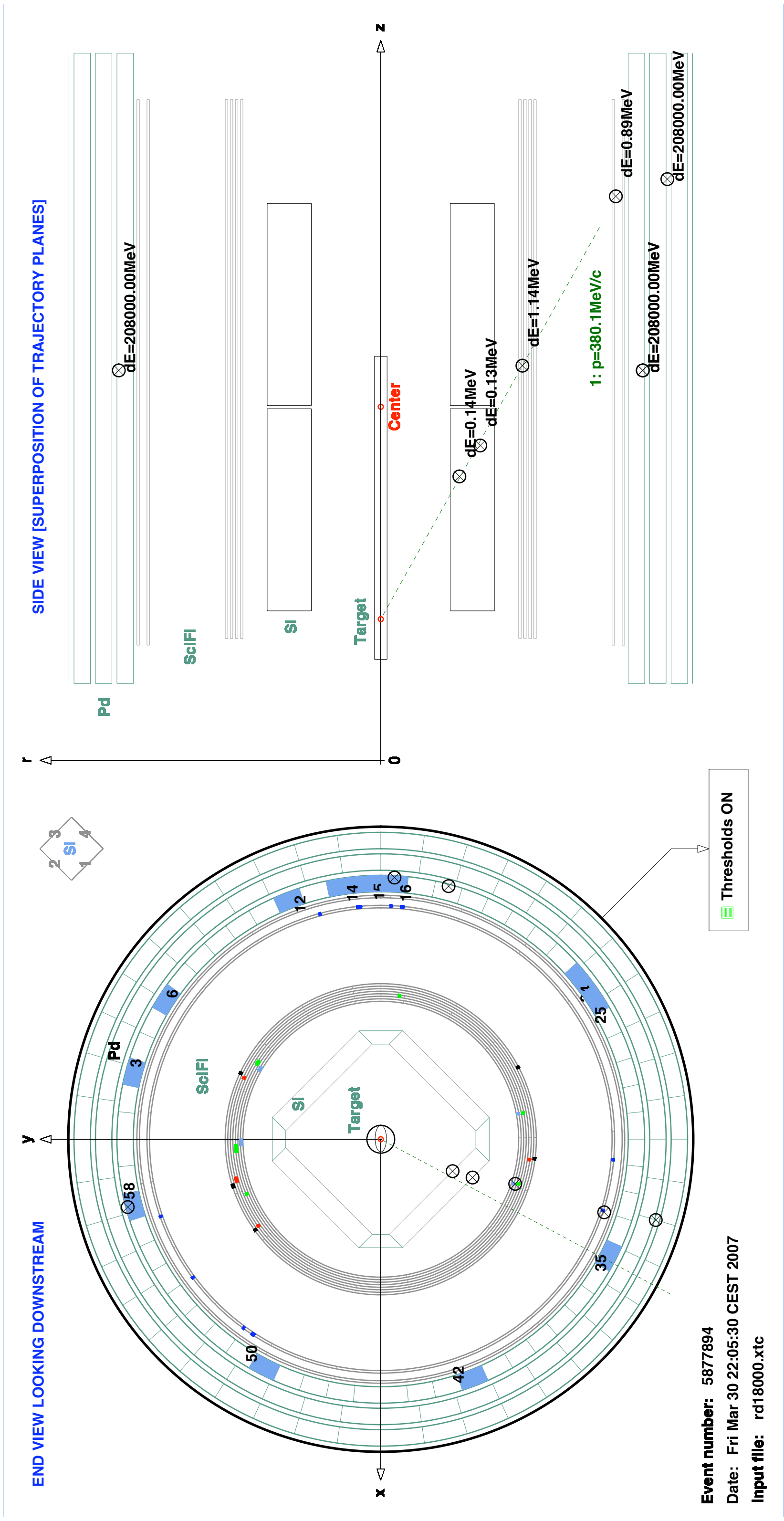

Figure 4.24: Sample Event Display image showing a reconstructed track from experimental data. The track passes through both SSD and SFT layers, with the left side showing the curvature of the track away from the straight line path, which in this case depicts the track ϕ_t angle.

Chapter 5

Hard Electroproduction of Real Photons with an Unpolarised Deuterium Target

Throughout the operational period of the HERMES experiment data were taken using a variety of targets, both polarised (in the transverse and longitudinal directions) and unpolarised. This chapter presents an analysis of all data taken with an unpolarised deuterium target and both the electron and positron beams of HERA prior to the installation of the Recoil Detector in 2006.

The aim of this analysis is to extract DVCS-related asymmetry amplitudes, as described in chapter 2. Of particular interest is the $\sin\phi$ moment of the Beam Spin Asymmetry amplitude, with a view to extracting a model dependent constraint on the total angular momentum of quarks in the neutron. This will be detailed in chapter 6.

5.1 Selecting the Event Sample

Following production by the HERMES offline software chain (as described in section 4.2), the experimental and Monte Carlo data files must be processed to find the events the analysis is concerned with and calculate kinematic properties of these events. This section will detail the selection process for these events. Some definitions of the kinematic variables are given along with some explanations of the features and limitations of the detectors in the HERMES spectrometer.

A "cut" is a condition applied to the data sample to remove unwanted events, due to various factors such as unwanted kinematics, data quality, and acceptance effects. These cuts can be applied at different levels of the HERMES data structure, as depicted in figure 5.1, at either the run, burst or event level. This will be noted for each cut detailed here.

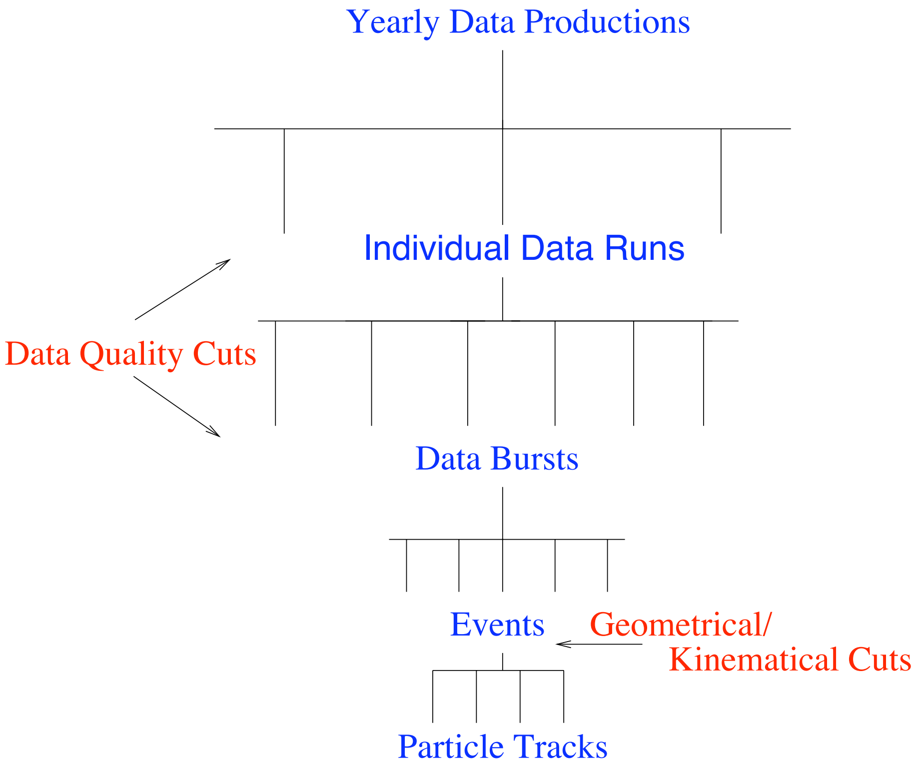

Figure 5.1: The HERMES data structure, showing the levels at which cuts are applied. Each fill is split into data runs due to file size considerations. A burst is analogous to the bunch structure of the beam, with each 10 second burst containing many events resulting from DAQ triggers. These are analysed as physics events. Taken from [Mur07].

The kinematics of a DIS event have been discussed in section 2.1.1 with the variables Q^2, x_B and t defined. Here the production of real photons is described, with the relevant kinematic variables defined along with the range of interest for these kinematics.

5.1.1 Kinematic Definitions

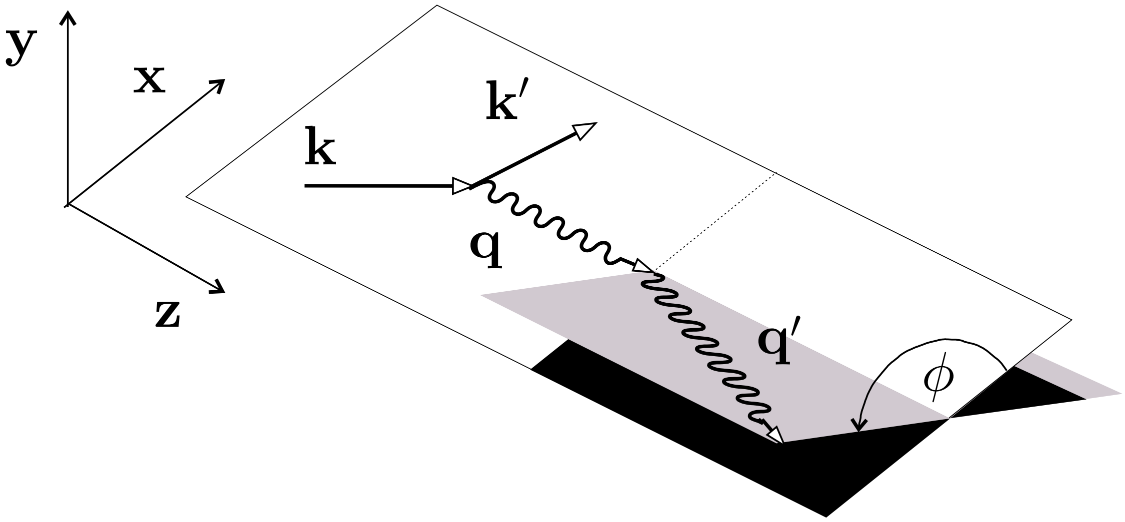

Figure 5.2: Definition of the scattering angle ϕ between the photon production plane and the lepton scattering plane. Also shown are the four-momenta of the incoming lepton $\mathbf{k}$, scattered lepton $\mathbf{k}'$, virtual photon $\mathbf{q}$ and produced photon $\mathbf{q}'$.

A DVCS event at HERMES involves a lepton scattering off a target nucleon via the exchange of a virtual photon, where lepton herein refers to the electron or positron HERA beam. A real photon is emitted and detected in the final state, along with the scattered lepton. The dominant modes of scattering for DVCS off a deuterium target at HERMES are coherent and incoherent. Coherent scattering preserves the deuteron in the final state, whilst in incoherent scattering the deuteron breaks up into a proton and neutron final state. In either case not all products from the final state are detected by the spectrometer. This analysis does not include data taken with the Recoil Detector installed, which can detect recoiling charged particles such as the deuteron or proton, as the detector is in commissioning at the time of writing. Additionally, the deuteron, proton or neutron can be excited in the final state, known as resonance scattering. Along with semi-inclusive scattering these are considered as background processes. The following definitions are used here:

- $\mathbf{P}$ is the four-momentum of the intial target particle, taken as being at rest. Fermi momentum is neglected in the quasi-elastic scattering case.

- $\mathbf{k}$ is the four-momentum of the initial electron/positron.
- $\mathbf{P}'$ is the four-momentum of the scattered target particle, not detected by the spectrometer.
- $\mathbf{k}'$ is the four-momentum of the scattered electron/positron, detected by the spectrometer.
- $\mathbf{q}'$ is the four-momentum of the produced photon, detected by the spectrometer.
- $\mathbf{q}$ is the four-momentum of the virtual photon, calculable from $\mathbf{k}'$ and $\mathbf{q}'$.

The interaction can be defined from these terms as:

$$e^{\pm}(\mathbf{k}) + D(\mathbf{P}) \rightarrow e^{\pm}(\mathbf{k}') + D'(\mathbf{P}') + \gamma(\mathbf{q}') \tag{5.1}$$

where $D'(\mathbf{P})$ can be the final state $d(\mathbf{P}')$ in the case of coherent scattering or $p(\mathbf{P}'_p)+n(\mathbf{P}'_n)$ in the case of incoherent scattering. Herein $\overset{\text{lab}}{=}$ denotes that the fixed target lab frame is used.

The scattering angle ϕ as shown in figure 5.2 is the azimuthal angle between the lepton scattering plane and the vector of the produced photon, calculated from

$$\phi = \frac{\vec{q} \times \vec{k} \cdot \vec{P}_\gamma}{|\vec{q} \times \vec{k} \cdot \vec{P}_\gamma|} \cdot \arccos\left(\frac{\vec{q} \times \vec{k}}{|\vec{q} \times \vec{k}|} \cdot \frac{\vec{q} \times \vec{P}_\gamma}{|\vec{q} \times \vec{P}_\gamma|}\right). \tag{5.2}$$

Results given later are binned in three kinematic variables. The first of these is Q^2, defined as

$$Q^2 = -\mathbf{q}^2 = -(\mathbf{k} - \mathbf{k}')^2 \overset{\text{lab}}{=} 4EE' \sin^2\left(\frac{\theta}{2}\right), \tag{5.3}$$

the negative square of the four-momentum of the exchange virtual photon, calculable from the difference in four-momentum of the initial and scattered lepton.

The energy of the virtual photon, ν, is defined as

$$\nu = \frac{\mathbf{P.q}}{M_N} \overset{\text{lab}}{=} E - E' \tag{5.4}$$

where M_N is the rest mass of the target nucleon, E is the energy of in the incoming lepton and E' that of the scattered lepton.

In the case of DIS, the kinematic variable x-Bjorken or x_B is the fraction of the four-momentum of the nucleon carried by the struck parton. In the DVCS process x_B can be interpreted as the momentum fraction lost by the nucleon [Die07a]. x_B is the second binning kinematic variable, defined as

$$x_B \equiv \frac{Q^2}{2\mathbf{P}.\mathbf{q}} \overset{\text{lab}}{=} \frac{Q^2}{2M_N\nu}. \tag{5.5}$$

The four-momentum transfer to the nucleon is denoted Δ, with the Mandelstam variable t being the square:

$$\Delta = \mathbf{P} - \mathbf{P}' \tag{5.6}$$

$$t = \Delta^2 \tag{5.7}$$

and t can be calculated from either the nucleon or the photon in the interaction:

$$t = (\mathbf{P} - \mathbf{P}')^2 = (\mathbf{q} - \mathbf{q}')^2 \overset{\text{lab}}{=} -Q^2 - 2E_\gamma(\nu - \sqrt{\nu^2 + Q^2}\cos\theta_{\gamma\gamma^*}) \tag{5.8}$$

where E_γ is the energy of the produced photon and $\theta_{\gamma\gamma^*}$ is the polar angle between the virtual and produced photons, given by

$$\theta_{\gamma\gamma^*} = \arccos\frac{\vec{q}\cdot\vec{q'}}{|\vec{q}||\vec{q'}|}. \tag{5.9}$$

This analysis considers data taken without the Recoil Detector, hence the scattered nucleon is not detected and t is calculated using the photon.

The missing mass of the interaction is defined as

$$M_X^2 = M_N^2 + 2M_N(\nu - E_\gamma) + t. \tag{5.10}$$

Assuming an exclusive event sample gives $M_X \equiv M_N$, thus equation (5.10) can be rearranged to provide a new method to calculate the energy of the produced photon,

$$E_\gamma = \frac{t}{2M_N} + \nu. \tag{5.11}$$

This can be substituted into equation (5.8) to calculate t without the need for energy measurements of the produced photon, known as "constrained t" or t_c:

$$t_c = \frac{-Q^2 - 2\nu(\nu - \sqrt{\nu^2 + Q^2}\cos\theta_{\gamma\gamma^*})}{1 + \frac{1}{M_N}(\nu - \sqrt{\nu^2 + Q^2}\cos\theta_{\gamma\gamma^*})}. \tag{5.12}$$

At HERMES the only measurement of the photon momentum is provided by the calorimeter, with a resolution of approximately 5%, an order of magnitude higher than the charged particle momentum reconstruction. The position of the produced photon, and hence the angle $\theta_{\gamma\gamma^*}$, can be measured more accurately by the calorimeter than the energy of the photon. Thus by using t_c as the third binning variable rather than t a source of systematic uncertainty can be avoided. Further discussion of the effects of using t_c rather than t can be found in [Ell04] and [Ye06].

A final definition is necessary for cuts applied to produce the DIS event sample. The DIS process is described in section 2.1.1, with DVCS/BH events a subset of the DIS event sample. W^2 is the squared invariant mass of the proton-virtual photon system, defined as

$$W^2 = (\mathbf{P} + \mathbf{q})^2 \overset{\text{lab}}{=} M_N^2 + 2M_N\nu - Q^2. \tag{5.13}$$

Target Nucleon Mass

The variables x_B, W^2, t_c and M_X^2 above all depend on the mass of the target nucleon, M_N, as used above in calculations in the lab frame. For coherent scattering this mass should be the mass of the deuteron, $\sim 1.876\,GeV/c^2$, while for incoherent scattering the proton mass, $\sim 0.938\,GeV/c^2$, or neutron mass, $\sim 0.940\,GeV/c^2$, should be used. However, at the event selection level the exclusive peak contains a mixture of coherent and incoherent scattering. This makes it difficult to establish which mass to include in calculations which must be used in the event selection process. Furthermore, using different target nucleon masses would require that event selection cuts on these variables are adjusted for each target case.

Studies [Haa05, YM08] have shown that using the proton mass as opposed to the nucleon mass for the target being analysed does not significantly change the DVCS candidate data sample, and hence the extracted asymmetries are unchanged in comparison with the statistical and systematic uncertainties. Therefore for consistency with other DVCS analyses at HERMES the proton mass is used in all calculations and cuts are based on the proton mass values.

5.1.2 Event Selection Cuts

Detailed here are cuts applied to the data sample to produce a sample of DIS events, with further cuts used to provide a DVCS candidate event sample also described.

Data Quality Cuts

The HERMES spectrometer was operational for 11 years, with many studies made over that time to establish criteria to reject invalid data. Bad bursts may arise from poor beam conditions, rise time from detectors or other such factors. The data quality group at HERMES provides a 32 bit pattern for each burst to allow analysers to reject unwanted bursts based on criteria of their choosing.

The analysis detailed here used the burst pattern `0x501e13dc` (2005) or `0x503e13dc` (all other analysed years) which correspond to the following conditions, with bit numbering from 0 to 31:

- Bits 2 & 30: Check that the dead time of trigger-21, the main physics event trigger, is acceptable. Trigger-21 corresponds to a sufficient energy deposition in the calorimeter and signals in the H0, H1 and H2 hodoscopes. For further details see section 3.3.3.
- Bit 3: Check the burst length, t_{burst}, is acceptable, i.e. $0 \leq t_{burst} \leq 11$ seconds.
- Bit 4: Check for acceptable beam current, i.e. $2 \leq I_{beam} \leq 50\, mA$, where the lower cut removes small count rates and the upper cut removes unphysical current values.
- Bit 6: Removes the first burst of a run, when detectors may be in their rise time period and not fully operational.
- Bits 7 & 8: Removes bad μDST records, the last burst of a fill and data with no PID information, depending on the production year being analysed.
- Bit 9: Removes data marked unanalysable in the log book. The shift leader in charge of data taking at the time can mark runs as unacceptable if the data

taking conditions are suboptimal, which may not be obvious from automated monitoring systems.

- Bit 12: Removes bursts with no logbook data quality information available
- Bits 17 → 20: Checks for hardware problems in the Calorimeter (17), Hodoscope H2 and Luminosity Monitor (18), TRD (19), and tracking planes (20), where the tracking planes include the FC, BC, DVC and VC detectors.
- Bit 21: Removes bursts with unacceptable calorimeter performance for 2000 data. The bit is not checked for 2005 data, and has no effect for all other years.
- Bit 28: Checks that the beam polarisation has been measured within 5 minutes of the data taking period in question.

All other bits are considered irrelevant to this analysis, such as target polarisation conditions since this analysis concerns unpolarised deuterium only and other such factors not needed here.

In addition to these conditions, the DVCS group has agreed on further straightforward data quality cuts to be used. These are also applied at the burst level. From this point, quantities written as `table.variable` refer to the named variable contained in the specified μDST table.

- `g1DAQ.bProdMethods & 0x00800 != 1` rejects bursts where no working beam polarimeter was available.
- `g1Beam.rPolFit != 0 && fabs(g1Beam.rPolFit)`$<$`80` rejects bursts where no beam polarisation was measured and that the value is in the range accurately measurable by the polarimeters.
- `0.8<g1DAQ.rDeadCorr21<=1.0` ensures that the DAQ is active for more than 80% of the burst for trigger-21, the main HERMES physics event trigger.
- `5<g1Beam.rLumiRate<3000` ensures that the measured luminosity rate is reasonable.

- `g1Quality.iTrdDQ==3` ensures that the TRD is operating correctly in both the top and bottom halves of the spectrometer.
- `fabs(g1Beam.rHeraElEnergy) > 27.0` ensures the beam energy is correct.
- `g1Quality.iExpTarg == 2` ensures the target gas is deuterium, used as a cross check that the correct runs are used.

If a burst passes each of these conditions it is marked as analysable and the analysis continues to the track level. There are further conditions to be met at this level due to geometrical features of the spectrometer.

Geometrical Cuts

The HERMES spectrometer has several unique geometrical features that can cause internal deflections of particle tracks, or cause uncertainties in the accuracy of the track reconstruction. Cuts are applied to minimise these effects, detailed in the following:

- $\mid x^{e^\pm}_{calo} \mid < 1750\,\texttt{mm}, 300\,\texttt{mm} \mid y^{e^\pm}_{calo} \mid < 1080\,\texttt{mm}$ ensures that the scattered lepton is detected in the fiducial volume of the calorimeter and hence its energy is correctly reconstructed.
- $\mid z^{e^\pm}_{vtx} \mid < 180\,\texttt{mm}$ ensures that the interaction originates from within the target cell.
- $\mid t^{e^\pm}_{vtx} \mid < 7.5\,\texttt{mm}$ limits the transverse vertex position of the interaction, the radial distance of closest approach of the reconstructed track to the beam line position. The cut ensures this is small enough to limit background from potential interactions with material outside of the target cell.
- $|$`smTrack.rxOff+172`$\times \tan\theta_x \mid < 310\,\texttt{mm}$`,`
  $|$`smTrack.ryOff+181`$\times \tan\theta_y \mid > 70\,\texttt{mm}$`,`
  $|$`smTrack.ryOff+383`$\times \tan\theta_y \mid < 540\,\texttt{mm}$`,`
  $|$`smTrack.rXpos+108`$\times$`smTrack.rXslope`$| \leq 1000\,\texttt{mm}$ and

$|$`smTrack.rYpos+108`$\times$`smTrack.rYslope`$|\leq$ 540 `mm` ensure that the lepton track does not get deflected by the septum magnet plates which lie in possible track trajectories in the spectrometer.

- $|\, x^{\gamma}_{calo} \,|<$ 1250 `mm, 330 mm<`$|\, y^{\gamma}_{calo} \,|<$ 1050 `mm` ensures that the calorimeter is able to correctly reconstruct the energy of the photon. This cut differs from the corresponding lepton cut given above due to the different geometry of photon and lepton clusters in the calorimeter.
- `5 mrad`$\leq \theta_{\gamma\gamma^*} \leq$`45 mrad` places limits on the polar angle between the virtual photon and real photon. The azimuthal angle ϕ is not defined in the region $\theta_{\gamma\gamma^*} \leq 0$, therefore a lower cut is used to prevent the possibility of undefined ϕ values in the event sample arising from smearing effects in the $\theta_{\gamma\gamma^*}$ reconstruction. An upper cut is necessary since, for angles $\theta_{\gamma\gamma^*} > 70\,\mathrm{mrad}$, ϕ acceptance is not complete. Monte-Carlo studies show that for $\theta_{\gamma\gamma^*} > 45\,\mathrm{mrad}$ the sample is dominated by background events. See [Ell04] for more information on this cut.

Following these geometrical considerations, cuts are applied to extract the required physics events.

DIS Cuts

The DVCS/BH events are a subset of the DIS event sample at HERMES. Many analyses from different analysis groups at HERMES have refined the DIS cuts over the years, with those currently used as follows:

- `g1Track.PID2 + g1Track.PID5 > 2` ensures the charged track is identified as a lepton by the HERMES PID system.
- The lepton track must be of the same charge as the beam.
- `smTrack.bTrigMask&(1<<20)` checks that trigger-21 fired.

- `(g1Track.iSelect & 0x0100) && (g1Track.iSelect & 0x0200)` ensures that the correct track reconstruction method is used for the scattered lepton, i.e. that the lepton was tracked by all the tracking detectors in the spectrometer.

- `smCluster.rPulsPre` > 1 `MeV` ensures the photon deposits sufficient energy in the preshower detector to produce a shower in the calorimeter, thus permitting accurate energy reconstruction.

- 5 `GeV` $<|$`smCluster.rE`$|< E_{beam}$ ensures that the energy of the photon is sufficient that the calorimeter can accurately reconstruct it, but not larger than kinematically possible.

- $W^2 > 9\,\mathrm{GeV}^2$ ensures that the Monte Carlo fragmentation model operates correctly. This model is used to estimate and subtract background.

- $Q^2 > 1\,\mathrm{GeV}^2$ selects DIS processes in the hard scattering regime where factorisation is valid. It would be preferable to have $Q^2 \gg 1\,\mathrm{GeV}^2$, but this would exclude too many events from the sample as at HERMES kinematics the data set decreases exponentially with linear increases in Q^2, as shown in figure 5.4.

- $\nu < 22\,GeV$ discards events in which the efficiency of the calorimeter energy reconstruction is questionable. This is used in conjunction with the minimum photon energy cut detailed previously, $E_\gamma > 5\,\mathrm{GeV}$.

DVCS Candidate Event Cuts

In order to provide a sample of DVCS-related candidate events from the DIS set of events, the following cuts are applied:

- A check is made that there is exactly one charged track found, the scattered lepton, and a single trackless cluster in the calorimeter, the produced photon.

- $-2.25\,GeV^2 < M_X^2 < 2.89\,GeV^2$ is the standard cut on the missing mass M_X^2 of the interaction, defined in equation (5.10). This cut is chosen such that the calculated missing mass is consistent with that of a proton (see section

5.1.1) corresponding to the exclusive peak in the distribution from a hydrogen analysis (see figure 5.3). The cut assists the removal of background from e.g. associated production, with the upper limit chosen such that the contribution from DVCS/BH events and associated production is equal, based on Monte Carlo studies [Ye06].

Investigations showed that the missing mass distributions changed for different running periods [MHM$^+$08]. This is related to the replacement of the Čerenkov detectors in 1998, which lead to changes in the acceptance of the HERMES spectrometer. The effect is also dependent on the beam charge with which the data were taken.

Fits were made to the M_X^2 distributions from each data set to find the shift in the mean of the distribution. Table 5.1 shows the adjustment made to the M_X^2 cut window as a result of this shift in the mean. As the origin of this effect is not fully understood, a systematic uncertainty is also assigned to the result to account for this effect, see section 5.4.3, at the level of $< 1\%$.

- $|t_c| < 0.7\,GeV^2$ is also used to reject background events in conjunction with the missing mass cut. Exclusive events have vanishing momentum transfer, with Monte Carlo studies [Ell04] showing background domination at larger values of $-t_c$. The cut was chosen based on these studies. A $-t_c$ distribution is shown in figure 5.4.

- $0.03 < x_B < 0.35$ and $Q^2 < 10\ GeV^2$ define a strict kinematic region for the remaining binning variables of the analysis. These cuts reject few events, as the vast majority of DVCS candidate events which pass the missing mass and t_c cuts given above are also allowed by the x_B and Q^2 cuts. See figure 5.4 for distributions of these variables.

Running Period	Mean M_X^2 (GeV^2)	Shift (GeV^2)	M_X^2 Window (GeV^2)
Run 1 e^+, 96d0 & 97d1	1.153	0.0158	[-2.02, 2.81]
Run 1 e^-, 98d0	1.000	-0.125	[-2.38, 2.77]
Run 2 e^+, 99c0 & 00d2	1.125	0.000	[-2.25, 2.89]
Run 2 e^-, 05c1	1.043	-0.082	[-2.33, 2.81]

Table 5.1: The adjustments made to the missing mass window depending on the data set being analysed. The replacement of the Čerenkov detectors in 1998 changed the acceptance of the HERMES experiment. This caused shifts in the missing mass window, dependent on the beam charge in use and compensated for as detailed here.

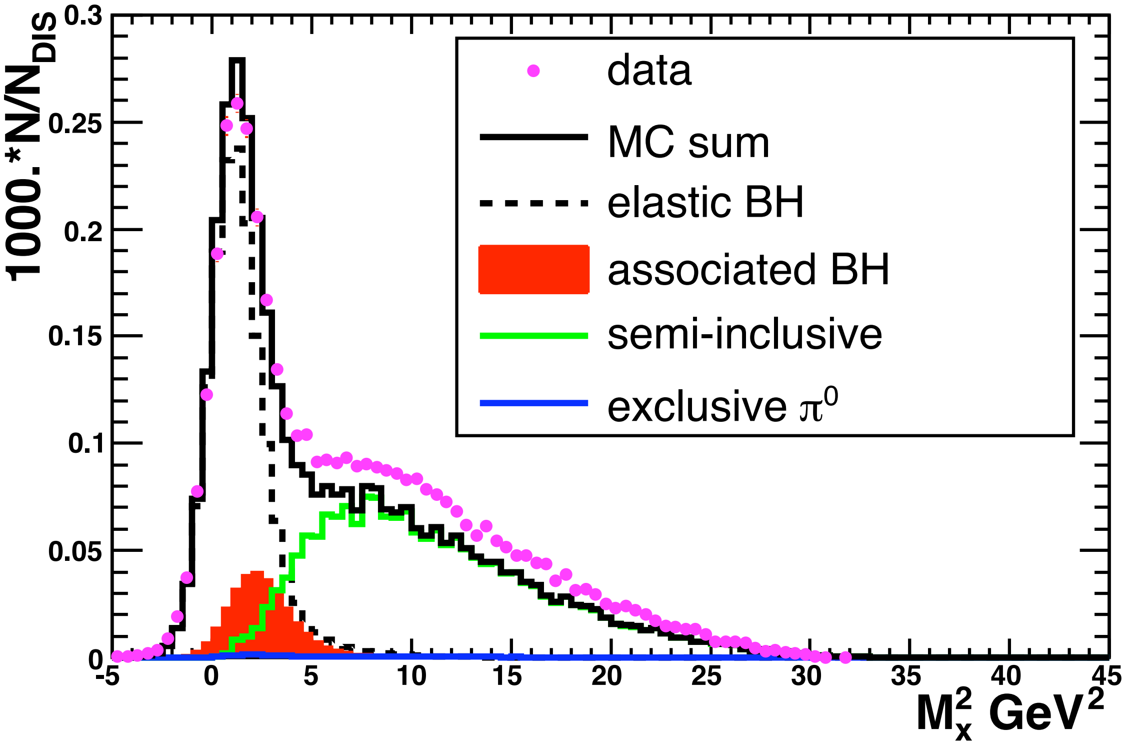

Figure 5.3: The missing mass distribution at HERMES kinematics from a Monte Carlo simulation for a Hydrogen target. The missing mass cut of $-2.25\,GeV^2 < M_X^2 < 2.89\,GeV^2$ is chosen to isolate the DVCS/BH sample. Associated production provides the main source of background, at the level of 10%. Due to smearing effects in the detector the cut must also include the negative region. Taken from [ZL08].

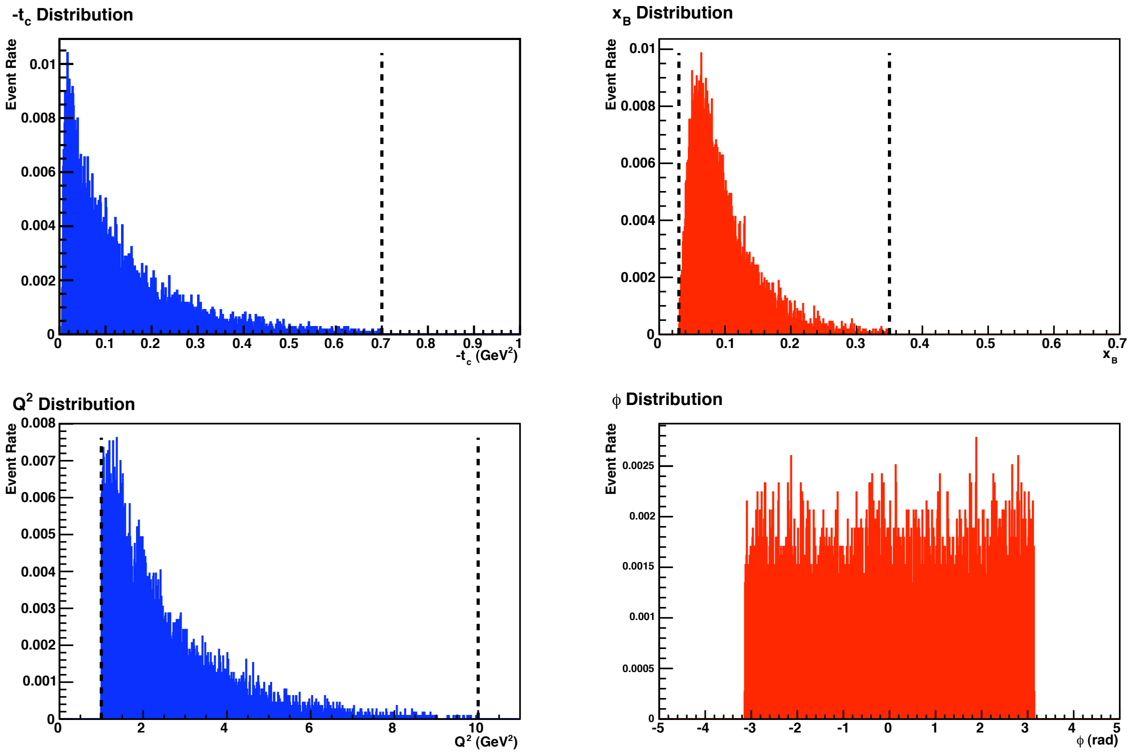

Figure 5.4: Distributions of the $-t_c$, Q^2, x_B and ϕ kinematic variables, normalised to the total number of events. The extracted asymmetry amplitudes, shown in figures 5.15, 5.16 and 5.17, have a sinusoidal dependence on ϕ, while the results are binned against $-t_c$, Q^2 and x_B. The dashed lines represent the cuts applied to the DVCS candidate data sample, with no cuts applied to ϕ.

5.2 Cross Check of Event Sample

In order to ensure the accuracy of the data analysis a cross check was carried out between the event samples of the author and of Hrachya Marukyan of Yerevan Physics Institute, Armenia. Independent analysis programs were used by each analyser to extract the sample of DVCS-related candidate events. These samples were compared to ensure that they matched as closely as possible, including the accuracy of calculated kinematic variables.

Table 5.2 shows the result of the cross check of both analysers for all data sets analysed. The data set column shows the year with the data production also indicated. The beam helicity is also shown, as both beam helicity states must be used in order to extract beam spin asymmetries. The number of DIS events and the average beam

Analyser	Data Set	Beam Helicity	N_{DIS}	$\langle P_{\mathrm{beam}} \rangle$	$N_{e\gamma}$ Candidate
Gordon	96d0	pos.	1530242	0.5164	1559
Hrachya			1529169	0.5164	1560
Gordon	97d1	neg.	1752315	-0.5105	1806
Hrachya			1751136	-0.5105	1805
Gordon	98d0	neg.	920178	-0.3069	990
Hrachya			921134	-0.3069	990
Gordon	99c0	pos.	172557	0.4175	193
Hrachya			172450	0.4175	193
Gordon	99c0	neg.	31591	-0.5523	26
Hrachya			31552	-0.5524	26
Gordon	00d2	pos.	242556	0.5581	271
Hrachya			242414	0.5581	272
Gordon	00d2	neg.	1058880	-0.5845	1128
Hrachya			1058097	-0.5845	1128
Gordon	05c1	pos.	2348426	0.3771	2612
Hrachya			2346956	0.3772	2614
Gordon	05c1	neg.	2346776	-0.3547	2563
Hrachya			2345337	-0.3547	2563

Table 5.2: Table of results from the author and Hrachya Marukyan, showing the data sets used and the numbers of DIS and DVCS candidate events selected from the data. Variations are acceptable and arise from different variable precisions used in the analyses.

polarisation value are used to normalise the data set in the asymmetry extraction detailed later.

Differences between the results from each analyser are acceptable, arising from the choice of double precision (Gordon) and float precision (Hrachya) variables in the analysis code. In total there are 11148 DVCS/BH candidate events to be used in the extraction of asymmetries, with a difference in the samples of 5 events, or $\sim 0.04\%$.

5.3 Extraction of Asymmetries

In order to extract DVCS-related asymmetry amplitudes from the data sample shown in table 5.2, a fit must be made. A fitting function is chosen such that Beam Spin Asymmetry (BSA) amplitudes, from both the DVCS and Interference components of the cross section, and Beam Charge Asymmetry (BCA) amplitudes can be extracted simultaneously using a Maximum Likelihood fitting technique. These asymmetries depend on ϕ, as described in section 2.3. The fitting function used and the motivation for using general Maximum Likelihood fitting rather than the more common Least Squares technique, itself a particular case of Maximum Likelihood fitting, will be detailed here.

5.3.1 Least Squares Fitting

Least Squares (or χ^2) fitting is conventionally used in physics experiments to extract information from a data set. The values of a parameter set $[a_1 \dots a_n]$ are varied to minimise the probability density function (p.d.f.) [Bev94] given by:

$$\chi^2 = \sum_{i=1}^{n} \left\{ \frac{1}{\sigma_i^2} [y_i - y(x_i)]^2 \right\} \tag{5.14}$$

where σ_i is the deviation of the data point y_i from the mean distribution of the bin being fitted, and $y(x_i)$ is the function chosen to describe the data.

Often there is no function that conveniently describes the data set. In this case the data set is histogramed into frequencies, with a function describing the histogram shape used in the fit. This introduces problems as the binning and range of the histogram are arbitrary, usually chosen to “best fit” the histogram shape by eye, with no fixed approach.

Choosing the bin size to be the resolution of the measurements can also introduce problems. Empty bins can influence the fit. If the events in a bin do not conform to a Gaussian distribution around the bin center this can also influence the fit. This can lead to irreproducible results from analysis of the same data set by independent analysers.

Least Squares fitting is often used as it relatively simple to implement and uses little computing power. A fit must be made to the bins of the histogram only, not each data point, which may be more numerous by orders of magnitude. The $\chi^2/d.o.f.$ parameter provides a measure of the fit quality.

In the case of DVCS-related asymmetry extraction the statistics in question are relatively low. The binning of histograms of this data set would be difficult as empty bins and event distributions in each bin could influence the fit result. Thus a different technique must be used.

5.3.2 Maximum Likelihood Fitting

Maximum Likelihood fitting is used in high energy physics experiments as an alternative to Least Squares fitting detailed above. The data set is not binned in histograms, a fit is made over the data points themselves. A fitting function is used to describe the data which has its basis in the theoretical dependence of the asymmetries on ϕ.

In Maximum Likelihood fitting the values of a parameter set $[a_1 \dots a_n]$ are varied to maximise the likelihood function:

$$\mathcal{L}(\vec{\alpha}) = \prod_{i}^{N} \frac{p(x_i, \vec{\alpha})}{\mathcal{N}(\vec{\alpha})} \tag{5.15}$$

where $p(x_i, \vec{\alpha})$ is the probability of parameter set $\vec{\alpha}$ describing each data point x_i and N is the total number of events. The expected value of the number of events, $\mathcal{N}(\vec{\alpha})$, can be interpreted as the normalisation of the extended probability density function $\mathcal{P}(x_i, \vec{\alpha}) \equiv p(x_i, \vec{\alpha})\mathcal{N}(\vec{\alpha})$ [LY07]:

$$\mathcal{N}(\vec{\alpha}) = \int \mathcal{P}(x_i, \vec{\alpha}) dx \tag{5.16}$$

In practice, maximising the likelihood function leads to computationally large values of the function due to the number of events in a typical analysis of a high energy physics experiment. This can be problematic as a large product of small values may have rounding errors in current computing environments. The negative log likelihood is analytically simple at its minimum and is found at the same parameter set $\vec{\alpha}$ as the maximum likelihood. Hence in this analysis the minimisation of the negative log likelihood is carried out using the following function:

$$-\ln \mathcal{L}(\vec{\alpha}) = -\sum_{i}^{N} \ln \mathcal{P}(x_i, \vec{\alpha}) + N \ln \mathcal{N}(\vec{\alpha}) \tag{5.17}$$

Minimisation is carried out using the MINUIT package from CERN [JR75].

The Maximum Likelihood method is not always the optimal approach. By running over each event rather than a histogram containing many events per bin the method is slower than Least Squares fitting. However, modern computing speeds make this a minor consideration. There is no standard quality of fit measure such as Least Squares' $\chi^2/d.o.f.$ parameter. However, the benefits of an unbinned fit outweigh these limitations.

Standard or Extended Maximum Likelihood?

In section 5.3.2 above the equations (5.15) and (5.17) are known as the Standard Maximum Likelihood (SML) method. However, in particle physics experiments the observed number of events may have a Poisson fluctuation about the expected value $\mathcal{N}(\vec{\alpha})$, which may be dependent on the parameters $\vec{\alpha}$ [LY07]. In this case the maximum likelihood method is extended to include this Poisson probability density function, giving the Extended Maximum Likelihood (EML) method [Bar90]:

$$\mathcal{L}(\vec{\alpha}) = \frac{\mathcal{N}(\vec{\alpha})^N e^{-\mathcal{N}(\vec{\alpha})}}{N!} \prod_{i}^{N} \frac{p(x_i, \vec{\alpha})}{\mathcal{N}(\vec{\alpha})} \tag{5.18}$$

and the negative log likelihood used in the analysis:

$$-\ln \mathcal{L}(\vec{\alpha}) = -\sum_{i}^{N} \ln \mathcal{P}(x_i, \vec{\alpha}) + \mathcal{N}(\vec{\alpha}) \tag{5.19}$$

The difference in the extracted asymmetry amplitudes using either SML or EML is insignificant in comparison with the statistical and systematic uncertainties of the measurement, as shown in section 5.4.1. This agrees with the findings shown in [LAC86].

Reference [Bar90] shows that for an experiment where the expected number of events is not fixed, using the EML method can give improved results over those from the

SML method. For the EML method the normalisation is not fixed to the expected number of events; rather it is allowed to vary. In the case of measurements of DVCS at HERMES, the number of events is not fixed, the data taking period is fixed by time constraints on the use of the HERA accelerator. Thus the normalisation should not be fixed to the expected number of events, hence the EML approach is most suitable and will give a better estimation of parameters and their uncertainties [Bar90]. As such the results in this thesis will be shown using the EML method (unless stated otherwise).

5.3.3 Fitting Function

As first proposed in [LY07], this analysis will extract the BCA and BSA amplitudes from Interference and DVCS terms of the $e\gamma$ cross section simultaneously. The fitting function must be normalised as discussed in section 5.3.2. This normalisation should account for the efficiency and acceptance of the HERMES spectrometer.

The total number of expected events depends on the integrated Luminosity L, detection efficiency ϵ and the total unpolarised cross section σ^0_{UU}. This is related to the cross section shown in equation (2.65), with the total number of $e\gamma$ events given by:

$$\mathbf{N} = L(P,\eta)\epsilon(x,P,\eta)\sigma^0_{UU}(x)[1+\eta A_C(x,\vec{\alpha})+PA^{DVCS}_{LU}(x,\vec{\alpha})+P\eta A^{\mathcal{I}}_{LU}(x,\vec{\alpha})] \quad (5.20)$$

where P denotes the beam polarisation, η denotes the beam charge and x denotes the set of measurements. ϵ and σ^0_{UU} have no dependence on the parameter set $\vec{\alpha}$ and thus can be ignored.

The fitting function to be minimised is given by

$$-\ln\mathcal{L}(\vec{\alpha}) = -\sum_i^N \ln[1+\eta_i A_C(x_i,\vec{\alpha})+P_i A^{DVCS}_{LU}(x_i,\vec{\alpha})+P_i\eta_i A^{\mathcal{I}}_{LU}(x_i,\vec{\alpha})]+\mathcal{N}(\vec{\alpha}) \quad (5.21)$$

for each event i, with the normalisation given by

$$\mathcal{N}(\vec{\alpha}) = \sum_i^N K(P_i,\eta_i)[M_1+M_2A_C(x_i,\vec{\alpha})+M_3A^{DVCS}_{LU}(x_i,\vec{\alpha})+M_4A^{\mathcal{I}}_{LU}(x_i,\vec{\alpha})], \quad (5.22)$$

with

$$K(P_i, \eta_i) = \begin{cases} \frac{1}{2}\frac{1}{\overset{\rightarrow}{L^{+}}}\frac{1}{1-\langle \overset{\rightarrow}{P^{+}}\rangle/\langle \overset{\leftarrow}{P^{+}}\rangle} & (P > 0, \eta = 1) \\ \frac{1}{2}\frac{1}{\overset{\leftarrow}{L^{+}}}\frac{1}{1-\langle \overset{\leftarrow}{P^{+}}\rangle/\langle \overset{\rightarrow}{P^{+}}\rangle} & (P < 0, \eta = 1) \\ \frac{1}{2}\frac{1}{\overset{\rightarrow}{L^{-}}}\frac{1}{1-\langle \overset{\rightarrow}{P^{-}}\rangle/\langle \overset{\leftarrow}{P^{-}}\rangle} & (P > 0, \eta = -1) \\ \frac{1}{2}\frac{1}{\overset{\leftarrow}{L^{-}}}\frac{1}{1-\langle \overset{\leftarrow}{P^{-}}\rangle/\langle \overset{\rightarrow}{P^{-}}\rangle} & (P < 0, \eta = -1) \end{cases} \tag{5.23}$$

and

$$M_1 = L^+ + L^- \tag{5.24}$$

$$M_2 = L^+ - L^- \tag{5.25}$$

$$M_3 = L^+\langle P^+\rangle + L^-\langle P^-\rangle \tag{5.26}$$

$$M_4 = L^+\langle P^+\rangle - L^-\langle P^-\rangle, \tag{5.27}$$

where +(-) denotes the beam charge, → (←) denotes positive (negative) beam helicity and $\langle P\rangle$ denotes the average polarisation. At HERMES the number of DIS events is often used in place of luminosity measurements in the normalisation. This removes a source of systematic uncertainty from the luminosity monitor measurement, described in section 3.3.4.

The asymmetry amplitudes are given by

$$\begin{aligned} A_C(x_i, \vec{\alpha}) &= A_C^{\cos 0\phi} + A_C^{\cos\phi}\cos(\phi) + A_C^{\cos 2\phi}\cos(2\phi) + A_C^{\cos 3\phi}\cos(3\phi) \\ A_{LU,DVCS}(x_i, \vec{\alpha}) &= A_{LU,DVCS}^{\sin 0\phi} + A_{LU,DVCS}^{\sin\phi}\sin(\phi) \\ A_{LU,\mathcal{I}}(x_i, \vec{\alpha}) &= A_{LU,\mathcal{I}}^{\sin 0\phi} + A_{LU,\mathcal{I}}^{\sin\phi}\sin(\phi) + A_{LU,\mathcal{I}}^{\sin 2\phi}\sin(\phi). \end{aligned} \tag{5.28}$$

5.3.4 Cross Check of Results

Figures 5.5, 5.6 and 5.7 show results of the Extended Maximum Likelihood fit applied to the dataset given in section 5.2 for both analysers. The extracted BCA and BSA amplitudes are in excellent agreement given the difference in the data sets from the use of double or float precision in analysis programs.

Studies have shown that the event sample is dominated by incoherent scattering at $t_c \leq -0.2$. Figure 5.8 shows results for the asymmetry amplitudes for both analysers

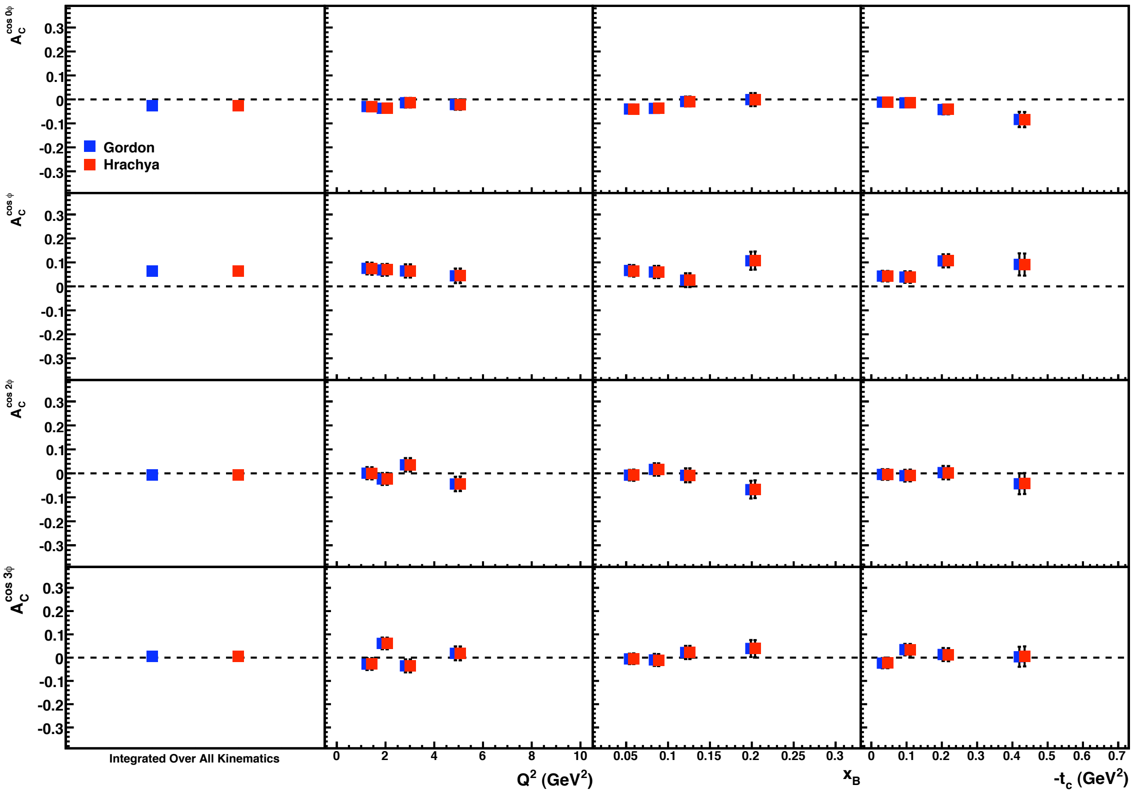

Figure 5.5: Results of cross check with Hrachya Marukyan of BCA amplitudes from the data set given in section 5.2 at HERMES. The results are shown integrated over all kinematics (leftmost column) and binned in Q^2 (second column), x_B (third column) and t_c (rightmost column). Results are in excellent agreement in all kinematic bins. Error bars are statistical uncertainties only.

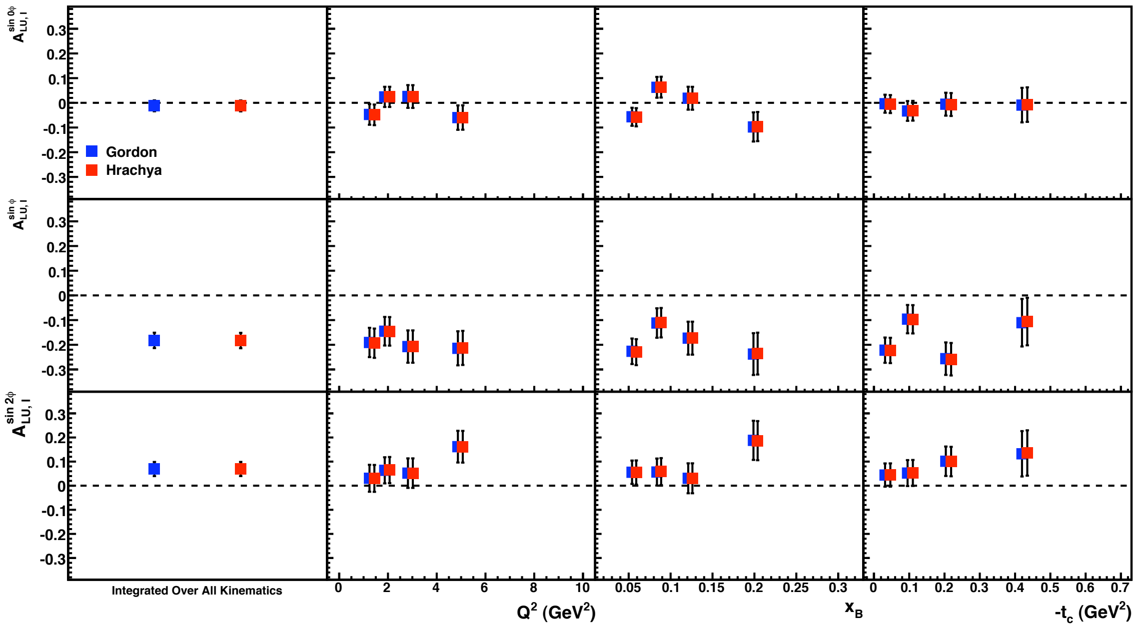

Figure 5.6: Results of cross check with Hrachya Marukyan of BSA amplitudes from the Interference cross section term from the data set given in section 5.2 at HERMES. The results are shown integrated over all kinematics (leftmost column) and binned in Q^2 (second column), x_B (third column) and t_c (rightmost column). Results are in excellent agreement in all kinematic bins. Error bars are statistical uncertainties only.

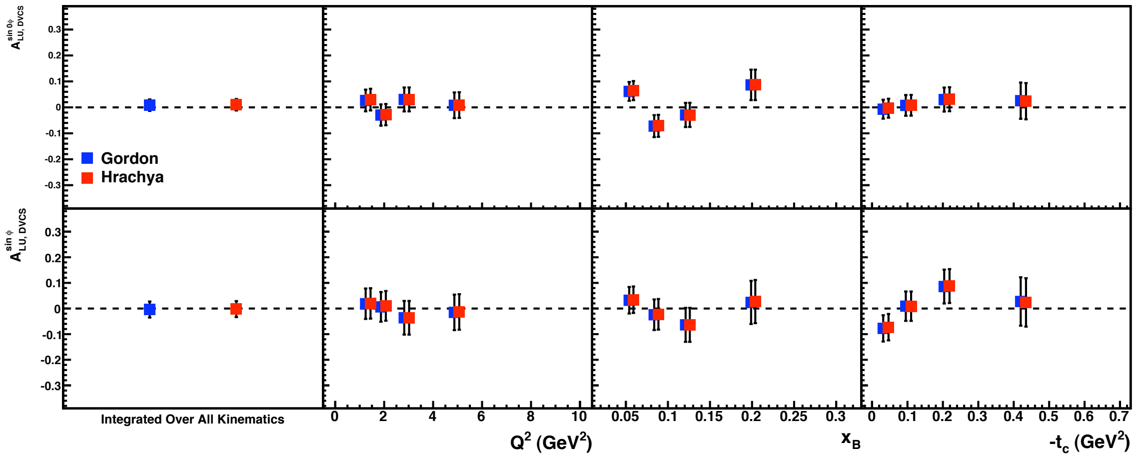

Figure 5.7: Results of cross check with Hrachya Marukyan of BSA amplitudes from the squared DVCS cross section term from the data set given in section 5.2 at HERMES. The results are shown integrated over all kinematics (leftmost column) and binned in Q^2 (second column), x_B (third column) and t_c (rightmost column). Results are in excellent agreement in all kinematic bins. Error bars are statistical uncertainties only.

in the incoherent scattering dominated region. This result will be used in further analysis in chapter 6.

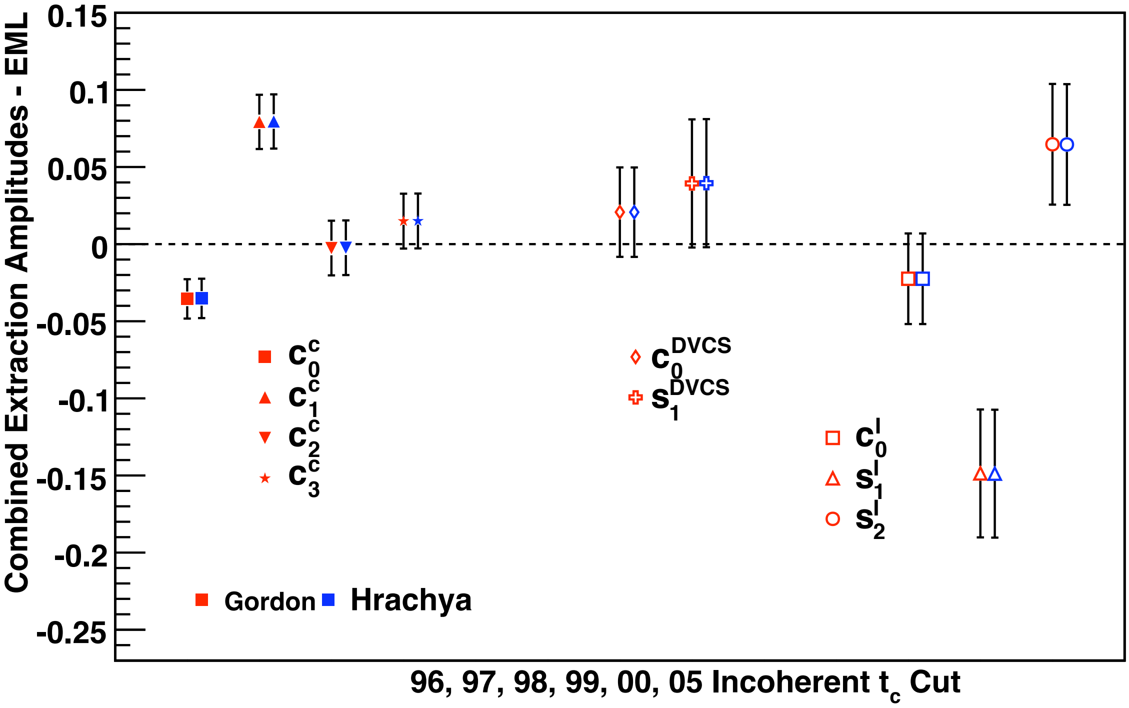

Figure 5.8: Results of cross check with Hrachya Marukyan of DVCS-related amplitudes in the incoherent scattering dominated region from the data set given in section 5.2 at HERMES. A cut on t_c is used to produce an incoherent enriched data sample. Error bars are statistical uncertainties only. Results are shown integrated over all kinematics and are in excellent agreement.

5.4 Systematic Uncertainties

Results shown in section 5.3.4 are shown with statistical uncertainties only. Here a discussion of the various contributions to the systematic uncertainty of the results will be given, followed by tables 5.3, 5.4 and 5.5 summarising the values of the systematic uncertainties applied to the final results. A Monte Carlo study was performed by Hrachya Marukyan to quantify contributions to the systematic uncertainty, taken from [MHM$^+$08] and noted as such where appropriate.

5.4.1 Fitting Function

The choice of the SML or the EML fitting technique and the number of parameters in the fit may have an effect on the extracted asymmetry amplitudes. This effect is investigated here.

SML vs. EML

Figures 5.9, 5.10 and 5.11 show results for the BCA and BSA amplitudes extracted using both SML and EML fitting. The results are very similar across all kinematic bins, with differences of less than 0.25%, and hence no contribution to the total systematic uncertainty is made from the use of EML rather than SML fitting.

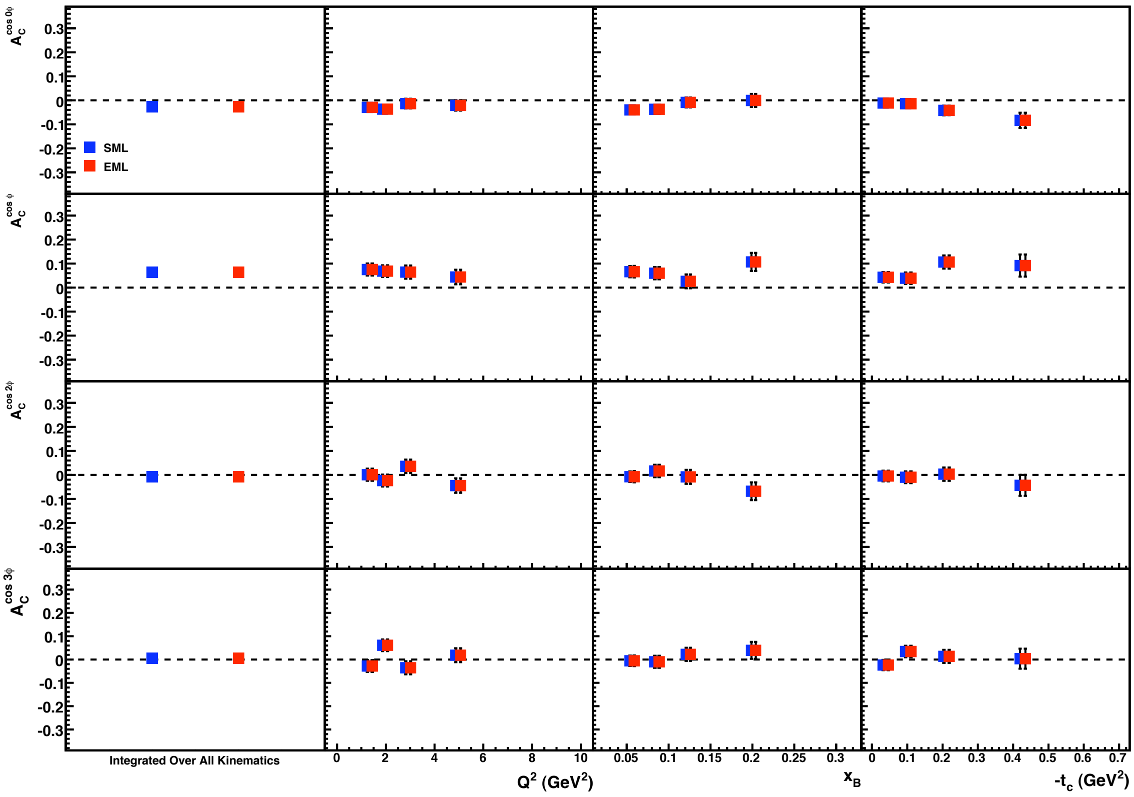

Figure 5.9: BCA amplitudes extracted using SML and EML. The results are shown integrated over all kinematics (leftmost column) and binned in Q^2 (second column), x_B (third column) and t_c (rightmost column). Results are in good agreement in all kinematic bins. Error bars are statistical uncertainties only.

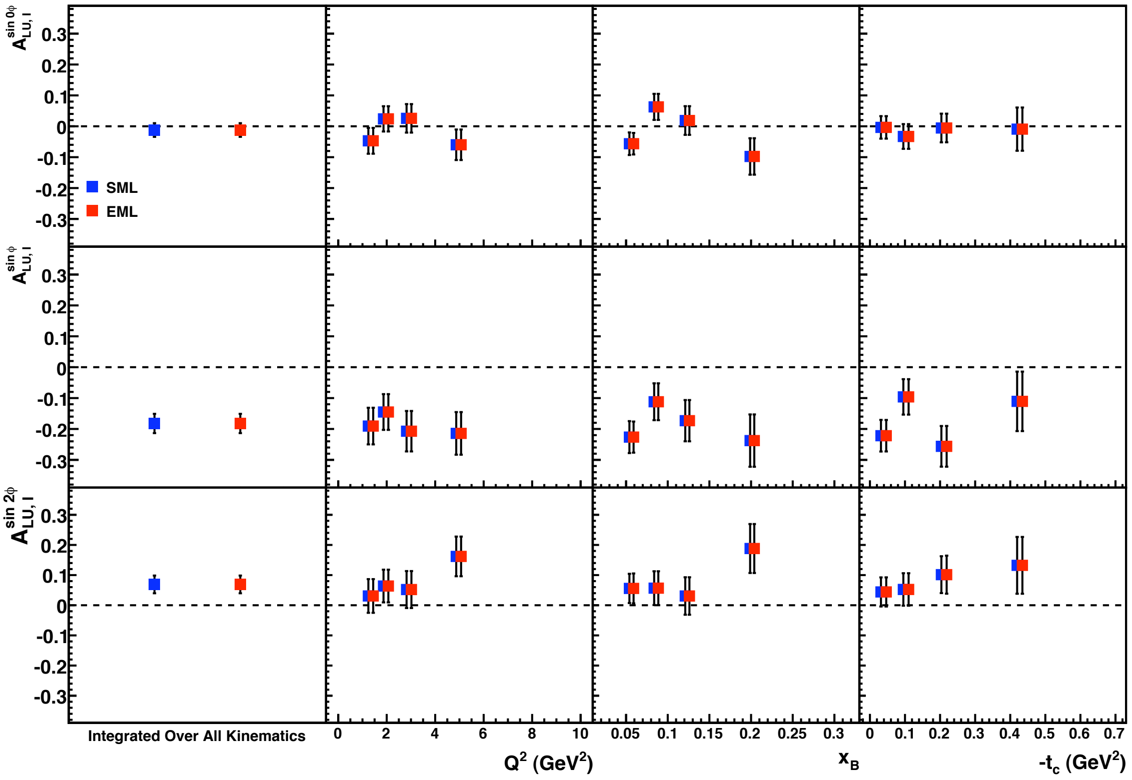

Figure 5.10: BSA amplitudes from the Interference cross section term extracted using SML and EML. The results are shown integrated over all kinematics (leftmost column) and binned in Q^2 (second column), x_B (third column) and t_c (rightmost column). Results are in good agreement in all kinematic bins. Error bars are statistical uncertainties only.

Number of Parameters

The fitting function given in equation (5.21) has 9 parameters, defined in equation (5.28). To investigate the influence of the number of parameters in the fit on the extracted asymmetry amplitudes, a second fitting function was used with 13 parameters:

$$\begin{aligned}
A_C(x_i,\vec{\alpha}) &= A_C^{\cos 0\phi} + A_C^{\cos\phi}\cos(\phi) + A_C^{\sin\phi}\sin(\phi) + A_C^{\cos 2\phi}\cos(2\phi) + A_C^{\cos 3\phi}\cos(3\phi) \\
A_{LU,DVCS}(x_i,\vec{\alpha}) &= A_{LU,DVCS}^{\sin 0\phi} + A_{LU,DVCS}^{\sin\phi}\sin(\phi) + A_{LU,DVCS}^{\cos\phi}\cos(\phi) + A_{LU,DVCS}^{\sin 2\phi}\sin(2\phi) \\
A_{LU,\mathcal{I}}(x_i,\vec{\alpha}) &= A_{LU,\mathcal{I}}^{\sin 0\phi} + A_{LU,\mathcal{I}}^{\sin\phi}\sin(\phi) + A_{LU,\mathcal{I}}^{\cos\phi}\cos(\phi) + A_{LU,\mathcal{I}}^{\sin 2\phi}\sin(\phi). \qquad (5.29)
\end{aligned}$$

The extra parameters relate to higher twist processes and sinusoidal dependences which are expected to be negligible in the corresponding asymmetry.

Figures 5.12, 5.13 and 5.14 show the extracted BCA and BSA amplitudes using a 9

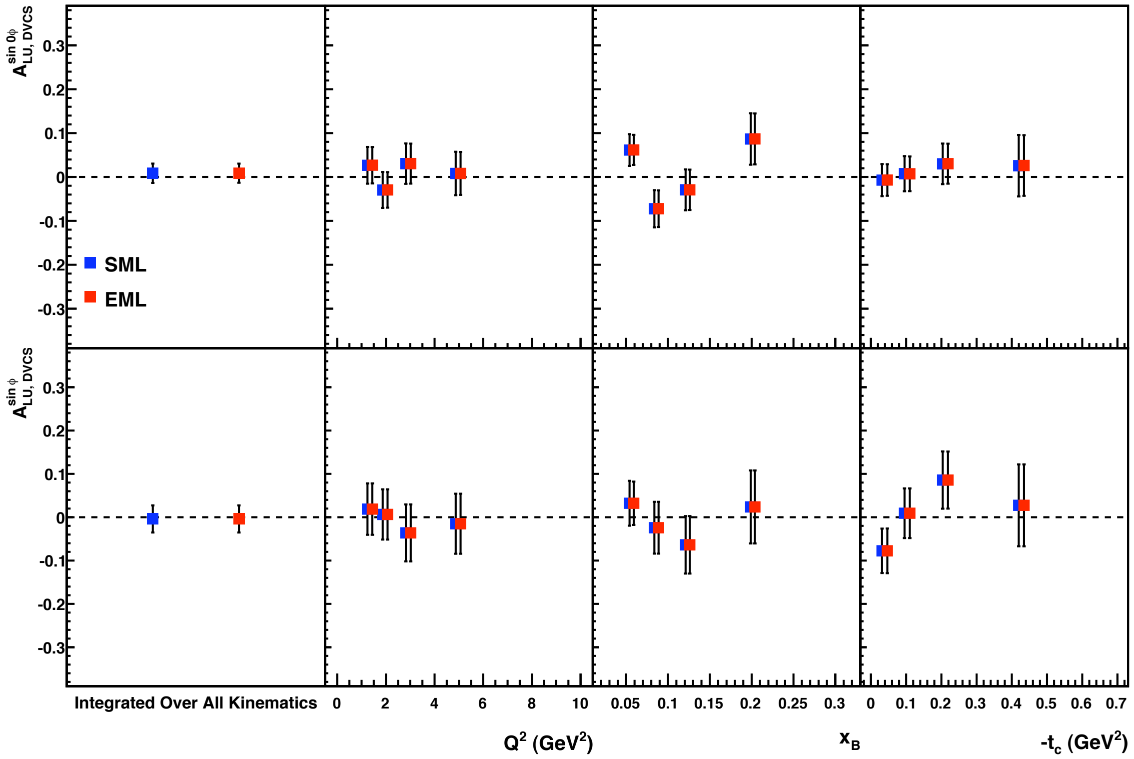

Figure 5.11: BSA amplitudes from the squared DVCS cross section term extracted using SML and EML. The results are shown integrated over all kinematics (leftmost column) and binned in Q^2 (second column), x_B (third column) and t_c (rightmost column). Results are in good agreement in all kinematic bins. Error bars are statistical uncertainties only.

parameter or 13 parameter EML fit. The difference in the amplitudes is $\sim$ 3%, insignificant with respect to the statistical uncertainties of the measurements, $\sim$ 23%, thus are not included in the final systematic uncertainty. This procedure serves as a cross-check of the method; the number of parameters used in the fit does not significantly alter the results.

5.4.2 Luminosity

As noted in section 5.3.3, the number of DIS events is used to normalise the fitting function in the extraction of asymmetry amplitudes. Alternatively, the luminosity can be used in this normalisation. However, the integrated luminosity is measured using the luminosity monitor, which introduces systematic uncertainties (see section 3.3.4). Studies [Ell04] have shown that asymmetries extracted with either normal-

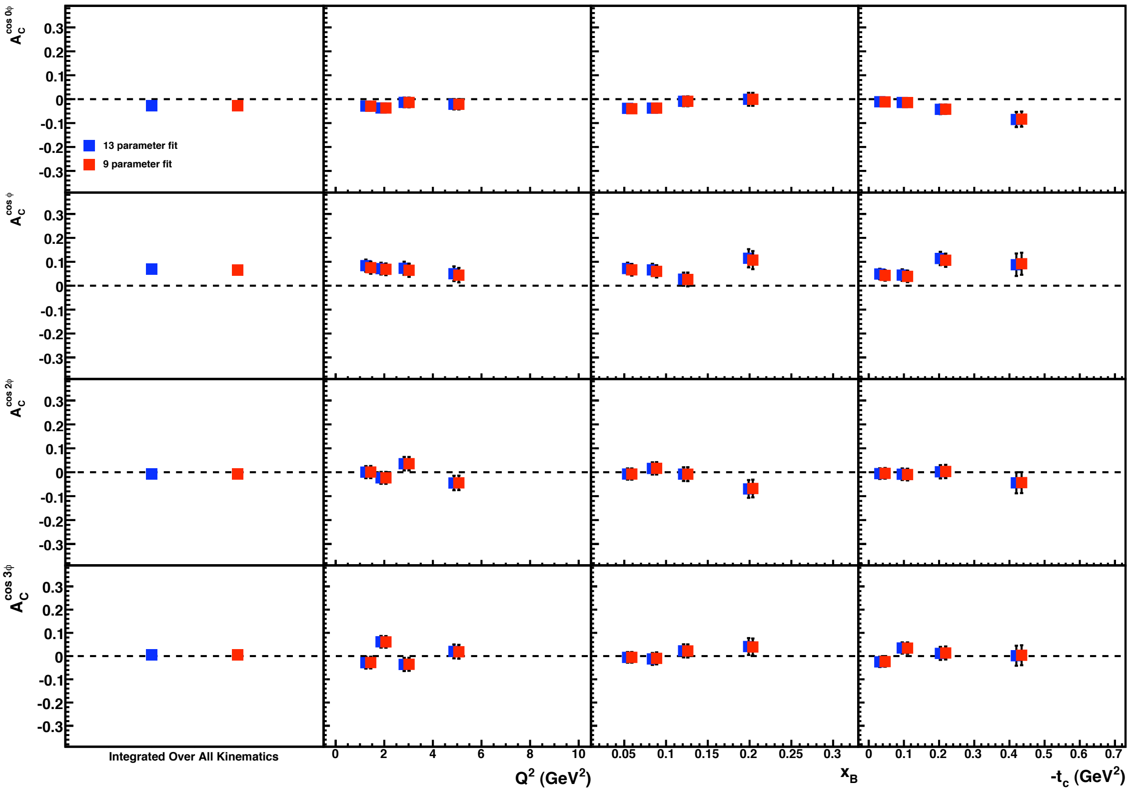

Figure 5.12: BCA amplitudes extracted using 9 parameters and 13 parameters in the EML fit. The results are shown integrated over all kinematics (leftmost column) and binned in Q^2 (second column), x_B (third column) and t_c (rightmost column). Results are in good agreement in all kinematic bins. Error bars are statistical uncertainties only.

isation do not change the extracted amplitudes. Thus the number of DIS events is preferred in this analysis.

5.4.3 Missing Mass Corrections

As described in section 5.1.2, the missing mass distribution changes depending on the data set being analysed [MHM+08]. The cut used in the analysis is altered for each data set to take account of this effect. Furthermore, the difference in the extracted asymmetry amplitudes between using the "standard" M_X^2 window and the adjusted M_X^2 windows is found, with a quarter of this difference assigned as a systematic uncertainty. As this effect is not fully understood, with four different shifts observed, this systematic uncertainty should overestimate the effect on the

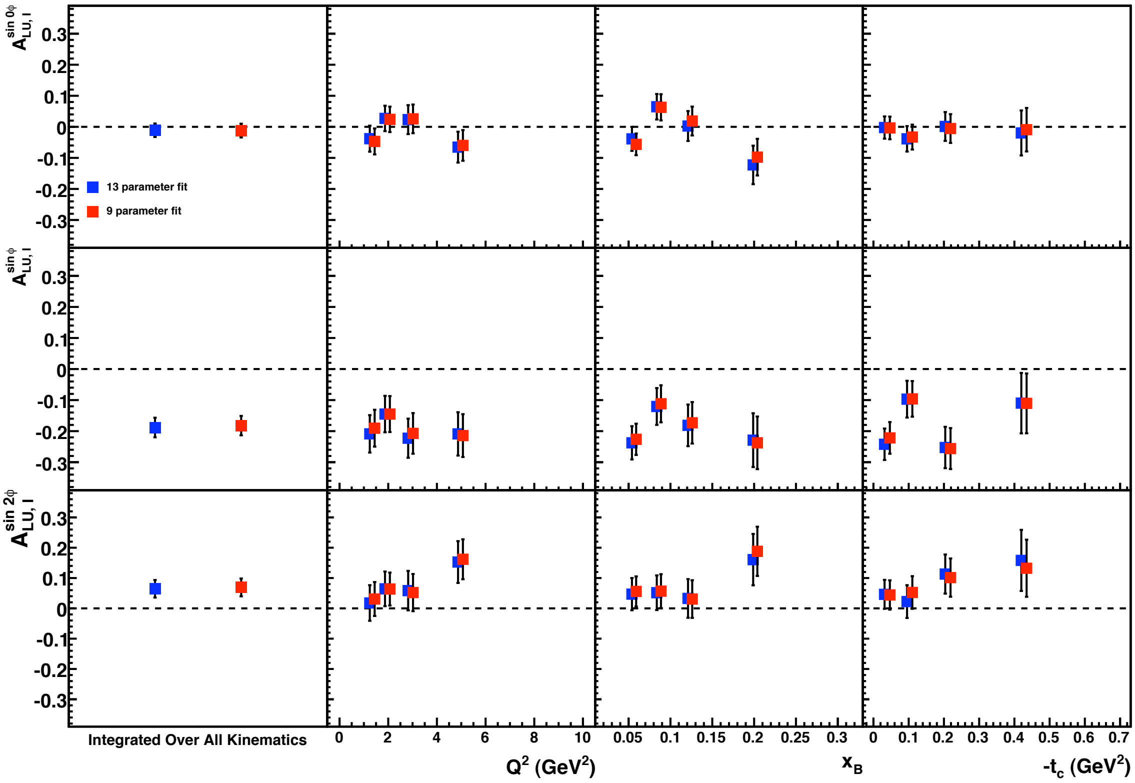

Figure 5.13: BSA amplitudes from the Interference cross section term extracted using 9 parameters and 13 parameters in the EML fit. The results are shown integrated over all kinematics (leftmost column) and binned in Q^2 (second column), x_B (third column) and t_c (rightmost column). Results are in good agreement in all kinematic bins. Error bars are statistical uncertainties only.

results.

5.4.4 Calorimeter Photon Cluster Energy Miscalibration

To establish exclusivity in the event sample a cut on the missing mass M_X^2 is used. This cut is heavily dependent on the energy of the produced photon, measured at HERMES using the calorimeter only. The ability of the calorimeter to accurately reconstruct these photons is a matter of debate in the collaboration.

In order to remove some of the reliance on the calorimeter, the squared four-momentum transfer t is calculated without the use of the energy of the photon, giving the “constrained t” or t_c, as noted in section 5.1.1. This removes a source of

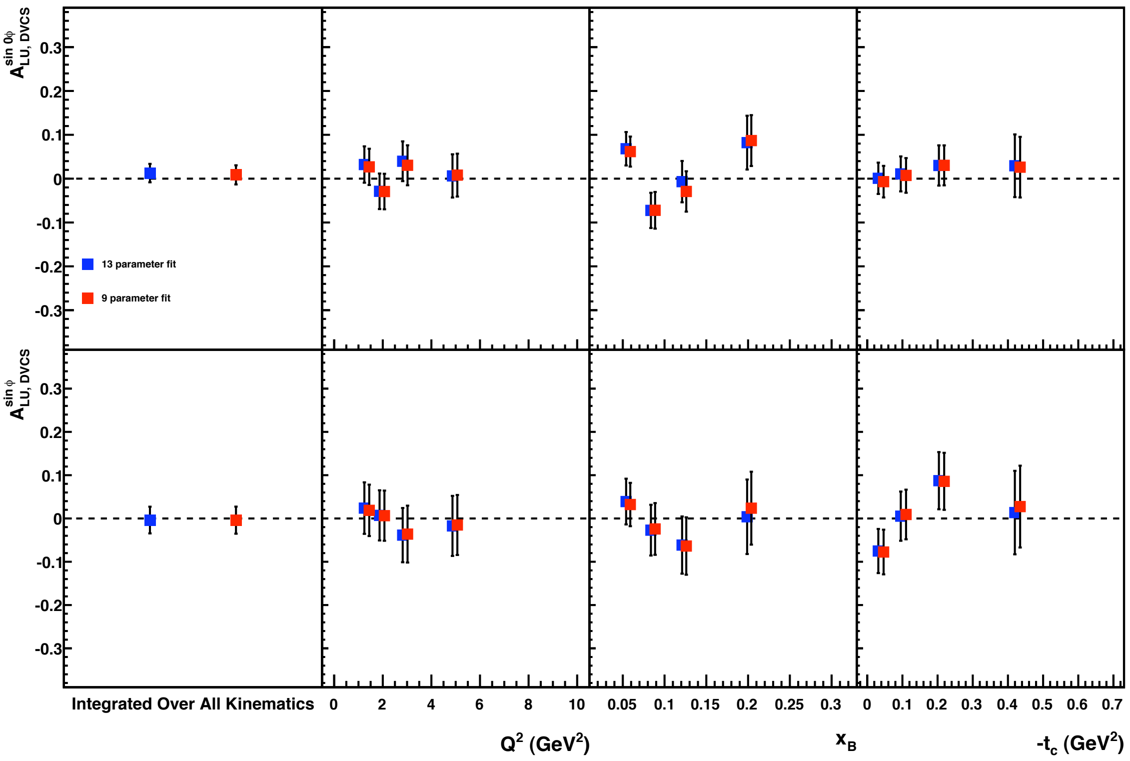

Figure 5.14: BSA amplitudes from the squared DVCS cross section term extracted using 9 parameters and 13 parameters in the EML fit. The results are shown integrated over all kinematics (leftmost column) and binned in Q^2 (second column), x_B (third column) and t_c (rightmost column). Results are in good agreement in all kinematic bins. Error bars are statistical uncertainties only.

systematic uncertainty.

Investigations [Ye06] into the effect of the possible miscalibration of the calorimeter on the extracted Transverse Target Spin Asymmetries showed that the effect was negligible, at the level of less than 1%. As such the DVCS group at HERMES does not consider possible calorimeter miscalibration as a significant systematic uncertainty contribution.

5.4.5 Background Contributions

The main sources of background for the DVCS Candidate sample for the analysis of deuterium data are Semi-Inclusive DIS (SIDIS) production and Exclusive π^0 production. The latter is found to be small [Kra05, Ye06] and corrections are not required.

The SIDIS background must be corrected for, with 80% of this background arising from decay photons of π^0 particles. Without the use of the Recoil Detector it is impossible to remove the background from resonance excitations due to the limited M_X^2 resolution.

A study [MHM⁺08] was performed to measure the asymmetry of the SIDIS background and correct the measured asymmetries according to:

$$A_{excl.} = \frac{1}{1 - f_{SIDIS}} (A_{meas.} - f_{SIDIS} A_{SIDIS}) \,, \tag{5.30}$$

where f_{SIDIS} (A_{SIDIS}) denotes the relative contribution (asymmetry) of the semi-inclusive DIS process. A systematic uncertainty for background contributions, δ^{bg}, is calculated from

$$\begin{aligned} \delta_f &= \frac{A_{meas.} - A_{SIDIS}}{(1 - f_{SIDIS})^2} * \delta f_{SIDIS} \,, & (5.31) \\ \delta_A &= \frac{-f_{SIDIS}}{1 - f_{SIDIS}} * \delta A_{SIDIS} \,, & (5.32) \\ \delta^{bg} &= \sqrt{\delta_f^2 + \delta_A^2} \,, & (5.33) \end{aligned}$$

where δf_{SIDIS} (δA_{SIDIS}) is the statistical uncertainty of the extracted f_{SIDIS} (A_{SIDIS}).

5.4.6 The “Four in One” Method

The systematic effects from the acceptance of the spectrometer, fixed bin width, smearing and spectrometer misalignment have been studied using MC simulations [MHM⁺08]. Past DVCS analyses have simulated each effect separately, adding each resulting systematic uncertainty in quadrature to produce an overall systematic uncertainty. This approach is valid only when the effects are not correlated and are symmetric, which may not be the case for the effects listed previously. Recent DVCS analyses at HERMES have simulated each effect simultaneously, with the difference between simulated and reconstructed asymmetries used to calculate a systematic uncertainty from the four possible effects at once. This is known as the “Four in One” method. A final systematic uncertainty from this method is calculated from a RMS average of uncertainties from different GPD models used in the MC generator. This approach is used here, with further details available in [MHM$^+$08]. The systematic uncertainty contributions from shifts in the missing mass distributions and the contributions from background are not correlated to the four effects in the “Four in One”, therefore these are not included in this method.

Spectrometer Acceptance

The HERMES experiment uses a forward angle spectrometer. This does not provide 4π acceptance of reaction products. A study is made to compare extracted asymmetries from MC generated in the HERMES acceptance with those generated in a 4π acceptance, with any resulting difference a source of systematic uncertainty, as part of the “Four in One” method.

As the four contributions to the “Four in One” method are studied simultaneously, estimates of the magnitude of systematic uncertainties from individual effects are not available. Estimates are available from [Ye06] where the contributions were studied individually. The spectrometer acceptance is found to be the dominant contribution, with an uncertainty of 17.8% in the extracted asymmetry amplitude.

Spectrometer Misalignment

There are two types of misalignment of the HERMES spectrometer: internal and external. Internal misalignment refers to offsets or rotations of the positions of individual subdetectors relative to each other, arising from factors such as support structure relaxation. Periodically during data taking periods HERMES takes alignment runs without an active magnetic field in the spectrometer, producing perfectly straight tracks which can be used for alignment of the subdetectors. With sufficient statistics taken during these runs, the subdetectors can be aligned with a precision better than the resolution of each subdetector. Corrections are applied to the tracking algorithms during data processing, thus no correction must be made to the DVCS-enriched candidate data sample.

External misalignment refers to offsets or rotations of the spectrometer as a whole with respect to the external coordinate system and the beam line. This cannot be corrected for in the data. As such an artificial misalignment of the spectrometer is simulated in MC, with differences between generated and reconstructed asymmetries assigned as a systematic uncertainty, as part of the "Four in One" method. Reference [Ye06] gives the systematic uncertainty from spectrometer misalignment as 2.1% of the extracted asymmetry amplitude.

Smearing

Due to shifts and biases in the resolution of the HERMES spectrometer subdetectors, smearing effects can take place. These effects can occur when the incident particle on a detector surface is not reconstructed in the correct position, leading to differences in the reconstructed kinematics of the event and altering the measured asymmetry. This effect is simulated in the "Four in One" MC and thus taken into account. Reference [Ye06] gives the systematic uncertainty from smearing as 11.6% of the extracted asymmetry amplitude.

Fixed Bin Width

Due to limited statistics available in the measurement of the asymmetries, the results are binned in four bins of Q^2, x_B and t_c. Due to aforementioned acceptance and smearing effects, the reconstructed asymmetries may differ from the MC generated asymmetries in a particular bin. These differences form part of the "Four in One" method systematic uncertainty. This effect has not been previously studied in HERMES DVCS analyses and no estimates for the systematic uncertainty of this contribution are available.

5.4.7 Final Systematic Uncertainties

The total systematic uncertainty for each asymmetry is calculated from a quadratic sum of the contributions from the background correction, shifts in the M_X^2 window and the "Four in One" method. Tables 5.3, 5.4 and 5.5 show the $A_C^{\cos\phi}$, $A_{LU,DVCS}^{\sin\phi}$ and $A_{LU,I}^{\sin\phi}$ asymmetry amplitudes with details of the contributions to the total systematic uncertainties. Table 5.6 and 5.7 show the overall results with systematic and statistical uncertainties for the BSA and BCA amplitudes respectively.

Kinematic bin	$A_C^{\cos\phi} \pm \delta_{stat.}$	SIDIS π^0	M_X^2 shift	4-in-1	Sys. sum
Overall	0.067 ± 0.015	0.001	0.000	0.027	0.027
$-t_c \leq 0.06$ GeV^2	0.044 ± 0.023	0.001	0.000	0.015	0.015
$0.06 < -t_c \leq 0.14$ GeV^2	0.041 ± 0.026	0.001	0.000	0.023	0.023
$0.14 < -t_c \leq 0.30$ GeV^2	0.113 ± 0.032	0.003	0.001	0.023	0.023
$0.30 < -t_c \leq 0.70$ GeV^2	0.094 ± 0.050	0.001	0.001	0.040	0.040
$0.03 < x_B \leq 0.07$	0.066 ± 0.030	0.000	0.001	0.032	0.032
$0.07 < x_B \leq 0.10$	0.063 ± 0.029	0.001	0.001	0.025	0.025
$0.10 < x_B \leq 0.15$	0.028 ± 0.031	0.001	0.001	0.022	0.022
$0.15 < x_B \leq 0.35$	0.120 ± 0.043	0.006	0.000	0.015	0.016
$1.0 < Q^2 \leq 1.5$ GeV^2	0.077 ± 0.029	0.002	0.000	0.029	0.029
$1.5 < Q^2 \leq 2.3$ GeV^2	0.073 ± 0.027	0.002	0.001	0.028	0.028
$2.3 < Q^2 \leq 3.5$ GeV^2	0.067 ± 0.030	0.001	0.002	0.017	0.017
$3.5 < Q^2 \leq 10.0$ GeV^2	0.046 ± 0.032	0.001	0.000	0.024	0.024

Table 5.3: Summary of systematic uncertainty contributions for the asymmetry amplitude $A_C^{\cos\phi}$ extracted over all data and for each kinematic bin. The total systematic uncertainty is a quadratic sum of the SIDIS background, M_X^2 shift and the “4-in-1” method contributions.

5.5 Final Results

Figures 5.15, 5.16 and 5.17 show results for BCA and BSA amplitudes with the total systematic uncertainty indicated in bands. The model curves shown are for the “VGG” model and the “Dual” model of GPDs, see section 2.1.5. In order to best describe the experimental data, the models are used to calculate asymmetries from a combination of neutron and proton cross section results. This should approximate incoherent scattering off the deuteron, in the impulse approximation and neglecting Fermi motion, and are thus denoted “Incoherent” on the results.

By varying the unknown free parameters b_{val} and b_{sea} bands are produced for the VGG model. Both models are shown for fixed values of $J_u = 0.2$ and $J_d = 0.0$, as

Kinematic bin	$A_{LU,DVCS}^{\sin\phi} \pm \delta_{stat.}$	SIDIS π^0	M_X^2 shift	4-in-1	Sys. sum
Overall	-0.007± 0.033	0.006	0.002	0.003	0.007
$-t_c \leq 0.06$ GeV^2	-0.074 ± 0.053	0.008	0.001	0.011	0.014
$0.06 < -t_c \leq 0.14$ GeV^2	0.005 ± 0.061	0.010	0.001	0.004	0.011
$0.14 < -t_c \leq 0.30$ GeV^2	0.085 ± 0.070	0.007	0.006	0.007	0.012
$0.30 < -t_c \leq 0.70$ GeV^2	0.020 ± 0.098	0.017	0.005	0.003	0.018
$0.03 < x_B \leq 0.07$	0.032 ± 0.052	0.017	0.005	0.007	0.019
$0.07 < x_B \leq 0.10$	-0.020 ± 0.063	0.007	0.001	0.007	0.010
$0.10 < x_B \leq 0.15$	-0.076 ± 0.071	0.027	0.004	0.009	0.029
$0.15 < x_B \leq 0.35$	0.015 ± 0.095	0.020	0.005	0.005	0.021
$1.0 < Q^2 \leq 1.5$ GeV^2	0.012 ± 0.062	0.021	0.000	0.006	0.022
$1.5 < Q^2 \leq 2.3$ GeV^2	0.013 ± 0.061	0.008	0.001	0.016	0.018
$2.3 < Q^2 \leq 3.5$ GeV^2	-0.045 ± 0.068	0.027	0.003	0.005	0.028
$3.5 < Q^2 \leq 10.0$ GeV^2	-0.018 ± 0.072	0.013	0.003	0.006	0.015

Table 5.4: Summary of systematic uncertainty contributions for the asymmetry amplitude $A_{LU,DVCS}^{\sin\phi}$ extracted over all data and for each kinematic bin. The total systematic uncertainty is a quadratic sum of the SIDIS background, M_X^2 shift and the “4-in-1” method uncertainties.

expected from Lattice QCD [OBG$^+$07, HSB$^+$08], a theoretical framework based on numerical calculations to predict properties of Quantum Chromodynamics.

Both the factorised and the Regge-type t-dependence hypotheses are available for the VGG model, with only Regge-type available for the Dual model. The $A_C^{\cos\phi}$ dependence on t, shown in figure 5.15, disfavours the factorised t-dependence ansatz, in agreement with previous results at HERMES [ZL08, A$^+$08]. Both the VGG and Dual Regge-type t-dependence agree with the experimental results. As expected, the $A_C^{\cos\phi}$ is the dominant non-zero asymmetry amplitude for the BCA, with higher twist contributions $A_C^{\cos 2\phi}$ and $A_C^{\cos 3\phi}$ compatible with zero, as predicted by both models.

The $A_{LU,DVCS}^{\sin 0\phi}$ amplitude is included in the fitting function as a cross check that

Kinematic bin	$A_{LU,I}^{\sin\phi} \pm \delta_{stat.}$	SIDIS π^0	M_X^2 shift	4-in-1	Sys. sum
Overall	-0.191 ± 0.035	0.004	0.000	0.075	0.075
$-t_c \leq 0.06$ GeV^2	-0.229 ± 0.063	0.003	0.002	0.034	0.034
$0.06 < -t_c \leq 0.14$ GeV^2	-0.103 ± 0.062	0.003	0.000	0.036	0.036
$0.14 < -t_c \leq 0.30$ GeV^2	-0.273 ± 0.076	0.007	0.001	0.027	0.028
$0.30 < -t_c \leq 0.70$ GeV^2	-0.109 ± 0.101	0.002	0.004	0.024	0.024
$0.03 < x_B \leq 0.07$	-0.232 ± 0.083	0.001	0.004	0.091	0.091
$0.07 < x_B \leq 0.10$	-0.115 ± 0.066	0.002	0.002	0.081	0.081
$0.10 < x_B \leq 0.15$	-0.183 ± 0.076	0.005	0.005	0.063	0.063
$0.15 < x_B \leq 0.35$	-0.263 ± 0.097	0.014	0.002	0.051	0.053
$1.0 < Q^2 \leq 1.5$ GeV^2	-0.202 ± 0.071	0.004	0.004	0.082	0.082
$1.5 < Q^2 \leq 2.3$ GeV^2	-0.153 ± 0.064	0.002	0.001	0.079	0.079
$2.3 < Q^2 \leq 3.5$ GeV^2	-0.215 ± 0.072	0.001	0.006	0.067	0.067
$3.5 < Q^2 \leq 10.0$ GeV^2	-0.222 ± 0.074	0.002	0.003	0.052	0.052

Table 5.5: Summary of systematic uncertainty contributions for the asymmetry amplitude $A_{LU,I}^{\sin\phi}$ extracted over all data and for each kinematic bin. The total systematic uncertainty is a quadratic sum of the SIDIS background, M_X^2 shift and the "4-in-1" method contributions.

the fitting procedure is correct and should be compatible with zero. The $A_{LU,DVCS}^{\sin\phi}$ term is a higher-twist amplitude and is therefore suppressed by $\sim \frac{1}{Q}$. Both models predict that the $A_{LU,DVCS}^{\sin 0\phi}$ and $A_{LU,DVCS}^{\sin\phi}$ amplitudes are compatible with zero, with the experimental results of figure 5.16 in agreement.

As for the $A_{LU,DVCS}^{\sin 0\phi}$ amplitude, the $A_{LU,I}^{\sin 0\phi}$ amplitude should be compatible with zero. The $A_{LU,I}^{\sin\phi}$ term is the dominant non-zero asymmetry amplitude for the BSA from the Interference term. The Dual model appears to describe the data more accurately than the VGG models, for both Regge-type and factorised t-dependence, when integrated over all kinematics, as shown in figure 5.17. However, when looking at the $-t$, Q^2 and x_B dependences it is more difficult to distinguish between models when taking account statistical and systematic uncertainties.

The $A_{LU,I}^{\sin 2\phi}$ term is of higher twist and should therefore be suppressed. The experimental results show a positive value compatible with 0 within 2σ. The VGG model shows a non-zero negative value, in disagreement with experiment.

Kinematic bin	$\langle -t \rangle$ (GeV^2)	$\langle x_B \rangle$	$\langle Q^2 \rangle$ (GeV^2)	$A_{LU,DVCS}^{\sin\phi}$ $\pm\delta_{stat} \pm \delta_{syst}$	$A_{LU,I}^{\sin\phi}$ $\pm\delta_{stat} \pm \delta_{syst}$	$A_{LU,I}^{\sin 2\phi}$ $\pm\delta_{stat} \pm \delta_{syst}$
Overall	0.13	0.10	2.5	-0.007 ± 0.033 ± 0.007	-0.191 ± 0.035 ± 0.075	0.072 ± 0.031 ± 0.008
$-t \leq 0.06$ GeV^2	0.03	0.08	1.9	-0.074 ± 0.053 ± 0.014	-0.229 ± 0.063 ± 0.034	0.045 ± 0.050 ± 0.017
$0.06 < -t \leq 0.14$ GeV^2	0.10	0.10	2.5	0.005 ± 0.061 ± 0.011	-0.103 ± 0.062 ± 0.036	0.056 ± 0.057 ± 0.011
$0.14 < -t \leq 0.30$ GeV^2	0.20	0.11	2.9	0.085 ± 0.070 ± 0.012	-0.273 ± 0.076 ± 0.028	0.106 ± 0.066 ± 0.014
$0.30 < -t \leq 0.70$ GeV^2	0.42	0.12	3.5	0.020 ± 0.098 ± 0.018	-0.109 ± 0.101 ± 0.024	0.140 ± 0.100 ± 0.012
$0.03 < x_B \leq 0.07$	0.11	0.05	1.4	0.032 ± 0.052 ± 0.019	-0.232 ± 0.083 ± 0.091	0.055 ± 0.053 ± 0.013
$0.07 < x_B \leq 0.10$	0.11	0.08	2.1	-0.020 ± 0.063 ± 0.010	-0.115 ± 0.066 ± 0.081	0.061 ± 0.059 ± 0.008
$0.10 < x_B \leq 0.15$	0.14	0.12	3.1	-0.077 ± 0.071 ± 0.029	-0.183 ± 0.075 ± 0.063	0.032 ± 0.066 ± 0.006
$0.15 < x_B \leq 0.35$	0.20	0.20	5.0	0.015 ± 0.095 ± 0.021	-0.263 ± 0.097 ± 0.053	0.208 ± 0.092 ± 0.012
$1.0 < Q^2 \leq 1.5$ GeV^2	0.09	0.06	1.2	0.012 ± 0.062 ± 0.022	-0.202 ± 0.071 ± 0.082	0.032 ± 0.058 ± 0.019
$1.5 < Q^2 \leq 2.3$ GeV^2	0.11	0.08	1.9	0.013 ± 0.061 ± 0.018	-0.153 ± 0.064 ± 0.079	0.068 ± 0.058 ± 0.012
$2.3 < Q^2 \leq 3.5$ GeV^2	0.14	0.11	2.8	-0.045 ± 0.068 ± 0.028	-0.215 ± 0.072 ± 0.067	0.054 ± 0.064 ± 0.017
$3.5 < Q^2 \leq 10.0$ GeV^2	0.20	0.17	4.9	-0.018 ± 0.072 ± 0.015	-0.222 ± 0.074 ± 0.052	0.168 ± 0.070 ± 0.005

Table 5.6: Results of the asymmetry amplitudes $A_{LU,DVCS}^{\sin\phi}$, $A_{LU,I}^{\sin\phi}$ and $A_{LU,I}^{2\sin\phi}$ extracted over all data and for each kinematic bin. Statistical and total systematic uncertainties are shown for each asymmetry amplitude.

Kinematic bin	$A_C^{\cos 0\phi}$ $\pm\delta_{stat} \pm \delta_{syst}$	$A_C^{\cos \phi}$ $\pm\delta_{stat} \pm \delta_{syst}$	$A_C^{\cos 2\phi}$ $\pm\delta_{stat} \pm \delta_{syst}$	$A_C^{\cos 3\phi}$ $\pm\delta_{stat} \pm \delta_{syst}$
Overall	-0.028 ± 0.010 ± 0.015	0.067 ± 0.015 ± 0.027	-0.007 ± 0.014 ± 0.008	0.005 ± 0.014 ± 0.002
$-t \leq 0.06$ GeV^2	-0.012 ± 0.016 ± 0.009	0.044 ± 0.023 ± 0.015	-0.005 ± 0.023 ± 0.003	-0.024 ± 0.023 ± 0.003
$0.06 < -t \leq 0.14$ GeV^2	-0.014 ± 0.019 ± 0.016	0.041 ± 0.026 ± 0.023	-0.009 ± 0.023 ± 0.009	0.036 ± 0.026 ± 0.007
$0.14 < -t \leq 0.30$ GeV^2	-0.044 ± 0.022 ± 0.015	0.113 ± 0.032 ± 0.023	0.003 ± 0.029 ± 0.021	0.013 ± 0.027 ± 0.004
$0.30 < -t \leq 0.70$ GeV^2	-0.087 ± 0.036 ± 0.012	0.094 ± 0.050 ± 0.040	-0.044 ± 0.046 ± 0.026	0.006 ± 0.044 ± 0.007
$0.03 < x_B \leq 0.07$	-0.041 ± 0.020 ± 0.006	0.066 ± 0.030 ± 0.032	-0.008 ± 0.024 ± 0.011	-0.005 ± 0.023 ± 0.003
$0.07 < x_B \leq 0.10$	-0.038 ± 0.020 ± 0.016	0.063 ± 0.029 ± 0.025	0.017 ± 0.027 ± 0.014	-0.011 ± 0.027 ± 0.009
$0.10 < x_B \leq 0.15$	-0.009 ± 0.022 ± 0.022	0.028 ± 0.031 ± 0.022	-0.009 ± 0.031 ± 0.013	0.023 ± 0.030 ± 0.005
$0.15 < x_B \leq 0.35$	-0.001 ± 0.030 ± 0.024	0.120 ± 0.043 ± 0.016	-0.074 ± 0.042 ± 0.014	0.043 ± 0.041 ± 0.004
$1.0 < Q^2 \leq 1.5$ GeV^2	-0.031 ± 0.020 ± 0.011	0.077 ± 0.029 ± 0.029	0.000 ± 0.026 ± 0.005	-0.028 ± 0.027 ± 0.002
$1.5 < Q^2 \leq 2.3$ GeV^2	-0.038 ± 0.019 ± 0.016	0.073 ± 0.027 ± 0.028	-0.024 ± 0.026 ± 0.010	0.064 ± 0.028 ± 0.006
$2.3 < Q^2 \leq 3.5$ GeV^2	-0.014 ± 0.021 ± 0.018	0.067 ± 0.030 ± 0.017	0.037 ± 0.029 ± 0.011	-0.037 ± 0.029 ± 0.008
$3.5 < Q^2 \leq 10.0$ GeV^2	-0.022 ± 0.023 ± 0.013	0.046 ± 0.032 ± 0.024	-0.045 ± 0.032 ± 0.019	0.019 ± 0.031 ± 0.008

Table 5.7: Results of the asymmetry amplitudes $A_C^{\cos n\phi}$ extracted over all data and for each kinematic bin. Statistical and total systematic uncertainties are shown for each asymmetry amplitude.

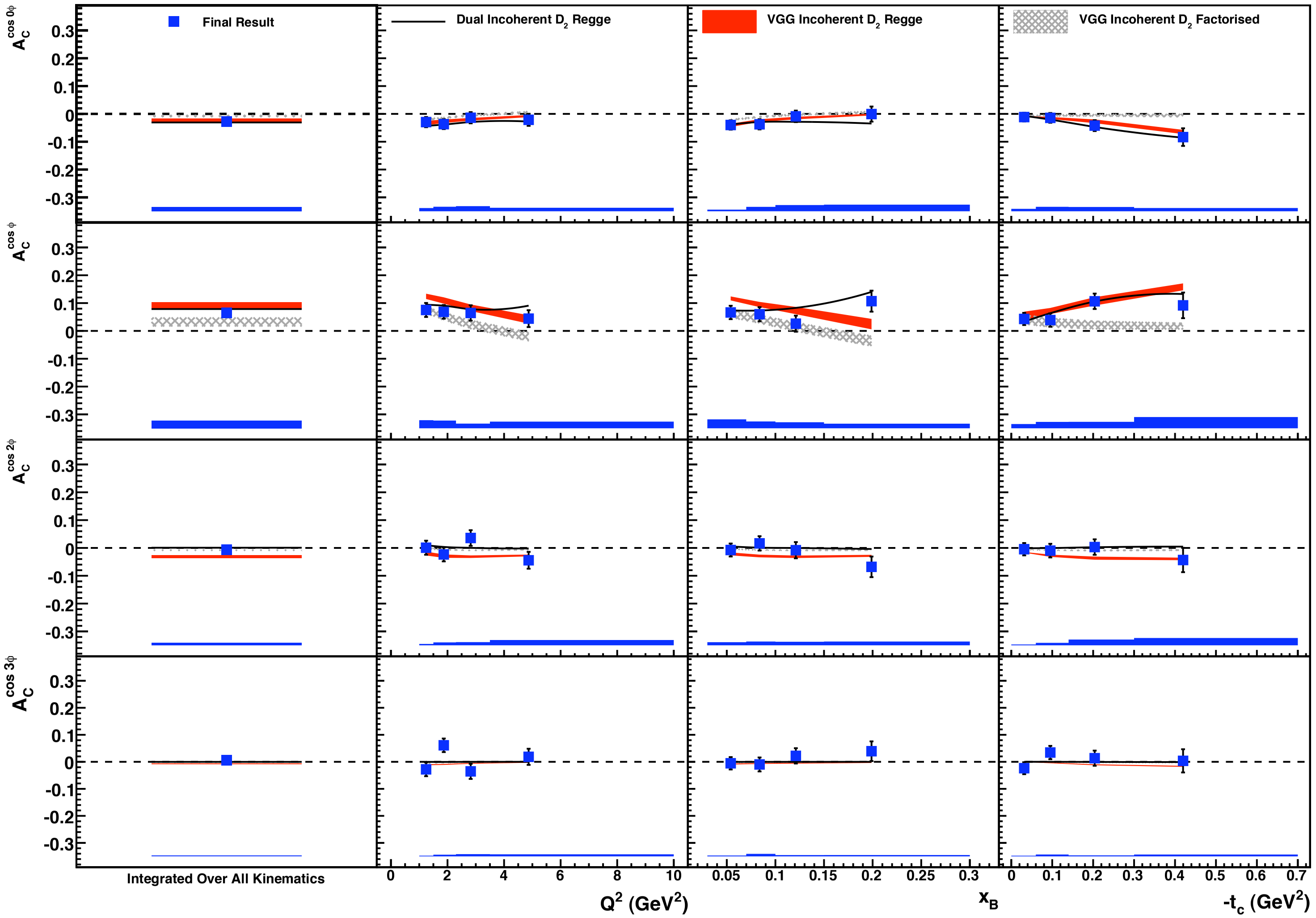

Figure 5.15: BCA amplitudes compared with the Dual and VGG models, see section 2.1.5. The results are shown integrated over all kinematics (leftmost column) and binned in Q^2 (second column), x_B (third column) and t_c (rightmost column). Statistical (bars) and systematic (bands) uncertainties are shown.

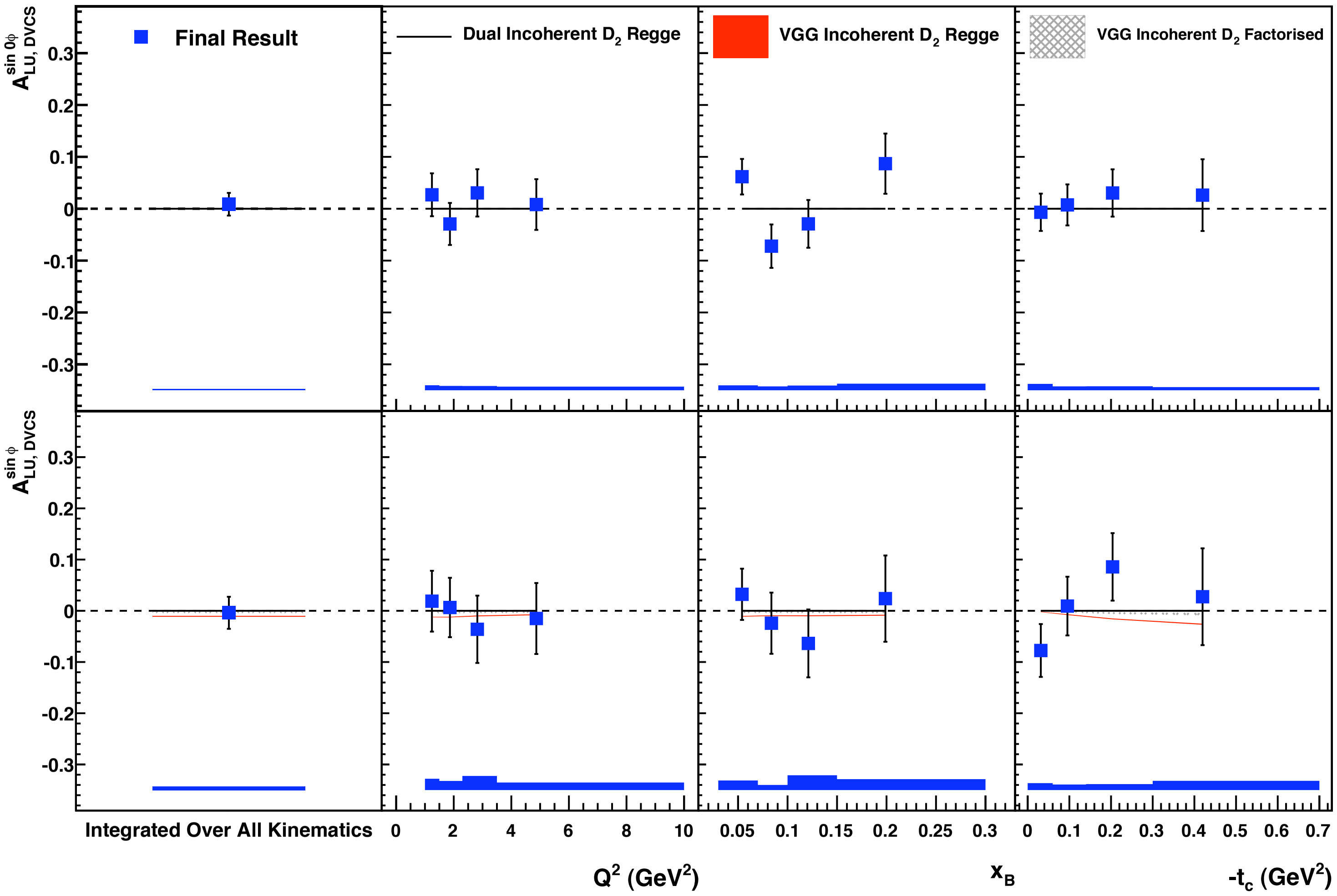

Figure 5.16: BSA amplitudes from the squared DVCS cross section term compared with the Dual and VGG models, see section 2.1.5. The results are shown integrated over all kinematics (leftmost column) and binned in Q^2 (second column), x_B (third column) and t_c (rightmost column). Statistical (bars) and systematic (bands) uncertainties are shown.

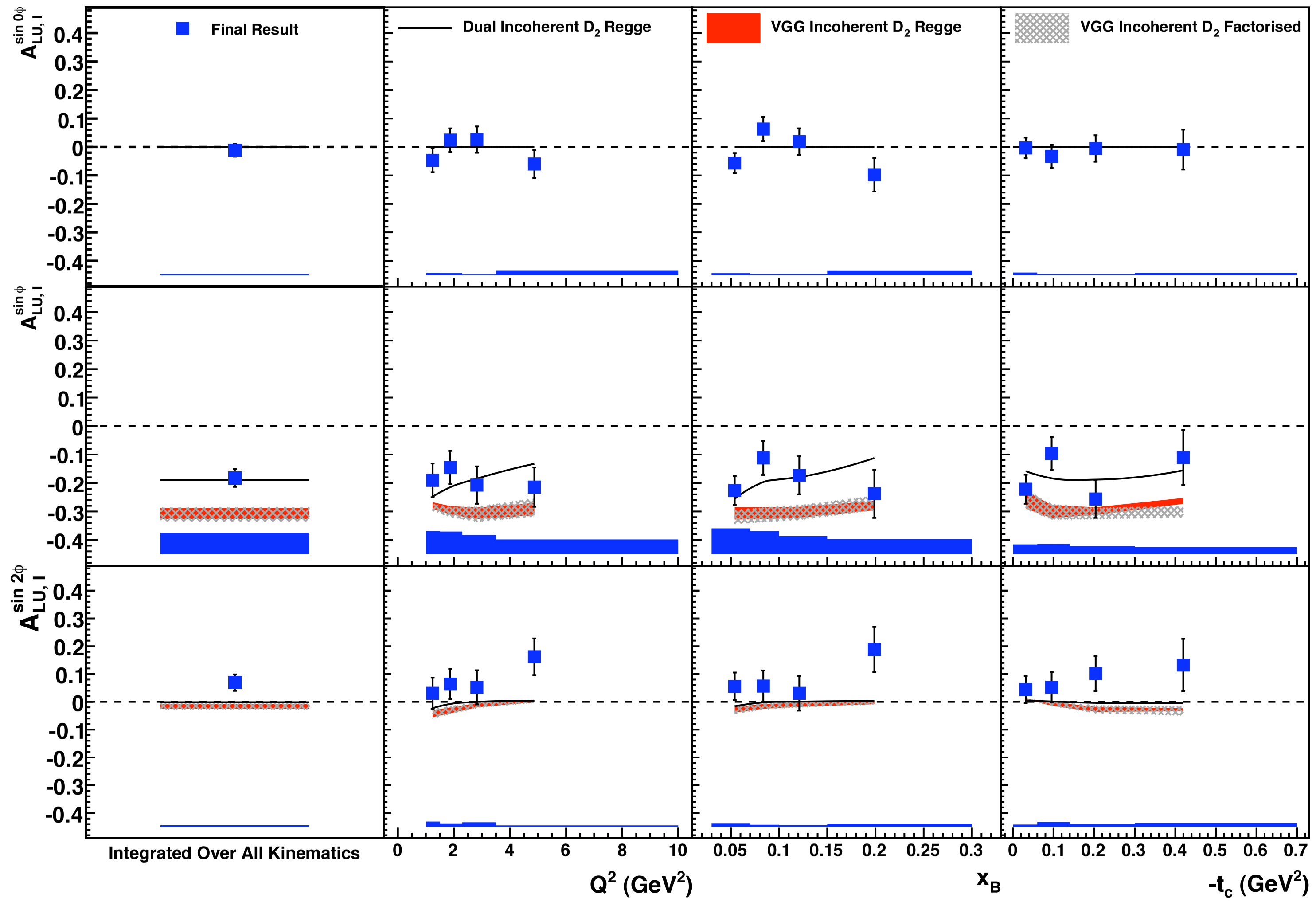

Figure 5.17: BSA amplitudes from the Interference cross section term compared with the Dual and VGG models, see section 2.1.5. The results are shown integrated over all kinematics (leftmost column) and binned in Q^2 (second column), x_B (third column) and t_c (rightmost column). Statistical (bars) and systematic (bands) uncertainties are shown.

Chapter 6

Investigation of a Model Dependent Constraint of J_u and J_d from the Neutron

6.1 Background

Methods to constrain the total angular momentum of up and down quarks in the nucleon have been outlined in [M$^+$07, A$^+$08] for the neutron and proton respectively. The GPD E can be parameterised with J_u and J_d as free parameters in models of GPDs [GPV01, GT06], see section 2.1.5 for details. Certain DVCS asymmetries are expected to be sensitive to the GPD E, and hence the value of these asymmetries can constrain J_u and J_d.

For the proton the Transverse Target Spin Asymmetry (TTSA) shows sensitivity to E:

$$A_{TTSA} \approx A_1 \sin(\phi - \phi_s)\cos(\phi) + A_2 \cos(\phi - \phi_s)\sin(\phi) \tag{6.1}$$

where

$$A_1 \propto -\frac{t}{4m_N^2} \cdot (F_2 \cdot \Im\mathcal{H} - F_1 \cdot \Im\mathcal{E}) \tag{6.2}$$

$$A_2 \propto -\frac{t}{4m_N^2} \cdot (F_2 \cdot \Im\tilde{\mathcal{H}} - F_1 \cdot \Im\tilde{\mathcal{E}}) \tag{6.3}$$

and $\mathcal{E}$ ($\mathcal{H}$) is the Compton Form Factor related to the GPD E (H), as shown in equation (2.57).

For the neutron the Beam Spin Asymmetry (BSA) is also sensitive to the GPD E, as shown in section 2.3.1:

$$A_{LU,I} \propto F_1 \cdot \mathcal{H} + \xi(F_1 + F_2) \cdot \tilde{\mathcal{H}} - \frac{t}{4m_N^2} \cdot F_2 \cdot \mathcal{E} \qquad (6.4)$$

where as before F_1 (F_2) are the Dirac (Pauli) form factors.

With HERMES having already published results for the proton, investigations were made to produce a complementary result for the neutron with HERMES data. These investigations are detailed here.

6.2 Extracting the Neutron Contribution

At Jefferson Lab Hall A, analysers are able to measure differential cross sections with deuterium and hydrogen targets. For deuterium the cross section may be decomposed into coherent and incoherent scattering contributions:

$$D(\vec{e}, e'\gamma) = d(\vec{e}, e'\gamma)d + n(\vec{e}, e'\gamma)n + p(\vec{e}, e'\gamma)p + ... \qquad (6.5)$$

with contributions from meson production channels as background [M+07].

In order to isolate the neutron contribution a measured proton cross section contribution from a companion hydrogen target experiment can be subtracted from the total cross section. A cut on the kinematic variable t is used to separate the neutron contribution in the incoherent scattering region from the coherent scattering data.

At HERMES the analysis is more complex. Differential cross sections are not measured, asymmetries are extracted from the data directly. A cut on t can be used to produce an incoherent enriched sample, but the neutron contribution can not be isolated by subtracting the proton asymmetry from this sample.

6.3 Results from Deuterium Analysis

Using results from the analysis procedure detailed in chapter 5, the $\sin\phi$ moment of the BSA from the Interference term of the cross section, $A_{LU,I}^{\sin\phi}$, is to be compared with the models of GPDs given in section 2.1.5.

Figure 5.8 shows the results of this extraction from two analysers, Hrachya Marukyan and the author. A cut on t_c is applied to provide an incoherent scattering enriched sample, $0.073 \leq -t_c \leq 0.7$, with the lower limit defining the beginning of the incoherent scattering dominated region, calculated from the relative contributions of incoherent and coherent scattering in Monte Carlo simulations. The upper limit is the standard t_c cut chosen to aid background subtraction in the exclusive sample. The result for comparison with models is

$$A_{LU,I}^{\sin\phi} = -0.149 \pm 0.041_{\mathrm{stat}} \pm 0.041_{\mathrm{syst}} \tag{6.6}$$

where the systematic uncertainty is calculated following the same procedure as described in section 5.4.

6.4 Model Asymmetry

The neutron (n) and proton (p) Beam Spin Asymmetries are calculated from the following:

$$A_{LU,I}^{p(n)} = \frac{d\sigma(\overset{\rightarrow}{e^+}, p(n)) - d\sigma(\overset{\leftarrow}{e^+}, p(n))}{d\sigma(\overset{\rightarrow}{e^+}, p(n)) + d\sigma(\overset{\leftarrow}{e^+}, p(n))} \tag{6.7}$$

where $d\sigma$ denotes the differential cross section provided by model calculations, $\rightarrow$ ($\leftarrow$) denotes positive (negative) beam helicity and e^+ the positron beam.

This model neutron asymmetry cannot be directly compared to the experimental deuterium result given above. A suggestion was made by Morgan Murray and confirmed by Markus Diehl [Die07b] to combine the modeled proton and neutron cross sections for different beam helicities to calculate a model asymmetry for incoherent scattering off deuterium, which could be directly compared with the result given in section 6.3.

This model asymmetry is calculated from the following:

$$A_{LU,I}^{d} = \frac{d\sigma(\overset{\rightarrow}{e^+}, p) - d\sigma(\overset{\leftarrow}{e^+}, p) + d\sigma(\overset{\rightarrow}{e^+}, n) - d\sigma(\overset{\leftarrow}{e^+}, n)}{d\sigma(\overset{\rightarrow}{e^+}, p) + d\sigma(\overset{\leftarrow}{e^+}, p) + d\sigma(\overset{\rightarrow}{e^+}, n) + d\sigma(\overset{\leftarrow}{e^+}, n)} \tag{6.8}$$

6.5 VGG Model

The VGG code [VGG03] can be used to calculate Beam Spin Asymmetries and differential cross sections for both proton and neutron targets, see section 2.1.5 for more information about this model. The cross sections for both the proton and the neutron and for both beam helicity states can be calculated directly by the VGG code. The target polarisation contribution was averaged out to provide an unpolarised target cross section for each beam helicity state and target. This allows the calculation of a model deuterium asymmetry as given in equation (6.8).

The VGG code (January 2002 version) allows the user to select model parameters and provide interaction kinematics to the calculation. Options were chosen to best match those used in [Mur07, M$^+$07] for consistency of result comparisons, with kinematics calculated for the incoherent scattering enriched data sample. The inputs to the code are given in Appendix A.

6.5.1 VGG Model Asymmetry Results

A Least Squares fit was made to extract the $\sin\phi$ moment of the calculated VGG model asymmetry. Figure 6.1 shows the model $\sin\phi$ asymmetry amplitude for deuterium as calculated by equation (6.8) plotted against J_u and J_d. In order to extract a constraint band, this model asymmetry value must be compared with that extracted from data, with a minimum $\chi^2 + 1$ band found and projected onto the $J_u - J_d$ axes. However, the plot in figure 6.1 does not give the expected result: the shape of the curve is not as expected from reference [M$^+$07] and the data asymmetry value of -0.149 lies in the region of large positive values of J_d and/or large negative values of J_u. This differs from the expected values given by Lattice QCD [OBG$^+$07, HSB$^+$08] and phenomenological models [Kro07] of $J_u \approx 0.2, J_d \approx 0.0$.

In order to investigate this further, the values calculated by the VGG code for the cross sections were investigated. Table 6.1 shows VGG asymmetry values for proton, neutron and deuterium for $J_u = 0.2, J_d = 0.0$ calculated using equations (6.7) and (6.8). The proton cross section is larger in magnitude than the neutron cross sec-

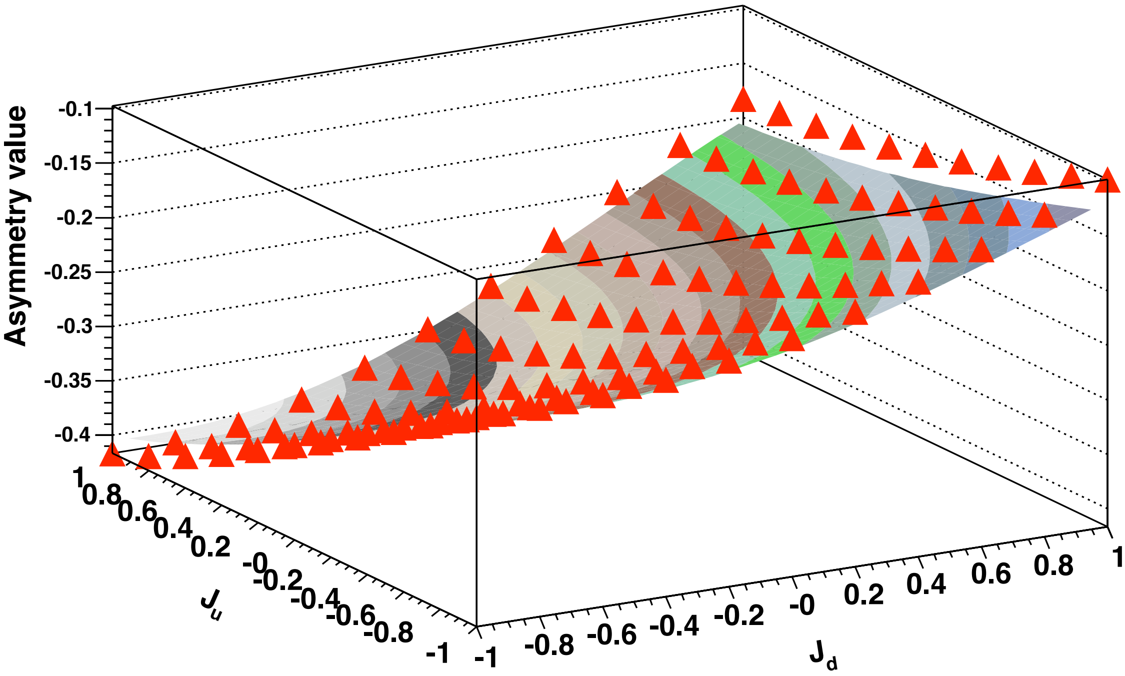

Figure 6.1: VGG deuterium $\sin\phi$ asymmetry amplitude vs. J_u and J_d, calculated from equation (6.8). The surface is a result of a 2 dimensional, 5th order polynomial fit, chosen for maximum flexibility in the fit. The coloured bands illustrate the curvature of the fitted surface. The shape of the distribution and resultant fit is not as expected from [M$^+$07] and the data asymmetry of -0.149 does not lie near $J_u \approx 0.2$, $J_d \approx 0.0$ as predicted by Lattice QCD [OBG$^+$07, HSB$^+$08] and phenomenological models [Kro07].

tion. Hence the proton contribution dominates the neutron in the overall deuterium asymmetry, and therefore dominates the $\sin\phi$ asymmetry amplitude fitted to these asymmetries.

Figure 6.2 shows these VGG calculated asymmetry amplitudes plotted against J_u and J_d, with the neutron predictions on the top and proton on the bottom. When compared with figure 6.1 it can be seen that the deuterium asymmetry amplitude has a similar magnitude to the proton asymmetry amplitude. The neutron asymmetry amplitude ranges from -0.4 to 0.4 over the given range of J_u and J_d, -1 to 1. The proton asymmetry amplitude also shows sensitivity in this range, from -0.45 to -0.15. Reference [GPV01] states that varying J_u from 0.1 to 0.4 changes the BSA amplitude from the proton by around 10%, a variation can be seen in the proton

Phi (°)	Proton A^p_{BSA}	Neutron A^n_{BSA}	Deuterium A^d_{BSA}
0	0	0	0
10	-0.0594	-0.0115	-0.0518
20	-0.1170	-0.0226	-0.1020
30	-0.1713	-0.0330	-0.1492
40	-0.2212	-0.0421	-0.1919
50	-0.2658	-0.0495	-0.2293
60	-0.3046	-0.0549	-0.2605
70	-0.3372	-0.0579	-0.2845
80	-0.3626	-0.0586	-0.3007
90	-0.3800	-0.0571	-0.3082
100	-0.3880	-0.0539	-0.3064
110	-0.3849	-0.0492	-0.2949
120	-0.3691	-0.0436	-0.2739
130	-0.3394	-0.0371	-0.2437
140	-0.2950	-0.0302	-0.2053
150	-0.2365	-0.0229	-0.1602
160	-0.1655	-0.0154	-0.1097
170	-0.0852	-0.0077	-0.0558
180	0	0	0
$\sin\phi$ Amplitude	-0.3890	-0.0568	-0.3085

Table 6.1: Table showing VGG asymmetry values for proton, neutron and deuterium for $J_u = 0.2, J_d = 0.0$ calculated using equations (6.7) and (6.8). Also shown are the fitted $\sin\phi$ asymmetry amplitudes. The proton contribution dominates the neutron in the overall deuterium asymmetry in this model.

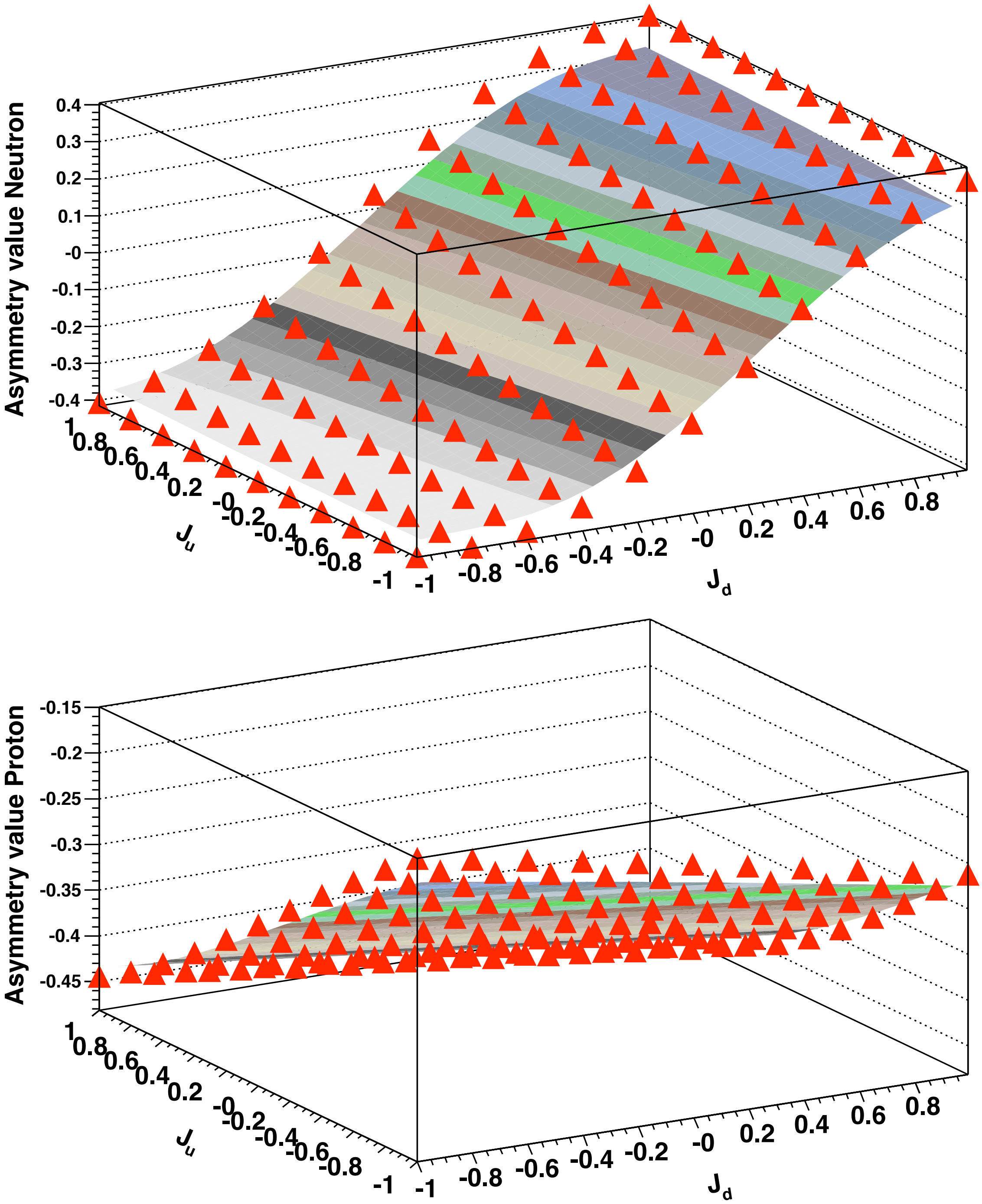

Figure 6.2: VGG $\sin\phi$ asymmetry amplitude vs. J_u and J_d for neutron (top) and proton (bottom) targets, calculated from equation (6.7). The surfaces are a result of a 2 dimensional, 5th order polynomial fit, with the coloured bands illustrating the curvature of the surface. The neutron result shows the largest sensitivity to J_u and J_d as expected from the kinematic sensitivity to GPD E. However, the proton also shows some sensitivity, leading to problems when combining the two results using equation (6.8).

distribution of figure 6.2 which becomes the dominant sensitivity when combined with the neutron distribution due to the relative magnitudes of the cross sections and their contribution to the modeled deuterium asymmetry.

The proton contribution dominates the calculated deuterium asymmetry, leading to a sensitivity similar to that of the proton rather than the neutron asymmetry. Hence when comparing the data asymmetry amplitude to the model calculation amplitude the expected values of J_u and J_d are not found at the model calculation point. The model asymmetry calculation made by combining the proton and neutron results may be too crude to accurately describe the deuterium data.

6.5.2 Constraint of J_u and J_d using Deuterium from VGG

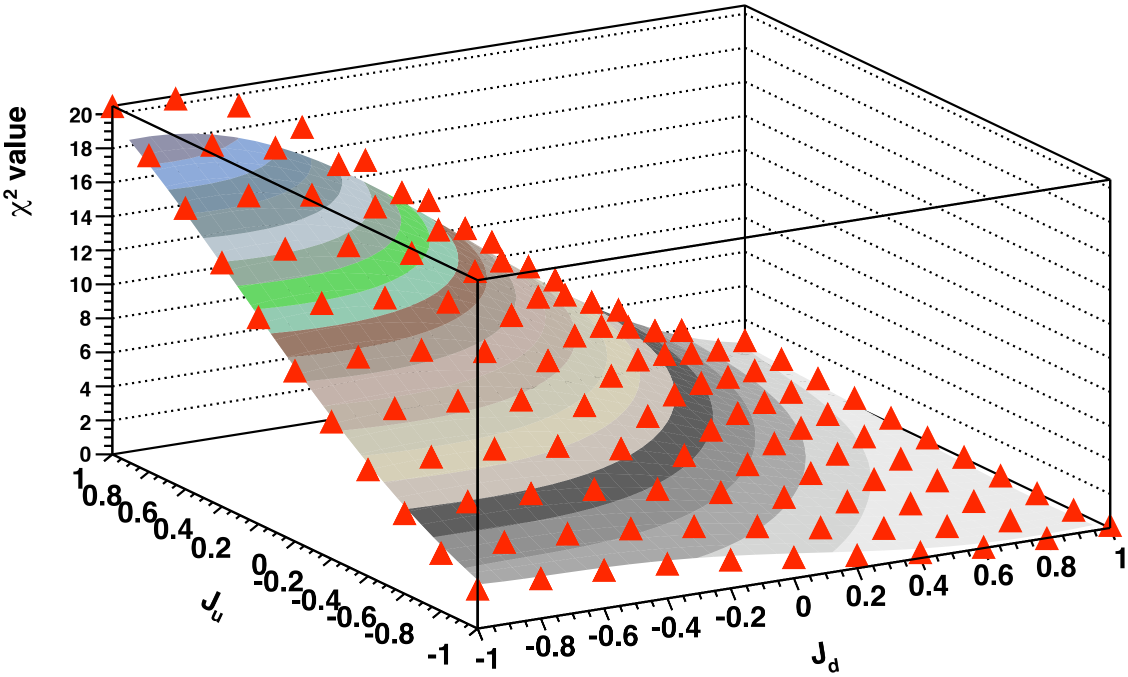

Figure 6.3: χ^2 difference calculated for each point calculated by the VGG code compared with the result given in equation (6.6). A 2 dimensional, 5th order polynomial was fitted to these points to produce the surface shown.

The χ^2 difference between the VGG model deuterium asymmetry calculated using equation (6.8) and the measured result given in equation (6.6) was calculated for each point in the $J_u - J_d$ plane. A 5 degree polynomial, chosen to give the most flexibility to the fit, was fitted to these χ^2 points to produce the surface shown in figure 6.3. The minimum $\chi^2 + 1$ area was found and projected onto the $J_u - J_d$ axes, shown in figure 6.4. An exponential fit is made to the resultant curve to give a relation between J_u and J_d shown below:

$$J_u = -2.8 - 1.4\ J_d + 1.1\ e^{J_d} + 1.0\ e^{2J_d} - 0.1\ e^{3J_d} - 0.2\ e^{4J_d} + 0.1\ e^{5J_d}. \qquad (6.9)$$

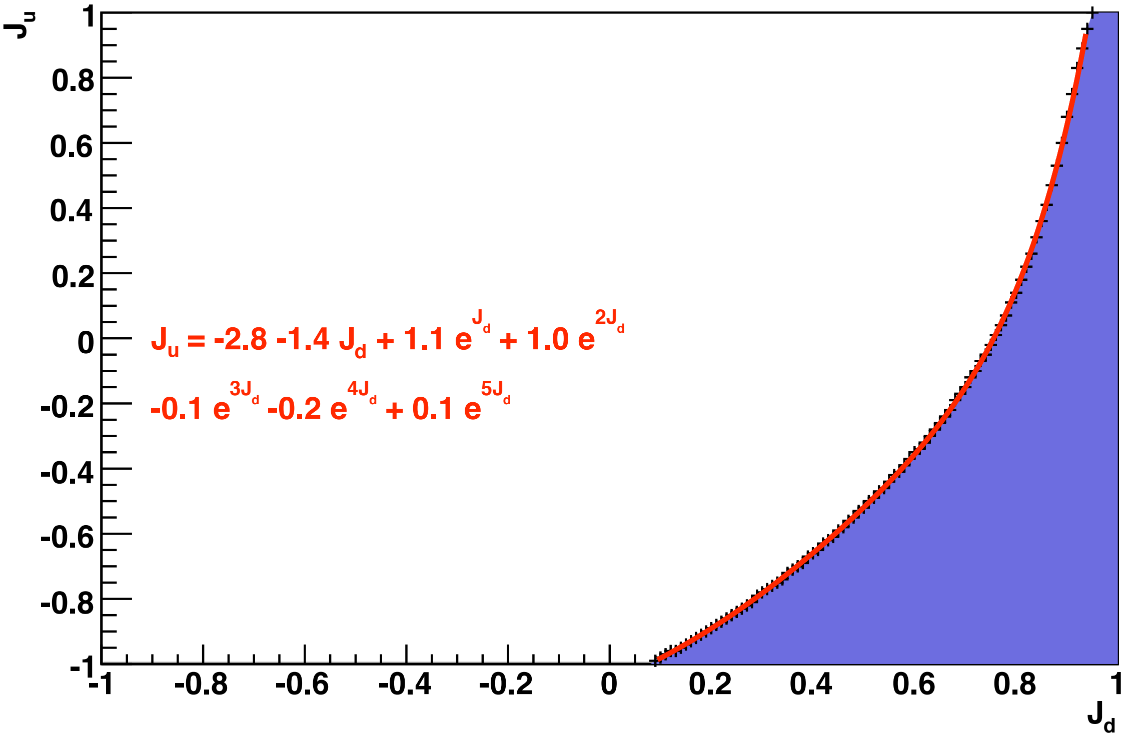

Figure 6.4: Projection of minimum $\chi^2 + 1$ surface shown in figure 6.3 onto the $J_u - J_d$ axes. A fitted exponential relation between J_u and J_d is shown. The shaded area indicates the constrained J_u, J_d values from this comparison of the VGG model and the HERMES deuterium data.

6.6 Dual Parameterisation Model from Guzey et al.

An alternative to the VGG model is the Dual model, as described in section 2.1.5. This model calculates Compton Form Factors from the dual parameterisation of GPDs given in [GT06]. These CFFs are combined with the Belitsky-Müller-Kirchner expressions for DVCS asymmetries [BMK02]. The model allows the calculation of the BSA, BCA and TTSA for the proton and the neutron for a range of values of J_u and J_d and interaction kinematics x_B, Q^2 and t. Code provided by Hongxue Ye [Ye08] allows the extraction of the cross sections used in the calculation, allowing the model asymmetry given in equation (6.8) to be calculated. This model provides results over the same range of J_d as those calculated with the VGG code, but over a narrower range of J_u, $-0.6 \leq J_u \leq 0.6$. Results were calculated at the same x_B, t and Q^2 as used in the VGG calculations, with a Regge inspired ansatz for the t dependence also used in both models.

6.6.1 Dual Parameterisation Model Asymmetry Results

As for the VGG model results, a fit was made to extract the $\sin\phi$ moment of the Dual Parameterisation model asymmetry. Figure 6.5 shows this model $\sin\phi$ asymmetry amplitude for deuterium as calculated by equation (6.8) plotted against J_u and J_d. The shape of the 2 dimensional, 5th order polynomial fit is closer to that expected, with no distortion at large J_u, small J_d as seen in figure 6.1.

In order to investigate the Dual Parameterisation model behaviour in a similar manner to the VGG model, the proton and neutron asymmetries were extracted from the model. These are shown in figure 6.6, plotted against J_u and J_d with the neutron target on the top and proton on the bottom. As in the VGG model case, when compared with figure 6.5 it can be seen that the deuterium asymmetry amplitude has a magnitude similar to the proton asymmetry amplitude. The neutron asymmetry amplitude ranges from -0.3 to 0.4 over the given range of J_u and J_d. The proton asymmetry amplitude also shows sensitivity in this range, from -0.3 to -0.18,

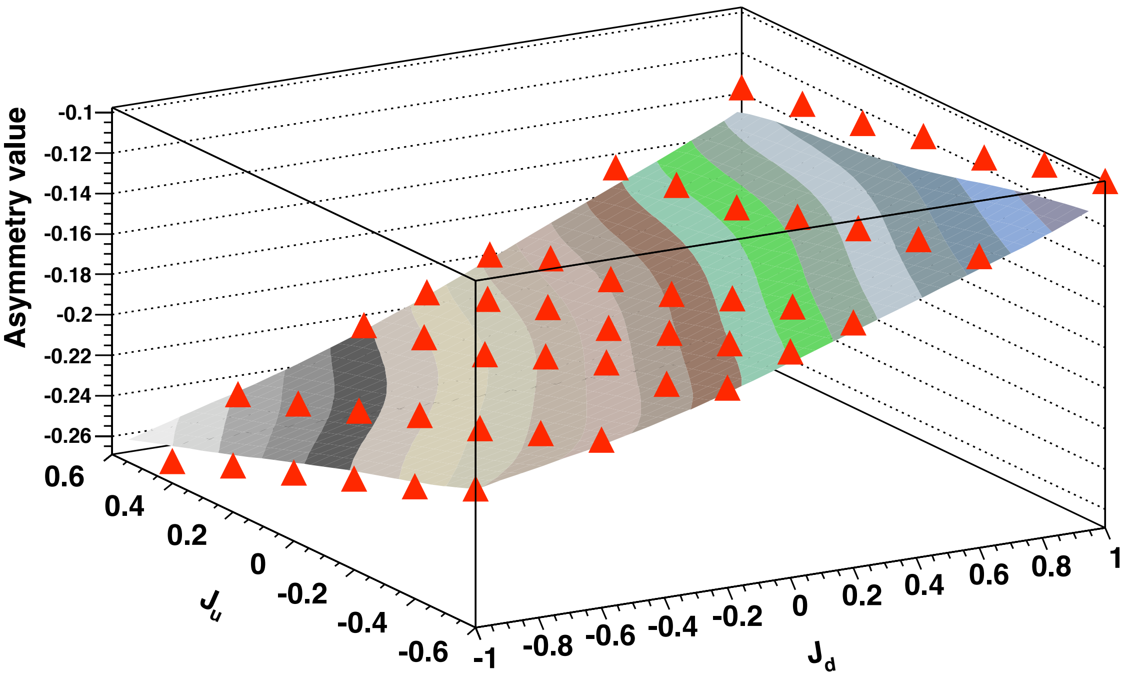

Figure 6.5: Dual Parameterisation model deuterium $\sin\phi$ asymmetry amplitude vs. J_u and J_d, calculated from equation (6.8). The surface is a result of a 2 dimensional, 5th order polynomial fit, whose shape is not distorted as seen in figure 6.1. The coloured bands illustrate the curvature of the fitted surface.

both similar to the variations given by the VGG results.

As per the VGG model results, the proton cross section is larger in magnitude than the neutron cross section. Thus the proton contribution dominates the calculated deuterium asymmetry from the Dual Parameterisation model, leading to a sensitivity similar to that of the proton rather than the neutron asymmetry.

6.6.2 Constraint of J_u and J_d using Deuterium from Dual Parameterisation Model

Following the same procedure as for the VGG model, the χ^2 difference between the Dual Parameterisation model deuterium asymmetry and the measured result given in equation (6.6) was calculated for each point in J_u/J_d space. A 2 dimensional, 5th order polynomial was fitted to these χ^2 points to produce the surface. The minimum

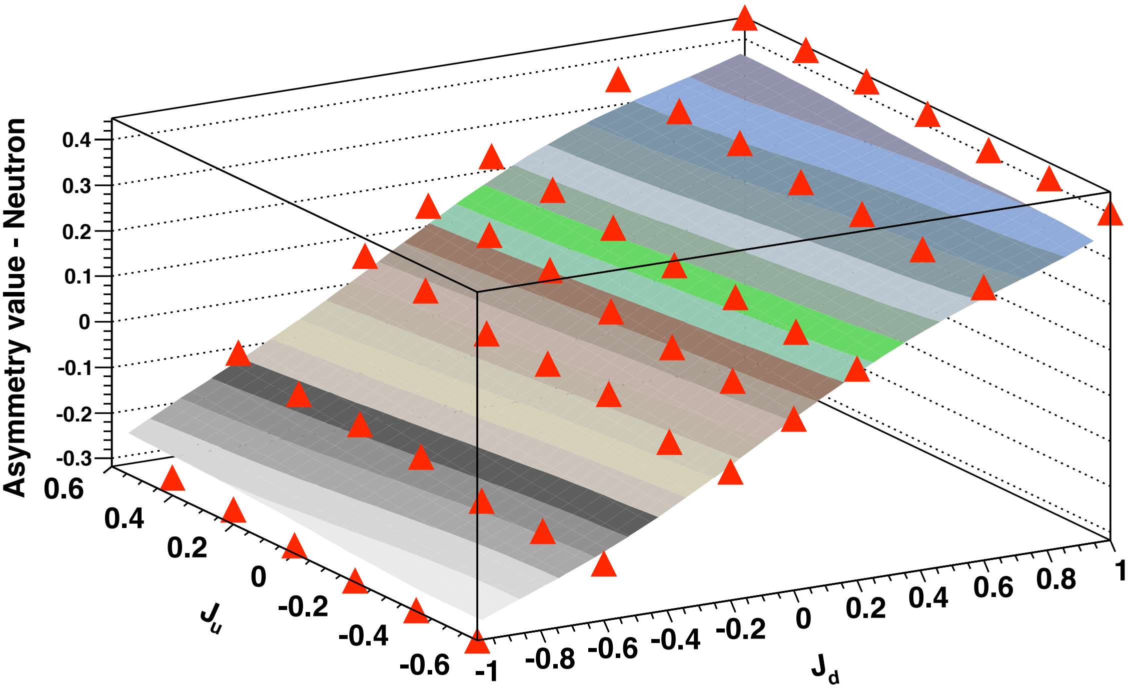

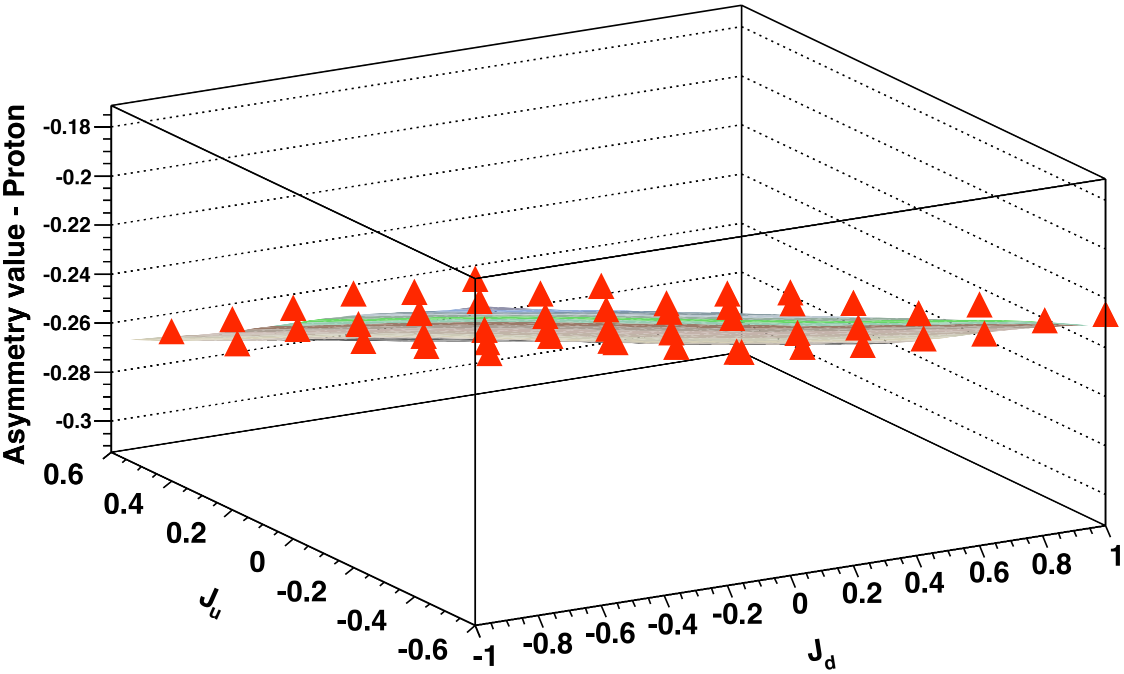

Figure 6.6: Dual Parameterisation model $\sin\phi$ asymmetry amplitude vs. J_u and J_d for neutron (top) and proton (bottom) targets, calculated from equation (6.7). The surfaces are a result of a 2 dimensional, 5th order polynomial fit. The neutron result shows the largest sensitivity to J_u and J_d as expected. As per the VGG results, the proton also shows some sensitivity, leading to problems when combining the two results using equation (6.8).

$\chi^2 + 1$ area was found and projected onto the $J_u - J_d$ axes, shown in figure 6.7.

The range of values of the Dual Parameterisation model asymmetry shown in figure 6.5, $-0.26 \leq A_{LU,I}^{\sin\phi} \leq -0.1$, is smaller than that of the VGG model results of figure 6.1, $-0.4 \leq A_{LU,I}^{\sin\phi} \leq -0.1$. When the χ^2 difference is calculated, the systematic and statistical uncertainties of the experimental result lead to a χ^2 value between the minimum, 0, and 1 across most of the given range of J_u and J_d. Thus the Dual Parameterisation model does not provide a useful constraint using this method.

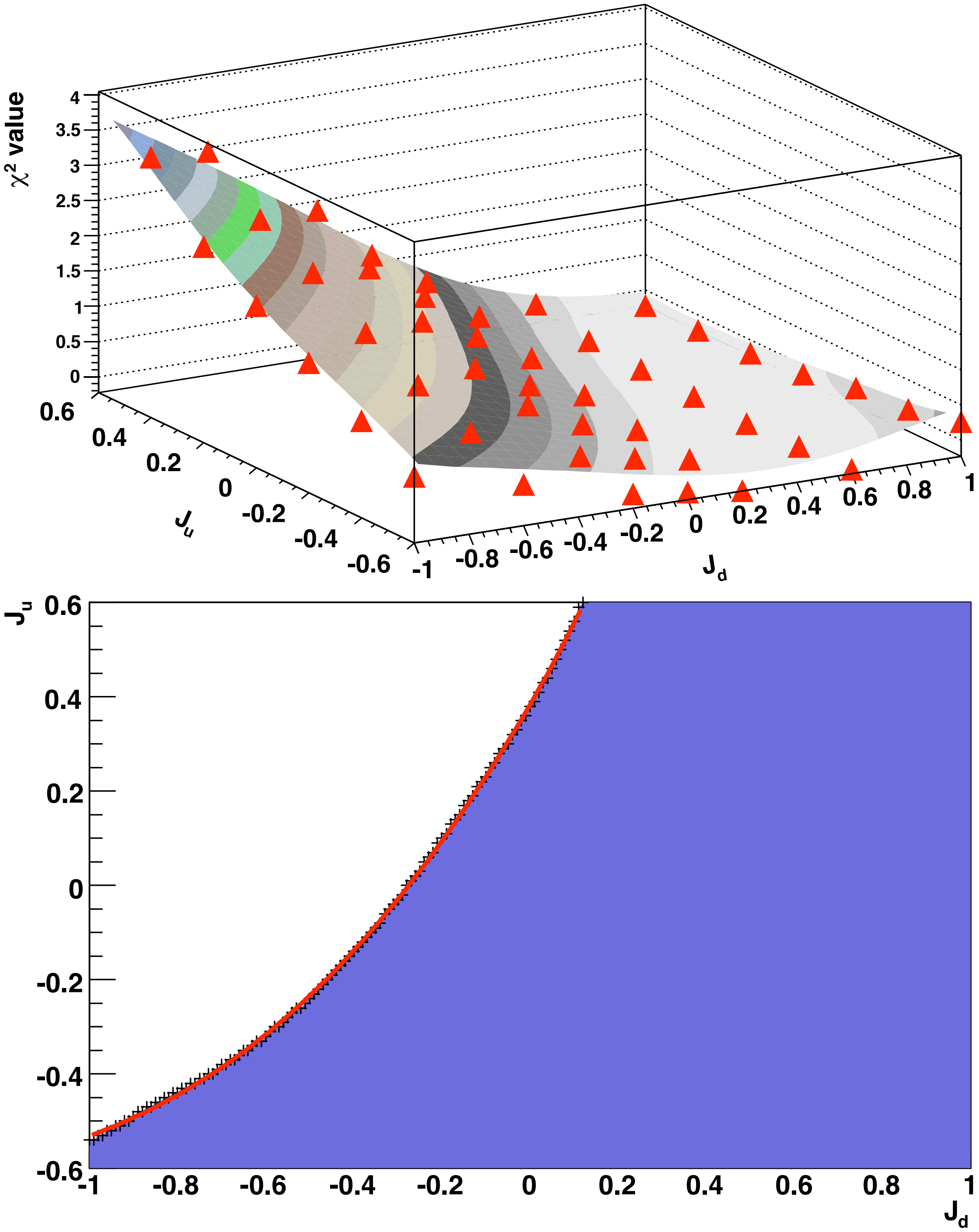

Figure 6.7: χ^2 difference calculated for each point calculated by the Dual Parameterisation model compared with the result in equation (6.6) (top). A 2 dimensional, 5th order polynomial was fitted to these points to produce the surface shown. The statistical and systematic uncertainties of the experimental result lead to a χ^2 value between 0 and 1 across the range of J_u and J_d when projected onto the $J_u - J_d$ axes (bottom). The shaded area indicates the constrained J_u, J_d values from this comparison of the Dual Parameterisation model and the HERMES deuterium data.

6.7 Constraint Comparison and Discussion

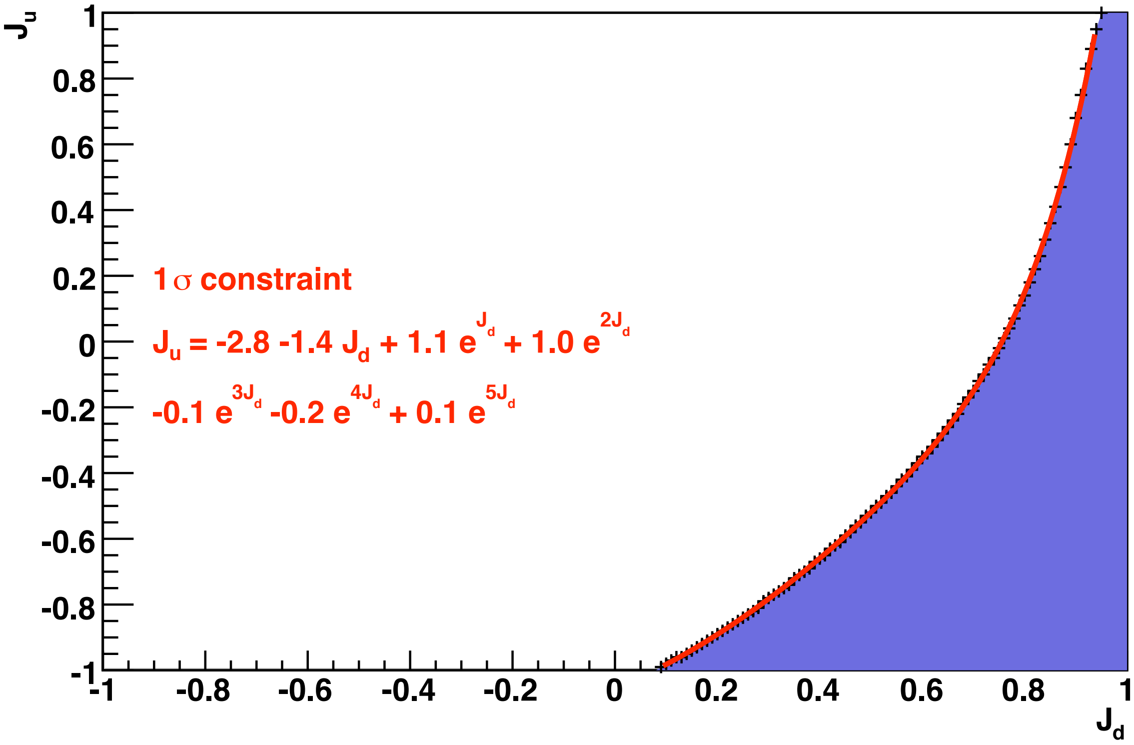

Figure 6.8: "1σ" constraint from VGG model, corresponding to the minimum $\chi^2 + 1$ surface projection shown in figure 6.3. The shaded area indicates the constrained J_u, J_d values from this comparison of the VGG model and the HERMES deuterium data.

Reference [A$^+$08] shows the constraints from HERMES transversely polarised hydrogen data and Jefferson Lab (JLab) unpolarised deuterium data. A comparison is now made with these constraints and those presented in this work from unpolarised deuterium data taken at HERMES. The constraint from HERMES deuterium data using the Dual Parameterisation model is not considered due to the breadth of the constraint. When considering the constraint from the Double Distribution model, the constraint arising from the minimum $\chi^2 + 1$, i.e. a "1σ" constraint shown in figure 6.8, does not coincide with both the HERMES and JLab results. By widening the constraint to 1.5σ and 2σ, shown in figure 6.9, the results are in agreement.

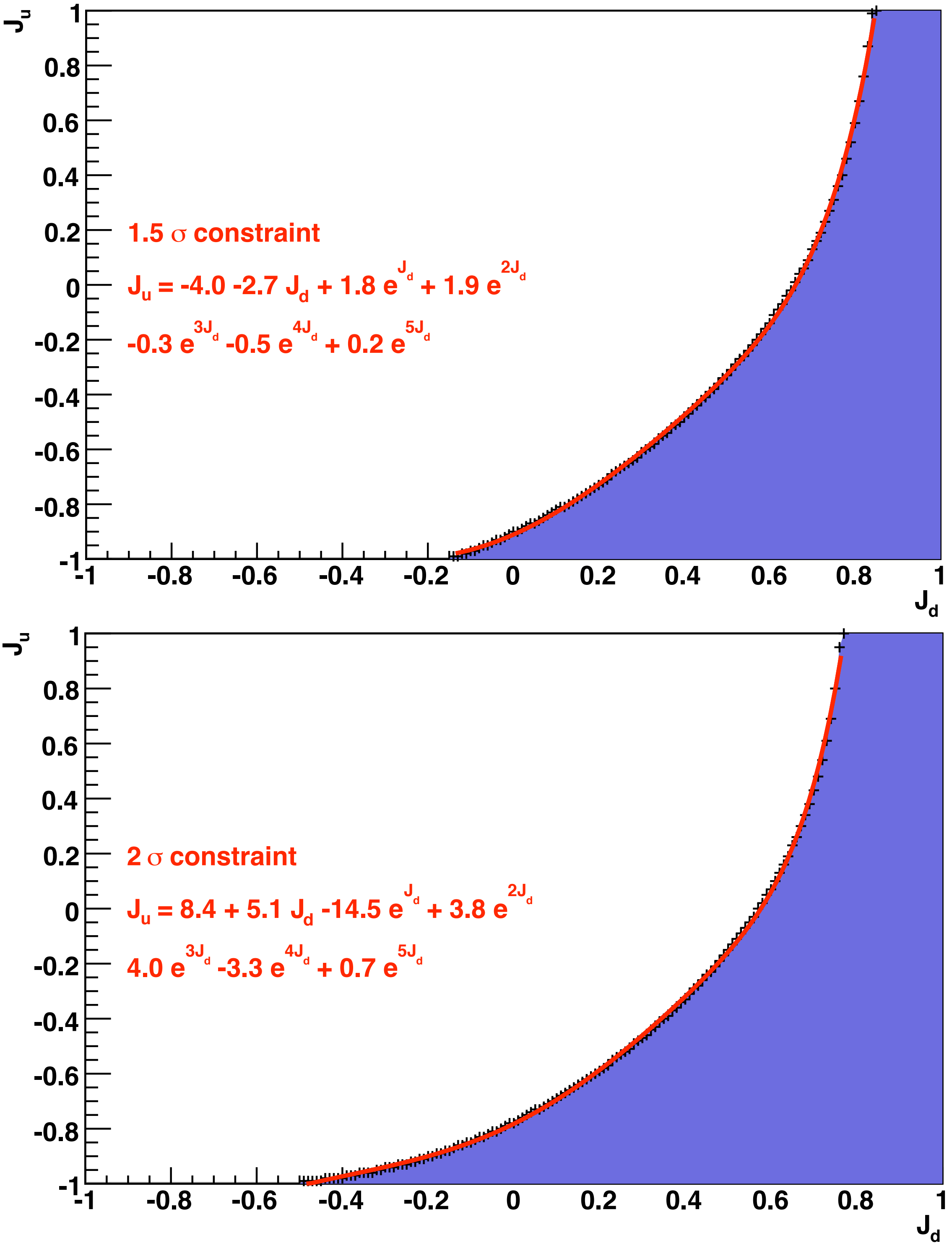

Figure 6.9: "1.5σ" constraint from VGG model (top) and "2σ" constraint (bottom), corresponding to the minimum $\chi^2 + 1.5$ and the minimum $\chi^2 + 2$ surface projections shown in figure 6.3. The shaded areas indicate the constrained J_u, J_d values from comparisons of the VGG model and the HERMES deuterium data.

For comparison, figure 6.10 includes the constraints shown in figures 6.8 and 6.9 to compare the various constraints. The three experimental results shown coincide in the green shaded region, but this region does not coincide with predictions by Lattice QCD and phenomenological models of GPDs by M. Diehl *et. al* [Kro07]. The experimental results from [M$^+$07, A$^+$08] do overlap this region.

A possible method has been outlined to constrain J_u and J_d using deuterium data taken at HERMES. However, the intersection of the calculated constraint from HERMES deuterium data with experimental constraints from hydrogen at HERMES and deuterium at Jefferson Lab Hall A do not agree with results from Lattice QCD. The HERMES proton and Hall A neutron constraints do intersect at an area approximately in agreement with Lattice QCD results.

The constraint is highly model dependent and relies on the sensitivity of the neutron BSA to J_u and J_d. The HERMES deuterium result cannot isolate the neutron BSA alone, therefore a model deuterium asymmetry calculated to compare with the experimental result. The neutron contribution to this model asymmetry is suppressed with respect to the proton contribution, while the proton demonstrates an unexpectedly large sensitivity to J_u and J_d, which dominates the neutron sensitivity.

In the future, GPD models of deuterium could provide a constraint from HERMES deuterium data. However, the deuteron is a spin-1 particle with 9 GPDs [KM03] and modern models are currently not available [Guz08b]. If models become available with a parameterisation of the deuteron GPDs using J_u and J_d as free parameters, a constraint from HERMES deuterium data could be made.

The highly model dependent bands of figure 6.10 illustrate that there is much work to be done before an experimental constraint on J_u and J_d can be obtained. However, they also illustrate that a process has been started that eventually, through improved models and higher precision data, from experiments such as those at Jefferson Lab and CERN, will yield such a constraint.

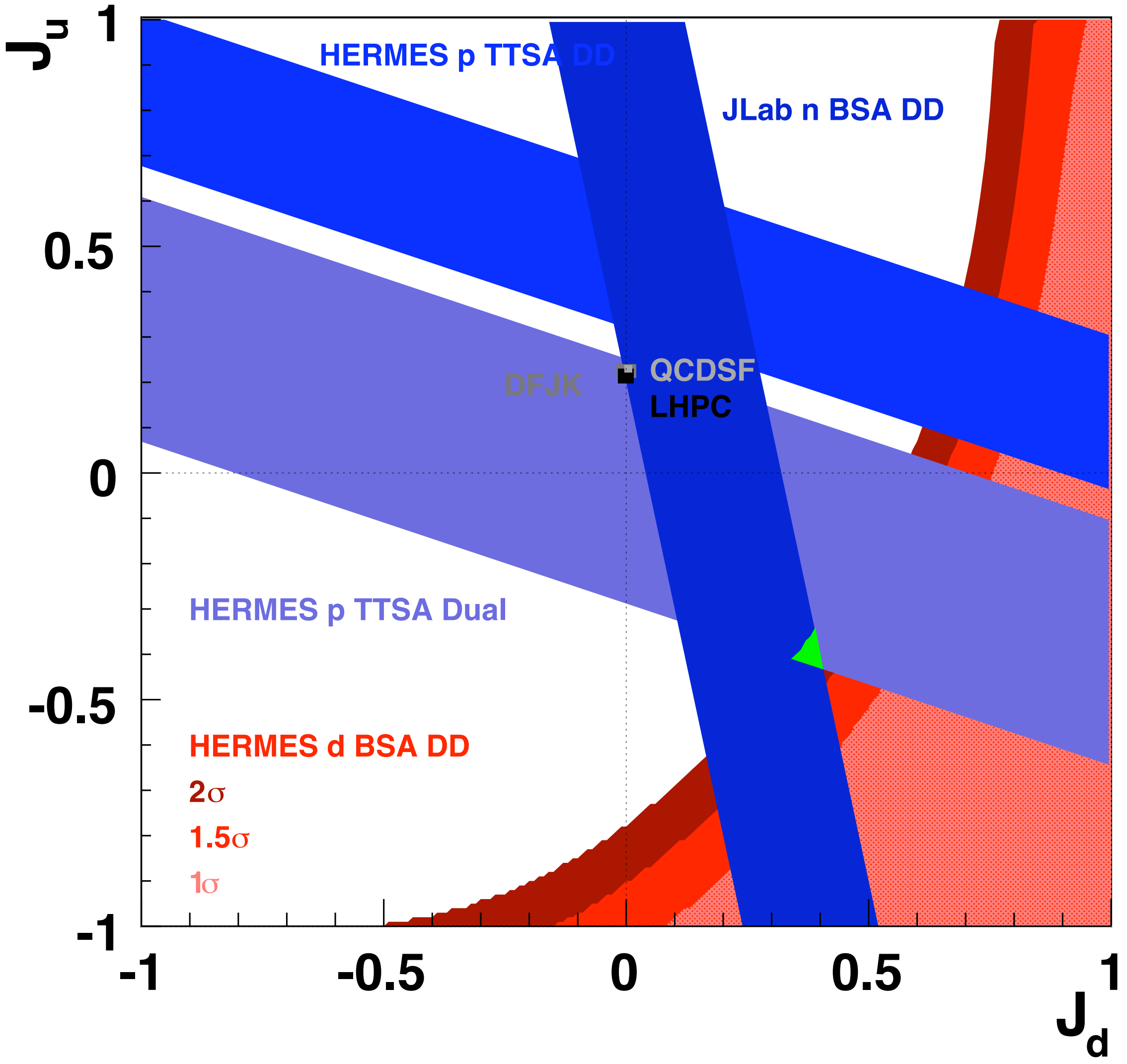

Figure 6.10: Constraints from HERMES transversely polarised proton data for Double Distribution (DD) and Dual Parameterisation (Dual) models and Jefferson Lab unpolarised deuterium data for the Double Distribution model, shaded blue. Results from Lattice QCD (QCDSF, [OBG$^+$07] and LHPC, [HSB$^+$08]) and phenomenological models (DFJK, [Kro07]) are also shown, shaded gray. Constraints from HERMES unpolarised deuterium for the Double Distribution model are shown, shaded red. Experimental results coincide in the green shaded region, however this does not match the predictions of Lattice QCD.

Chapter 7

Conclusion and Outlook

The hard electroproduction of a real photon and Deeply Virtual Compton Scattering-related process has been investigated using an unpolarised deuterium target at HERMES. This process is of physics interest as it allows access to the Generalised Parton Distribution framework, which in turn allows access to the total angular momentum of quarks in the nucleon. This forms one of the unknown pieces of the spin puzzle. One of the main goals of the HERMES experiment is to help to improve understanding of the contributions to the nucleon spin.

HERMES began the analysis of the DVCS process in 1998. The forward angle spectrometer was used to measure the final state photon and scattered lepton of the process, with the recoiling nucleon reconstructed using missing mass techniques for scattered nucleon detection. In November 2005 the Recoil Detector was installed to directly measure the recoiling nucleon, thus providing exclusive measurements at the event level.

A method for reconstructing the momentum of particles detected by the Recoil Detector has been investigated. Improvements to this method have been made based on studies of the method reconstruction accuracy and produced results. The method is now part of the standard software packages at HERMES. Members of the HERMES collaboration will use this method in future analysis of the DVCS process. Improvements will be made over the current DVCS analysis technique by allowing the recoiling nucleon to be identified. Events from associated production will be rejected, removing the largest source of background in current DVCS analyses at HERMES, to be studied in future work by the collaboration.

Measurements of the Beam Charge Asymmetry (BCA) and Beam Spin Asymmetries (BSA) from the DVCS squared term and Interference term of the $e\gamma X$ cross section have been made from DVCS/BH off an unpolarised deuterium target. These analyses use all data taken prior to the installation of the Recoil Detector, the largest data set currently available for DVCS-related analysis. Data quality cuts have been applied to obtain a DVCS candidate data sample, with sources of systematic uncertainty of the measurements also described.

Using results from this data analysis an investigation has been made into the constraint of the total angular momentum of up and down quarks in the nucleon, J_u and J_d. This constraint is heavily model dependent. The sensitivity of the experimental result arises from the dependence of the BSA from the neutron on the GPD E, which can be parameterised in terms of J_u and J_d. Due to the dominance of the proton contribution to the incoherent scattering cross section over the neutron contribution, the model used to describe the HERMES data does not provide a satisfactory constraint. Future models of GPDs which better describe the HERMES deuterium data may provide a new way to constrain J_u and J_d from this data.

Along with current and future exclusive analyses of DVCS at HERMES, measurements of DVCS are also made at experiments such as COMPASS at CERN and the Hall A and Hall B collaborations at Jefferson Lab. Each experiment covers a different kinematic range of the DVCS process, thus together provide valuable knowledge of DVCS and by extension GPDs. The upcoming upgrade of the Jefferson Lab accelerator to a 12 GeV electron beam will further improve the kinematic coverage of experimental measurements, see figure 7.1.

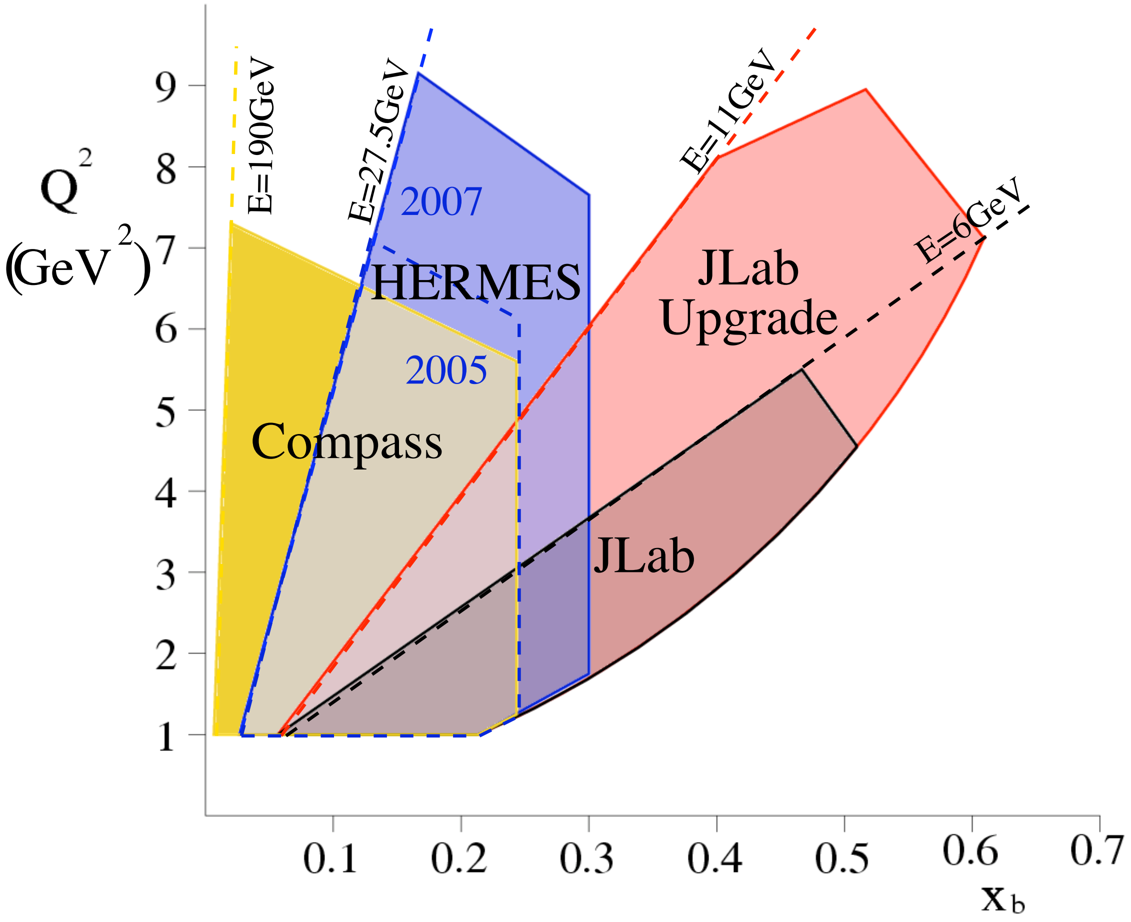

Figure 7.1: The DVCS kinematic range covered by DVCS experiments presently and over the next 15 years. The upgrade of JLab to a 12 GeV beam will further improve the kinematic coverage of experimental measurements. Taken from [Mur07].

Appendix A

Input to VGG Code

- 4: 2-body Doubly Polarised cross sections for (D)DVCS, polarised electron, polarised target.
- 3: Bethe-Heitler + DVCS contribution
- 1 (2): proton (neutron)
- 36: xi dependent parameterisation with MRST02 NNLO distribution
  N.B. chosen to match [M$^+$07]
- 2: evolution with scale_sqr = Q_sqr
- Give the value for the power b in the prole function for the valence contribution to H: 1
- Give the value for the power b in the prole function for the sea contribution to H: 9
- 2: Regge inspired ansatz for the t-dependence
- Enter slope alphap (GeV-2): 0.8
- 2: Do you want to evaluate the D-term contribution to GPD H? (No)
- 2: How do you want to evaluate GPD E? (double distribution contribution + D-term)

- 2: Give the model for the double distribution part of the GPD E (valence quark + VM contribution)
- (-1.0 - 1.0): Give the value of Ju (e.g. 0.3)
- (-1.0 - 1.0): Give the value of Jd (e.g. 0.1)
- 1: Do you want to evaluate the pi0 pole contribution (i.e. SPD Etilde)? (yes)
- 2: Include twist-3 corrections for L photon in Wandzura-Wilczek approximation
- 2: With (1) or without (2) Htilde ?
- 1: proton polarized along x-axis
- 2: positively charged lepton (HERMES, COMPASS)
  N.B. investigations showed that using (1) electron gave the same results with opposite sign, (2) positron was chosen to match the sign of the data asymmetry
- 27.56 - Give the value of beam energy in GeV (e.g. 27.)
- 3: As a function of Phi
- 2.894453: Give the value of Q^2 in GeV^2 (e.g. 5.0)
- 0.110276: Give the value of x B (e.g. 0.3)
- 0: Give the value of $Qprime^2$ in GeV^2 (e.g. 2.0)
- 0.204835: Give the value of -t (in GeV^2)
- 0: Give the first value for the angle phi (in deg) to calculate
- 10: Give the step in the angle phi (in deg) (e.g. 10.)
- 180: Give the last value in the angle phi (in deg) (e.g. 180.)

Bibliography

[A+76] M. J. Alguard et al. Deep inelastic scattering of polarized electrons by polarized protons. *Phys. Rev. Lett.*, 37:1261, 1976.

[A+88] J. Ashman et al. An Investigation of the Spin Structure of the Proton in Deep-Inelastic Scattering of Polarized Muons. *Phys Lett B*, 206:364, 1988.

[A+89] J. Ashman et al. An Investigation of the Spin Structure of the Proton in Deep-Inelastic Scattering of Polarized Muons on Polarized Protons. *Nucl. Phys.*, B328:1, 1989.

[A+98a] The HERMES Collaboration: K. Ackerstaff et al. The HERMES Spectrometer. *NIM A*, 417:230, 1998.

[A+98b] H. Avakian et al. Performance of the Electromagnetic Calorimeter of the HERMES Experiment. *NIM A*, 417:69, 1998.

[A+01] The HERMES Collaboration: A. Airapetian et al. Measurement of the Beam-Spin Azimuthal Asymmetry Associated with Deeply-Virtual Compton Scattering. *Phys. Rev. Lett.*, 87:182001, 2001.

[A+07a] The HERMES Collaboration: A. Airapetian et al. Precise Determination of the Spin Structure Function g1 of the Proton, Deuteron, and Neutron. *Phys. Rev.*, D75:012007, 2007.

[A+07b] The HERMES Collaboration: A. Airapetian et al. The Beam–Charge Azimuthal Asymmetry and Deeply Virtual Compton Scattering. *Phys. Rev. D*, 75:011103, 2007.

[A^+08] The HERMES Collaboration: A. Airapetian et al. Measurement of Azimuthal Asymmetries With Respect To Both Beam Charge and Transverse Target Polarization in Exclusive Electroproduction of Real Photons. *JHEP*, 06:066, 2008.

[B^+94] D. P. Barber et al. The HERA Polarimeter and the First Observation of Electron Spin Polarization at HERA. *NIM A*, 338:166, 1994.

[B^+01] T. Benisch et al. The luminosity monitor of the HERMES experiment at DESY. *Nuclear Instruments and Methods A*, 471:314–324, 2001.

[B^+02] M. Beckmann et al. The Longitudinal Polarimeter at HERA. *NIM A physics/0009047 DESY 00-106*, 479:334–348, 2002.

[B^+03] C. Baumgarten et al. A Gas Analyzer for the Internal Polarized Target of the HERMES Experiment. *NIM A*, 508:268, 2003.

[Bar90] R. Barlow. Extended Maximum Likelihood. *Nuclear Instruments and Methods*, A 297:496–506, 1990.

[Bas08] S. Bass. *The Spin Structure of the Proton.* World Scientific, 2008.

[BDDM04] A. Bacchetta, U. D'Alesio, M. Diehl, and C. A. Miller. Single-spin Asymmetries: The Trento Conventions. *Phys. Rev. D*, 70:117504, 2004.

[Bev94] R. Bevington. *Data Reduction and Error Analysis for the Physical Sciences.* McGraw-Hill, 1994.

[BM81] L. Bugge and J. Myrheim. Tracking and Track Fitting. *Nuclear Instruments and Methods*, 179:365 – 381, 1981.

[BMK02] A. V. Belitsky, D. Muller, and A. Kirchner. Theory of Deeply Virtual Compton Scattering on the Nucleon. *Nuclear Physics B*, 629:323, 2002.

[BS86] J. Buon and K. Steffen. HERA Variable-Energy “Mini” Spin Rotator and Head-on ep Collision Scheme with Choice of Electron Helicity. *NIM A*, 245 (2):248–261, 1986.

[Bur04] M. Burkardt. Generalized Parton Distributions for Large x. *Phys. Lett. B*, 595:245, 2004.

[Cha93] G. Charpak. Electronic imaging of ionizing radiation with limited avalanches in gases. *Rev. Mod. Phys.*, 65(3):591 – 598, 1993.

[Col93] The HERMES Collaboration. HERMES Collaboration Technical Design Report. HERMES Internal Report 93-015, July 1993.

[Col02] The HERMES Collaboration. The HERMES Recoil Technical Design Report. HERMES Internal Report 02-003, 2002.

[Col07] The HERMES Collaboration. Shift Primer. *HERMES Internal Document, unpublished*, 2007.

[Die07a] M. Diehl. GPDs: physics, properties, and models. Lectures at HERMES DVCS Week, unpublished, September 2007.

[Die07b] M. Diehl. Private communications, November 2007.

[DMR$^+$88] F. M. Dittes, Dieter Mueller, D. Robaschik, et al. The Altarelli-Parisi Kernel as Asymptotic Limit of an Extended Brodsky-Lepage Kernel. *Phys. Lett.*, B209:325–329, 1988.

[DPP89] D. Diakonov, V. Yu. Petrov, and M. Praszalowicz. Nucleon Mass and Nucleon Sigma Term. *Nucl. Phys.*, B323:53, 1989.

[Due95] M. Dueren. The HERMES Experiment: From the Design to the First Results, 1995. Habilitation thesis, University Erlangen-Nuernberg, DESY Grey Report: DESY-HERMES 95-02.

[Ell04] F. Ellinghaus. *Beam Charge and Beam Spin Azimuthal Asymmetries in Deeply Virtual Compton Scattering*. PhD thesis, DESY-Thesis-2004-005, 2004.

[Els02] U. Elschenbroich. Analysis of Luminosity Data for Different Years. HERMES Internal Report 02-013, 2002.

[Els03] U. Elschenbroich. Single Spin Azimuthal Asymmetry in Exclusive Electroproduction of ρ^0 Mesons. HERMES Release Report, February 2003.

[F$^+$00] R. Fruehwirth et al. *Data Analysis Techniques for High Energy Physics.* Cambridge University Press, 2nd edition, 2000.

[Fey69] R. P. Feynman. Very High-Energy Collisions of Hadrons. *Phys. Rev. Lett.*, 23(24):1415–1417, December 1969.

[Fru87] R. Fruehwirth. Application of Kalman Filtering to Track and Vertex Fitting. *Nuclear Instruments and Methods in Physics Research*, A 262:444–450, 1987.

[GHH$^+$07] M. Gockeler, Ph Hagler, R. Horsley, et al. Probing Nucleon Structure on the Lattice. *Eur. Phys. J.*, A32:445–450, 2007.

[GM64] M. Gell-Mann. A schematic model of baryons and mesons. *Phys. Lett*, 8:214–15, 1964.

[GPV01] K. Goeke, M. V. Polyakov, and M. Vanderhaeghen. Hard Exclusive Reactions and the Structure of Hadrons. *Progress in Particle and Nuclear Physics*, 47:401, 2001.

[GT06] V. Guzey and T. Teckentrup. The dual parameterization of the proton generalized parton distribution functions H and E and description of the DVCS cross sections and asymmetries. *Phys. Rev. D*, 74:054027, 2006.

[Guz08a] V. Guzey. Neutron contribution to nuclear DVCS asymmetries. *0801.3235*, 2008.

[Guz08b] V. Guzey. Private communications, January 2008.

[Haa05] S. Haan. Deeply virtual compton scattering on neon. Master's thesis, Universitaet Leipzig, 2005.

[Hoe06] M. Hoek. *Design and Construction of a Scintillating Fibre Tracker for measuring Hard Exclusive Reactions at HERMES.* PhD thesis, Universitaet Giessen, 2006.

[HS84] J. C. Hart and D. H. Saxon. Track and vertex fitting in an inhomogeneous magnetic field. *Nuclear Instruments and Methods in Physics Research*, 220:309–326, 1984.

[HSB+08] Ph. Hagler, W. Schroers, J. Bratt, et al. Nucleon Generalized Parton Distributions from Full Lattice QCD. *Phys. Rev. D*, 77:094502, 2008.

[Jaf96] R. L. Jaffe. Spin, twist and hadron structure in deep inelastic processes. Notes for Lectures Presented at the International School of Nucleon Structure, The Spin Structure of the Nucleon, Erice, 3–10 August 1995, 1996.

[Ji97a] X. Ji. Deeply Virtual Compton Scattering. *Phys. Rev. D*, 55:7114, 1997.

[Ji97b] X. Ji. Gauge-Invariant Decomposition of Nucleon Spin and Its Spin-Off. *Phys. Rev. Lett.*, 78:610, 1997.

[JR75] F. James and M. Roos. Minuit: A System for Function Minimization and Analysis of the Parameter Errors and Correlations. *Comput. Phys. Commun.*, 10:343–367, 1975.

[K+01] R. Kaiser et al. A large acceptance recoil detector for HERMES. *DESY-PRC*, page 36, 2001. DESY-PRC-97-06-ADD.

[Kai97] R. Kaiser. *Measurement of the Spin Structure of the Neutron using Polarised Deep Inelastic Scattering.* PhD thesis, Simon Fraser University, 1997.

[KM03] A. Kirchner and D. Muller. Deeply virtual Compton scattering off nuclei. *European Physical Journal C*, 32:347, 2003.

[KN02] V. A. Korotkov and W. D. Nowak. Future Measurements of Deeply Virtual Compton Scattering at HERMES. *European Physical Journal C*, 23:455, 2002.

[Kop06] M. Kopytin. *Longitudinal Target-Spin Azimuthal Asymmetry in Deeply-Virtual Compton Scattering.* PhD thesis, Humboldt-Universitaet zu Berlin, August 2006.

[Kra05] B. Krauss. *Deeply Virtual Compton Scattering and the HERMES-Recoil Detector*. PhD thesis, Friedrich-Alexander-Universitaet Erlangen-Nuernberg, 2005.

[Kro07] P. Kroll. Hard exclusive scattering at Jlab, 2007. Invited talk presented at the workshop on Exclusive Processes at High Momentum Transfer, Newport News, Virginia USA, May 2007.

[LA88] E. Leader and M. Anselmino. A crisis in the parton model: where, oh where is the proton's spin? *Z. Phys.*, C41:239, 1988.

[LAC86] L. Lyons, W.W.M. Allison, and J. Pañella Comellas. Maximum Likelihood or Extended Maximum Likelihood? An Example from High Energy Physics. *Nuclear Instruments and Methods*, A245:530–534, 1986.

[LB80] G. P. Lepage and S. J. Brodsky. Exclusive Processes in Pertubative Quantum Chromodynamics. *Phys. Rev. D*, 22:2157, 1980.

[LPR$^+$06] I. Lehmann, V. Prahl, C. Riedl, et al. Heating Studies on the HERMES Target Cell. *HERMES Internal Report*, 06-080, 2006.

[LY07] X. Lu and Z. Ye. Simultaneous Extraction of the BSAs and the BCA Associated with DVCS with the Extended Maximumn Likelihood Method. HERMES Internal Note, February 2007.

[M$^+$07] M. Mazouz et al. Deeply Virtual Compton Scattering off the Neutron. *Physical Review Letters*, 99:242501, 2007.

[Mak02] N. C. R. Makins. HERMES Software Boot Camp. HERMES Internal Documentation, 2002.

[MHM$^+$08] H. Marukyan, G. Hill, C. A. Miller, et al. DVCS Analysis on Unpolarized Deuterium. *HERMES Internal Release Report, unpublished*, 2008.

[MR00] I. V. Musatov and A. V. Radyushkin. Evolution and Models for Skewed Parton Distributions. *Phys. Rev. D*, 61:074027, 2000.

[MRG+94] D. Mueller, D. Robaschik, B. Geyer, et al. Wave Functions, Evolution Equations and Evolution Kernels from Light-Ray Operators of QCD. *Fortschritte der Physik*, 42:101, 1994.

[MRS+03] A. D. Martin, R. G. Roberts, W. J. Stirling, et al. Uncertainties of Predictions from Parton Distributions. I: Experimental errors. ((T)). *Eur. Phys. J.*, C28:455–473, 2003.

[Mue08] D. Mueller. Private communications, March 2008.

[Mur07] M. Murray. *DVCS at HERMES: The Recoil Detector & Transverse Target Spin Asymmetries.* PhD thesis, University of Glasgow, 2007.

[N+03] A. Nass et al. The HERMES polarized atomic beam source. *NIM A*, 505:633, 2003.

[OBG+07] QCDSF/UKQCD Collaboration: M. Ohtani, D. Brommel, M. Gockeler, et al. Moments of generalized parton distributions and quark angular momentum of the nucleon, 2007. Presented at 25th International Symposium on Lattice Field Theory, Regensburg, Germany, 30 Jul – 4 Aug 2007.

[Osb06] A. Osborne. *Exclusive ρ^0 Meson Cross Section Ratios on Deuterium and Hydrogen Targets.* PhD thesis, University of Glasgow, 2006.

[Pol99] M. V. Polyakov. Hard exclusive electroproduction of two pions and their resonances. *Nuclear Physics B*, 555:231, 1999.

[PS02] M. V. Polyakov and A. G. Shuvaev. On ”dual” parametrizations of generalized parton distributions. hep-ph/0207153, 2002.

[PTG93] ECP Division Programming Techniques Group. *ADAMO Reference Manual.* CERN, 3.3 edition, December 1993.

[PW99] M. V. Polyakov and C. Weiss. Skewed and Double Distributions in Pion and Nucleon. *Phys. Rev. D*, 60:114017, 1999.

[Rad97] A. V. Radyushkin. Nonforward parton distributions. *Phys. Rev. D*, 56:5524, 1997.

[Rad99] A. V. Radyushkin. Double Distributions and Evolution Equations. *Phys. Rev. D*, 59:014030, 1999.

[Rad00] A. V. Radyushkin. Generalized Parton Distributions. *hep-ph/0101225*, 2000.

[S$^+$01] CLAS Collaboration: S. Stepanyan et al. Observation of exclusive DVCS in polarized electron beam asymmetry measurements. *Phys. Rev. Lett.*, 87:182002, 2001.

[Sch07] L. Schoeffel. Deeply Virtual Compton Scattering at HERA II. *arXiv:0705.2925v2 [hep-ph]*, 2007.

[She05] C. Shearer. *Spin Density Matrix Element Extraction for the ρ^0 Vector Meson on Hydrogen and Deuterium Targets at HERMES.* PhD thesis, University of Glasgow, 2005.

[SPI08] SPIRES High-Energy Physics Literature Database. http://www.slac.stanford.edu/spires/hep, 2008.

[ST64] A. A. Sokolov and I. M. Ternov. On polarization and spin effects in synchrotron radiation theory. *Sov. Phys. Doklady*, 8:1203, 1964.

[TW01] A. W. Thomas and W. Weise. *The Structure of the Nucleon.* Wiley-VCH, 2001.

[VGG99] M. Vanderhaeghen, P. A. M. Guichon, and M. Guidal. Deeply Virtual Electroproduction of Photons and Mesons on the Nucleon : Leading Order Amplitudes and Power Corrections. *Physical Review D*, 60:094017, 1999.

[VGG03] M. Vanderhaeghen, P. A. M. Guichon, and M. Guidal. Computer Code for the Calculation of DVCS and BH Processes in the Reaction $ep \rightarrow e'p'\gamma$. Private Communications, 2003.

[Wak07] M. Wakamatsu. On the D-term of the nucleon generalized parton distributions. *Phys. Lett. B*, 648:181–185, 2007.

[Wan95] W. Wander. DAD - Distributed ADAMO Database System at HERMES. Proceedings of CHEP 95, Rio de Janeiro, 1995.

[Wan97] W. Wander. *Reconstruction of High Energy Scattering Events in the HERMES Experiment.* PhD thesis, Friedrich-Alexander-Universitaet Erlangen-Nuernberg, 1997.

[Ye06] Z. Ye. *Transverse Target-Spin Asymmetry Associated with Deeply Virtual Compton Scattering on the Proton and A Resulting Model-Dependent Constraint on the Total Angular Momentum of Quarks in the Nucleon.* PhD thesis, Universitaet Hamburg, 2006.

[Ye08] H. Ye. Private communications, February 2008.

[YM08] H. Ye and H. Marukyan. Nuclear DVCS Analysis. *HERMES Release Report*, 2008.

[Zih04] B. Zihlmann. Magnet status. Recoil Group Meeting, DESY Hamburg, 2004.

[ZL08] D. Zeiler and X. Lu. Combined Analysis of the Deeply Virtual Compton Scattering Process on the Proton. *HERMES Internal Release Report, unpublished*, 2008.